THÈSE

présentée en vue de l'obtention du

DOCTORAT DE L'UNIVERSITÉ PARIS 7 - DENIS-DIDEROT

Spécialité: Astrophysique et Méthodes Associées

par

RICARDO DEMARCO

Propriétés physiques et l'évolution des Baryons dans les amas de galaxies proches et distants.

Soutenue le 11 décembre 2003 devant le jury composé de

Mme. Monique Arnaud	Examinateur
M. James G. Bartlett	Président
Mme. Florence Durret	Directrice de thèse
M. Guy Mathez	Rapporteur
Mme. Sophie Maurogordato	Rapporteur
M. Piero Rosati	Co-Directeur de thèse

Institut d'Astrophysique de Paris - European Southern Observatory

Résumé de la Thèse

Mon travail de thèse s'inscrit dans le cadre de la formation et de l'évolution des galaxies et des amas de galaxies. Ces structures, constituant l'Univers actuel, résulteraient de la croissance de fluctuations primordiales probablement d'origine quantique (par exemple dans le cas de modèles inflationnaires) d'un champ gaussien. Cet univers, chaud a l'origine, subit jusqu'à présent un phénomène d'expansion qui a pour effet de le refroidir.

Sous l'effet de la gravité, les fluctuations primordiales suffisamment importantes peuvent alors croˆet certaines peuvent aller jusqu'à se découpler localement de l'expansion générale subie par l'univers et ses grandes structures. Ce phénomène, *l'instabilité gravitationnelle*, est selon l'hypothèse actuelle, le mécanisme de formation des structures observées aujourd'hui: galaxies, amas de galaxies, filaments, etc ...

Dans cette évolution cosmologique des structures, les amas de galaxies jouent un rôle primordial. En effet, ce sont les systèmes liés gravitationnellement les plus massifs qui ont gardé jusqu'à aujourd'hui des informations sur leurs conditions initiales. Ils ont donc un rôle cosmologique de grande importance. Leur étude permet de comprendre la physique impliquée dans les procédés de formation et d'évolution des systèmes auto-gravitants jusqu'à l'époque actuelle. De plus, ils représentent des laboratoires idéaux pour étudier les effets d'environnement sur la formation et l'évolution des galaxies. Il s'avère donc très utile d'étudier ces systèmes sur les échelles de temps les plus grandes possibles, c'est à dire depuis les époques les plus reculées de l'Univers jusqu'à son âge actuel. Un tel axe de recherche permet à la fois d'obtenir des informations de nature cosmologique, c'est à dire concernant les propriétés statistiques de la formation des structures, et d'étudier la formation et l'évolution de structures de plus petite échelle telles que les galaxies elliptiques.

Dans ce cadre de recherche, mes travaux se sont concentrés sur deux sujets principaux:

- l'étude des propriétés thermodynamiques et relations d'échelle dans les amas proches (Demarco et al. 2003).
- l'étude des propriétés spectro-photométriques des galaxies dans les

amas distants (Lidman et al. 2003; Rosati et al. 2004; Blakeslee et al. 2003; Toft et al. 2003)

L'étude des amas proches

Même si l'hypothèse de formation des amas de galaxies par amplification gravitationnelle de fluctuations primordiales est communément admise, les détails de ces procédés de formation ne sont pas compris dans leur totalité. L'étude de la structure et des propriétés des halos de matière noire (Dark Matter, DM) ainsi que le plasma inter-amas (Intra Cluster Medium, ICM) des systèmes virialisés apportent d'importantes informations concernant la physique impliquée dans les processus de formation et d'évolution des amas de galaxies. De nos jours, ces études ont connu d'importantes améliorations grâce au développement des techniques d'observation, couplées aux simulations numériques réalisées sur des ordinateurs de plus en plus performants.

De nombreux travaux récents se sont axés sur ce sujet. Des études de la matière noire froide (Cold Dark Matter, CDM) ont été réalisées à l'aide de simulations numériques à N corps par Navarro et al. (1996, 1997). Elles ont suggéré un profil de matière noire universel dans les galaxies et les amas de galaxies, indépendamment de leur masse ou de la cosmologie considérée. Cependant ce résultat a été contredit par Jing & Suto (2000). Du côté observationnel, de nombreux travaux semblent montrer un désaccord entre le profil mentionné ci-dessus et celui mesuré au centre des galaxies à faible brillance de surface (Low Surface Brightness, LSB; Flores & Primack 1994; Moore et al. 1999). Bien que d'autres travaux prétendent que les données disponibles pour les galaxies naines ainsi que les LSB sont en accord avec le profil universel (van den Bosch & Swaters 2001), les études de micro-lentilles gravitationnelles en direction du centre de notre galaxie soutiennent l'incompatibilité existante entre les profils prédits par les simulations numériques et l'évidence observationnelle (Binney & Evans 2001).

Afin de participer à ce débat et d'y apporter de nouveaux éléments, nous nous sommes tournés vers un autre type de données observationnelles: les rayons X. A l'échelle des amas de galaxie, observer dans ce domaine de longueurs d'ondes permet d'obtenir d'importantes informations concernant le milieu chaud intra-amas (ICM). La distribution de la densité de ce milieu ainsi que la répartition de température au sein d'un amas de galaxies sont des quantités d'importance fondamentale car elles permettent de déterminer la distribution d'entropie spécifique de l'ICM, donnant ainsi d'importantes informations concernant les processus non gravitationnels internes et externes qui peuvent contribuer à l'histoire thermique de l'ICM. Ces processus sont par exemple le préchauffage externe, l'injection d'énergie par les vents résultant de l'explosion de supernovae (Brighenti & Mathews 2001; Dos Santos & Doré 2002).

La première étude présentée dans cette thèse s'intéresse aux propriétés physiques du gaz à l'intérieur des amas de galaxies (Demarco et al. 2003), basée sur des observations du satellite ROSAT.

Elle repose sur l'idée suivante: partant de l'hypothèse selon laquelle le plasma observé en rayons X dans les amas de galaxies est faiblement dissipatif, les amas considérés comme structures auto-gravitantes possèdent très probablement des propriétés similaires à celles trouvées récemment dans les galaxies elliptiques, elles aussi considérées comme des systèmes auto-gravitants. Plus précisément, les galaxies elliptiques semblent avoir une entropie spécifique intégrée constante et obéir à une relation d'échelle qui relie leur énergie potentielle à leur masse. Ces propriétés peuvent être interprétées comme dues à des processus physiques impliqués dans la formation et l'évolution de ces structures.

Les halos de matière noire modélisés au moyen de simulations numériques présentent également de telles relations d'échelle, c'est à dire reliant leur énergie potentielle à leur masse avec des caractéristiques similaires à celles obtenues dans le cas des galaxies elliptiques. De plus, ces relations sont très proches de celles obtenues à partir de considérations théoriques très simples.

Nous avons donc voulu tester ces hypothèses pour le gaz intra-amas et les halos de matière noire dans les amas de galaxies. Pour cela, nous avons analysé des images obtenues avec le détecteur PSPC du satellite ROSAT pour 24 amas de galaxies et ajusté une loi de Sérsic aux profils de densité du gaz de façon à reproduire leur brillance de surface dans le domaine des rayons X. Ces amas sont des systèmes proches, avec des décalages vers le rouge entre 0.01 et 0.3. Notre analyse de ces amas nous a conduits à des résultats nouveaux et intéressants qui nous donnent des indices pour mieux comprendre la physique présente dans la formation de ce type de structures. Les résultats les plus importants sont :

- Le profil de Sérsic peut aussi être utilisé pour décrire la distribution de gaz dans le milieu intra-amas. Ce profil, qui ne requiert pas l'hypothèse d'un milieu à température uniforme, peut être considéré comme une alternative au modèle isotherme couramment utilisé, appelé β-model.

- Au première ordre, l'entropie spécifique intégrée sur tout l'amas est à peu près la même dans tous les amas. La même conclusion est obtenue pour la matière noire. Ce résultat est analogue à l'entropie spécifique presque constante trouvée par Lima Neto et al. (1999) parmi les galaxies elliptiques dans des amas de galaxies.

- Au deuxième ordre, l'entropie spécifique intégrée sur tout l'amas est proportionnelle au logarithme de la masse du gaz. D'une façon analogue, l'entropie spécifique intégrée de la matière noire est proportionnelle au logarithme de la masse de la matière noire. Ce résultat est aussi analogue à celui trouvé pour les galaxies elliptiques dans des amas de galaxies et pour des galaxies modelisées numériquement (Márquez et al. 2000, 2001).

- L'énergie potentielle de l'amas est corrélée à sa masse dynamique. Cette corrélation est très proche de la relation auto-similaire théorique $U \propto M^{5/3}$ déduite à partir de la conservation de la masse et de l'énergie d'une structure pendant toute son évolution. Ce comportement est aussi observé dans des galaxies elliptiques réelles (Márquez et al. 2001) et tirées des simulations numériques (Lanzoni 2000; Jang-Condell & Hernquist 2001).

Au vu des similitudes entre les rélations d'échelle observées dans les amas de galaxies et les galaxies elliptiques on peut donc considérer les galaxies elliptiques comme des amas miniature. Les relations entropie-masse et énergie potentielle-masse sont des conséquences des processus physiques suivis par ces structures au cours de leur histoire évolutive. Des fénomènes de fusion entre amas et de dissipation d'énergie jouent un rôle important dans la production de l'entropie, sans affecter la conservation de masse et d'énergie pendant la formation et l'évolution des amas.

L'étude des amas distants

Comprendre l'histoire de la formation des galaxies est un des sujets très etudiés aujourd'hui en cosmologie observationnelle. Le développement des techniques observationnelles plus avancées et des télescopes plus puissants permet maintenant de faire la découverte de galaxies très lointaines (e.g. Steidel et al. 1996, 1999; Dey et al. 1998) et d'obtenir une vue sans précédent des populations de galaxies dans l'univers distant ($z > 1$), un pas crucial dans la recherche de l'époque de la première lumière des galaxies. Une vision complète du problème en question doit inclure l'étude des galaxies dans le champ et dans les amas de galaxies.

Bien qu'il y ait encore beaucoup à apprendre de l'étude des galaxies de type tardif, dans ce travail de thèse je me suis concentré sur les galaxies de type précoce, une classe d'objets qui a été le sujet d'un grand nombre d'études pendant les dernières années car ce sont les galaxies les plus massives connues et qui ont des populations d'étoiles vieilles.

Les galaxies de type précoce dans les amas proches montrent des régularités remarquables dans leurs propriétés spectro-photométriques comme par exemple le plan fondamental et la relation couleur-magnitude (CM). L'environnement joue un rôle important dans ces caractéristiques, et puisque les amas représentent des régions spéciales dans l'univers et peuvent être détectés à grand décalage spectral, les amas constituent des laboratoires idéaux pour étudier les effets de l'environnement sur les propriétés des galaxies.

Pour expliquer la formation des galaxies de type précoce, deux modèles ont été proposés : celui appelé le Modèle Classique (e.g. Eggen, Lynden-

Bell & Sandage 1962; Larson 1975; Arimoto & Yoshii 1987) et le Modèle Hiérarchique basé sur des modèles de matière noire froide (Kauffmann 1996; Kauffmann & Charlot 1998a, 1998b). Les regularités que présentent les galaxies de type précoce dans leurs propriétés observées à tous les redshifts peuvent être utilisées pour contraindre les modèles mentionnés ci-dessus. En particulier, l'étude des amas de galaxies avec un décalage spectral supérieur ou de l'ordre de 1 est le moyen le plus direct pour faire des progrès significatifs dans ce sujet.

Dans cet esprit, nous avons conduit un relevé spectroscopique et photométrique complet et sans précédent sur deux des amas massifs les plus distants connus jusqu'à aujourd'hui dans l'hemisphère austral : RX J0152.7-1357 à $z = 0.837$ et RDCS J1252.9-2927 à $z = 1.237$. Ces deux amas ont été sélectionnés comme sources X étendues dans le ROSAT Deep Cluster Survey (RDCS, Rosati et al. 1995, 1998).

La confirmation spectroscopique de 78 galaxies appartenant à RX J0152.7-1357 et 36 appartenant à RDCS J1252.9-2927 est le résultat d'un suivi spectroscopique extensif des ces deux amas et d'une méthode efficace de sélection basée sur la distribution des galaxies dans l'espace des couleurs. La haute qualité de nos données spectroscopiques nous a permis de faire une caractérisation précise des populations stellaires dans les galaxies de ces systèmes à grand décalage spectral, nous permettant de mieux contraindre le mode et l'époque de formation des galaxies de type précoce dans les amas. L'imagerie dans le domaine X (Maughan et al. 2003; Rosati et al. 2004), optique (Blakeslee et al. 2003) et proche-infra rouge (Lidman et al. 2003), couplée avec l'information spectroscopique, est en train de livrer une description complète de la structure interne et de la dynamique de ces amas. Actuellement une étude avec les données de la camera ACS sur la morphologie des galaxies est en cours. Ceci nous permettra de mieux comprendre les effets de l'environnement sur la population des galaxies et les effets d'évolution par type de galaxie.

Dans le cas de l'amas RX J0152.7-1357 , nous arrivons à la conclusion que ce système est clairement un système dynamiquement jeune. La structure filamentaire observée dans la distribution des galaxies de RX J0152.7-1357 est en bon accord avec la distribution de l'émission X du milieu intra-amas (Maughan et al. 2003). Il y a une forte évidence de sous-structures présentes dans ce système (Girardi et al., en préparation), ce qui appuie l'image d'un amas dans une phase de fusion. Un résultat important est la découverte d'une dizaine de galaxies qui se retrouvent bien dans la séquence rouge de l'amas mais qui montrent de la formation d'étoiles. Ces galaxies sont dans les régions extérieures de l'amas et leur spectre peut être décrit comme le spectre d'une galaxie de type E+A avec [OII] superposé. Le spectre observé et les couleurs rouges des galaxies montrent l'existence d'une population vieille d'étoiles avec une population jeune, toutes les deux dans une même galaxie. La formation d'étoiles observée trouve une explication naturelle, mais surprenante, dans les images ACS qui montrent clairement la présence de disques autour de noyaux rouges dans beaucoup de cas.

RDCS J1252.9-2927 montre un état de relaxation très avancé, malgré une petite élongation dans sa distribution de galaxies et dans son émission X. L'analyse de toutes les données photométriques disponibles (Lidman et al. 2003, Blakeslee et al. 2003, Rosati et al., en préparation) montre que les galaxies de type précoce dans les amas de galaxies deviennent plus bleues quand le décalage spectral augmente. Les modèles montrent que ces couleurs peuvent être produites par des étoiles jeunes de quelques Gans, ce qui donne un décalage spectral de formation $z_f \sim 3$. De cette façon, les galaxies de type précoce auraient été formées à ce décalage spectral par une flambée de formation d'étoiles suivie par une évolution seulement de leur luminosité, ce qui appuie le Modèle Classique. Une analyse détaillée de la masse dynamique de chaque amas, basée sur les données spectroscopiques qui nous sont disponibles, est en cours. Des estimations de la masse à partir des données X (Maughan et al. 2003; Rosati et al. 2004) montrent que RX J0152.7-1357 et RDCS J1252.9-2927 sont des amas très massifs à décalage spectral autour de 1. L'existence de structures si massives et si distantes donne encore des arguments en faveur d'un univers de basse densité.

Finalement, l'ensemble des sujets astrophysiques abordés durant cette thèse m'a permis d'acquérir les connaissances nécessaires pour pouvoir interpréter le grand ensemble de données à l'acquisition duquel j'ai participé.

La plus grande partie de cette thèse a été consacrée à l'étude des amas distants. Les données réunies pour ce travail constituent l'un des ensembles les plus complets et les meilleurs disponibles pour des amas de galaxie à grand décalage spectral. Une fraction très importante de temps a été dediée à mettre ensemble ces données, un effort qui a demandé la préparation des observations, leur exécution, la réduction et la calibration des données jusqu'à avoir un produit de haute qualité. Je crois que les premiers résultats obtenus sont un bon indicateur de la qualité et du potentiel de cet ensemble de données et plus d'informations seront obtenues lors de la poursuite de l'analyse.

Contents

Abstract

My Ph.D. work was concentrated on two topics. One is devoted to the study of thermodynamical properties and scaling relations in nearby clusters (Demarco et al. 2003a) and the other one is aimed at carrying out an unprecedented study on the cluster internal dynamics and spectro-photometric properties of galaxies in the two most distant massive clusters of galaxies known today in the southern sky (Demarco et al. 2003b). Clusters of galaxies offer unique possibilities to understand the physics involved during the formation and later evolution of self-gravitating structures down to the present epoch. Moreover, they are ideal laboratories to study the effects of environment on the formation and evolution of galaxies. By pushing these studies to large redshifts, one can obtain essential information to understand the mode and epoch of formation of elliptical galaxies, which dominate present-day clusters. In what follows, I summarize the main conclusions of the two topics I have worked on.

1. **Nearby clusters** (in collaboration with F. Durret) : In this work I analyzed a sample of 24 galaxy clusters with $0.01 < z < 0.3$, observed with the ROSAT PSPC. The main goal of this work was to test whether clusters of galaxies, considered as self-gravitating structures, share similar thermodynamical properties and scaling relations as those already observed in cluster ellipticals (Márquez et al. 2001). By running a dedicated code (Magnard 2002) to model the X-ray surface brightness of clusters I was able to fit a Sérsic profile to the ICM gas distribution and derive temperature and dynamical mass profiles, as well as the total potential energy, specific entropy and mass for the gas and DM components. We found that: 1) the Sérsic law parameters (intensity, shape and scale) describing the X-ray gas emission are correlated two by two, with a strong correlation between the shape and scale parameters; 2) the hot gas in all these clusters roughly has the same integrated specific entropy, although a second order correlation between this integrated specific entropy and both the gas mass and the dynamical mass is observed; 3) a scaling law links the cluster potential energy to its total mass, with the same slope as that derived for elliptical galaxies (Márquez et al. 2001) and for dark matter halo simulations (Lanzoni 2000; Jang-Condell & Hernquist 2001). Comparable relations are obtained for the dark

matter component. All these correlations are probably the consequence of the formation and evolution processes undergone by clusters of galaxies and suggest that ellipticals can be considered as scaled down versions of clusters.

2. **Distant clusters** (in collaboration with P. Rosati): The aim of this ESO Large Programme (PI : P. Rosati) is to make the most extensive spectro-photometric survey of galaxies in the two distant massive clusters RXJ0152 at z=0.837 and RDCS1252 at z=1.237, selected from the ROSAT Deep Cluster Survey (Rosati et al. 1998), in order to provide stronger constraints on the epoch at and the way in which early type galaxies were formed, only possible by studying clusters at redshifts similar or greater than unity, and to firmly characterize the dynamical state of the clusters. Very deep wide-area near-IR imaging with the VLT and NTT (e.g. Lidman et al. 2003) and optical Keck imaging have been obtained, observations which are also supported by Chandra (e.g. Rosati et al. 2003) and HST+ACS data on both clusters. My work was mainly concentrated on the spectroscopic survey of these clusters carried out with FORS1/2 at the VLT. I took an active part on the target selection and mask design process as well as in some of the observing runs as visiting astronomer. The spectral data reduction was accomplished with the assistance of a dedicated software (Demarco 2003), specially developed to reduce FORS2 MOS data. The spectroscopic work yielded 78 secure cluster members for RJX0152 (Demarco et al., in prep.) and 36 secure members for RDCS1252, the latter being the survey with the largest number of spectroscopically confirmed members in a $z > 1$ cluster. We observe significant substructure in RXJ0152, and the filamentary structure observed in its galaxy distribution agrees very well with the X-ray distribution (Maughan et al. 2003) of the ICM, which supports the picture of a cluster in a merging phase. Moreover, we observe, for the first time, red galaxies with on-going star formation in RXJ0152. This discovery points toward a complex star formation history of galaxies in clusters. By studying the CM diagram in RDCS1252 (Lidman et al. 2003) and its Luminosity Function (Toft et al. 2003), we set new constraints on the formation redshift of the early-type galaxies. Moreover, spectroscopy of the 10 brightest members shows for the first time a clear signature of a young ($\sim$ 1 Gyr) stellar population living in early-type galaxies in that cluster. The data reduction phase is completed and I am now actively involved in the interpretation of this large imaging and spectroscopic data set to test models of galaxy formation and evolution. Recent spectacular HST+ACS imaging of these two clusters will be crucial in this endeavor.

Acknowledgments

The work presented in the following pages has been carried out at the Institute d'Astrophysique de Paris (IAP) and at the European Southern Observatory (ESO) headquarter in Garching near Munich. During all these years as a graduate student I have got the great pleasure and privilege of meeting many wonderful people, learning from them and sharing with them exciting and extraordinary moments. I feel very fortunate for having had such an enriching experience.

My deep thanks go to my thesis advisor Florence Durret for her friendship and constant encouragement during all these years. Her supervision, help and support have been extraordinarily important to me, and I would like to thank her for introducing me into the X-ray world of galaxy clusters. I am deeply grateful to my co-advisor Piero Rosati for his friendship, his infinite patience, his criticism and guidance. I am much indebted to him for all his help, for sharing his experience and teaching me most of what I know on observational cosmology and spectroscopy. His constant support and encouragement have been fundamental. It has been a great pleasure to collaborate with Florence and Piero. My heartfelt thanks to them.

I would like to thank Daniel Gerbal for his encouragement, motivating discussions and enthusiasm, which have been very important to me. I want to thank Jacqueline Bergeron, Bob Fosbury, François Hammer, Bruno Leibundgut, Pierre Léna, Dominique Proust, Brigitte Rocca-Volmerange and Daniel Rouan for all their kind support and help. Thanks to the referees, Sophie Maurogordato and Guy Mathez, for reading this thesis and making comments which have helped to improve it and thanks to all my collaborators. I am grateful to Frédéric Magnard for his patience at explaining me the use of his fitting code and for answering my many questions about the reduction and analysis of ROSAT data and computing issues. I would like to thank Héctor Flores, Gastão Lima-Neto and Gary Mamon for helpful discussions and Martino Romaniello for all his help on technical issues about FORS.

I want to thank Carla Avelans, Aurore Bacmann, Nate Bastian, Stéphane Blondin, Hervé Bouy, Carlos De Breuck, Nausicaa Delmotte, Emmanuel Di Folco, Stefano Ettori, Stefan Guilliard, Maren Hempel, Harald Kuntschner, Elena Pancino, Antonello Piemonte, Marina Rejkuba and Manuela Zoccali for their support and for all those extraordinary moments we shared together. I thank Raphaël Lescouzères, Vincenzo Mainieri, Chris Mullis, Rita Mullis, Roy van Boekel, Silvie van Boekel and Benoît Vandame for their warm friendship, enlightening discussions, for all the fun and the great time we had at home, climbing mountains and walls or jumping off a plane, and for being always an important support in this wonderful journey. My deep thanks to Thomas Masseron for his strong support, warm company and hospitality, and for sharing a lot of wisdom. My gratitude goes to Gianfranco Bertone, Jérémy Blaizot, Sébastien Fromang, Damien Le Borgne, María Rodríguez, Philippe Salomé, Juan Carlos Suárez and MyHa Vuong for their support and help during all these years since the beginning of the graduate school. I am grateful to Alessandro Rettura for his great enthusiasm, support and for many helpful discussions and suggestions that helped me to write the present manuscript. I want to thank Claudia Isola, Silvia Vicente and Viktor Ziskin for their encouragement specially in the difficult moments of the last part of the thesis. I thank Nick Seymour for reading and making corrections to chapter 1. Thanks to Brice Ménard for many nice moments and adventures in South America, Paris and Munich, for encouragement and for his kind help with the abstract in French. I thank Hervé Bouy for his help making some of the figures in chapter 5, and I would like to thank the staffs of IAP and ESO for their warm hospitality and support.

I am deeply grateful to Héctor Flores, Rosa Duarte and Alienor Flores for being such a strong source of encouragement and support which has been a fundamental element to achieve my goal of the Ph.D. My heartfelt thanks to them for making me part of their family and for sharing so many wonderful moments. My deep thanks to Roberto Abuter, Carolina Grebe and their children, Francisca, María, Nicolás and Sofía for their great support and help, their warm hospitality, and for all the nice moments we spent together. I have to thank Patricia Arévalo and Jorge Cuadra for their kind hospitality and for all their patience and help. I thank Antonia Alvarado, Nicolás González, Patricio Lagos and Victor Ramírez for their encouragement and I thank Pablo Torres for his help and support. My special thank to Rodrigo Olea, partner of "cordada", for showing me the beginning of the way to professional astronomy, for being always a source of encouragement and for all the mountains we have done together. My gratitude also goes to the people of the faculty of physics at the *Universidad Católica de Chile* and in the *Asociación Chilena de Astronomía y Astronáutica* who helped me grow.

Finally, I deeply thank to my family, in the distant Chile, for the huge amount of encouragement and support that always has given to me. My deepest thanks go to my parents, Alfonso Demarco and Margarita López for their love and for the encouragement to study what I most like, astronomy. I specially thank my mother for her tremendous amount of support and sacrifice that has allowed me to reach this goal and attain my dream.

Introduction

The present work is devoted to the study of the internal structure and evolution of clusters of galaxies and to the study of the spectro-photometric properties of cluster galaxies with the aim of understanding how and when cluster early-types are formed, therefore providing valuable information about the origin of clusters of galaxies themselves. Throughout the chapters below I will present the most relevant characteristics of galaxies and clusters of galaxies as well as the comological context in which they are inserted and their importance as probes of the formation and evolution of structures in the Universe.

Most of the mass in the universe is in the form of non-luminous, collisionless matter called dark matter (DM), so that any theory aimed at describing the formation of galaxies and clusters has to include an appropriate description of the DM. The most favored theories of structure formation are those based on Cold Dark Matter (CDM; see Primack 1996). Galaxies would be formed in the peaks of DM density fluctuations, galaxy formation being strongly favoured within large-scale density perturbations, which will eventually form a cluster of galaxies (Kaiser 1984; Kolb & Turner 1990).

Galaxies are then self-gravitational systems composed of a DM halo within which stars, gas and dust can be distributed in different ways, giving rise to several galaxy morphologies. Clusters of galaxies are larger gravitationally bound structures, constituting a collection of galaxies embedded in a hot thin gas in the gravitational potential created by the cluster DM halo. The velocity dispersion of the galaxies in clusters is typically $\sim$ 800 - 1000 $km\ s^{-1}$. The scale of a cluster of galaxies is of the order of a few Mpc, and the mass varies between 10^{14} and $10^{15} M_{\odot}$. Less massive systems, or groups, form an extension of clusters toward smaller scale and temperature systems. However only a small fraction of all the galaxies in the local universe belong to some bound structure such as a group or cluster of galaxies, most of them being found in the field.

The first observations of galaxies other than ours and the discovery of clusters of galaxies goes back to the XVIIIth century with the systematic surveys of the sky conducted by Charles Messier and Wilhelm Herschel. Their observations made possible the creation of the first catalogs of nebular objects, thus marking the first steps towards the understanding of the extragalactic nature of galaxies and their distribution in space. This distribution of galaxies is far from being homogeneous but is rather clumpy. Perhaps the first written reference about the clustering of galaxies is the one of the French astronomer Charles Messier in his famous "Catalogue des nébuleuses et des amas d'étoiles" (Messier 1784). Messier noticed the important concentration of "nebulae" in Virgo. He wrote:

> *"La constellation de la Vierge, & sur-tout l'aile boréale est une des constellations qui renferme le plus de nébuleuse ... Toutes ces nébuleuses paroissent sans étoiles."*

This is a clear reference to the Virgo cluster of galaxies. The extragalactic nature of these nebulae was completely unknow at that epoch. However, Herschel was one of the first to suggest that the stellar system we inhabit was indeed a "nebula" like many others he had observed, and that these nebulae should be systems located far outside our own (Herschel 1785). The evidence of galaxy clustering started to accumulate rapidly. John Herschel's General Catalogue and Dreyer's New General Catalogue and Index Catalogue indicated the existence of several nearby galaxy clusters such as the Coma cluster and the Perseus cluster. The "Great Debate" between Shapley and Curtis in 1920 (see Smith 1982), about the actual size of our own galaxy and the nature of the "nebulae" was not able to give clear answers to these questions. It was not before 1925 that Edwin P. Hubble's observations of Cepheid variables in the Andromeda Nebula gave the final and conclusive answer about the extragalactic nature of nebulae, confirming Herschel's idea. Hubble also noted that our own Galaxy was a member of an association of galaxies, which he named "The Local Group" (Hubble 1936). Meanwhile, the work of Zwicky led to the discovery of several new clusters and he first estimated the mass of a galaxy cluster (Zwicky 1933), thus establishing the need for DM. Zwicky also noted that the Local Group may be part of the Virgo cluster (Zwicky 1938). The Palomar Sky Survey photographs allowed George O. Abell to catalog 2712 of the very richest nearby clusters (Abell 1958), his paper "The Distribution of Rich Clusters of Galaxies" being a milestone in the science of galaxy clusters. But not only galaxies are grouped into clusters; galaxy clusters are also gathered into even larger structures such as the Shapley concentration (Shapley 1930) which is the richest supercluster in the local universe (see eg., Reisenegger et al. 2000). More historical notes about the study of galaxy clusters can be found in Abell (1975) and Biviano (2000).

Clusters of galaxies are fundamental objects in modern cosmology. They constitute ideal probes to be used to understand the formation and evolution of structures in the universe. They represent regions where mass overdensities have reached maximum amplitudes and the study of their correlation in space can be used to estimate the power spectrum of density fluctuations in the universe. The mass function of galaxy clusters is sensitive to the cosmological parameters defining the geometry and dynamics of the universe, therefore the observation of clusters of galaxies up to cosmological distances can deliver strong constraints on the cosmological model (Bahcall & Cen 1993; Bahcall, Fan & Cen, 1997; Fan, Bahcall & Cen 1997). Moreover, galaxy clusters are ideal laboratories to study the effects of environment on the formation and evolution of galaxies. An outstanding question is to understand the mode and epoch of formation of elliptical galaxies, which dominate present-day clusters. Predictions on the spectro-photometric properties of early-type galaxies in clusters based on hierarchical models of galaxy formation (Kauffmann 1996, Kauffmann & Charlot 1998a, 1998b) differ significantly at redshifts greater than 1 from models in which ellipticals formed at high redshift in a monolithic collapse (Eggen, Lynden-Bell & Sandage 1962). The difficulty of finding clusters at redshift ≥ 1 has not enabled to address properly these issues. However, in the past few years the new generation of ground-based and space-based telescopes, such as VLT, Keck, HST and Chandra, have allowed the confirmation of more distant clusters and also a more detailed study of their internal structure. Studying distant clusters is important to understand galaxy formation and evolution as well as to constrain the cosmological model. Nearby clusters also offer unique possibilities to study in great detail the properties of the different galaxy populations, their dynamics and the cluster structure. In particular, a detailed study of the X-ray emission of clusters can give important clues to better understand the physics involved during the formation and later evolution of these self-gravitating structures down to the present epoch.

From this point of view, the present work comprises two main subjects. One of them is concentrated on the study of the thermodynamical properties of nearby clusters based on X-ray observations obtained with the ROSAT satellite (Demarco et al. 2003a). The other one is an unprecedented study of the galaxy populations of two of the most distant massive clusters known to date in the southern sky, selected from the ROSAT Deep Cluster Survey (Rosati et al., 1998). As part of a VLT large program dedicated to these clusters, very deep wide-area near-IR imaging with VLT and NTT (Lidman et al. 2003) and extensive VLT spectroscopy (Demarco et al. 2003b) have been obtained. The main issues I will address in these two topics are: (a) the thermodynamical evolution of clusters and the similarities between nearby clusters and early-type galaxies in local clusters, and (b) the spectro-photometric properties of galaxies in high redshift clusters and the mode and epoch of formation of early-type galaxies.

This thesis is structured in the following manner. In chapter 1 I will present the cosmological context in which galaxy clusters are inserted and I will describe their structural design. In chapter 2 I present the ROSAT data and the analysis that I carried out in order to address point (a). The corresponding results and conclusions are given in the paper presented in chapter 3. Chapter 4 is devoted to the main characteristics of galaxy spectra and I describe the FORS2 multi-object spectroscopic data reduction process I performed to analyse the data obtained from the above mentioned VLT large program. All this work is the basis for the analysis presented in chapter 5, aimed at addressing point (b). Part of the results already obtained on the corresponding study are presented in the papers of chapter 6. I will conclude with a summary of the main results of this thesis research and with a description of the future work to develop.

Chapter 1

The scientific framework

In this chapter I intend to provide a review of the physical processes and cosmological issues related to clusters of galaxies. Firstly, I will introduce important elements of modern cosmology such as the cosmological parameters, the redshift and distance estimators. I will follow by briefly introducing the main ideas of structure formation in order to afterwards describe the main components of the cluster structure. I will talk about the main emission mechanisms observed in clusters and the way in which astronomers use this information to study clusters and obtain the observational data that show the way to a better understanding of the physical phenomena responsible for the structures we see.

1.1 Elements of modern cosmology

1.1.1 The cosmological parameters

Since gravity is the major driver of these processes, I will start by reviewing the basics aspects of the standard cosmological model, which refers to the solutions of Einstein's field equations under the hypothesis that the Universe is homogeneous and isotropic on very large scales. This standard cosmological model provides the theoretical background required to study the evolution of the primordial density fluctuations that will form large scale structures in the Universe.

Einstein's field equations describe the gravitational effects produced by a given mass in space-time, and can be written as

$$G_{\mu\nu} = R_{\mu\nu} - \frac{1}{2} g_{\mu\nu} R - \Lambda g_{\mu\nu} = \frac{8\pi G}{c^4} T_{\mu\nu} \tag{1.1}$$

where, $R_{\mu\nu}$ is the Ricci tensor, R is the scalar curvature, Λ is the cosmological constant (see Carroll, Press & Turner 1992) and $g_{\mu\nu}$ is the metric tensor. Roughly speaking, the metric tensor is a function that tells us how to compute the distance between any two points in space-time. In General

Relativity this distance or line element, ds, is related to the metric tensor by:

$$ds^2 = g_{\mu\nu} dx^\mu dx^\nu \tag{1.2}$$

with $x^0 = ct$ and x^1, x^2, and x^3 the space-time coordinates.

As already mentioned, the standard model assumes that beyond a certain distance from us, the universe becomes uniform and isotropic, which is known as the Cosmological Principle (CP). Although we know that the CP is not true in our local neighborhood, the remarkable isotropy of the CMB (Bennett et al. 2003) provides the strongest support to it. In the same way, the distribution of galaxies on large scales, as seen by the 2dFGRS (Colles et al. 2001, 2003; figure 1.1), suggest the validity of the CP.

It can be shown (see Weinberg 1972) that a metric compatible with the Cosmological Principle is the Friedmann-Robertson-Walker (FRW) metric given by the line element

$$ds^2 = c^2 dt^2 - a(t)^2 \left[\frac{dr^2}{1 - kr^2} + r^2 (d\theta^2 + sin^2\theta d\phi^2) \right] \tag{1.3}$$

where r, θ and ϕ are comoving coordinates, i.e., coordinates measured by observers at rest with respect to the local matter distribution. The scale factor, $a(t)$, gives the temporal evolution of the spatial term and k is a constant that can take the values -1, 0 and 1, which represent respectively an open universe (infinite, hyperbolic space), a flat universe (infinite, flat space) and a closed universe (finite, spherical space).

On the right side of Eq. (1.1), the energy-momentum tensor $T_{\mu\nu}$ can be considered as the "source" of gravitation, and it contains all the mass density and pressure terms describing the system (see Weinberg 1972). Thus Eq. (1.1) relates locally the matter and energy (right side) to the geometry of the space-time (left side). In the simplest case of a perfect fluid, the energy-momentum tensor turns out to be

$$T_{\mu\nu} = (\rho c^2 + p) U_\mu U_\nu + p g_{\mu\nu} \tag{1.4}$$

where U is the velocity of the fluid in the space-time and ρ and p its density and pressure respectively.

Replacing Eqs. (1.2), (1.3) and (1.4) into Einstein's field equations (Eq. (1.1)), and assuming a pressureless universe, $p = 0$, which is the case of our matter-dominated observable universe, we obtain the following equation describing the evolution of the scale factor:

$$\left(\frac{\dot{a}}{a}\right)^2 = \frac{8\pi G}{3} \rho_M - \frac{kc^2}{a^2} + \frac{1}{3} \Lambda c^2 \tag{1.5}$$

The solutions of equation (1.5) describe the evolution of the universal expansion as a result of the three competing terms : the matter term

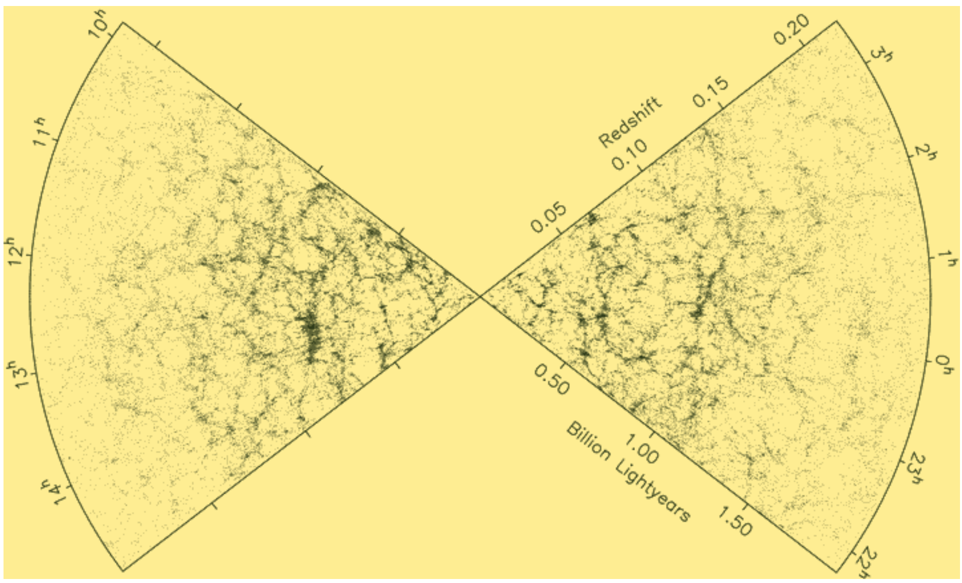

Figure 1.1: Map of the galaxy distribution obtained by the 2dFGRS (Colles et al. 2001, 2003). The survey covers an area of $\sim$ 1500 square degres selected from the APM Galaxy Survey in regions of the North and South Galactic Poles. The median redshift of the survey is $\bar{z} \sim 1$ and spectra for 245,591 objects, mainly galaxies, have been obtained. The similarity between the two slices suggest the validity of the Cosmological Principle on large scale structures.

(containing ρ_M), the curvature term (containing k) and the cosmological constant term (containing Λ). We can rewrite this equation in a very simple way, by introducing the cosmological parameters. Let us define

$$\frac{\dot{a}(t)}{a(t)} \equiv H(t) \ , \tag{1.6}$$

where $H(t)$ is the Hubble parameter. At the present epoch, $t = t_0$, the Hubble parameter is $H_0 = (\dot{a}(t_0)/a(t_0))$, the constant of the Hubble law (Hubble 1929, Hubble & Humason 1931). We then define

$$\Omega_M \equiv \frac{8\pi G \rho_{M0}}{3H_0^2} \tag{1.7}$$

$$\Omega_\Lambda \equiv \frac{\Lambda}{3H_0^2} \tag{1.8}$$

$$\Omega_k \equiv -\frac{k}{a_0^2 H_0^2} \tag{1.9}$$

where all the '0' sub-indexes refer to quantities measured at $t = t_0$. With these definitions, Eq. (1.5) can be rewritten as

$$H^2(t) = H_0^2 \left\{ \Omega_M \left(\frac{a_0}{a(t)}\right)^3 + \Omega_k \left(\frac{a_0}{a(t)}\right)^2 + \Omega_\Lambda \right\} \tag{1.10}$$

Then, for $t = t_0$ Eq. (1.10) becomes

$$\Omega_M + \Omega_\Lambda + \Omega_k = 1 \tag{1.11}$$

The matter density parameter Ω_M can be written in the form $\Omega_M = \rho_{M0}/\rho_{crit0}$, where $\rho_{crit0} = 3H_0^2/(8\pi G)$ is the critical density of the universe today, which separates open and closed models in a matter dominated universe. It is important to note that, in general, all the above parameters are time dependent. By replacing Eq. (1.11) into Eq. (1.10) we obtain the following equation for the scale factor:

$$\dot{a} = H_0 a_0 \left\{ \Omega_M \left(\frac{a_0}{a} - 1\right) + \Omega_\Lambda \left[\left(\frac{a}{a_0}\right) - 1\right] + 1 \right\}^{1/2} \tag{1.12}$$

1.1.2 Redshift and distances

In astronomy, the **redshift** refers to the shift towards longer wavelengths of the spectrum of an astronomical object which is moving away from us (Doppler effect). In cosmology, the main detectable source of movement comes from the expansion of the universe, described by the scale factor $a(t)$. The relation between the receding velocity of the object and it spectral shift is given by

$$z \equiv \frac{\lambda - \lambda_0}{\lambda_0} = \sqrt{\frac{1+\frac{v}{c}}{1-\frac{v}{c}}} - 1 \tag{1.13}$$

which turns out to be $z \simeq (v/c)$ for $(v/c) << 1$. Here λ_0 corresponds to the wavelength measured in the laboratory. The redshift can be used to estimate the distance d to an object by using Eq. (1.13) and the Hubble law, the latter relating the velocity v of the object to its distance d from us (Hubble 1929, Hubble & Humason 1931). Since the photon arriving from the astronomical object has traveled through an expanding universe, its wavelength is also affected by the universal expansion, increasing at the same rate as the universe does. Hence, we can rewrite the redshift of the object in terms of the scale factor as well:

$$1 + z = \frac{a_0}{a(t)} \tag{1.14}$$

where a_0 is the scale factor today at $t = t_0$. In this way, by integrating Eq. (1.10) and using the above relation, we obtain the lookback time, $\tau(z)$, of an object at redshift z:

$$\tau(z) = H_0^{-1} \int_0^z (1+z')^{-1}[\Omega_M(1+z')^3 + \Omega_k(1+z')^2 + \Omega_\Lambda]^{-1/2} dz' \tag{1.15}$$

By integrating this equation up to infinity, i.e. $z \to \infty$, we obtain the age of the universe which is proportional to H_0^{-1}. The proportionality constant depends on the cosmological parameters Ω_M, Ω_k and Ω_Λ.

Now we want to estimate the distance to an astronomical object which is located at a comoving distance r_1 at $t = t_1$. Let us assume that the luminosity of such an object at the time t_1 is L. Let us say that over a time Δt_1 the object emits N photons of mean energy E, which, at $t = t_0$, will be distributed over a shell of radius $a_0 r_1$ centered on the object. $a_0 r_1$ is indeed the distance between us and the source at $t = t_0$. Since the photon energy is proportional to λ^{-1} and hence proportional to the scale factor a, at $t = t_0$ the photons will have an energy $E_0 = Ea/a_0 = E(1+z)^{-1}$ and will take a time $\Delta t_0 = \Delta t_1 a_0/a = \Delta t_1(1+z)$ to cross the shell. The observed flux will be then

$$f = \frac{NE_0}{4\pi a_0^2 r_1^2 \Delta t_0} = \frac{N\frac{E}{\Delta t}}{4\pi a_0^2 r_1^2 (1+z)^2} = \frac{L}{4\pi d_L^2} \tag{1.16}$$

where we have defined $d_L = a_0 r_1 (1+z)$ as the luminosity distance of the object. Photons follow geodesic trajectories defined by $d\theta = d\phi = 0$ and the distance element is $ds = 0$. Then from Eq. (1.3) we can obtain that the comoving coordinate r_1 is related to the time t_1 by

$$\int_{t_1}^{t_0} \frac{cdt}{a(t)} = \int_0^{r_1} \frac{dr}{\sqrt{1-kr^2}} = f(r_1) \tag{1.17}$$

By using Eq. (1.10) in Eq. (1.17) we could solve r_1 as a function of the cosmological parameters and then obtain the luminosity distance d_L as a function of Ω_M, Ω_k and Ω_Λ, i.e. $d_L = d_L(z, \Omega_M, \Omega_k, \Omega_\Lambda)$. However this is complicated and there is no analytical solution for the general case. In the case $\Omega_k = 0$ and $\Omega_\Lambda = 0$, the following analytic expression can be obtained for the luminosity distance (Mattig 1958):

$$d_L = \frac{2cH_0^{-1}}{\Omega_M^2}\{\Omega_M z + (\Omega_M - 2)((\Omega_M z + 1)^{1/2} - 1)\} \tag{1.18}$$

Another way to estimate the distance to the same source is by measuring its angular size $\Delta\theta$ on the plane of the sky. If the proper diameter of the object is D then by definition we have $D = a(t_1)r_1\Delta\theta$. We already saw that $r_1 = d_L/(a_0(1+z))$, therefore the following relation gives the definition of the angular diameter distance d_A:

$$d_A \equiv \frac{D}{\Delta\theta} = a(t_1)r_1 = \frac{a(t_1)d_L}{a_0(1+z)} = \frac{d_L}{(1+z)^2} \tag{1.19}$$

While the luminosity and angular diameter distances depend on the cosmological parameters, there is a direct observable of an object which remarkably does not depend on them: its surface brightness. Let us take the same source as before. If Σ_{int} is its intrinsic bolometric surface brightness, i.e. the emitted power per unit area per unit solid angle, and Ω the solid angle spanned by the source as observed from our frame, then the luminosity L will be (see Eq. (1.16))

$$L = 4\pi d_L^2 f = 4\pi\Sigma_{int}\Omega d_A^2 \tag{1.20}$$

From this equation we obtain the following relation between the intrinsic bolometric surface brightness and the observed bolometric surface brightness of the object:

$$\Sigma_{obs} = \frac{f}{\Omega} = \Sigma_{int}\left(\frac{d_A}{d_L}\right)^2 = \frac{\Sigma_{int}}{(1+z)^4} \tag{1.21}$$

This effect is extremely important in cosmology because it has a dramatic effect on the visibility of objects at high redshift. It is the surface brightness which drives the detection of objects rather than its flux; it decreases very rapidly with z so very extended objects which are far from us will become undetectable even if they have comparable fluxes to those of less extended detected sources.

1.2 Structure formation and Clustering

Recent observations of the Cosmic Microwave Background (CMB; Penzias & Wilson 1965) obtained by WMAP (Bennett et al. 2003) provided us with a new and detailed vew of the early universe, at about 400,000 years after the Big Bang. The WMAP data shows with high resolution the temperature fluctuations, of the order of $\Delta T \sim 10^{-5}$ K (Hinshaw et al. 1996a; Bennett et al. 2003) on an otherwise uniform CMB at a temperature $T \sim 3K$, which are the direct signature of small density fluctuations that constitute the seeds of galaxies and clusters of galaxies.

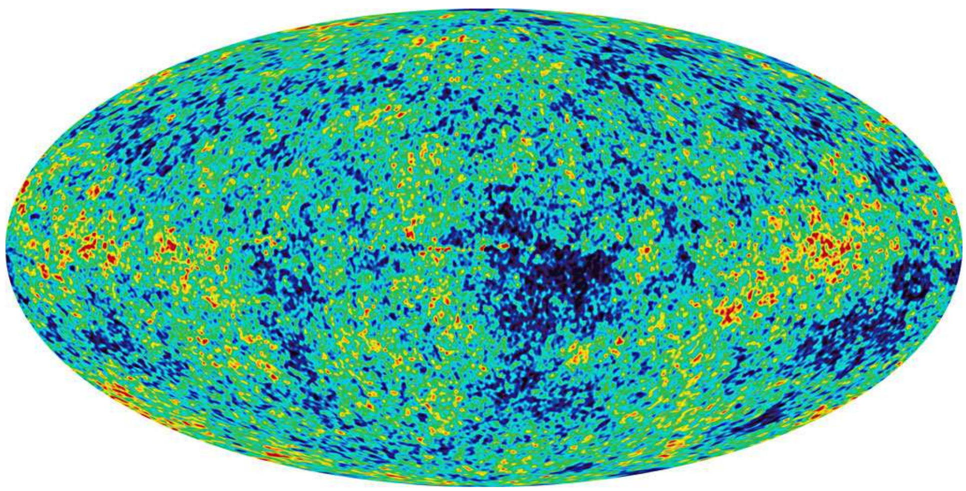

Figure 1.2: The first detailed, all-sky picture of the early universe. The WMAP image reveals temperature fluctuations (shown as color differences) that correspond to the seeds that grew to become the galaxies (Bennett et al. 2003).

1.2.1 From density inhomogeneities to clusters

The CMB represents the most distant epoch in the past of the universe that we can observe directly with our telescopes. It is a sort of "limit" to our observable universe, because no radiation could escape from earlier times to reach us today. The strong coupling of radiation and matter by Compton scattering in the early universe prevented photons from travelling large distances. With the expansion and cooling of the universe, this radiation-dominated phase became matter-dominated at a redshift $z = 2.4 \times 10^4 \Omega_M h^2$ (see Longair 1998). The universe continued cooling down and the electrons and atoms started to recombine. At a redshift $z \simeq 1500$ and at temperature $T \simeq 4000$ K 50% of the gas was ionized and this epoch is called the *epoch of recombination*. At a redshift $z > 1000$ the interaction between matter and radiation was dominated by Thomson scattering, however at about $z \sim 550h^{2/5}\Omega_M^{1/5}$ (see Longair 1998) this thermal coupling between matter and radiation ceased on what is called the *last scattering surface.* This last scattering surface is what we observe with COBE and WMAP, the instant when the universe becomes transparent to radiation. Photons start traveling freely the large cosmic distances, carrying to us the information about small inhomogeneities in the density field which were created when the universe was still in its radiation-dominated phase. These density fluctuations would form galaxies and clusters of galaxies when matter becomes the dominant form of energy in the universe. Understanding the details on the origin of these fluctuations is an active area of theoretical cosmology and high energy physics research. Once these inhomogeneities are created, their evolution will be determined by the mass scale of the inhomogeneity relative to the Jeans mass at a given time. At redshifts $z << 2.4 \times 10^4\Omega_M h^2$, once matter and radiation are completely decoupled, density inhomogeneities with masses greater than the Jeans mass will start growing until they become non-linear. At this stage, they will evolve rapidly, collapsing by their own gravity to form bound structures such as galaxies and clusters of galaxies.

To get a better idea of how these inhomogeneities evolve to form structures such as clusters of galaxies, it is useful to review some elements of classical fluid dynamics which are relevant to the problem. In spite of the fact that most of the matter in the universe is in the form of non-baryonic dark matter, which makes the problem more complex, the picture I present below is enough to provide a clear and simple image of the mechanism behind the formation of galaxies and clusters.

To begin, lets us imagine a region of the universe in expansion with the Hubble flow, in the center of which there is an overdensity Δ which was created at some moment in the early and radiation-dominated universe. This perturbation in the mean density will also produce a perturbation in the Hubble flow, in the pressure inside the perturbed region, and in the gravitational potential, which can be described by:

$$\Delta \equiv (\rho - \rho_0)/\rho_0 = \delta\rho/\rho_0, \quad \mathbf{v} = \mathbf{v_0} + \delta\mathbf{v_0}, \quad p = p_0 + \delta p, \quad \phi = \phi_0 + \delta\phi \tag{1.22}$$

where ρ_0 is the unperturbed mean density of the universe at the time of the perturbation, $\mathbf{v_0}$ is the unperturbed Hubble flow and p_0 and ϕ_0 are the unperturbed pressure and gravitational potential respectively. In the early stages of the development of a density perturbation, the density contrast Δ in Eq. (1.22) is $\Delta << 1$, we are in the linear regime. The standard equations of gas dynamics for a fluid in a gravitational field can be used to describe the evolution of the perturbation. These equations are:

$$\textit{Equation of continuity}\ : \quad \frac{\partial \rho}{\partial t} + \nabla \cdot (\rho \mathbf{v}) = 0 \tag{1.23}$$

$$\text{Equation of motion}\ :\quad \frac{\partial \mathbf{v}}{\partial t} + (\mathbf{v}\cdot\nabla)\mathbf{v} = -\frac{1}{\rho}\nabla p - \nabla\phi \tag{1.24}$$

$$\text{Poisson's equation}\ :\quad \nabla^2\phi = 4\pi G\rho \tag{1.25}$$

In an expanding universe, the position $\mathbf{x}$ of a particle can be written as $\mathbf{x} = a(t)\mathbf{r}$, where $a(t)$ is the scale factor of the metric and $\mathbf{r}$ is the associated comoving coordinate. Then, the perturbation in velocity can be written as $\delta\mathbf{v} = a(t)(d\mathbf{r}/dt)$. Taking this into account and replacing Eq. (1.22) into Eqs. (1.23), (1.24) and (1.25), we obtain (see Longair 1998 for a detailed derivation) :

$$\frac{d^2\Delta}{dt^2} + 2\left(\frac{\dot a}{a}\right)\frac{d\Delta}{dt} = \frac{c_s^2}{\rho_0 a^2}\nabla^2\delta\rho + 4\pi G\delta\rho \tag{1.26}$$

where $c_s^2 = \delta p/\delta\rho$ is the sound speed. Looking for a solution for Δ of the form $\Delta \propto exp\{i(\mathbf{k}\cdot\mathbf{r} - \omega t)\}$, where $\mathbf{k}$ is the wavevector in comoving coordinates, we obtain:

$$\frac{d^2\Delta}{dt^2} + 2\left(\frac{\dot a}{a}\right)\frac{d\Delta}{dt} = (4\pi G\rho - k^2c_s^2)\Delta \tag{1.27}$$

In the case of a matter-dominated universe, we have $k^2c_s^2/(4\pi G\rho) << 1$, and Eq. (1.27) can be written as :

$$\frac{d^2\Delta}{dt^2} + 2\left(\frac{\dot a}{a}\right)\frac{d\Delta}{dt} = \frac{3}{2}\Omega_M H_0^2 a^{-3}\Delta \tag{1.28}$$

where the evolution of the scale factor $a(t)$ is given by Eq. (1.12). This equation has two linearly independent solutions, one corresponding to a decaying mode and another corresponding to a growing mode. Linear cold dark matter perturbations Δ grow at a rate that does not depend on their comoving spatial scale (Peebles 1980). The solution for the linear growing mode, the one that will develop to form a bound structure after collapse, turns out to be (Heath 1977, Carroll, Press & Turner 1992):

$$\Delta(t) = \frac{5\Omega_M}{2}(a_0H_0^2)\left(\frac{1}{a(t)}\frac{da(t)}{dt}\right)\int_0^{a(t)/a_0}\frac{da'}{(\frac{da'}{dt})^3} \tag{1.29}$$

where the integral can be solved out in terms of elliptic functions. In the matter-dominated phase and during the linear regime, the density contrast increases proportionally to the scale factor, i.e. $\Delta \propto a(t)$, which implies $\Delta \propto (1+z)^{-1}$. At some point, the density perturbation will become non-linear, i.e. $\Delta \geq 1$. In the non-linear regime, the density perturbation will grow until reaching its turn-around radius to collapse afterwards to form a bound virialized structure. The behavior of the density contrast in this regime can well be described by a spherical collapse model. To better understand the evolution of the density perturbation I will concentrate on the behavior of a shell of matter inside the perturbation. Let us thus consider a spherical shell of radius r inside the density inhomogeneity. If $\rho(t)$ is the density within the shell and $\rho_b(t) = (6\pi G t^2)^{-1}$ is the background density of the universe at time t, the density contrast within the shell will be $\Delta(t) = (\rho/\rho_b) - 1$. If M is the mass enclosed by the shell, supposed to be constant (we assume that there is no shell crossing so M remains constant), the evolution of the shell can be parametrized by the following set of equations (see Peebles 1993):

$$r = A(1 - cos\eta), \quad t = B(\eta - sin\eta), \quad A^3 = GMB^2 \tag{1.30}$$

Under this parametrization, it can be shown (see Padmanabhan 1996) that the evolution of a spherical overdense region can be described by the following set of equations:

$$r(t) = \frac{r_i}{2\Delta_i}(1 - cos\eta) \tag{1.31}$$

$$1 + z = \left(\frac{t}{t_i}\right)^{-2/3}(1 + z_i) \tag{1.32}$$

$$\Delta = \frac{\rho(t)}{\rho_b(t)} - 1 = \frac{9}{2}\frac{(\eta - sin\eta)^2}{(1 - cos\eta)^3} - 1 \tag{1.33}$$

where t_i is the time at some initial epoch and z_i, r_i and Δ_i are the redshift, the radius of the shell and the density contrast at the time t_i. The radius of maximum expansion of the shell, the turn-around radius r_{ta}, is obtained when $cos(\eta)$ attains its minimum , for $\eta = \pi$ (see Padmanabhan 1996):

$$r_{ta} = r_i \frac{a_0}{a(t_i)} \Delta_i^{-1}(1 + z_i)^{-1} \tag{1.34}$$

The redshift and the density contrast at the turn-around are respectively :

$$z_{ta} = \frac{\Delta_i(1 + z_i)}{(3\pi/4)^{2/3}} - 1 \tag{1.35}$$

$$\Delta_{ta} = \frac{9\pi^2}{16} - 1 \simeq 4.55 \tag{1.36}$$

For example, if we consider density inhomogeneities in the early universe at $z \simeq 10000$ with density contrast $\Delta \simeq 10^{-3}$, then, by using Eq. (1.35), we obtain that such a density perturbation would reach a maximum expansion at a redshift $z_{ta} \simeq 4.7$, and Eq. (1.36) would give us the density contrast of the perturbation at z_{ta} which turns out to be $\Delta_{ta} \simeq 4.6$, clearly in the nonlinear regime. Following the evolution of our test shell, after reaching its r_{ta}, point at which its velocity is zero (note here that the shell is completely decoupled of the Hubble flow), the shell will start to contract, collapsing toward the center. This final point in its evolution corresponds to $\eta = 2\pi$. We can therefore use Eq. (1.32) to obtain the redshift z_{coll} at which the shell has collapsed:

$$z_{coll} = \frac{\Delta_i(1+z_i)}{(2\pi)^{2/3}(3/4)^{2/3}} \tag{1.37}$$

It is important to say that the hypothesis of a constant mass M within the shell of radius r during the whole evolution of the shell is only valid for the collisional component of the matter density. The shells made of a collisionless component (dark matter) will cross the central regions of the overdensity (e.g. Fillmore & Goldreich 1984), and they will reach virial equilibrium by violent relaxation. In practice, the collisional matter will suffer a shock before reaching the center, producing also a central virialized structure (e.g. Bertschinger 1985). However, both collisional and collisionless components of the density will behave in a similar way, as a presureless gas, in the region outside of the shock. The forming structure will become virialized at a redshift that I will call z_f or redshift of formation of the virialized object. The virial theorem (see section 1.4.1) can be used to compute the "virial radius" of the collapsing mass M, which turns out to be:

$$r_{vir} = \frac{1}{2} r_{ta} \tag{1.38}$$

This implies that the density inside the virialized shell is $\rho_{vir} = 2^3\rho_{ta}$. Since $\rho_{ta} \simeq \rho_b(t_{ta})$ and $\rho_b(t_{ta}) = [(1+z_{ta})/(1+z_f)]^3\rho_b(t_f)$, where t_f is the time associated to the formation redshift z_f, it is possible to obtain the virial density as a function of the formation redshift:

$$\rho_{vir} \simeq 170\rho_0(1+z_f)^3 \tag{1.39}$$

and also the associated density contrast:

$$\Delta_{vir} \equiv \frac{\rho(t_f) - \rho_b(t_f)}{\rho_b(t_f)} \simeq 44.8 \times \left(\frac{1+z_{ta}}{1+z_f}\right)^3 - 1 \simeq 178 \tag{1.40}$$

Since $\Delta_{vir} \sim 200$, the virial radius r_{vir}, within which the overdensity is $\Delta = \Delta_{vir}$, is commonly refered to as r_{200}. Once the shell has reached a virialized state, its density and size will not change. However, since $\rho_b \propto a^{-3}$, the density contrast $\Delta(t)$ will increase as $\Delta \propto a^3(t)$ for $t > t_f$.

Now we can, for example, estimate the redshift of formation of a virialized object such as a cluster of galaxies. By using Eq. (1.7) we can write $\rho_0 = 3H_0^2\Omega_M/(8\pi G)$ and by using the virial theorem (see section 1.4.1) we find that the virial density can be written as $\rho_{vir} \simeq 3v^6/(4\pi G^3 M^2)$. Assuming isotropy we have $v = 3\sigma$ where σ is the radial velocity dispersion of particles within the virialized structure. Putting all this into Eq. (1.39) gives:

$$1 + z_f \simeq 3.5 \left(\frac{\sigma}{100\ km\ s^{-1}}\right)^2 \left(\frac{M}{10^{12} M_\odot}\right)^{-2/3} (\Omega_M h^2)^{-1/3} \qquad (1.41)$$

From this simple calculation we can make an estimate of the formation epoch for a cluster of galaxies. Typical values for the velocity dispersion of galaxies in clusters are about 1000 km s^{-1} and values for the mass of massive system are 10^{15} M$_\odot$. With these numbers we obtain formation redshifts near of $z_f \sim 3$ and densities of about $\rho_{vir}/\rho_0 \sim 10^4$, for $\Omega_M h^2 \sim 1$. However is important to say that the formation redshift for clusters derived above may be considered as an upper limit because massive clusters are observed to be forming even at a redshift below 1 (see section 5.3.1). Massive elliptical galaxies, as those populating the center of rich clusters, should have been formed before, by a redshift below 10. I will discuss in more detail the epoch of formation of massive elliptical galaxies in clusters in chapter 5.

Throughout the above description a lot of physical details have been swept under the carpet. The simple analytical model of the spherical collapse is a very good start into the problem of cluster formation, however a more detailed and deep understanding of the physics behind can only be achieved by numerical simulations and by comparing the real data with those models. For instance, a complete description of the formation of galaxies and clusters of galaxies should include the presence of gas and dark matter (e.g., Fillmore & Goldreich 1984; Bertschinger 1985, 1998), take into account a non-spherical symmetry of the density perturbations (e.g., Peacock & Heavens 1985) and include models describing the star formation history in galaxies (e.g., Kennicutt 1998).

1.2.2 The correlation function

The main effect of gravity is the one of attracting matter, being completely described by Eq. (1.1). This attraction between objects with non-zero mass causes them to form bound systems such as clusters of galaxies. Looking at Fig. (1.1) one realizes immediately that galaxies are not uniformly distributed on the sky, at least on small scales. The distribution is clumpy, and this grouping ranges from small groups to large structures such as clusters. The clustering is due to gravity and it can be described in terms of spatial two-point correlation functions, which can be obtained by counting the number of pairs of galaxies in a survey on a given scale. The correlation function describes the excess of probability of finding a galaxy at a distance r of another galaxy randomly selected from the field of view, with respect to a random distribution. The correlation function gives the probability $dP(r)$ of finding simultaneously a galaxy within a volume dV_1 and a galaxy within a volume dV_2, both galaxies separated by a distance r and both volumes being disjointed. If N_{obs} is the local observed number of pairs of galaxies and N_{rand} is the number of pairs of galaxies in an artificial catalog of galaxies randomly distributed within a volume $r \pm dr/2$, the two-point correlation function $\xi(r)$ and the probability $dP(r)$ can be written as:

$$\xi(r) = \frac{N_{obs}(r)}{N_{rand}(r)} - 1 \tag{1.42}$$

$$dP = \bar{n}^2(1 + \xi(r))dV_1 dV_2 \tag{1.43}$$

where $\bar{n}$ is the average number density of galaxies. Another estimator used for $\xi(r)$, alternative to Eq. (1.42), is the estimator of Landy & Szalay (1993). In analogy, we can also define the angular correlation function $\omega(\theta)$ as:

$$dP = \bar{n}^2(1 + \omega(\theta))d\Omega_1 d\Omega_2 \tag{1.44}$$

where $d\Omega_1$ and $d\Omega_2$ are the solid angle elements corresponding to the volumes dV_1 and dV_2 respectively. Studies of the correlation function based on large galaxy surveys (Davies & Peebles 1983; Hawkins et al. 2003) show that ξ, in scales smaller than 10 h^{-1} Mpc, can be well represented by a power law of the form:

$$\xi(r) = \left(\frac{r}{r_0}\right)^{-\gamma} \tag{1.45}$$

where r_0 is a characteristic scale at which the correlation function $\xi = 1$. This may be interpreted, roughly speaking, as the scale at which a perturbation becomes non-linear, i.e. $\Delta \sim 1$. It is possible to show that if $\xi(r) \propto r^{-\gamma}$ then the angular correlation function is $\omega(\theta) \propto \theta^{1-\gamma}$. In the case of the galaxy-galaxy correlation, it has been observed that $r_{0gg} \simeq 5$ h^{-1} Mpc and $\gamma_{gg} \simeq 1.67$ (Hawkins et al. 2003), and that on scales greater than about 20 h^{-1} Mpc, $\xi(r)$ drops below a power law. This indicates that galaxies start being clustered at scales of $\simeq 5$ h^{-1} Mpc, which is about the size of rich clusters of galaxies. The same method, when applied to clusters shows that clusters of galaxies start becoming correlated at much larger scales with values for r_0 and γ of $r_{0cc} \simeq 15 - 26$ h^{-1} Mpc (e.g. Bahcall 1988, 1992; Gonzalez, Zaritsky & Wechsler 2002) and $\gamma_{cc} \simeq 2$ (Gonzalez, Zaritsky & Wechsler 2002). These observations show that clusters of galaxies are more strongly correlated in space than galaxies. Since the correlation of galaxies and clusters of galaxies depends on the underlying cosmology, the study of the correlation function, in particular the dependence of r_0 on Ω_M, can provide important constraints on the cosmological parameter Ω_M (see e.g. Hawkins et al. 2003). Moreover, there is important evidence showing that the cluster correlation function depends also on cluster richness due to the observed richness-r_0 correlation (see Bahcall et al. 2003, and references therein).

1.2.3 The power spectrum and mass function

In this section I will show that the observed correlation function can be used to obtain important hints on the power spectrum of the initial field of density fluctuations. The space distribution of the primordial density inhomogeneities that gave rise to galaxies, clusters of galaxies and, in general, the large scale structure of the universe, can be described by the density contrast $\Delta(\mathbf{r})$, where $\mathbf{r}$ is the position vector. This density contrast can be thought as the result of combining several density perturbations of different sizes and amplitudes. The decomposition of Δ in its different constituent density modes can then be done in Fourier space, where the amplitude of perturbations of different scales, defined by the wavelengths λ, can be found. In this way, if the wavevector associated to a density perturbation of size λ is $\mathbf{k} = (2\pi/\lambda)\ \mathbf{i}$, the density contrast in Fourier space can be expressed as (Peebles 1993):

$$\Delta(\mathbf{r}) = \frac{(2\pi)^{3/2}}{V^{1/2}} \sum_{\mathbf{k}} \Delta_{\mathbf{k}} e^{i\mathbf{k}\cdot\mathbf{r}} \tag{1.46}$$

where V is the volume of a box with periodic boundary conditions, used for discretizing and normalizing the Fourier transform. Following Peebles 1993, we know that the two-point correlation function ξ and the density contrast $\Delta(\mathbf{r})$ are related by $\xi(r) =< \Delta(\mathbf{x})\Delta(\mathbf{x}+\mathbf{r}) >$. By performing the corresponding algebra, this relation leads us to the following equation for the two-point correlation function:

$$\xi(\mathbf{r}) = \frac{1}{(2\pi)^3} \int \frac{\mid \Delta_{\mathbf{k}} \mid^2}{V} e^{i\mathbf{k}\cdot\mathbf{r}} d^3\mathbf{k} = \frac{1}{(2\pi)^3} \int P(\mathbf{k}) e^{i\mathbf{k}\cdot\mathbf{r}} d^3\mathbf{k} \tag{1.47}$$

where we have defined

$$P(k) \equiv \mid \Delta_k \mid^2 V^{-1} \tag{1.48}$$

as the power spectrum of the density fluctuations. We then see that the two-point correlation function is the Fourier transform of the power spectrum of the density contrast. In principle, we do not know the form of $P(k)$, however, considering that the correlation function is observed to be a power law and considering also theoretical arguments from inflationary standard models, it is reasonable to think that the power spectrum should also have the form of a power law, i.e.,

$$P(k) = \mid \Delta_k \mid^2 \propto k^n \tag{1.49}$$

This assumption implies that the correlation function can be written as

$$\xi(r) \propto \int_0^{k_{max} \simeq (1/r)} \frac{sin(kr)}{kr} k^{n+2} dk \propto r^{-(n+3)} \tag{1.50}$$

Since the mass within the fluctuation on the scale r is proportional to r^3, we can then write the two-point correlation function in terms of the mass scale M as

$$\xi(M) \propto M^{-(n+3)/3} \tag{1.51}$$

We can also relate ξ to the root-mean-square density fluctuation on the mass scale M, $\Delta(M)$, in the following way:

$$\Delta(M) =< \Delta^2 >^{1/2} \propto M^{-(n+3)/6} \tag{1.52}$$

Values of $n \geq -3$ give density contrasts that vanish at very large mass scales, in agreement with an isotropic and homogeneous universe. It is also possible to compute the fluctuations in mass due to density inhomogeneities present on a scale r. In general, the variance of the fluctuation in mass on a scale r, which is a measure of the amplitude of the power spectrum, is given by (see e.g. Rosati, Borgani & Norman 2002)

$$\sigma_r^2 = \left\langle \left(\frac{\delta M}{M} \right)_r^2 \right\rangle = \frac{1}{(2\pi)^3} \int P(k) W^2(kr) d^3k \tag{1.53}$$

where $W(kr)$ is the Fourier transform of a window function $W(\mathbf{r})$ that can be spherical or gaussian (see e.g. Padmanabhan 1996). It is common to find in the literature the value of σ_8 which is the variance in mass fluctuations on scales of 8 h^{-1} Mpc. This value has been chosen since the galaxy two-point correlation function is $\xi \sim 1$ on this scale. By determining the galaxy two-point correlation function from observations, one could use Eq. (1.50) to obtain a value for the index n. This value, however, would not correspond to the index n_i of the initial power spectrum $P(k, t_i)$ of density fluctuations. The latter should have evolved considerably since an early epoch at $t = t_i$ due to non-linear effects as the virialization of systems on scales smaller than r_0 was taking place. The temporal evolution of the initial power spectrum, in the linear regime and for a gaussian random field of density fluctuations, is given by the following equations (Bardeen et al. 1986) :

$$P(k,t) = \left(\frac{b(t_i)}{b(t)} \right)^2 T^2(k, t_i) P(k, t_i) \tag{1.54}$$

where $b(t)$ in the matter dominated regime in a $\Omega_M = 1$, $\Omega_\Lambda = 0$ universe corresponds to the scale factor $a(t)$ of the universe. For redshifts below $z \sim$

100, the transfer function T(k,t) becomes time independent (Bardeen et al. 1986). In the case of Cold Dark Matter models and adiabatic fluctuations, the Transfer function can be well represented by

$$T(q) = \frac{ln(1+2.34q)}{2.34q}(1+3.89q+(16.1q)^2+(5.46q)^3+(6.71q)^4)^{-1/4} \quad (1.55)$$

where $q = k/(h\Gamma)$ and the shape parameter Γ is given by $\Gamma \simeq \Omega_M h$. Now we can use the Press-Schechter (PS) formalism (Press & Schechter 1974) to compute the mass function of collapsed and virialized objects, corresponding to places where the linear density contrast has exceeded some critical contrast Δ_c at a given redshift z. Assuming that the distribution of density fluctuations in a CDM model is gaussian, the probability that the density contrast in a randomly placed window exceeds $\Delta_c(z)$ is

$$P(>\Delta_c) = \frac{1}{(2\pi)^{1/2}} \int_{\Delta_c/\sigma_r}^{\infty} e^{-x^2/2} dx \quad (1.56)$$

where $x = \Delta_c(z)/\sigma_r$. Thus, the comoving number density of collapsed objects in the mass range $[M,\ M + dM]$ is given by the PS approximation (see Peebles 1993):

$$\frac{dn}{dM} = \left(\frac{2}{\pi}\right)^{1/2} \frac{d\ ln(\sigma_r^{-1})}{d\ ln(M)} \frac{\rho_0}{M^2} x e^{-x^2/2} \quad (1.57)$$

where ρ_0 is the mean mass density today. N-body simulations of cluster formation show that the PS formalism (Eq. (1.57)), although it is a good approximation to describe the evolution of the mass function of clusters with cosmic time, has to be modified if one wants to take into account more realistic scenarios of halo formation (Sheth & Tormen 1999). N-body simulations can then be used to study the dependence of the mass function of halos on cosmology and redshift. This dependence is given by σ_r and $\Delta_c(z)$ which are in turn dependent on the cosmology (see Rosati, Borgani & Norman 2002, and references therein). Therefore, the mass function of halos can be used to predict the comoving number density of cluster halos with masses greater than M as a function of redshift for a given cosmology, as shown in figure 1.3. Comparing predictions for the evolution of the cluster abundance with observations of the number density of galaxy clusters in a wide redshift range, specially up to redshifts similar or greater than 1, provides the strongest constraints on the values of σ_8 and Ω_M (e.g. Bahcall & Cen 1993; Bahcall, Fan & Cen, 1997; Fan, Bahcall & Cen 1997) since this evolution is driven by σ_8 and Ω_M (Fan, Bahcall & Cen 1997). Once the amplitude of the power spectrum is fixed by using the COBE normalization recipe (Bunn & White 1997; Hu & White 1997), a one-to-one relation between σ_8 and the shape parameter Γ is found. This can be expressed as a relation between σ_8

and Ω_M of the form $\sigma_8 = \eta\Omega_M^{-\alpha}$ with $\eta = 0.3-0.6$ and $\alpha = 0.4-0.6$, almost independent of a cosmological constant (Viana & Liddle 1996; Borgani et al. 1999; Pierpaoli, Scott & White 2001; Rosati, Borgani & Norman 2002 and references therein; Bahcall et al. 2003).

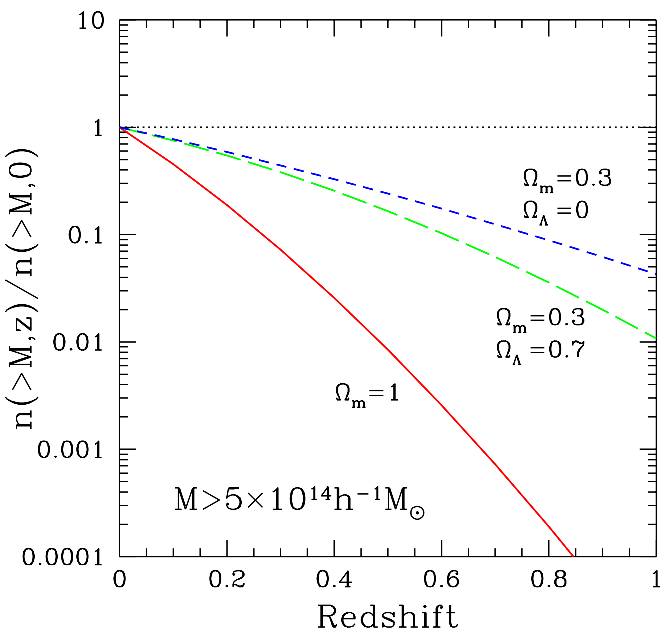

Figure 1.3: Evolution of the cluster number density with redshift. The curves on the figure where obtained with $\sigma_8 = 0.5$ for $\Omega_M = 1$ model and $\sigma_8 = 0.8$ for the low-density ones (from Rosati, Borgani & Norman 2002).

1.2.4 Number counts and luminosity function

Number counts refers to the surface density on the sky of a given class of objects as a function of the limiting flux f_{lim} of the observations. We can also compute the volume density of a class of objects by counting them on a surface $d\Omega$ and within a redshift range dz, so that the observed volume element is $dzd\Omega$. This observed volume element is associated to the comoving volume element dV defined by the line element of the metric (see Eq. 1.3) by means of the equation (Carroll, Press & Turner 1992) :

$$dV = a_0^3 \frac{r^2}{(1-kr^2)^{1/2}} dr d\Omega = \frac{d_M^2(z)}{(1+\Omega_k H_0^2 d_M^2(z))^{1/2}} \frac{\partial(d_M)}{\partial z} dz \; d\Omega \tag{1.58}$$

with $d_M(z, \Omega_M, \Omega_\Lambda) = d_L(z, \Omega_M, \Omega_\Lambda)(1+z)^{-1}$.

The count of sources can also be done according to their intrinsic luminosity L so that the space density of objects can be computed as a function of L. The number of sources per unit volume with luminosities in the range L to $L+dL$ is described by the **luminosity function** (LF) $\phi(L)$, so that the number density of counts dn is given by $dn = \phi(L)dL$. The most commonly used function to describe the data is the one proposed by Schechter (1976):

$$\phi(L) = \frac{\phi_*}{L_*} \left(\frac{L}{L_*}\right)^{-\alpha} e^{-L/L_*} \tag{1.59}$$

where L_* is the characteristic luminosity of the population of objects and corresponds to the luminosity over which the exponential term in Eq. (1.59) dominates, i.e. the bright end of the LF. At low luminosities, the LF behaves as a power law in L of index $-\alpha$. The normalisation ϕ_* determines the volume density of sources n_0 as $n_0 = \int_0^\infty \phi(L)dL = \phi_*\Gamma(1-\alpha)$ and the luminosity density of all sources is given by $\epsilon_L = \int_0^\infty L\phi(L)dL = \phi_* L_* \Gamma(2-\alpha)$. The number of sources per unit solid angle and redshift, in the luminosity range L to $L+dL$ is given by Eqs. (1.58) and (1.59) as:

$$dn \left\{ \frac{dV}{d\Omega dz} \right\} = \phi(L) \frac{dV dL}{d\Omega dz} \tag{1.60}$$

Eq. (1.60) can thus be used together with number counts to infer the cosmological model and any possible evolution of $\phi(L)$.

Studying the evolution of the halo mass function, introduced in section 1.2.3, requires to compute the observed comoving volume density of a class of objects, such as clusters of galaxies, as a function of redshift, based on the known local comoving density of such a class. Solutions to Eq. (1.57) can be obtained by numerical simulations of structure formation, where the mass of every object can be measured directly as well as the number of objects of a given mass within a given volume. Unfortunately, the mass is not a direct astronomical observable so it has to be estimated by other methods. Since the X-ray luminosity of a cluster is correlated to its mass content through the mass-temperature and luminosity-temperature relations (see section 1.3.2) , the X-ray LF (XLF; see figure 1.4) of clusters turns out to be the most suitable quantity to be used in order to trace observationally the evolution with redshift of the theoretical PS mass function. The relation between the LF and the PS mass distribution is given by (see Borgani et al. 1999):

$$\phi(L)dL = \frac{dn(M)}{dM} \frac{dM}{dL} dL \tag{1.61}$$

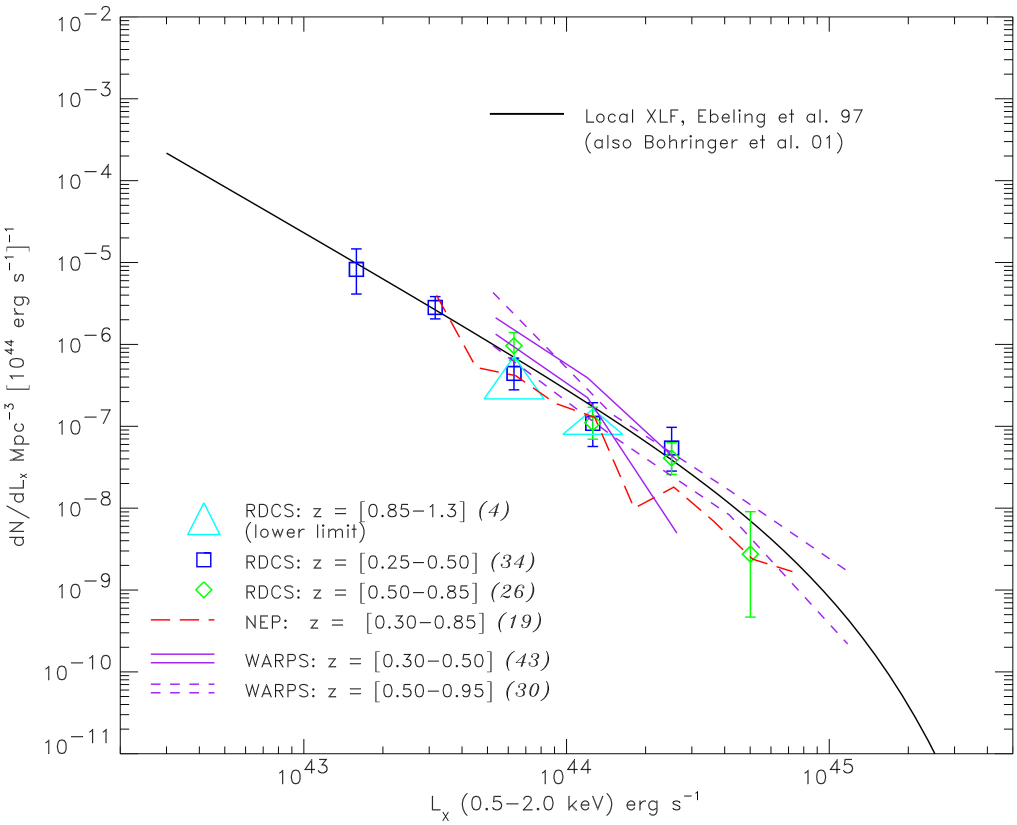

Figure 1.4: X-ray luminosity function of distant galaxy clusters. Numbers in square brackets give the redshift interval. The number within round brackets indicates the number of clusters in the corresponding redshift range (Rosati, Borgani & Norman 2002).

where the term dM/dL can be computed from the mass-temperature and luminosity-temperature relations. Clusters of galaxies are among the most X-ray luminous sources in the universe and therefore X-ray surveys can be used to extend the study of the evolution of the cluster abundance up to high redshifts. The first step is to measure the local ($z < 0.3$) cluster XLF, which should be compared to the LF measured in different redshift bins centered at different redshifts in order to search for any evolution. Several independent surveys using different selection techniques seem to converge to the following local values for the local cluster XLF parameters (see Rosati, Borgani & Norman 2002, and references therein): $\phi_* \simeq 1 \times 10^{-7}$ h_{50}^3 Mpc^{-3} (with 50 % variation), $L_* \simeq 4 \times 10^{44} erg\ s^{-1}$ (0.5-2 keV) and $\alpha \simeq 1.8$ (with 15 % variation). By assuming no evolution of the local XLF, the local ϕ_* value multiplied by the volume probed by the survey (see section 1.5) gives an estimate of the number of clusters with L_* one expects to discover as a function of z. Observation of the XLF at redshift $z > 0.3$ shows that its faint-to-moderate part is consistent with no evolution predictions (Rosati et al. 1995, 1998; Jones et al. 1998, Vikhlinin et al. 1998a). However, the situation toward the bright end of the XLF is unclear. There has been evidence of a negative evolution with redshift (Gioia et al. 1990a; Henry et al. 1992; Nichols et al. 1999; Rosati et al. 2000; Gioia et al. 2001), indicating a dearth of high luminous and massive clusters at $z > 0.3$. However, this evolution of the bright end of the XLF has been a matter of debate for several years. A significant progress on the subject needs even larger volumes in order to detect rare systems with $L_X > L_*$. Rosati et al. (2000) used a maximum-likelihood approach to compare the observed cluster distribution on the (L_X,z) plane with that expected from an evolving Schechter function defined by: $\phi(L) = \phi_0(1+z)^A L^{-\alpha} exp(-L/L_*)$, with $L_* = L_{*0}(1+z)^B$ and being ϕ_0 and L_{*0} the local XLF values. Rosati et al. (2000) find that the model with A=B=0 is excluded at more than 3σ level when luminous clusters are included. However, the same analysis confined to clusters with $L_X < L_*$ show consistency with no evolution, i.e., A=B=0. I will discuss briefly the galaxy luminosity function in clusters and in the field in section 1.3.1.

1.3 Internal structure of Clusters

1.3.1 Galaxy content

In what follows, I intend to give a short general introductory review about what we know about galaxies, focusing more on cluster galaxies, which is the subject developed in chapter 5.

Galaxies can be considered as the building blocks of the universe. A major fraction of the galaxies in the present time universe are found isolated, known as field galaxies. Only about 5 % of the galaxies in the local universe belong to gravitationally bound structures such as small groups and clusters of galaxies. The morphology of galaxies is quite varied. However, in spite of this, they can be separated according to three main morphological categories: elliptical galaxies, spiral galaxies and irregular galaxies. The classification introduced by Hubble (Hubble 1936), and shown here in Fig. 1.5, has been the basis for more modern classification schemes (see Roberts & Haynes 1994, and references therein).

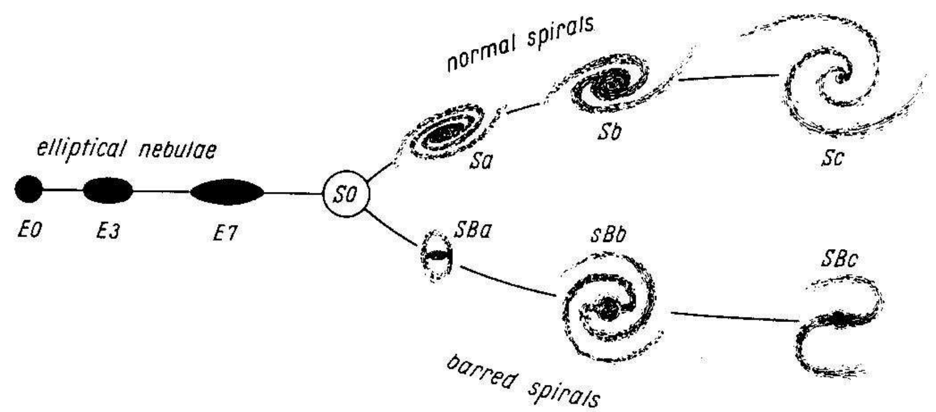

Figure 1.5: Hubble's original tuning-fork diagram as presented in "The realm of the Nebulae" (Hubble 1936) and reprinted by Sandage (1975).

Hubble arranged galaxies in a continuous sequence starting from the left with elliptical galaxies and ending to the right with spiral galaxies. Hubble suggested that galaxies evolved from the left-hand end of the sequence to the right, which is the reason why elliptical and S0 galaxies are refered to as **early-type** galaxies and spirals as **late-type**. We know today that this evolutionary scheme is not actually the case. Spirals were ordered into two branches that Hubble named "normal spirals" and "barred spirals", however we know nowadays that this distinction is rather unclear since most of the "normal" spiral galaxies do present a bar structure. The Hubble sequence refers to intrinsically luminous and passive galaxies to which one has to incorporate the populations of dwarf and irregular galaxies. In addition to this, there are several other categories of galaxies which present special characteristics. These categories correspond to cD galaxies (Beers & Geller 1983), Seyfert galaxies (Seyfert 1943), QSOs, Quasars (Schmidt 1963), N galaxies (Morgan & Dreiser 1983) and BL Lac objects. The importance of the Hubble sequence resides in the observed correlation between physical properties of galaxies and their location, based on their morphology, in the sequence. The scheme proposed by Hubble reflects important underlaying regularities in the processes of formation and evolution of galaxies (see Larson 1992, and references therein). Some examples of the main galaxy-types are shown in figure 1.6.

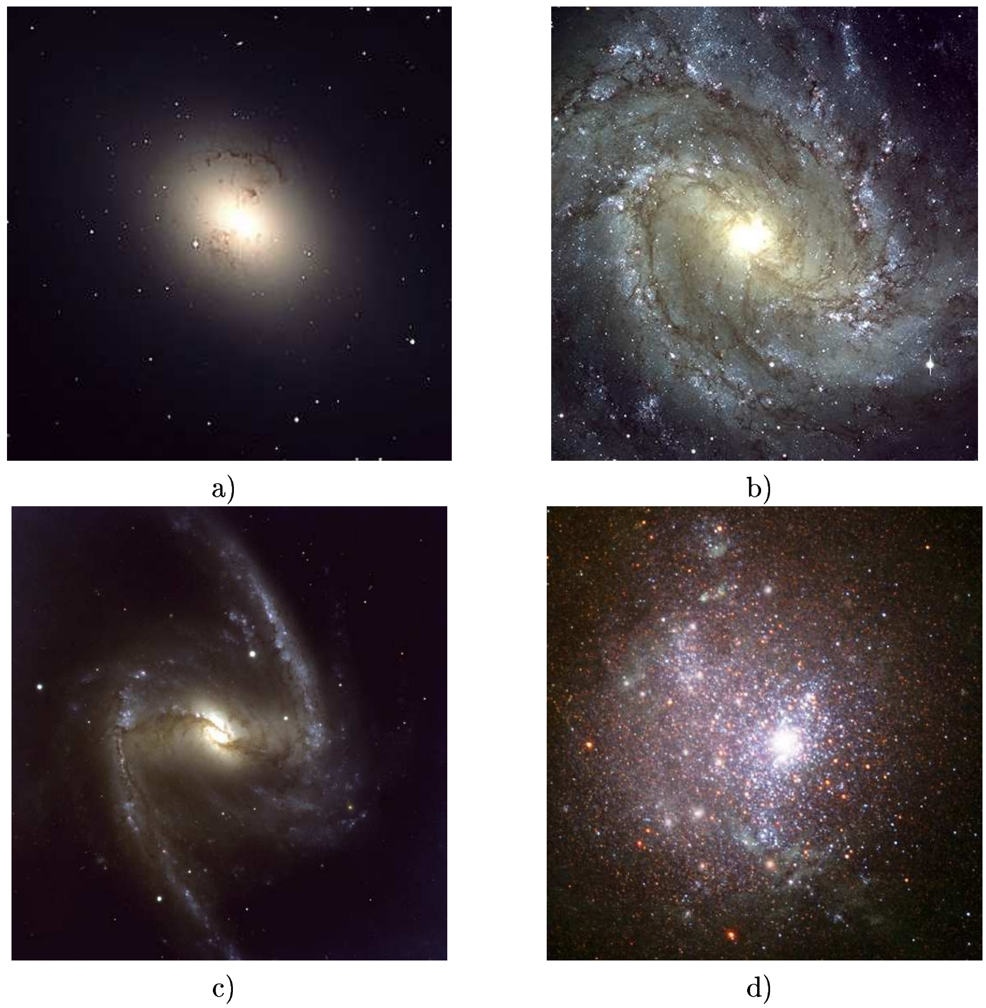

Figure 1.6: Examples of different morphological types of galaxies in the local universe. a) Giant elliptical galaxy NGC1316 in Fornax (photo ESO; http://www.eso.org/outreach/info-events/ut1fl/astroimages.html). b) Spiral galaxy M83 (photo ESO). c) Barred spiral galaxy NGC1365 in Fornax (photo ESO). d) Dwarf irregular galaxy NGC1705 (photo STScI/NASA; http://hubble.stsci.edu/newscenter/archive/2003/07/image/a).

Early-type galaxies

Elliptical galaxies show a wide range in mass, spanning from $\sim 10^6 M_\odot$ in the case of dwarf ellipticals to $\sim 10^{13} M_\odot$ for massive ellipticals. The mass-to-light ratio in ellipticals may vary from ~20 to ~70, and their typical velocity dispersion is $\sigma \sim 200 - 300\ km\ s^{-1}$. The stellar component of ellipticals mainly correspond to old stars (G- and K-type giants), although the existence of a young stellar population living in early-types has been observed in high redshift clusters (see section 5.4.2), and an intermediate-age population in local ellipticals. B-V colors of local ellipticals are $\sim 0.9 - 1.0$ and they are strongly correlated to their central velocity dispersion σ_0 and Mg_2 indices (Guzman et al. 1992), in the sense that ellipticals with higher Mg_2 indices present a higher central velocity dispersion and also are redder (see Binney & Merrifield 1998, and references therein). This correlation indicates that more massive ellipticals are redder. In addition to these, color and metallicity gradients have also been observed in this type of galaxy (Franx, Illingworth & Heckman 1989; Peletier et al. 1990; Davies, Sadler & Peletier 1993). Another important correlation is the one given by the relation $L_e \sim \sigma_0^4$ (Faber & Jackson 1976), i.e., that more luminous ellipticals have larger central velocity dispersions, where L_e corresponds to the luminosity interior to the effective radius R_e of the galaxy. The effective radius R_e turns out to be also correlated with the mean surface brightness I_e interior to R_e (Djorgovski & Davies 1987). All these correlations can be interpreted as elliptical galaxies lying on a surface in the space defined by the parameters $logR_e$, I_e and $log\sigma_0$. This surface is called the **fundamental plane** of elliptical galaxies (Djorgovski & Davies 1987; Dressler et al. 1987a; Joergensen, Franx & Kjaergaard 1996). Here, it is important to note the implication of two of the above mentioned correlations. Since the B-V color is correlated to σ_0 and the latter is in turn correlated to the luminosity L_e, it then follows that more luminous ellipticals are also redder galaxies. Ellipticals are observed to occupy a locus corresponding to a line in the color-magnitude space. This very important correlation is known as the **color-magnitude** (CM) relation for early-type galaxies (Bower, Lucey & Ellis 1992; Terlevich, Caldwell & Bower 2001). This relation is of high importance in modern cosmology because it can be used to constrain the epoch of formation of elliptical galaxies as well as to provide with important clues about the mode of formation of these galaxies. I will refer to this subject in detail in chapter 5, where I will show the application of the CM diagram to high redshift clusters of galaxies. In terms of morphology, and following Hubble's classification, ellipticals can be organized as a function of their projected ellipticity $\epsilon = b/a$. Thus we can put ellipticals into classes designated as En, where $n = 10(1-\epsilon)$. Observed ellipticities range between 1 and 0.3. In spite of its apparent simplicity, the internal structure of ellipticals can be much richer and complicated (see de Zeeuw et al. 2002).

S0 galaxies are very similar to elliptical galaxies in many respects. They have similar range in mass, the most massive ones reaching up to $10^{12}M_\odot$. Their stellar component and B-V colors are those of ellipticals and their mass-to-light ratios are of the same order as those observed in ellipticals as well. S0 galaxies possess a central spheroidal component, the bulge, surrounded by a large region which is generaly structureless. In contrast to ellipticals, S0 galaxies may sometimes contain some dust in their extended structure, believed to be intrinsically flat. According to the amount of dust present in the disk-like component, S0s can be grouped into three classes, $S0_1$, $S0_2$ and $S0_3$. The $S0_1$ class contains galaxies without signs of dust absorption whereas class $S0_3$ contain galaxies with clear signatures of dust in the form of ring-like features surrounding the central bulge. These galaxies, also called lenticular, represent the transition between ellipticals and spiral galaxies and they are considered as early-type galaxies as well. As well as spirals, S0 galaxies can also be barred.

Late-type galaxies

Spiral galaxies are probably the most beautiful expression of galactic-like objects. Their main characteristic are the spiral arms which develop around the central bulge component. These galaxies have more varied characteristics and complexity compared to early-type galaxies. The mass range for spirals goes from $\sim 10^9 - 10^{12}M_\odot$, and their mass-to-light ratio, depending on the morphological type, can vary from 10 to 30. Luminosities for spirals are observed to be in the range of $L_B \sim 10^8 - 10^{11}L_\odot$. The average color of spirals will also depend on the morphological type, going from $B-V \sim 0.7$ in the case of Sa to $B-V \sim 0.5$ in the case of Sc galaxies. Both "Normal" and barred spirals present a central bulge component made of old stars of population II. In the case of most barred galaxies, the bar structure at the center is quite notorious and the spiral arms emanate from the ends of the bar. In "normal" galaxies, on the other hand, the spiral arms come out directly from the central bulge. In many cases the bar-like structure is too small to be detected at first glance, which leads to consider real barred galaxies as "normal" spirals. There is observational evidence pointing out that our Galaxy is a barred galaxy (Stanek et al. 1997). Following Binney & Merrifield (1998), the morphological classes in which spirals can be grouped depends on three criteria: 1) the relative importance of the bulge and outlying disk in producing the overall light distribution of the galaxy; 2) the tightness with which the spiral arms are wound; and 3) the degree to which the spiral arms are resolved into stars and individual HII regions.

Sa and SBa galaxies are dominated by the large central bulge of red G- and K-type stars, and the spiral arms are tightly wound around the bulge. In general, these galaxies are as red as early-type galaxies with some young stars in the disk component. The amount of gas present in these systems is only of about 1%, and some traces of HII regions can be seen. Sb and SBb galaxies have an intermediate size bulge at the center surrounded by more open spiral arms. Many young stars and HII regions are present in the arms while the old stellar component resides in the nucleus. This makes them be redder in the center and bluer in the region of the arms. The amount of gas is between 2 and 5% and the average stellar component corresponds to stars of type between F and K. Sc and SBc have a small, red central bulge and blue, open and clumpy arms. The gas content is between 5 and 10%, and the arms are populated by a large number of young stars and HII regions. In average, these galaxies are dominated by stars from A- to F-type. The arms of these galaxies, as well as the arms in Sb and SBb spirals, are the home of massive, blue O- and B-type stars.

Finally, there is a third major class of galaxies which do not have any given symmetry : Irregular galaxies. These galaxies do not have a bulge and do not present clear traces of arms. They are dominated by young blue stars and HII regions. Their gas content is between 10 and 50% and the dominant stellar populations are from A- to F-type stars. Bright knots are visible in these galaxies which contain O and B stars.

Following Hubble's sequence, more detailed classifications have been introduced afterward, defining intermediate classes as Sab, Sbc and Scd spirals (and the equivalent for barred galaxies) to the rather broad ones exposed above. In addition, morphological types to take into account, for example, the existence of galaxies with rings in their outer and inner regions, have also been defined (see Binney and Merrifield 1998, and references therein). For a more detailed discussion about the physical properties of the different galaxy types, see the review by Roberts & Haynes (1994).

Galaxies in clusters

In this part I will refer to one of the three main components of clusters of galaxies which is the galaxy content. In the following chapters I will discuss in detail the dynamics and spectro-photometric properties of galaxies in clusters. Here I will just introduce some important generalities.

Galaxies in clusters represent only about 10% of the cluster total mass, thus being the minority component. The galaxy content of clusters is made up by a mixture composed by all the galaxy types described above. The fraction of each galaxy type present in the mixture will be different from cluster to cluster and to the one in the field. Typical values are shown in table 1.1. The fraction of galaxies in clusters with richness $R \geq 0$ and within the Abell radius $R_A = 1.5h^{-1}$ Mpc (Abell 1958) is $\sim 5\%$. This number increases with increasing R_A and with decreasing richness threshold. For instance, the median number of galaxies per cluster for $R \geq 0$ systems, within R_A and with apparent magnitudes $m \leq m_3+2$ (Abell 1958) is $\langle N_R \rangle \simeq 50$, m_3 being the photo-red magnitude of the third brightest cluster member.

The number of galaxies increases to fainter luminosities as described by the Schechter LF (see Eq. (1.59)). In the field, the average number density of bright galaxies with $L \geq L_*$ of all morphological types is $n_{field} \sim 1.5 \times 10^{-2}\ h^3\ \mathrm{Mpc}^{-3}$. In clusters of richness $R \geq 0$, this number density of $L \geq L_*$ within R_A is $n_{cluster} \sim 3\ h^3\ \mathrm{Mpc}^{-3}$. The resulting average galaxy overdensity in $R \geq 0$ clusters within R_A turns out to be $n_{cluster}/n_{field} \sim 200$, which is twice the typical galaxy overdensity threshold for the same richness clusters within the same Abell radius (see Bahcall 1999). In the central region of clusters, this overdensity can reach values of up to 10^5. Nearby clusters can be well identified in the optical because of their high galaxy density contrast. However, for distant clusters, this becomes more difficult due to the faintness of the sources. Then other properties of clusters should be used for their detection at high redshift (see section 1.3.2). The density distribution of galaxies in the central regions of clusters can be approximated by an isothermal King model (King 1972), given by:

$$n_{gal}(r) = n_{gal_0}\left(1 + \left(\frac{r}{r_c}\right)\right)^{-3/2} \tag{1.62}$$

where n_{gal_0} is the central galaxy density and r_c is the cluster core radius. This galaxy density distribution profile is observed to be $n_{gal} \propto r^{2.4\pm0.2}$ for $r > r_c$, and in the case of rich compact clusters, the central number density of galaxies in the brightest 3 magnitude range is $n_{gal_0}(\Delta m \simeq 3) \sim 10^3\ h^3$ Mpc^{-3} (see Bahcall 1999, and references therein).

Cluster type	E	S0	Sp
Regular clusters (cD)	35%	45%	20%
Intermediate clusters (spiral-poor)	20%	50%	30%
Irregular clusters (spiral-rich)	15%	35%	50%
Field	10%	20%	70%

Table 1.1: Typical fractions of galactic content, according to galaxy type, within the Abell radius $R_A = 1.5h^{-1}$ Mpc for clusters of different types and for the field. The table was extracted from Bahcall (1999). See also Oemler (1974) and Dressler (1980).

The distribution of galaxies according to morphological type are clearly dependent on the environment conditions. More precisely, there is an observed morphology-density relation followed by galaxies (Oemler 1974; Dressler 1980; Postman & Geller 1984) showing that early-types prefer denser environments, in contrast to spirals which do the opposite. The fraction of E and S0 galaxies increases towards the center (Whitmore & Gilmore 1991) of rich compact clusters, while the fraction of spirals decreases in the same direction. In the case of Coma, for instance, the fraction of spirals in the core is close to zero. In the low density environment of the external regions of clusters, the fractions of the different morphological types remain approximately constant and equal to the average fractions in the field (see table 1.1). The dynamical time scale relevant to this problem is the collapse time. The dependence on density of the collapse time ($t_c \propto 1/\sqrt{\rho}$) provides a physical interpretation to the morphology-density relation (Dressler 1980; Postman & Geller 1984).

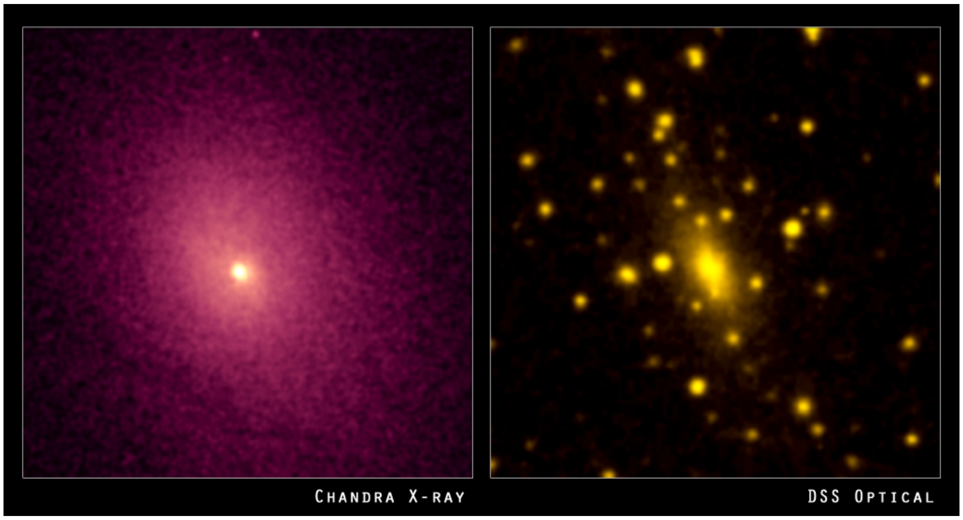

Figure 1.7: Cluster of galaxies A2029. The picture to the left shows the extended X-ray emission from the hot gas in the Intra Cluster Medium, as observed with Chandra. The X-ray emission shows a smooth increase all the way into the center. The picture to the right is the optical image of the cluster, showing a number of galaxy members. At the center of the cluster ther is a giant elliptical galaxy, that is thought to have been formed from the mergers of many smaller galaxies (Lewis et al. 2003)

The work of Butcher & Oemler (1978, 1984) has shown that the fraction of blue galaxies in clusters between $0 < z < 0.5$ increases with redshift. This effect has been confirmed by a number of works. Spectroscopic observations show that the blue cluster members are star-forming galaxies, mostly corresponding to disk-dominated spirals (Couch et al. 1994). Blue S0 galaxies are observed in the outer regions of clusters, consistent with hypothesis that galaxies are continously accreted into the cluster from the field (Van Dokkum et al. 1998a). The Butcher-Oemler effect may thus be interpreted as due to the transformation of blue field galaxies into red cluster galaxies from high redshift down to the present time. Moreover, the star formation activity in cluster galaxies can be induced by subcluster-subcluster mergers, consistent with hierarchical clustering models (see Metevier, Romer & Ulmer 2000, and references therein). On the other hand, observational evidence indicates the evolution of the morphology-density relation with redshift , as well as the evolution of the S0 and spiral fraction in clusters (Dressler et al. 1997). I will refer to the evolution of the color magnitude relation of cluster galaxies in chapters 5 and 6.

Important hints to understand the evolution of galaxies can be obtained through the study of the distribution of galaxy luminosities. When computing the LF of galaxies, summing over all galaxy types, the resulting overall distribution can well be fitted by a Schechter function (see Eq. (1.59)). However, the corresponding parameters ϕ_*, L_* and α are indeed environment dependent, and therefore the LF of galaxies in clusters will be different from the one for field galaxies. As shown by Binney & Merrifield (1998), the resulting LF in the B-band for cluster galaxies turns out to be steeper at the faint end compared to the field LF. This effect is due to a larger contribution of dwarf ellipticals in the cluster than in the field, although L_* is approximately the same in both environments. More recent observations confirm the steeper slope at the faint end for clusters, and also show that cluster galaxy LFs have characteristic magnitudes which are brighter than for the field (De Propris et al. 2003). Since the overall LF is the result of mixing appropriately the different galaxy types according to the environment, this difference can be naturally explained by the morphology-density relation (Dressler 1980; Dressler et al. 1997). Whereas Eq. (1.59) gives a good description for the overall galaxy luminosity distribution, a Schechter function is unable to fit every different galaxy type separately. Jerjen & Tammann (1997) computed the LF of galaxies, separated according to galaxy type, in nearby clusters. They found that spiral and S0 galaxies LFs can be well represented by a gaussian, with the mean magnitude and the dispersion being galaxy-type dependent (see their table 2). Elliptical galaxy LFs present a skewness towards faint magnitudes best represented by a modified gaussian with two wings of different dispersion (see Jerjen & Tammann 1997). In the case of dwarf ellipticals and dwarf S0 galaxies, their LFs are better described with a Schechter function.

At blue wavelengths (U- and B-band), the observed galaxy counts at the faint end exceed the predictions from no-evolution models by more than a factor of three. This effect, however, vanishes at redder wavelengths (Ferguson, Dickinson & Williams 2000). This faint blue galaxy excess, corresponding to galaxy types later than Sbc, has been observed to evolve significantly in redshift, indicating that late-type galaxies, mainly Sd and irregular galaxies, are the population which has undergone most of the evolution since $z \sim 1$ down to the present epoch (Lilly et al. 1995; Ellis et al. 1996; Ellis 1997, and references therein; Driver et al. 1998).

At infrared wavelenghts, the observed light becomes dominated by stars which constitute the average stellar component of galaxies. Hence, the K-band LF results to be the most appropriate tool to study galaxy luminosity distributions even up to high redshifts ($z \geq 1$). De Propris et al. (1999)

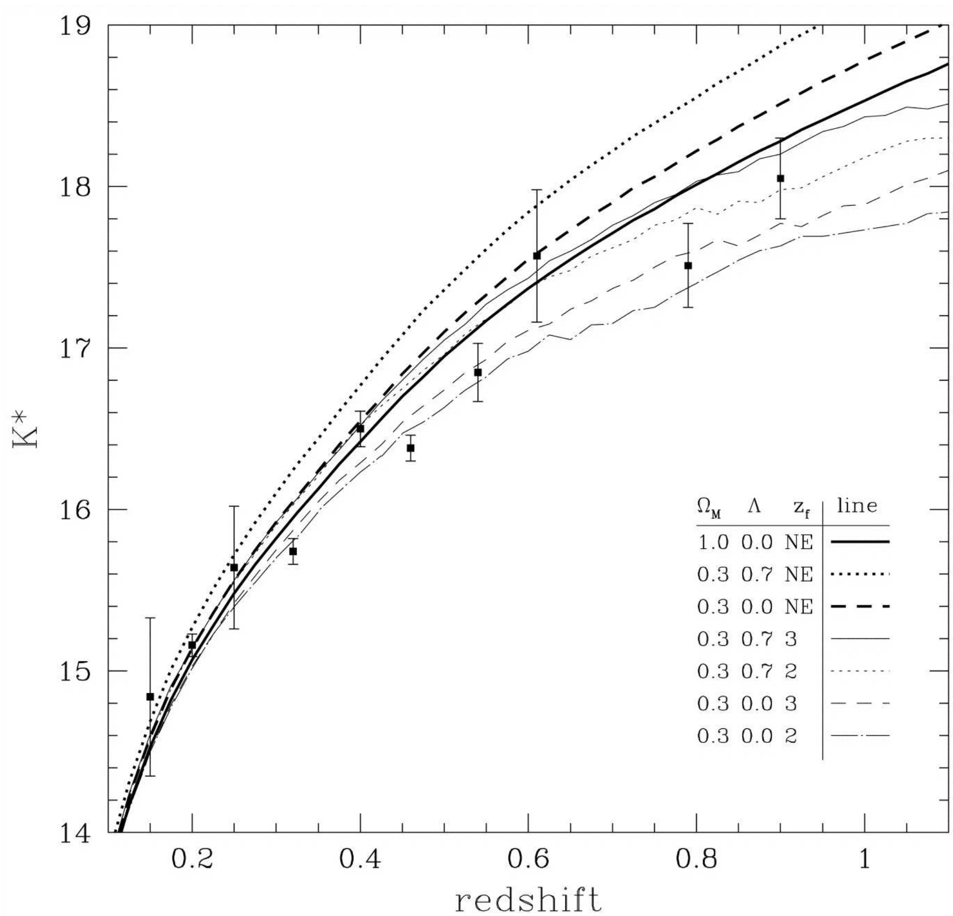

Figure 1.8: The evolution of the characteristic magnitude K_* with redshift, as shown in De Propris et al. 1999. The lines correspond to galaxy models computed with GISSEL (Bruzual & Charlot 1993), normalized to the Coma cluster $K^* = 10.9$ characteristic luminosity (De Propris et al. 1998). These models represent 0.1 Gyr starbursts with a Salpeter IMF, $Z = Z_\odot$, and $H_0 = 65$ Km s^{-1} Mpc^{-1}.

presented the galaxy K-band LF for a sample of clusters in the range $0.1 < z < 1$. They found K_* values brighter than would be expected for a non-evolving popoulation of early-type galaxies at $z > 0.4$, as shown in figure 1.8. This result is consistent with a pure, passive luminosity evolution of early-types.

1.3.2 The Intra Cluster Medium

General characteristics

Clusters of galaxies are powerful emitters of X-ray radiation, the most luminous X-ray sources after quasars. Typical X-ray luminosities of galaxy clusters are $L_X \sim 10^{43} - 10^{45}\ ergs\ s^{-1}$. X-ray emission associated with clusters was first detected in the early 70s (Fritz et al. 1971; Gursky et al. 1971a and 1971b) and observations by the UHURU satellite showed a number of important properties characterizing this emission. In particular, it was shown that the X-ray emission of clusters is extended (Kellogg et al. 1972; Forman et al. 1972). This extended emission comes from a very hot gas, usually at about 10^7 - 10^8 K and densities of the order of $\sim 10^{-3}\,cm^{-3}$, which is trapped in the potential well of the cluster (see figure 1.7). We can assume that this gas, totally ionized because of its high temperature, has the same composition as the primordial plasma : 75% of hydrogen and 25% of helium in mass, which gives us 7.7% for the number of He^{2+} ions and 92,3% for the number of H^+ ions. In terms of mass, the Intra Cluster Medium (ICM) gas represents about 20% of the total cluster mass. This X-ray emission is observed to be continuum emission and line emission. The continuum emission is due to three processes : thermal bremsstrahlung (free-free), recombination emission (free-bound) and two-photon decay of the metastable 2s states of hydrogenic and heliumlike ions (see Sarazin 1988, and references therein).

At the typical temperatures of galaxy clusters, $T \sim 5\ keV$, thermal bremsstrahlung is the dominant emission processes. Here, the free electrons in the ICM are decelerated when passing through the coulombian field of the ions, thus producing X-ray photons (see figure 1.9).

Let us assume that the ICM plasma has an electron number density $n_e(\mathbf{r})$ and an ion number density $n_i(\mathbf{r})$. If both components are in thermodynamical equilibrium at temperature T, then the velocity distribution of the electrons will follow a Maxwell law and the X-ray emissivity of the plasma, in units of $W\ m^{-3}\ Hz^{-1}$, is (Binney & Merrifield 1998):

$$\epsilon_\nu^{ff}(\mathbf{r}) = 5.44 \times 10^{-52}\overline{Z^2}n_e(\mathbf{r})n_i(\mathbf{r})T^{-1/2}(\mathbf{r})g^{ff}(Z,T(\mathbf{r}),\nu)e^{-h\nu/(kT(\mathbf{r}))} \tag{1.63}$$

where $\overline{Z^2}$ is the mean-square atomic charge on the ions. The coefficient $g^{ff}(Z,T(\mathbf{r}),\nu)$ is a correcting factor, called the Gaunt factor, which takes

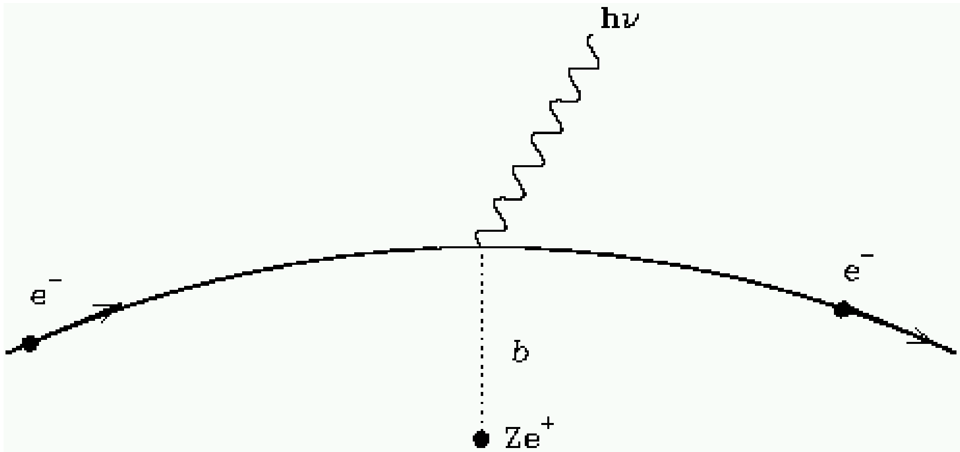

Figure 1.9: Bremsstrahlung emission. This emission is produced by the interaction between an electron and ion of charge Ze^+ in the hot plasma. The passage of the electron close to the ion makes the former decelerate and produce a photon of energy $h\nu$, where ν is the frequency of the photon. The wavelength $\lambda = c\nu^{-1}$ of the emitted photon falls well within the X-ray domain, which corresponds to wavelengths between $10^{-2} > \lambda > 10^{-3}\mu m$.

into account the quantum mechanical effects and the effect of distant collisions, and is a slowly varying function of frequency and temperature (see Karzas & Latter 1961 and Kellog, Baldwin & Koch 1975).

On the other hand, at lower temperatures, $T \sim 1\ keV$, the line emission of atoms like O, Ne, Mg, Si, Fe, etc., becomes quite important and has to be taken into account (Raymond & Smith 1977). In a galaxy cluster with a typical metallicity of $\simeq 0.3\ Z_\odot$ (Renzini 1997) at a temperature of 6 keV, about 8% of the X-ray luminosity comes from line emission, whereas in a group of galaxies at about 1 keV, the contribution of line emission may reach 50% (see Magnard 2002). This effect is shown in figure 1.10.

Gas distribution

As I have already shown in the previous section, in the case of clusters of galaxies the X-ray emissivity is mainly due to thermal Bremsstrahlung emission. This emission is created through the interaction between the charged particles in the hot plasma, hence it has a dependence on the square of the electronic density of the intra-cluster gas (see Eq. (1.63)). Owing to this dependency on density, the fitting of the X-ray surface brightness distribution can be used to obtain the distribution of the ICM gas density. The most popular model employed to represent the gas density profile in order to describe the X-ray surface brightness of a cluster is the so called isothermal β-model (Cavaliere & Fusco-Femiano 1976), which is given by the following expression:

$$n(r) = \frac{n_0}{(1 + (\frac{r}{r_c})^2)^{\frac{3}{2}\beta}} \tag{1.64}$$

A value of $\beta = 1$ corresponds to a King profile (King 1972), the analytic approximation to the isothermal sphere. This β-model, however, shows some limitations. It is based on the assumption that the ICM is at constant temperature everywhere, which is not always observed to be the case (De Grandi & Molendi 2002) and moreover, it has been seen that a single β value cannot always fit the X-ray surface brightness profile of clusters (Allen, Ettori & Fabian 2001; Allen, Schmidt & Fabian 2001; Hicks et al. 2002). Another limitation is the fact that the gas mass derived from this profile diverges, for values of $\beta \leq 1$, as the radius increases. It is therefore necessary to introduce a cutoff radius in these cases to avoid divergence when estimating the gas mass.

Another profile, that can be used to describe the distribution of gas in galaxy clusters (Demarco et al. 2003) is the so called Sérsic profile (Sérsic 1968; Ciotti & Bertin 1999):

$$\Sigma(s) = \Sigma_0 \, exp\left[-\left(\frac{s}{a}\right)^{\nu}\right] \tag{1.65}$$

characterized by three parameters: Σ_0 (intensity), a (scaling) and ν (shape). The advantage of this profile is to have a shape parameter, which makes any fitting process more flexible. By varying ν, one can describe from spherical bulges (smaller ν) to flat disks (larger ν). Moreover, the mass associated to this profile can be computed analytically, for any value of the model parameters, without introducing any cutoff radius. Note also that the Sérsic law (Eq. (1.65)) is a non-homologous generalization of the de Vaucouleurs $R^{1/4}$ profile (de Vaucouleurs 1948). The 3-D deprojection of such a profile corresponds to a generalized form of the Mellier-Mathez profile (Mellier & Mathez 1987) given by:

$$\rho_{gas}(r) = \rho_0 \, (r/a)^{-p} \, \exp[-(r/a)^{\nu}] \tag{1.66}$$

where ρ_0 is the volume gas density associated to the central column density Σ_0 and the parameters p and ν are related by the numerical approximation (Márquez et al. 2001):

$$p \simeq 1.0 - 0.6097\nu + 0.05563\nu^2 \tag{1.67}$$

which gives the best approximation to the Sérsic law when Eq. (1.66) is projected.

The Sérsic profile has been used to describe the light distribution of elliptical galaxies and bulge components (e.g., Caon et al. 1993; Marleau & Simard 1998; Graham 2003; Barraza, Binggeli & Jerjen 2003) and in chapter

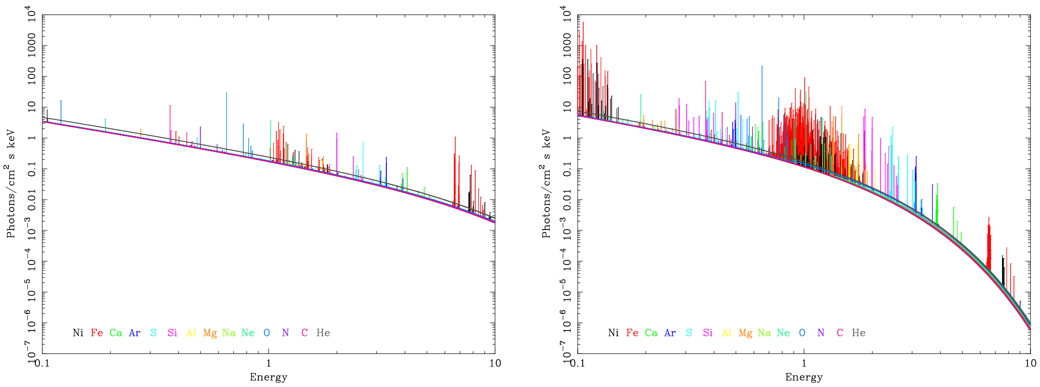

a) b)

Figure 1.10: This figure shows the bremsstrahlung continuum and line emission for clusters and groups of galaxies. a) Model Bremsstrahlung spectrum at a typical temperature of 6 keV. b) Similar spectrum but at a temperature of about 1 keV. At 6 keV about 8% of the X-ray emission comes from line emission, whereas at lower temperatures, this contribution increases up to 50%. Also, at low temperatures the continuum drops at high energies gets steeper (Magnard 2002).

2 I will show how it can also be used to model the gas distribution in the ICM.

Cooling Flow

The loss of energy due to X-ray emission causes the gas to cool down. If $\Lambda(T)$ is the gas cooling function (with T the gas temperature), and the plasma is in a chemical equilibrium state, the emission power of the gas per unit volume is:

$$\epsilon^{ff} = \int_0^\infty \epsilon_\nu^{ff}\, d\,\nu \; = \; n_e^2 \Lambda(T)$$

where n_e is the gas electronic density. Hence, the higher the electronic density is towards the cluster center, the higher the energy loss is in this region, producing a decrease of the central temperature and pressure. The latter becomes lower than that in the surrounding regions, thus producing a flux of matter at different phases towards the cluster center in order to increase the central density and reestablish the equilibrium. The observation of an excess of X-ray emission in the central region of clusters is a clear evidence for the presence of such a process (see Fabian 1994, and references therein).

We can define a characteristic cooling time, t_{cool}, for the gas. By assuming that the gas behaves as an ideal gas and by using the equipartition of energy theorem, we have:

$$t_{cool} = \frac{(3/2)\ k_B\ T \times (n_e + n_{H^+} + n_{He^{2+}})}{\epsilon^{ff}}$$

which can be rewritten as (e.g., Pislar 1998):

$$t_{cool} = 7.5 \times 10^{14} \frac{T^{1/2}}{n_e}\ (s)$$

with the temperature T in keV and n_e in cm^{-3}. This cooling time is shorter than the age of the cluster which is supposed to be of the order of the age of the universe. However, the structure of the ICM cooling has turned out to be more complex, as it has been shown by the new generation of X-ray satellites. Recent observations indicate the absence of metal lines associated with low temperature gas (e.g., Peterson et al. 2001; Tamura et al. 2001), in opposition to what the standard cooling flow model predicts. Moreover, observations of the fraction of cluster baryons locked into stars (e.g., Balogh et al. 2001; Bower et al. 2001) suggest the presence of feedback mechanisms to reheat the ICM (see Rosati, Borgani & Norman 2002, and references there in).

Temperature distribution of the ICM

Are clusters of galaxies in a hydrostatic equilibrium state? The answer is that, as long as the gravitational potential does not change on a sound crossing time, the gas motions are subsonic and the only important forces in the system are those due to gas pressure and gravity, this hydrostatic equilibrium state can be used as a good approximation for clusters. Simulations show that magnetic fields in clusters do not have a significant dynamical effect (e.g., Dolag & Schindler 2000), and observations of cooling flows in clusters show that gas motions towards the center are very subsonic except possibly very near the cluster core (see Sarazin 1988, and references therein). These observations then justify the validity of the hydrostatic equilibrium in clusters, for non-merging clusters at least. On the other hand, it is common to assume that the equation of state for an ideal gas is a good approximation for the ICM gas, although its application to self gravitating systems has been questioned in the past (e.g. Bonnor 1956, and references therein).

Therefore, the equation of hydrostatical equilibrium:

$$\nabla P(r) = -G \frac{M_{Dyn}(r)}{r^2} \rho_{gas}(r) \tag{1.68}$$

can then be combined with the equation of state for the hot intra-cluster plasma:

$$P(r) = \frac{\rho_{gas}(r)}{\mu m_p} k_B T_{gas}(r) \tag{1.69}$$

to provide the following equation from which the ICM temperature as a function of radius $T_{gas}(r)$ can be derived, once the gas number density as a function of radius $n_{gas}(r)$ and the distribution of total mass are known:

$$M_{Dyn}(r) = -\frac{k_B}{\mu m_p G} r^2 \left\{ T_{gas}(r) \frac{d\, \ln[n_{gas}(r)]}{dr} + \frac{dT_{gas}(r)}{dr} \right\} \tag{1.70}$$

where G is the gravitational constant, k_B is the Boltzman constant, μ is the plasma molecular weight (we assume $\mu = 0.6$ for the ICM) and m_p is the proton mass. The electron number density and the gas mass density are related by $n_{gas}(r) = \rho_{gas}(r)/(1.14\ m_p)$. The distribution of gas can be described by Eq. (1.64) or Eq. (1.66) and obtained from observations (see chapter 2). The total mass distribution, on the other hand, can be obtained by inferring the relative distribution between dark matter and gas (e.g., Gerbal et al. 1992; Durret et al. 1994) or by performing numerical simulation of dark matter halos (e.g., Navarro, Frenk & White 1996, 1997; Moore et al. 1999). If we use a Sérsic model for the gas density (Eq. (1.66)) and a power-law description of the relative distribution between gas and DM (Gerbal et al. 1992; Durret et al. 1994) given by $\rho_{DM}/\rho_{gas} = \kappa(r/a)^{-\alpha}$, the gas temperature profile can be obtained as a function of κ and α by replacing Eqs. (1.85) and (1.66) into Eq. (1.70) and performing a Gauss-Laguerre integration. The solution is of the form (Demarco et al. 2003):

$$T(r,\kappa,\alpha) = \left(\frac{w}{\nu a}\right)\left(\frac{r}{a}\right)^p e^{\left(\frac{r}{a}\right)^\nu} t(r,\kappa,\alpha) \tag{1.71}$$

where $w \equiv 4\pi\, G\, \frac{\mu m_p}{k_B}\, \frac{\rho_0 a^3}{\nu} = 1.54 \times 10^{38} \left(\frac{\rho_0 a^3}{\nu}\right)$ m keV, and

$$t(r,\kappa,\alpha) = \int_{\left(\frac{r}{a}\right)^\nu}^{\infty} \left\{ \kappa\gamma\left[\frac{3-(p+\alpha)}{\nu}, x\right] + \gamma\left[\frac{3-p}{\nu}, x\right] \right\} x^{-\frac{(p+\nu+1)}{\nu}} e^{-x} dx \tag{1.72}$$

Thermodynamics of Galaxy Clusters

Clusters of galaxies are self-gravitating structures which are normally considered as relaxed structures. This relaxation state is however not always the case, since some clusters are observed to have irregular shapes and indications of on-going mergers (e.g., Gioia et al., 1999; Hashimoto 2002; Maughan et al. 2003). I will present in detail one of such cluster with a clear on-going merger in chapter 5. Relaxed clusters can be considered in a quasi-equilibrium state attained after a violent relaxation process. This violent relaxation would have taken place in a time scale of the order of the collapse time $t_c \propto 1/\sqrt{G\rho}$. This characteristic time is much lower than the secular time scale defined by two-body interactions $t_{relax} \propto N/ln(N)$

(Binney & Tremaine 1987), where N is the number of particles (in our case galaxies) of the system, and which is of the order of 10^9 years. A perfect equilibrium state is never reached due to the interaction between particles which produce exchanges and losses of thermic energy. A clear example are cooling flows. Here, in order to recover hydrostatic equilibrium, the self-gravitating system contracts itself, increasing negatively its potential energy and therefore increasing its kinetic energy in order to keep its total energy constant. More thermal transfers occur between the particles, and the system evolves progressively. After the initial violent relaxation period, the cluster will evolve slowly, which allows us to consider relaxed clusters as systems in a quasi-equilibrium state. The second principle of thermodynamcs states that a system in equilibrium has a state of maximum entropy. For self-gravitating systems in quasi-equilibrium, such a state with an absolute maximum of entropy does not exist. The entropy is constantly increasing, but slowly, in the timescale given by t_{relax}, much longer than t_c, so it can be considered as quasi-constant. Therefore, it is important and interesting to study the specific entropy in clusters. The entropy is a fundamental tracer of the thermodynamical history of galaxy clusters.

The entropy content of a self-gravitating structure, integrated in its whole volume, can be obtained from the distribution function of particles in the phase space, $f(\mathbf{x}, \mathbf{v})$. The integrated specific entropy of such a system is given by the microscopic Boltzmann-Gibbs definition:

$$s = -\frac{\int f\, ln(f)\, d^3x\, d^3v}{\int f\, d^3x\, d^3v} \tag{1.73}$$

where the Boltzmann constant is $k_B = 1$. Note that this expresion gives us the specific entropy of the entire system because the integration covers the total volume in phase space. Moreover, this equation can be applied to both the gas and dark matter components of a cluster (Demarco et al. 2003). Now the problem is to compute the distribution function $f(\mathbf{x}, \mathbf{v})$. By knowing the mass density distribution of the system one can, in principle, obtain the distribution function, since, by definition, $\rho = \int f d^3v$. Inverting this relation, however, can be done when simplifying hypotheses are made. For instance, if we consider relaxed clusters as spherically symmetric systems without rotation, then the distribution function f, depends explicitly only on the total energy, and it can be obtained from the density profile by an Abel inversion (Binney & Tremaine 1987). In this way we have $f = f(\rho)$ and the integrated specific entropy can be computed numerically for a given density profile. In chapter 2, I apply this theoretical frame work to nearby clusters of galaxies, and I compute specific entropies assuming a Sérsic model for the gas density distribution (see Eq. (1.66)).

If clusters of galaxies are relaxed structures, then it is natural to think of galaxies and gas sharing the same dynamics imposed by the cluster potential. In this case, the velocity dispersion of galaxies can be used to obtain

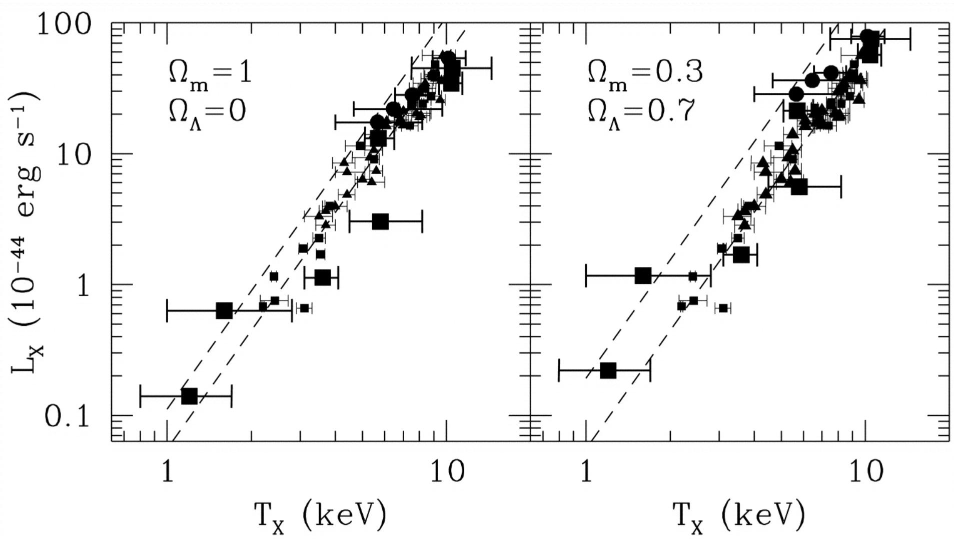

Figure 1.11: Luminosity-temperature relation for clusters of galaxies in two different cosmologies. Small triangles and squares correspond to nearby clusters (Markevitch 1998; Arnaud & Evrard 1999). Large circles correspond to clusters at $0.5 \leq z \leq 0.8$ (Della Ceca et al. 2000) and large squares are distant clusters with redshifts in the range $0.57 \leq z \leq 1.27$ (Borgani et al. 2001). Dashed lines indicate the $L_{bol} - T_X$ relation of Eq. (1.74) with $L_6 = 3$ and $\alpha = 3$, for A=0 (lower lines) and A=1 computed at $z = 1$ (upper lines). Figure taken from Borgani et al. 2001.

an estimate of the cluster temperature. This relation can be written as $k_B T \simeq \mu m_p \sigma^2 \simeq 6(\sigma/10^3\ km\ s^{-1})^2 keV$. Although with some scatter, observational data follow this relation (Wu, Xue & Fang 1999), indicating that the equilibrium state of clusters is a good approximation. Gas is seen to trace the galaxy distribution and the mass distribution of clusters. This is also the case in some non-virialized systems, as the one I will discuss in chapter 5.

If $f_{gas} = \rho_{gas}/\bar{\rho}$ is the gas fraction in the cluster, with $\bar{\rho}$ the mean cluster density, then from the Virial theorem (see section 1.4.1) we obtain $f_{gas} k_B T/(\mu m_p) \propto M/R$. This leads us to the following relation between cluster mass and temperature for local clusters: $M \propto (f_{gas} T)^{3/2}$. On the other hand, if the bolometric X-ray emissivity of the plasma is written as $\epsilon_X \propto n^2 \Lambda(T)$, with $\Lambda(T) \propto T^{1/2}$ and the number density is $n = f_{gas}\bar{\rho}/(\mu m_p)$, then the bolometric X-ray luminosity of the cluster will be $L_{bol} = \int \epsilon_X dV \propto f_{gas}^2 \bar{\rho} T^{1/2} M$. Using the above relation between mass and temperature, we finally obtain for local clusters $L_{bol} \propto f_{gas}^{7/2} \bar{\rho} T^2$. These relations, as theory predicts, indicate that clusters of different masses are just scaled versions of each other.

The predicted $T \propto M_{vir}^{2/3}$ scaling law is observed to hold for clusters with temperatures $T > 3$ keV (Allen, Schmidt & Fabian 2001), whereas in lower temperature systems the slope of the relation is observed to be steeper (Finoguenov, Reiprich & Böhringer 2001). In the case of the $L_{bol} - T_X$ relation, the discrepancies between theory and observations is even larger. Writing this relation in a more general form as (see Borgani et al. 2001):

$$L_{bol} = L_6 \left(\frac{T_X}{6KeV}\right)^{\alpha} (1+z)^A \left(\frac{d_L(z, \Omega_M, \Omega_\Lambda)}{d_L(z,1,0)}\right)^2 \times 10^{44} h^{-2} erg\ s^{-1} \quad (1.74)$$

observational evidence indicates values of $L_6 \simeq 3$ and $\alpha \simeq 2.5 - 3$ (see figure 1.11) for clusters with T_X of the order of and greater than 2 keV (see Wu, Xue & Fang 1999, and references therein). In the case of systems with T_X of the order of and below 1 keV, the slope steepens even more, being observed with a value of $\alpha \sim 5$ (e.g., Helsdon & Ponman 2000). These findings are consistent with the observed mass-luminosity relation, $L_X \propto M^{1.8\pm0.1}$ (Reiprich & Böhringer 2002). With respect to a possible evolution of the $L_{bol} - T_X$ relation, observations indicate that it is consistent with $A \approx 0$, i.e. no evolution, even up to redshifts greater than 1 (Arnaud & Evrard, 1999; Borgani et al. 2001; Stanford et al. 2001; Holden et al. 2002; Hashimoto et al. 2002). The departure of these relations from self-similar predictions, specially in low temperature systems, suggests that non-gravitational processes may be taking an active part during the formation and evolution of groups and clusters of galaxies. The existence of the so called entropy floor is thus reinforced (Ponman, Cannon & Navarro, 1999; Helsdon & Ponman 2000; Lloyd-Davies, Ponman & Cannon 2000).

1.3.3 Dark Matter Halos

About 70% of the mass of a galaxy cluster is in the form of matter which does not emit any kind of radiation, and therefore is called Dark Matter (DM). This special kind of matter is considered to be non-collisional and only interacts via gravitational attraction. Observational evidence in favour of its existence is more than clear: rotation curves in galaxies (Rubin, Thonnard & Ford 1980), mass-to-light ratios in clusters and gravitational lensing (e.g., Smail et al. 1997), to mention some. The exact nature of this kind of matter is still not clear, and several candidates have been proposed. One of the possible constituents of DM could be baryonic matter in the form of planets, brown dwarf stars or black holes. Another possibility could be relativistic particles called Hot and Warm DM, however, this kind of DM presents problems for the formation of structures. The favorite type of DM is the so called Cold Dark Matter (CDM), made of non-relativistic massive particles. Numerical simulations of structure formation show that this CDM is able to reproduce the degree of clustering and the structures we observe in the universe, such as galaxies, clusters of galaxies and voids, at different redshifts. Moreover, these CDM simulations can be used to set strong constraints on the cosmological model, i.e., Ω_M, Ω_Λ and σ_8.

The study of DM halos in clusters and galaxies through numerical simulations has been addressed by many authors (Navarro, Frenk & White 1996, 1997; Moore et al. 1999; Navarro 2001), undergoing remarkable progresses in the last decades owing to the development of more advanced computing facilities which perform such calculations. N-body simulations of DM halos clearly show cuspy DM density profiles for clusters of galaxies. In general, the DM density distribution can be well represented by a profile of the form:

$$\rho_{DM}(r) = \rho_s x^\alpha (1 + x^\beta)^\gamma \tag{1.75}$$

where $x = r/r_s$, with r_s being a characteristic radius, ρ_s a charactersitic density, and α, β and γ constants. The work of Navarro, Frenk & White (NFW; 1996, 1997) suggests that this profile is universal, independent of mass scale and cosmology, and is defined by the values of $\alpha = -1$, $\beta = 1$ and $\gamma = -2$. This indicates that at the cluster center, the DM distribution goes like $\rho_{DM} \propto r^{-1}$, in clear contrast to the distribution of gas, which is better approximated by a profile with a central core. The NFW profile tends to $\rho_{DM} \propto r^{-3}$ in the outer regions of simulated clusters. The universality of the NFW profile is however contradicted by Jing & Suto (2000), and simulations carried out by Moore and collaborators (1999) show that the profile given by Eq. (1.75) is better characterized by values of $\alpha = -1.5$, $\beta = 1.5$ and $\gamma = -1$, at galaxy and cluster scales. This profile turned out to be even steeper than the NFW profile, making worse the lack of ability of CDM models to reproduce the rotation curves of low surface brightness (LSB) galaxies (Flores & Primack 1994; Moore et al. 1999). Although other works claim that cuspy DM profiles are consistent with the available data for dwarfs and LSB galaxies (van den Bosch & Swaters 2001), microlensing studies towards the center of our galaxy also support the incompatibility between CDM simulations and observational evidence (Binney & Evans 2001).

1.4 Weighting Clusters of Galaxies

1.4.1 Virial Mass

Let us consider a system composed of N particles surrounded by an external medium of constant presure P_0 . This system could be a cloud of gas, a cluster of stars or a cluster of galaxies. The matter distribution of the system is described by its moment of inertia:

$$I = \sum_{i=1}^{N} m_i \mathbf{r_i} \cdot \mathbf{r_i} \tag{1.76}$$

where m_i and r_i are the mass and position vector respectively of the particle i. The temporal evolution of I is then given by

$$\frac{dI}{dt} = 2\sum_{i=1}^{N} m_i \mathbf{r_i} \cdot \mathbf{v_i} \tag{1.77}$$

with $\mathbf{v_i} = \dot{\mathbf{r_i}}$, which implies

$$\frac{1}{2}\frac{d^2 I}{dt^2} = \sum_{i=1}^{N}\{m_i v_i^2 + m_i \mathbf{r_i} \cdot \frac{d\mathbf{v_i}}{dt}\} = 2T + \sum_i \mathbf{r_i} \cdot \mathbf{F_i} = 2T + \Upsilon \tag{1.78}$$

where $T = 1/2\sum_i m_i v_i^2$ is the total kinetic energy of the particle system and $\Upsilon = \sum_i \mathbf{r_i} \cdot \mathbf{F_i}$ is the *virial* introduced by Clausius in 1870. $\mathbf{F_i}$ is the net force acting on particle i. Here we can decompose this force in a force due to collisions between particles or contact force, a force due to gravitation and a force produced by the external medium at constant presure P_0. Thus, we can write $\Upsilon = \sum_i \mathbf{r_i} \cdot \mathbf{F_i^{contact}} + \sum_i \mathbf{r_i} \cdot \mathbf{F_i^{gravity}} + \sum_i \mathbf{r_i} \cdot \mathbf{F_i^{pressure}}$. The first term of the right side is obviously equal to zero because of the action and reaction principle. The second term, however, turns out to be

$$\sum_i \mathbf{r_i} \cdot \mathbf{F_i^{gravity}} = \sum_i \mathbf{r_i} \cdot \left[\frac{\partial U}{\partial \mathbf{r_i}}\right] = -U \tag{1.79}$$

where U is the total potential energy of the system. Here we have used Euler's theorem after noting that U is a homogeneous function [1] of the vector $\mathbf{r_i}$. Finally, the last term can be rewritten as :

[1] An homogeneous function satisfies $f(tx, ty) = t^n f(x, y)$, for a fixed n.

$$\sum_i \mathbf{r_i} \cdot \mathbf{F_i^{pressure}} = -\int_\Sigma p(\mathbf{r})\hat{n} \cdot \mathbf{r}\ ds = -P_0 \int_\Sigma \mathbf{r} \cdot d\mathbf{s}$$

$$= -P_0 \int_V \nabla \cdot \mathbf{r} dV = -3P_0 V \tag{1.80}$$

where $p(\mathbf{r})$ is the pressure at position $\mathbf{r}$ on the surface Σ of the volume V which contains our system of particles, and $\hat{n}$ is a unitary vector normal to the surface Σ. In consequence, we can rewrite Eq. (1.78) as:

$$\frac{1}{2}\ddot{I} = 2T + U - 3P_0 V \tag{1.81}$$

If the system is in statical or quasi-statical equilibrium, $(1/2)\ \ddot{I} = 0$, so that equation 1.81 becomes:

$$2T + U - 3P_0 V = 0 \tag{1.82}$$

This important result in physics is known as the *Virial Theorem*. In the case of a cluster of galaxies, we have $P_0 V \ll min(T, \mid U \mid)$, so that Eq. (1.82) gives the well known relation:

$$2T = -U \tag{1.83}$$

This equation can be applied to clusters of galaxies in order to estimate their mass content. However, this is not a direct task because in general, it is necessary to make assumptions about the spatial distribution of the galaxies in the cluster. If we assume that the velocity distribution of the galaxies is isotropic, then $< v^2 >= 3 < v_{||}^2 >= 3\sigma_{||}^2$, where $\sigma_{||}$ is the observed velocity dispersion of galaxies along the line of sight. If the velocity dispersion is independent of the masses of the galaxies, then we have $T = (3/2)M\sigma_{||}^2$, where M is the total mass of the cluster. Assuming spherical symmetry, we can figure out from the observed surface distribution of galaxies a suitable weighted mean separation R_{cl} and write the potential energy as $U = -GM^2/R_{cl}$. In this way, Eq. 1.83 yields the following expression for the cluster virial mass:

$$M = 3\frac{\sigma_{||}^2 R_{cl}}{G} \tag{1.84}$$

1.4.2 X-ray and Sunyaev-Zel'dovich Mass

The X-ray surface brightness of galaxy clusters can be used to obtain their gas density distribution and temperature distribution as explained in section 1.3.2. Once the gas density and temperature distributions are known, the total mass of the cluster can be obtained by means of the hydrostatic equilibrium equation (Eq. (1.68)). Although the isothermality of the ICM is not a good enough approximation to real clusters (Markevitch et al. 1998;

Allen, Schmidt & Fabian 2001; De Grandi & Molendi 2002), this commonly used hypothesis allows to compute the dynamical (total) mass in a straightforward manner, once $\rho_{gas} = \rho(r)$ is known.

In chapter 2, I use X-ray data to derive the ICM density profile. Moreover, by using a power law relation between the distributions of dark matter and gas (Gerbal et al. 1992; Durret et al. 1994; Teyssier 2002), given by $\rho_{DM}/\rho_{gas} = \kappa(r/a)^{-\alpha}$, the Sérsic model defined by Eq. (1.66) provides the following expression for the total amount of mass contained within a spherical region of radius r:

$$M_{Dyn}(r,\kappa,\alpha) = \int_0^r \left[\kappa\left(\frac{u}{a}\right)^{-\alpha} + 1\right]\rho_{gas}(u)4\pi u^2 du =$$

$$\frac{4\pi\rho_0 a^3}{\nu}\left\{\kappa\,\gamma\left[\frac{3-(p+\alpha)}{\nu},\left(\frac{r}{a}\right)^{\nu}\right] + \gamma\left[\frac{3-p}{\nu},\left(\frac{r}{a}\right)^{\nu}\right]\right\} \tag{1.85}$$

where $\gamma(a,z)$ is the incomplete gamma function defined by $\gamma(a,z) = \int_0^z x^{a-1}e^{-x}dx$. Total gas and Dynamical masses are obtained by integrating Eqs. (1.66) and (1.85) up to infinity.

The Sunyaev-Zel'dovich (SZ) effect (Zel'dovich & Sunyaev 1969; Sunyaev & Zel'dovich 1970) is nowadays a powerful method to find clusters of galaxies and also to estimate the mass content of the gas present in the ICM. This effect is due to Compton scattering of the CMB photons by free electrons of the hot cluster gas. Clusters are thus detected as decrements in the intensity on CMB maps (Birkinshaw 1990, 2003). This intensity decrement is translated into a temperature variation ΔT_{SZ} which is related to the electronic density of the cluster by (see Grego et al. 2000):

$$\frac{\Delta T_{SZ}}{T_{CMB}} \approx -2\frac{k_B\sigma_T}{m_e c^2}\int n_e(l)T_e(l)dl \tag{1.86}$$

where σ_T is the Thomson scattering cross section, T_e the electron temperature of the cluster gas and n_e the electron density. The integral extends along the line of sight, dl. If we assume an isothermal β-model (Eq. (1.64)) to describe the electronic density distribution in the ICM, this distribution projects to a β model distribution of the SZ decrement if the system obeys spherical or ellipsoidal symmetry. Therefore, by fitting the two-dimensional SZ temperature decrement (see Eq. (1.86)), one can obtain the β-model parameters for the electronic density. Once the electronic density distribution is known, the gas density follows straightforwardly and the gas mass can be computed (e.g., Grego et al. 2000).

1.4.3 Gravitational Lensing Mass

To start, let us consider a point system of mass M. The geometry of the spacetime outside this object is described by the line element in Eq. (1.2), when the metric tensor corresponds to the "Schwarzschild geometry" (see Schutz 1990). In this case, the deflection angle of the light coming from a distant source behind the system and passing near it is given by:

$$\alpha = \frac{4GM}{bc^2} \tag{1.87}$$

where b is the impact parameter of the photon. This effect, predicted by Einstein's theory of gravity and confirmed observationally by Eddington, represents a powerful tool to trace the mass distribution of galaxy clusters. Clusters thus may behave as large lenses, deviating the trajectories of photons passing near them, in the same way as optical lenses do. By measuring the redshift of the cluster (lens), the redshift of the source whose light is being deflected by the cluster, and the position angle θ on the plane of the sky of the image of the lensed source, one may, in principle, obtain a reconstruction of the cluster mass distribution. Let D_{ol}, D_{ls} and D_{os} be the angular-diameter distances from the observer O to the lens L, from the lens to the source S and from the observer to the source, respectively. The impact parameter can be written as $b = D_{ol}\theta$, which gives us $\alpha(\theta) = 4GM/(c^2 D_{ol}\theta)$. In the general case of a cluster with a given mass distribution, and a source with a position angle β we have (see e.g., Binney & Merrifield 1998):

$$\beta = \theta - \frac{D_{ls}}{D_{os}}\alpha(\theta) \tag{1.88}$$

where the deflection angle α is related to the projected mass density of the cluster Σ as (see Mellier 1999) :

$$\alpha(\theta) = \frac{4G}{c^2} D_{ol} \int \Sigma(\theta) \frac{\theta - \theta'}{\mid \theta - \theta' \mid^2} d^2\theta' \tag{1.89}$$

The projected mass density can be put in terms of a projected Poisson equation:

$$\frac{\Sigma(\theta)}{\Sigma_{crit}} = \frac{4\pi G}{c^2}\frac{D_{ls}D_{ol}}{D_{os}}\Sigma(\theta) = \frac{1}{2}\nabla^2\phi(\theta) \tag{1.90}$$

where ϕ is the dimensionless gravitational potential projected along the line of sight (see Mellier 1999) and $\Sigma_{crit} = [c^2/(4\pi G)][D_{os}/(D_{ls}D_{ol})]$ is the critical projected mass density of the lens. The deformation of the source due to the lens can be described in terms of the magnification matrix:

$$\mathcal{A} = \frac{d\beta}{d\theta} = \begin{pmatrix} 1 - \kappa - \gamma_1 & \gamma_2 \\ \gamma_2 & 1 - \kappa + \gamma_1 \end{pmatrix} \tag{1.91}$$

where $\kappa = \Sigma(\theta)/\Sigma_{crit}$ and γ_1 and γ_2 are the components of the complex shear $\gamma = \gamma_1 + i\gamma_2$. γ_1 and γ_2 describe the anisotropic deformation produced by the tidal gravitational field of the cluster. Different values of β will produce different kinds of images. In some cases, the value of β corresponds to placing the source on one of the so-called caustic lines in the source plane. When this happens, the magnification of the source is infinite, and the resulting images are large arcs around the lens. The special case when source, lens and observer are perfectly aligned, produces a ring around the lens, called an "Einstein ring". The presence of gravitational arcs around clusters, give powerful constraints of the dynamical mass distribution in the cluster (e.g., Broadhurst et al. 2000). Obtaining $\Sigma(\theta)$ from the equations above, for a realistic model of the cluster potential, can be difficult. A good solution must reproduce the observed shape of the lensed images, described by γ_1 and γ_2, and predict the observed position of the images given by the corresponding β angle. Once the projected mass density has thus been obtained, the mass of the cluster can be computed by integrating $\Sigma(\theta)$. In section 5.5, I will report on the discovery of the most distant lens known today. The presence of two spectroscopically confirmed gravitational arcs gives us the possibility of applying the above theory in order to make a robust characterization of the cluster gravitational potential.

1.5 Surveys of galaxies and clusters

Our knowledge about the formation and evolution of structures such as clusters of galaxies has increased greatly during the last decade owing to the fast development of advanced instrumentation and new and efficient observational techniques. More powerful telescopes and detectors have become operational, both on the ground and in space, allowing a detailed study of these objects at different wavelengths. This multi-wavelength approach in the study of clusters allows us to probe different energy scales, from the high energy domain of X-rays down to the low energy domain of radio emission, thus yielding remarkable progress in our understanding of the physical mechanisms and conditions present in these objects. Understanding cluster evolution depends on our ability to detect these sources up to large look-back times. By comparing observed properties of clusters over a wide range in redshift, with comparable properties of the same class of objects in the local universe, one can set important constraints on their evolution. In this section I will try to summarize the most important observed properties of galaxy clusters that we know so far. I will start by introducing the basic aspects of one of the most useful tools of modern cosmology, the one that makes possible the detection and discovery of our objects of interest: galaxy and cluster surveys.

In general, a survey represents a powerful tool that can be used to learn about the evolutionary history of a given class of objects and to set constrains on the parameters describing the geometry and dynamics of our universe. The first step is to choose the class of objects to study. In the present work I concentrated on galaxies and clusters of galaxies. A previous knowledge on the nature of the sources chosen for the survey is very important in order to determine the *selection function*, i.e., the set of criteria which lead to the object detection. Here, the balance between the depth and the area of the survey as well as the selection of the observation bandpass are of great importance. The product {depth $\times$ survey area} remains approximately constant because of observing time constraints. This means that if we want to observe deep into the area covered by the detector, then we will have to spend most of the observing time on that region of interest, without moving onto another place on the sky. On the other hand, if we want to observe a large area on the sky, then we will not be able to spend much time only on a given limited region.

There are basically three different methods to select objects (see Rosati 2002): a flux limited selection, a colour selection and a narrow band filter selection.

1. **Flux limited selection**: with this method all the sources, with a given rest frame luminosity L, presenting observed fluxes greater than a given threshold, f_{lim}, are included in the sample. Note that the observed luminosity of the source depends on the passband used and so a k-correction is involved when obtaining the rest frame luminosity L from the corresponding observed luminosity. The maximum redshift at which an object with a given L is observed is given by the following relation $d_L(z_{max}) = \sqrt{L/(4\pi f_{lim})}$. All this, however, represents an ideal case. Sources are never detected by their flux, but rather by their surface brightness: a detection consists of an excess of flux within a given aperture, above a given threshold (normally a few times the rms σ of the surrounding background). Due to the cosmological dimming given by Eq. (1.21), extended sources will be the first to drop out of the sample if the limiting flux f_{lim} is not high enough as to cover the complete range of surface brightness of the class of objects being observed. Thus, the determination of the right f_{lim} is crucial.

2. **Colour selection**: With this method, the sources are selected on the basis of their flux and colours. This method, as I will show in sections 4.1.4 and 5.2.3, turns out to be extremely efficient at isolating objects in a given redshift range dz. However, this technique depends strongly on the knowledge of the spectral energy distribution of the object under consideration. In chapter 4 I will talk more about the spectrum of galaxies and how this determines the observed color of a source as a function of redshift.

3. **Narrow band filter selection**: this method selects sources showing a flux excess when observed through a narrow band filter, as compared to their broad band flux. Emission line galaxies are the most suited

objects for this kind of selection. If the λ_0 is the central wavelength of the narrow band filter and $\Delta\lambda$ its width, then a source with emission lines at $\lambda_{e.l.}$ will be detected at redshift $1 + z = (\lambda_0/\lambda_{e.l.})$ within a redshift range given by $\Delta z = \Delta\lambda/\lambda_{e.l.}$. The selection function in this case is determined by the equivalent width of the emission line. Some of the disadvantages of this method are the fact that it only probes a very narrow slice in redshift, and only a limited fraction of the galaxy population is selected, favouring galaxies with large equivalent widths. Moreover, the effect of reddening due to dust surrounding the object and along the line of sight to the object, has to be taken into account, otherwise dust absorption can affect significantly the selection function by absorbing the UV continuum and selectively suppressing different emission lines. In spite of all these limitations, this method has been successfully applied to the search of high redshift Lyα emitters, allowing to discover galaxies at redshift $z > 5$ (e.g., Rhoads, J. et al. 2003).

In the case of clusters of galaxies, X-ray selected samples offer several advantages with respect to sample selection based on other criteria. The X-ray emission of clusters is a clear indication of the existence of a physically bound object since it comes from the ICM confined in the cluster potential well, and its X-ray luminosity is correlated to the mass of the system. This emission is more concentrated than the optical galaxy distribution and since the surface density of X-ray sources is relatively low, clusters appear as high-contrast objects in the X-ray sky. Moreover, and very important, X-ray surveys give the possibility of defining flux-limited samples with well understood selection functions. The sky coverage of a given survey is a well defined function of the source flux, hence the corresponding search volume for a given limiting flux and for a cluster of given luminosity can be obtained by integrating Eq. (1.58) over the given survey area.

The first galaxy surveys probably started in the XVIII century with the pioneering work of Messier and Herschel, who first realized the existence of clusters of galaxies. The subsequent development of new observational techniques and instrumentation brought a considerable progress to the discovery of more clusters and distant galaxies. All this allowed Hubble to discover in the early twenties the expansion of the universe, thus opening a new era in cosmology. In the fifties, the Palomar Sky Survey plates were the basis of Abell's work, who provided the first extensive and statistically complete sample of galaxy clusters (Abell 1958). This work was later extended to the Southern hemisphere by Corwin and Olowin (Abell, Corwin & Olowin 1989). The advent of CCD detectors in the eighties started the modern era of observational cosmology, followed by the development of multiobject spectrographs in the nineties. These powerful tools together with the birth of new advanced observational facilities on the ground (e.g. Keck and VLT) and in space (e.g. HST, ROSAT, Chandra and Newton-XMM), allowed a number of major imaging and spectroscopic surveys to be carried out, giving us the possibility to discover and explore distant galaxies and galaxy clusters and to understand the structure and evolution of the universe.

Some important ground based surveys carried out in the past two decades are: the Automatic Plate-measuring Machine survey (APM; Maddox et al. 1990), the Center for Astrophysics survey (CfA; Huchra et al. 1990), the Canada-France Redshift Survey (CFRS; Lilly et al. 1995), the Las Campanas Redshift Survey (LCRS; Shectman et al. 1996), the Canadian Network for Observational Cosmology survey 2 (CNOC2; Yee et al. 2000), the 2dF Galaxy Redshift Survey (2dFGRS; Colles et al. 2001, 2003) and the Sloan Digital Sky Survey (SDSS; Strauss et al. 2002). On the other hand, among the major surveys conducted from space we can mention the Hubble Deep Field North and South (HDF-N and HDF-S; Williams et al. 1996; Ferguson, Dickinson & Williams 2000), the ROSAT All Sky Survey (RASS; Trümper 1993), the ROSAT Deep Cluster Survey (RDCS; Rosati et al. 1995, 1998), the Serendipitous High-Redshift Archival ROSAT Cluster Survey (SHARC; Burke et al. 1997), the Wide Angle Rosat Pointed X-Ray Survey of clusters (WARPS, Scharf et al. 1997; Perlman et al. 2002), the Lockman Hole with XMM (Hasinger et al. 2001), and the Chandra Deep Fields (Giacconi et al. 2002, Bauer et al. 2002). For a more complete description and review about these and other surveys see Rosati (2002) and Rosati, Borgani & Norman (2002), and references therein.

One very important characteristic of clusters is that their high X-ray luminosities make them detectable at high redshift. Therefore, X-ray surveys present advantages over optical surveys when searching for distant systems (e.g., Rosati et al. 1998; Gioia et al. 1990b; Henry et al. 1992; Romer et al. 2000; Stanford et al. 2002). The work I will present in chapter 5 was carried out on the two most distant massive clusters known today in the southern sky, both detected in the ROSAT Deep Cluster Survey (RDCS; Rosati et al. 1995, 1998). On the other hand, I will also show that color selection techniques can be very efficient to select cluster candidates for a subsequent redshift survey (see also chapter 5).

Chapter 2

The structure of nearby clusters

In this chapter I will present a study of the X-ray emission of galaxy clusters, aimed at characterizing the thermodynamical properties and structure of the nearby systems. The basic concepts and elements of cluster X-ray emission have already been introduced in section 1.3.2, and in this section I will just refer to them when needed. In particular, I will show interesting results about the specific entropy in clusters and scaling relations that can be interpreted as due to the evolution of these structures (see Demarco et al. 2003, the paper presented in the next chapter). This work represents the extension to the cluster scale of similar works already carried out in smaller systems such as elliptical galaxies. The conclusions from comparing the results obtained for both ellipticals and clusters are not obvious and very interesting.

Essentially, we wanted to check whether clusters of galaxies, as self-gravitating systems, also obey similar scaling relations as those already found in observed elliptical galaxies (see Gerbal et al. 1997; Lima Neto et al. 1999; Márquez et al. 2000; Márquez et al. 2001) and in numerical simulations (Márquez et al. 2000; Lanzoni 2000; Jang-Condell & Hernquist 2001).

2.1 Entropy and scaling relations

Elliptical galaxies in the local universe (see section 1.3.1) exhibit remarkable regularities in their spectro-photometric properties, such as their surface brightness profile, the correlation between color, velocity dispersion and Mg index, and the red sequence in a color magnitude diagram (as it will be discussed in chapter 5). The surface brightness profile of early-type galaxies can be well fitted by a Sérsic law (e.g., Caon, Capaccioli & D'Onofrio 1993; Prugniel & Simien 1997; Graham & Colless 1997), which is defined by Eq.

(1.65). This profile, which is more suited than the popular de Vaucouleurs profile to fit the surface brightness of ellipticals, can be used to compute specific entropies (see Eq. (1.73)) and total masses (see Eq. (1.85)). For a sample of 132 ellipticals belonging to three galaxy clusters, Márquez et al. (2001) found that the Sérsic parameters correlate two by two, and in the three-dimensional space defined by these three parameters they are located on a thin line. These properties have been interpreted as due to the fact that, to a first approximation, all these elliptical galaxies have the same specific entropy, as shown in figure 2.1-a (see Gerbal et al. 1997, Lima Neto et al. 1999, Márquez et al. 2000), and that a scaling law exists between the potential energy U and the mass M for these galaxies of the form $U \propto M^{1.72\pm0.03}$ as shown in figure 2.1-d (see Márquez et al. 2001). Each of these relations defines a two-manifold in the $[log\Sigma_0, loga, \nu]$ space. The thin line on which the galaxies are distributed in this space is the intersection of these two two-manifolds, as it is shown in figure 2.2. Such relations are most probably a consequence of the formation and evolution processes undergone by these objects, since theory predicts $U \propto M^{5/3}$ under the hypothesis that energy and mass are conserved. A second order relation between the specific entropy and mass has also been observed in ellipticals (Márquez et al. 2001), which can be interpreted as due to the merging history of the galaxies during their evolution (see Márquez et al. 2000). Entropy would be produced during merger events and it would be higher in systems which have undergone more interactions (see figure 2.1-b).

This self-similar relation between potential energy and mass for a given virialized structure at present time can be shown in a simple way. Let us consider the spherical collapse model already discussed in section 1.2.1. For instance, if the index i refers to the time at which a spherical perturbation attains its turnaround radius, the total energy of this structure at that time will be $E_i = K_i + U_i \simeq U_i \propto M_i^2/R_i$, being R_i the size of the collapsing region. Since $R_i \propto M_i^{1/3}$, then we have that $E_i \propto M_i^{5/3}$. On the other hand, once the final structure becomes virialized after the collapse, the virial theorem (Eq. 1.83) can be used to compute the final energy $E_f = K_f + U_f$ of the formed systems which is $E_f = U_f/2$. If energy and mass are conserved during the formation and evolution of the self-gravitational structure down to the present epoch, then we have $E_i = E_f$ and $M_i = M_f$. It is straightforward to conclude that $U_f \propto M_f^{5/3}$.

Interestingly, numerical simulations of cold dark matter haloes in two different mass ranges lead to a similar scaling law between the potential energy and mass of the haloes. In the mass range $4 \times 10^5 \leq M \leq 4 \times 10^8\ M_\odot$ (unvirialized clusters), Jang-Condell & Hernquist (2001) find a relation consistent with $U \propto M^{5/3}$, while in the mass range $10^{12} \leq M \leq 10^{15}\ M_\odot$ (virialized clusters) Lanzoni (2000) finds $U \propto M^{1.69\pm0.02}$.

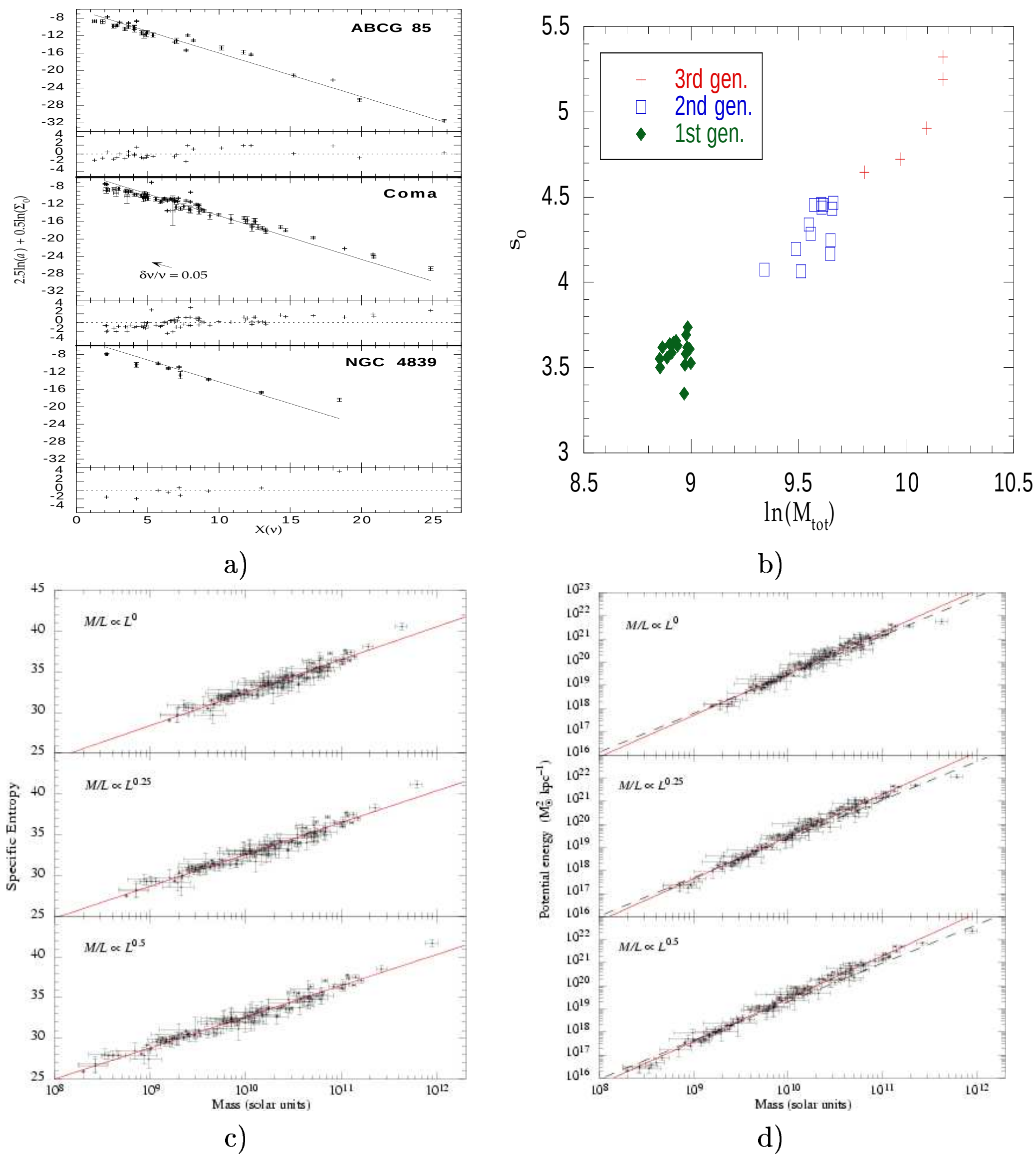

Figure 2.1: a) The specific entropy and residuals in the Sérsic parameters space. The linear relation defines an "Entropic Line", which corresponds to the Entropic Plane seen edge-on. The small scatter of ellipticals about this relation indicates that they have nearly the same specific entropy (see Lima Neto et al. (1999) for details). b) Specific entropy versus total mass for simulated ellipticals. These artificial galaxies are the remnants of different generation mergers (see Márquez et al. 2000). This relation is of second order compared to the dominant constant specific entropy. This plot shows the consequences of merging processes on the production of entropy. c) Observed specific entropy-mass relation for ellipticals, and d) observed potential energy-mass relation for ellipticals (Márquez et al. 2001).

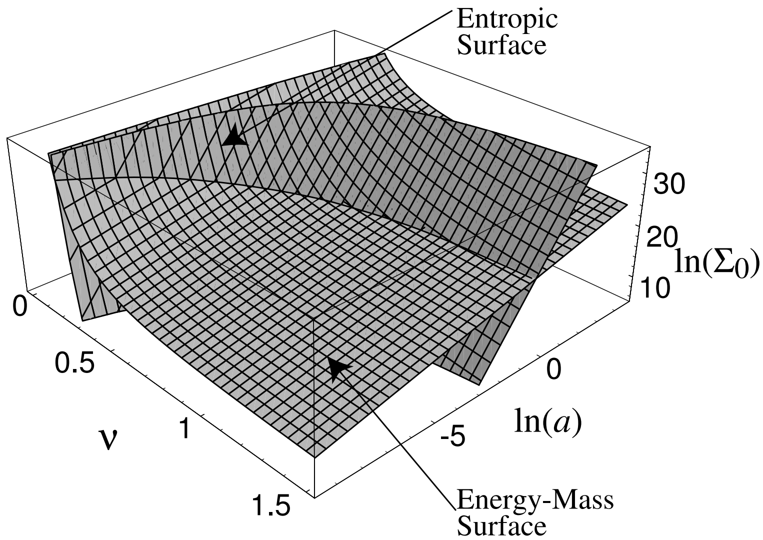

Figure 2.2: Three-dimensional representation of the specific entropy and energy-mass 2-manifolds, in the space defined by the Sérsic parameters: $\log\Sigma_0$, log a and ν (Márquez et al. 2001).

In what follows I will describe the data set of this study. A brief description of the telescope and the instrument used is presented, followed by the target selection criteria. I will afterward present the method used to fit the X-ray surface brightness of the clusters and I will discuss how the thermodynamical quantities of the clusters can be obtained from the X-ray cluster emission. In particular, model images will be used to recover the 3-D distribution of the ICM gas that we assume follows a Sérsic profile. Additional information on the code used to fit the X-ray surface brightness can be found in Magnard (2002). The full set of results are in Demarco et al. (2003), which will be presented in the following chapter.

2.2 X-ray observations

2.2.1 The X-ray telescope

The data I used to carry out this work correspond to X-ray pointed observations obtained with the PSPC-B (Position-Sensitive Proportional Counter B) of ROSAT (ROentgenSATellit; Trümper 1983). This satellite was the result of a joint collaboration between the *Max-Planck-Institut für extraterrestrische Physik* (MPE), the *National Aeronautics and Space Administration* (NASA) and the *British Science and Engineering Research Council.* ROSAT was proposed in 1975 and it was launched from Cape Canaveral on June 1st, 1990. It was placed on a circular orbit at 575 km of altitude and with a inclination angle of 53 degrees. The main scientific goals of the mission were: making the first All-Sky Survey on the X-ray and the extreme ultraviolet (XUV), and carry out a detailed study of X-ray and XUV sources through pointed observations. Finally, after more than seven years of service, ROSAT was shut down on February 12th, 1999.

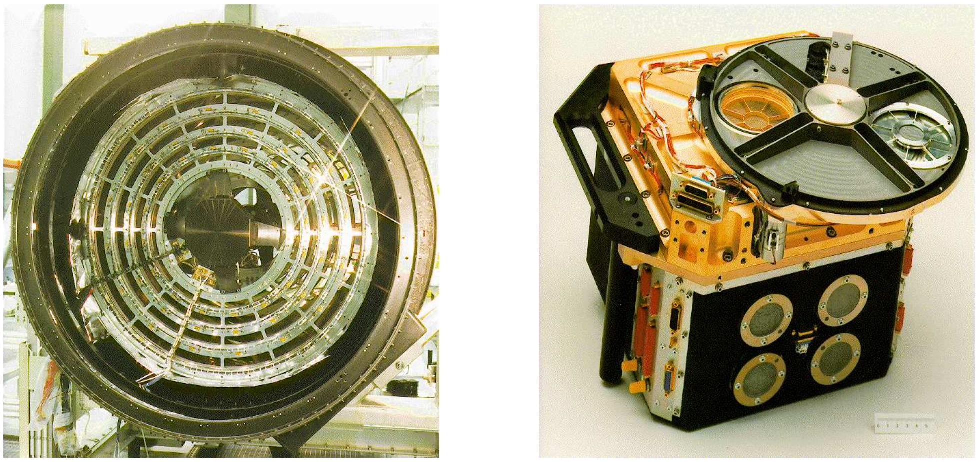

a) b)

Figure 2.3: a) The entrance aperture of the X-ray telescope. Four parabolic-hyperbolic mirror pairs fitted into each other form a Wolter Type-I Telescope with a focal length of 2.4 m. b) One of the two PSPC detectors of ROSAT with its filter wheel (ROSAT mission, Max-Planck-Institut für extraterrestrische Physik. http://www.xray.mpe.mpg.de/).

The two on-board PSPCs (see Fig. 2.3) are the main detectors of the X-ray telescope (XRT), mounted on a carrousel within the focal plane. The XRT is a 2.40m focal-length mirror assembly consisting of four nested Wolter-I mirrors with a maximum aperture of 83.5 cm (see Fig. 2.3). The PSPC window size is 8 cm in diameter and provides a 2° field of view. In order to avoid scientific targets being occulted by the opaque parts of the PSPC, ROSAT had a wobbling that changed its pointing ± 3' in 400 s. Inside the PSPC there is a system of two cathodes and two anodes. All cathodes and anodes are wire grids embedded in a gas mixture of 65% argon, 20% xenon and 15% methane. Inside the camera, the incident X-ray photon is absorbed by the gas producing a photo-electron. This electron is thermalized afterwards, ionizing other gas atoms and producing a number of secondary electrons which is proportional to the incident photon energy (hence the name of the detector). The secondary electrons pass through the first cathode towards the anode; a new ionization occurs and the signal induced on the cathode is used to determine the entrance point into the detector of the initial photon. The spatial resolution of the PSPC is 25" and

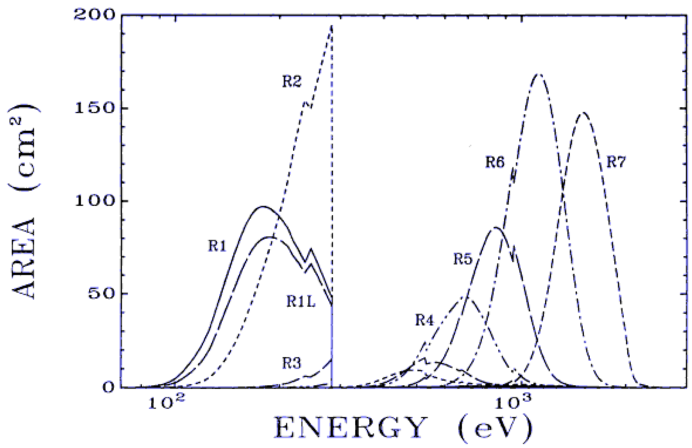

Figure 2.4: On-axis response curve for the ROSAT PSPC R1 to R7 bands. The sharp break at 0.284 keV is due to the carbon K_α absorption edge of the PSPC entrance window (Snowden et al. 1994).

its energy resolution is given by $\triangle E/E = 0.43\,\sqrt{0.93/E}$, corresponding to a resolution of 43% at 0.93 keV. The energy range used for the data analysis goes from 0.44 to 2 keV, corresponding to the R4 to R7 energy bands listed in table 2.1 and shown in figure 2.4, as taken from Snowden et al. (1994). These bands were chosen in order to avoid the low signal to noise ratio in the lower bands due to the high absorption by the hydrogen column, and problems due to the carbon K_α absorption produced by the PSPC entrance window.

Band Name	PI Channels	SASS Channels	Energy (keV)
R4	52-69	13-15	0.44-1.01
R5	70-90	16-18	0.56-1.21
R6	91-131	19-23	0.73-1.56
R7	132-201	24-30	1.05-2.04

Table 2.1: Broad energy bands definitions for ROSAT PSPC. Only the bands used in this work are listed. See Snowden et al. (1994) for the full listing of bands and information on the PI and ESAS energy channels.

2.2.2 Selection criteria

The raw data are PSPC pointed observations of clusters of galaxies, which were retreived from the public ROSAT archive at MPE [1]. The criteria employed to select our sample is summarized below:

- Exposure time: clusters were sorted according to exposure time, giving higher priority to those with longer exposures in order to have targets with a good signal-to-noise ratio.

- Geometry: priority was given to those clusters showing a regular and isotropic X-ray emission, without any apparent evidence for substructure or merging [2]. Only clusters appearing isolated on the plane of the sky were considered.

- Location on the focal plane: in order to minimize PSF effects and avoid the obscuration of the scientific target by the opaque parts of the PSPC window, we have chosen images where the cluster appears well on-axis.

- Light curve: only objects with a smooth light curve, i.e., with no strong scattered solar X-ray contamination were taken into account.

We thus built up a sample of 24 clusters, all of them in Abell's catalog (Abell 1958), with redshifts ranging between 0.01 and 0.3. Table 2.2 summarizes the data set. Redshifts were taken from the SIMBAD [3] data base (except for A2199 for which the redshift was obtained from Wu, Xue & Fang 1999), and gas temperatures and luminosities from Wu, Xue & Fang (1999), except for A2034 and A2382 for which temperatures are those quoted in Ebeling et al. (1996).

The presence of substructure in clusters of galaxies (e.g. Geller & Beers 1982; Jones & Forman 1992) is an important issue when studying their thermodynamical properties. Our selection criteria excludes objects with evident substructure and thus our sample is biased toward dynamically relaxed systems. This however does not present a problem since we are interested here only in relaxed objects, to which our theoretical models and assumptions apply better. Our conclusions will thus be applicable to this subset of the cluster population, and further studies with refined models should be carried out in order to include appropriately non-relaxed clusters in a same study.

---

[1] http://www.xray.mpe.mpg.de/rosat/archive/

[2] The cluster A1837, previously selected, was discarded during the analysis after recognizing irregularities in its X-ray surface brightness, which also agrees with its irregular optical distribution (Krywult, MacGillivray & Flin 1999).

[3] http://simbad.u-strasbg.fr/Simbad

Cluster	α (h m s)	δ (deg min sec)	z	T_0 (keV)	L_x (10^{44} erg s^{-1})	Exp. Time (sec)	ROR
A85	0:41:37.0	-9:20:36.0	0.0518	$6.20^{+0.40}_{-0.15}$	$19.52^{+1.35}_{-1.35}$	10238	800250p
A478	4:13:25.3	10:27:56.0	0.0881	$6.90^{+0.35}_{-0.35}$	$32.00^{+4.08}_{-4.08}$	21969	800193p
A644	8:17:26.0	-7:30:48.0	0.0704	$6.59^{+0.17}_{-0.17}$	$18.92^{+2.17}_{-2.17}$	10246	800379p
A1651	12:59:22.0	-4:11:12.0	0.0860	$6.10^{+0.20}_{-0.20}$	$18.78^{+2.21}_{-2.21}$	7429	800353p
A1689	13:11:34.0	-1:21:54.0	0.1810	$9.02^{+0.40}_{-0.30}$	$55.73^{+8.92}_{-8.92}$	13949	800248p
A1795	13:48:52.7	26:35:32.0	0.0631	$5.88^{+0.14}_{-0.14}$	$25.42^{+1.47}_{-1.47}$	25803	800055p
A2029	15:10:56.0	5:45:18.0	0.0765	$8.47^{+0.41}_{-0.36}$	$41.93^{+2.96}_{-2.96}$	12542	800249p
A2034	15:10:13.0	33:31:42.0	0.1510	7.00	6.86	8952	800349p
A2052	15:16:44.5	7:1:18.0	0.0348	$3.10^{+0.20}_{-0.20}$	$4.27^{+0.34}_{-0.34}$	6215	800275p
A2142	15:58:20.0	27:14:0.0	0.0899	$9.70^{+1.30}_{-1.30}$	$61.12^{+3.95}_{-3.95}$	6186	800096p
A2199	16:28:38.3	39:33:5.0	0.0299	$4.10^{+0.08}_{-0.08}$	$7.09^{+0.25}_{-0.25}$	40999	800644p
A2219	16:40:24.0	46:41:0.0	0.2250	$12.40^{+0.50}_{-0.50}$	$64.56^{+6.96}_{-6.96}$	11200	800571p
A2244	17:2:43.2	34:4:49.0	0.0970	$8.47^{+0.43}_{-0.42}$	$25.32^{+2.14}_{-2.14}$	2963	800265p
A2319	19:21:11.0	43:56:18.0	0.0559	$9.12^{+0.15}_{-0.15}$	$39.74^{+2.17}_{-2.17}$	3169	800073p-1
A2382	21:52:1.0	-15:38:54.0	0.0648	2.90	0.91	17444	800227p-1
A2390	21:53:34.0	17:40:12.0	0.2310	$11.10^{+1.00}_{-1.00}$	$63.49^{+14.87}_{-14.87}$	10335	800570p
A2589	23:23:57.2	16:46:43.0	0.0416	$3.70^{+1.30}_{-0.70}$	$3.42^{+0.38}_{-0.38}$	7293	800526p
A2597	23:25:18.0	-12:6:30.0	0.0852	$4.40^{+0.40}_{-0.70}$	$15.37^{+1.79}_{-1.79}$	7163	800112p
A2670	23:54:10.0	-10:24:18.0	0.0761	$4.45^{+0.20}_{-0.20}$	$4.97^{+0.92}_{-0.92}$	17679	800420p
A2744	0:14:20.0	-30:23:18.0	0.3080	$11.00^{+0.50}_{-0.50}$	$62.44^{+14.41}_{-14.41}$	13648	800343p
A3266	4:31:11.9	-61:24:23.0	0.0594	$8.00^{+0.30}_{-0.30}$	$16.48^{+0.64}_{-0.64}$	13547	800552p
A3667	20:12:30.0	-56:49:0.0	0.0552	$7.00^{+0.60}_{-0.60}$	$22.70^{+4.20}_{-4.20}$	12560	800234p
A3921	22:49:38.6	-64:23:16.0	0.0960	$4.90^{+0.55}_{-0.55}$	$10.92^{+1.52}_{-1.52}$	11997	800378p
A4059	23:57:6.9	-34:33:6.0	0.0460	$3.97^{+0.12}_{-0.12}$	$5.78^{+0.54}_{-0.54}$	5439	800175p

Table 2.2: Cluster sample and observational data from the literature. Coordinates correspond to J2000. Temperatures and luminosities are taken from Wu, Xue & Fang (1999), except for A2034 and A2382 for which the temperature and X-ray luminosity were taken from Ebeling et al. (1996). Error bars for these two clusters are not provided. The last column indicates the Rosat Observation Request (ROR) ID of the observation.

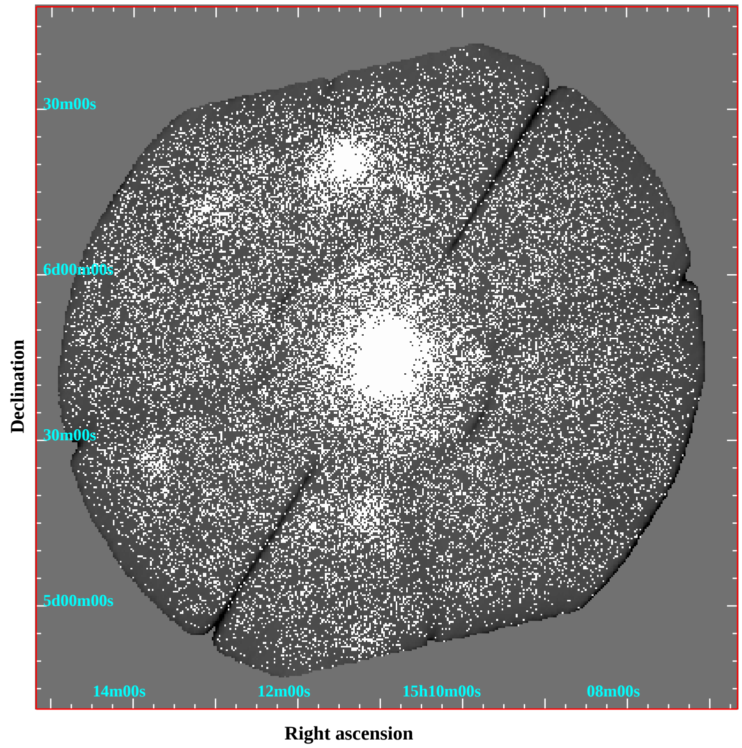

Figure 2.5: X-ray emission of the galaxy cluster A2020 as observed by ROSAT. The image has been treated with the Extended Source Analysis Software (ESAS) according to the procedures described in Snowden et al. (1994). The dark circular and radial features due to the opaque structure of the PSPC supporting window can also be seen.

2.2.3 Data reduction

The preparation of the raw data (XIMA$_{raw}$) was done by using the Extended Source Analysis Software (ESAS) developed by S. Snowden and collaborators (see Snowden et al. 1994, and references therein). The routines in the software provide the best available modeling and subtraction of the various non-cosmic background components and do the corrections for exposure, taking into account the effective time during which every pixel was exposed.

The non-cosmic background components can be identified in the corresponding light curve of the observation. This light curve is a plot showing the number of counts received by the detector per unit time (count rate) as a function of time. The different components of this background are:

- the charged particle background from the local environment.

- the afterpulse background consisting of all pulses occurring within 0.35 ms of a preceding event (or detection).
- the scattered solar X-ray background. This kind of contamination appears as sharply rising count rate enhancements in the light curve. They could also appear as falling count rate enhancements at the start of the observation intervals of the light curve (Snowden & Freyberg 1993).
- Short-Term Enhancements. This component appears as erratic and asymmetrical peaks anywhere in the observation intervals of the light curve.
- Long-Term Enhancements. These are seen as a gradual drift in the minimum count rate over many observation intervals.

All these components of the non-cosmic background and their modeling are described in detail in Snowden et al. (1994). The resulting models are then used to construct a background exposure (BACK) for each band. Also for each band, an exposure map (EXP) is created taking into account the wobbling of the satellite, the quantum efficiency of the gas in the PSPC which depends on the energy of the incident photon, the efficiency as a function of the position on the focal plane of the detector and vignetting effects. The final corrected surface brightness images (XIMA) for every band, will be given by:

$$XIMA = (XIMA_{raw} - BACK)/EXP$$

Finally, when producing the combined final image using the count rate from each band, the point sources are masked out and subtracted, excepting the cluster center. The final images thus obtained are 512×512 with a pixel scale of 14".947. An example of a final corrected image is shown in figure 2.5.

2.3 Data analysis: the fitting procedure

Once the images have been processed and calibrated, these are ready to be used in the modeling of the cluster X-ray surface brightness. In this section I review in some detail the method I used to make the synthetic images of the X-ray emission of the clusters. These images will then be used to obtain the gas density profile.

The main goal is to estimate physical quantities as the gas and DM mass, the total potential energy, the integrated specific entropy for the gas and DM and the gas temperature distribution for every cluster. This can be achieved by modeling the gas distribution of the cluster with a parameter-dependent profile. We choose the Sérsic profile (see sect. 1.3.2), defined by Eqs. 1.66 and 1.67 to describe the three-dimensional distribution of the gas within the cluster potential. The final set of Sérsic parameters should reproduce accurately the surface brightness profile of the real data.

The strategy to be used is then as follows. Starting with some initial guess for the Sérsic parameters, we build up a model for the spatial electronic density distribution of the gas. We use this profile to compute the three-dimensional X-ray emissivity of the gas which is then projected to produce an artificial image. This synthetic image is compared with the PSPC image. This procedure is executed iteratively, varying at every step the value of the model parameters, until a set of values yielding the 3-D electronic density profile that produces an X-ray surface brightness profile that best fits the observation is found.

A Maximum Likelihood approach is followed in order to find the best density profile. A dedicated code called FIT, developed by F. Magnard (see Magnard 2002 for a detailed description), was the main tool I used to carry out the fitting of the ROSAT PSPC images. It computes the associated likelihood function and performs a pixel-to-pixel fit of the data by using procedures in the MINUIT library of CERN (James 1994). The FIT function can produce both 2-D and 3-D models of the extended X-ray emission of a cluster.

The input parameters needed by FIT are the coordinates (in pixels) of the X-ray emission centroid, the redshift and the temperature of the cluster, the initial guess for the model parameters, the X-ray background, the ellipticity of the X-ray emission and position angle, and the parameters defining the cosmology. We assume $H_0 = 50\ km\ s^{-1}\ Mpc^{-1}$, $\Omega_0 = 1$ and $\Omega_\Lambda = 0$ throughout this analysis. In addition to this, FIT also requires a file with the definition of variables and functions to be used by MINUIT. These functions are MIGRAD and MINOS, the first one carries out the fit itself and the second one computes the parameter errors. Input images are the final calibrated image, background and exposure maps and the point source mask.

2.3.1 The Maximum Likelihood approach

We model the flux of photons arriving in every PSPC pixel and during the time interval T by a Poisson law. If μ_i is the mean number of photons per unit time arriving into the pixel i and N_i is the random variable representing the total number of photons arriving into the ith pixel, the probability of having n_i photons in this pixel will be:

$$p_{n_i,i} = Pr\{N_i = n_i\} = \frac{[\mu_i T]^{n_i}}{n_i!}\, e^{-\mu_i T} \tag{2.1}$$

This law has a mean $E\{N_i\} = \mu_i T$ and a variance $Var(N_i) = \mu_i T$, which correspond to the signal and the square of the noise at the given pixel. If now N is the total number of image pixels and since the fluxes from one pixel to another are independent, the total probability of having an image with n_i photons within the pixel i and during the time interval T is :

$$Pr_{tot} = \Pi_{i=1}^{N} p_{n_i,i} \tag{2.2}$$

We would like thus to use this formalism in order to find the best fit between our model, defined by the Sérsic parameters, together with the ellipticity ϵ of the cluster X-ray emission, and the PSPC image. The Maximum Likelihood method is well suited for this purpose. Let us consider that in every pixel i of the image there are y_i photons. If the number of photons in the ith pixel of our model is $y^i = y^i(\nu, a, n_{e0}, \epsilon)$ (computed from the Bremsstrahlung emission which depends on the electronic density) and if N is the number of pixels of the real and model images, the total probability of having the same number of photons in every pixel of the model and real image respectively, according to the equations 2.1 and 2.2, is

$$Pr_{tot}(\nu, a, n_{e0}, \epsilon) = \Pi_{i=1}^{N} \frac{[y^i(\nu, a, n_{e0}, \epsilon)]^{y_i}}{y_i!} e^{-y^i(\nu,a,n_{e0},\epsilon)} \tag{2.3}$$

From this equation we define the function:

$$C(\nu, a, n_{e0}, \epsilon) \equiv -ln(Pr_{tot}(\nu, a, n_{e0}, \epsilon)) = \sum_{i=1}^{N} (y^i - y_i\, ln(y^i) + ln(y_i!)) \tag{2.4}$$

where $L(\nu, a, n_{e0}, \epsilon) \equiv -C$ is the Maximum Likelihood function. Having the best fit between the model and the observation is equivalent to maximizing the likelihood function or minimizing the function given by Eq. 2.4, with respect to the model parameters. This minimization is carried out by the MIGRAD method in the MINUIT library of CERN (James 1994).

2.3.2 Surface brightness fitting

To start fitting the data, we need a first guess for the Sérsic parameters ν, a and n_{e0} (see section 1.3.2), together with a guess for the X-ray emission ellipticity. This first guess can be obtained by doing a direct fit of the X-ray surface brightness by a 2-D Sérsic profile (see Eq. (1.65)). This step is also performed by FIT. Once such starting values are obtained, the 3-D fit is executed.

The making of the three dimensional X-ray emission model requires the coordinates (in pixels) of the X-ray emission centroid, the central electronic density of the cluster, n_{e0} (in cm^{-3}) and the model parameters a (in kpc) and ν. The sky background (in $counts\ s^{-1}\ arcmin^{-2}$), the excentricity ϵ of the projected X-ray emission and the corresponding inclination angle, θ_0 (in degrees) are required as well. The mean gas temperature (in keV) is also an input parameter and is kept fixed during the fit, in the same manner as the background, the excentricity and position angle. The values for the cluster temperature were taken from Xu, Xue & Fang (1999), except for the clusters A2034 and A2382 for which the corresponding values were taken from Ebeling et al. (1996).

The three dimensional model of the X-ray emission, ϵ_ν, created by FIT takes into account not only the Bremsstrahlung free-free continuum but also the free-bound and bound-bound line emission (see section 1.3.2). An appropriate Gaunt factor is thus used. All frequencies are integrated within a pass band defined by the four energy bands considered and the resulting model is then projected by integrating it along the line of sight:

$$\epsilon(s) = 2 \int_{z=0}^{+\infty} \int_{\nu_{min}}^{\nu_{max}} \epsilon_\nu(s^2 + z^2)\xi(\nu)\, d\nu\, dz$$

with $s^2 = x^2 + y^2$, where x and y are the directions perpendicular to the line of sight and z is the coordinate along the line of sight. This integral is performed by taking into account the energy response function $\xi(\nu)$ of the PSPC. The projected image is finally convolved with the PSPC PSF to produce the synthetic image $Im_{syn} = Im_{syn}(n_e(n_{e0}, \nu, a), \epsilon)$ that is compared with the real ROSAT image (see Magnard 2002). The PSPC PSF varies as a function of energy and position over the focal plane of the detector. A FWHM=2 pixels, corresponding approximately to the central PSF of the PSPC, was used. From here on, MIGRAD starts searching for the maximum of the Likelihood function by changing the initial value of the non-fixed parameters and repeating the procedure described above. Creating a 512×512 pix^2 image with a new set of parameter values takes of the order of 50 seconds. In order to decrease the computing time, the original size of the ROSAT images was reduced by trimming off the outer region of the frames where the noise starts to dominate the X-ray signal. Once the minimum of the function C is found, FIT gives as final result the value for each model parameter with the corresponding error bar. These error bars are computed with the MINUIT error function MINOS, which calculates parameter errors taking into account both parameter correlations and non-linearities. Resulting errors correspond to a 1σ deviation (see James 1994 for details).

2.3.3 Scale parameter and central density

Due to the ellipticity of the X-ray emission, the scale parameter a given by FIT corresponds to the semi-major axis of the X-ray emission as seen on the plane of the sky. Supposing that all the clusters are oblate spheroids, i.e., that the third axis along the line of sight is a major axis a and if b is the semi-minor axis, we define the ellipticity of the projected X-ray emission by $e = \sqrt{1-(b/a)^2}$. In order to use the scale parameter a obtained for this geometry into our spherically symmetric models an equivalent scale parameter had to be defined. This new scale is defined as $a_{eq} = (a^2 b)^{1/3}$ and will be used instead of a to compute the specific entropy (Eq. 1.73), the dynamical mass (Eq. 1.85) and the potential energy of a spherically symmetric X-ray region.

Whereas the fitting process directly gives us the best estimates for the scale a and shape ν parameters, the central electronic number density n_{e0} obtained by FIT is not accurate enough, and it has to be estimated by another method. In order for the n_{e0} normalization to give the observed number of counts, we first compute the cluster flux F, after subtraction of point sources and background. The masked source pixel counts were set to the mean value taken within ellipses. Then n_{e0} was chosen so that a bremsstrahlung XSPEC [4] model convolved by a hydrogen column absorption would give the same flux as seen by ROSAT:

$$F = \frac{3.02\times10^{-15}}{4\pi d_L^2}\int n_e n_I dV =$$

$$\frac{3.02\times10^{-15}}{4\pi d_L^2}\;\frac{2^{2+\frac{2p-3}{\nu}}}{\nu} a^3 {n_{e0}}^2 \pi \Gamma\left[\frac{3-2p}{\nu}\right]$$

where d_L is the luminosity distance to the cluster (see section 1.1.2), and n_I is the number density of plasma ions.

An example of the quality of the fitting procedure and the ability of the Sérsic model to reproduce the X-ray emission of galaxy clusters is shown Figs. 2.6 and 2.7. Figure 2.6 shows the X-ray image of A478 on top of which the X-ray iso-contours of the image (in red) and the iso-contours of the corresponding Sérsic model (in blue) are overlaid. Cross-section cuts of the same X-ray image on the x- and y- direction are shown in Fig. 2.7. Each cut passes through the center of the image and the corresponding Sérsic model given by the fit is also overlaid (red curve).

During the fitting process, the gas temperature is kept constant, as a first approximation. However, the exact shape of the temperature profile is not crucial when finding the set of values for the Sérsic parameters, because the emissivity does not have a strong dependence on temperature as compared to its dependence on density (see Eq. (1.63)); indeed, we find that modifying the temperature profile changes the values of the Sérsic parameters by at most a few percent (see Demarco et al. 2003). The scale and shape parameters changed by about 1%, and the central electronic density by 4% with respect to the isothermal fit. This lack of sensitivity on temperature

[4] http://heasarc.gsfc.nasa.gov/docs/xanaud/xspec/

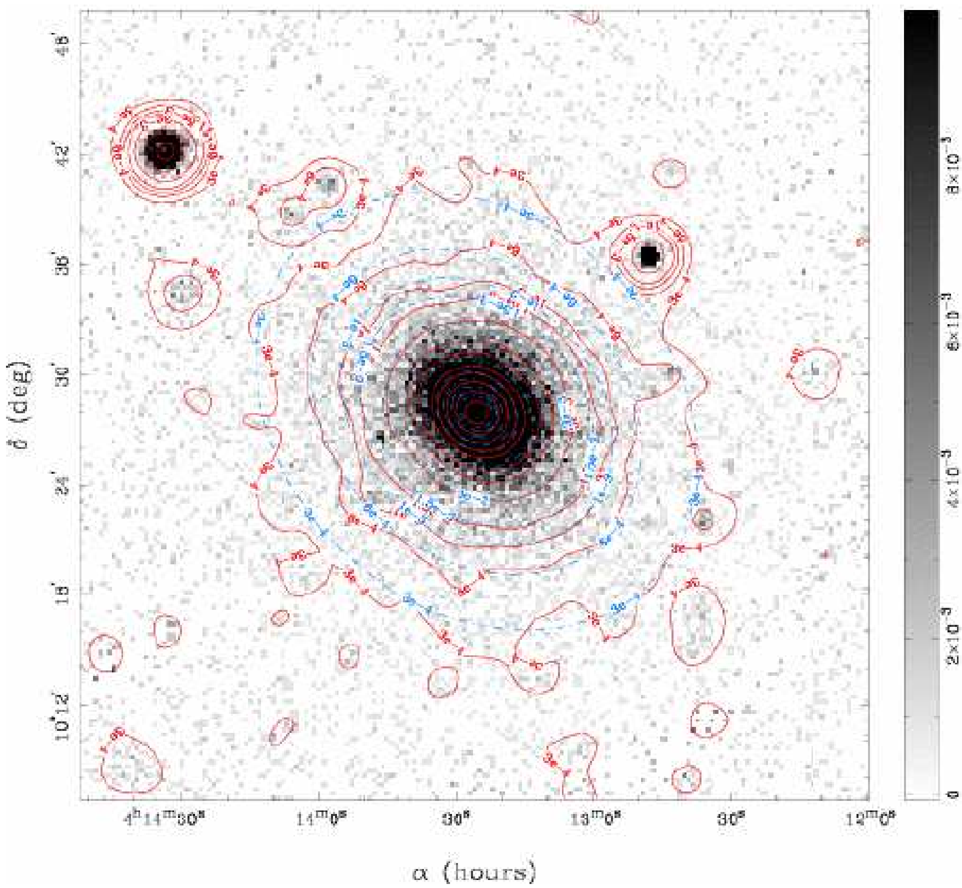

Figure 2.6: X-ray iso-contours (in red) are overlaid on top of the PSPC image of the cluster A478. The iso-contours from the derived Sérsic model are shown in blue. The good agreement between model and observation confirms the quality of our fitting procedure and the ability of the Sérsic model to reproduce the X-ray emission of galaxy clusters (Magnard 2002).

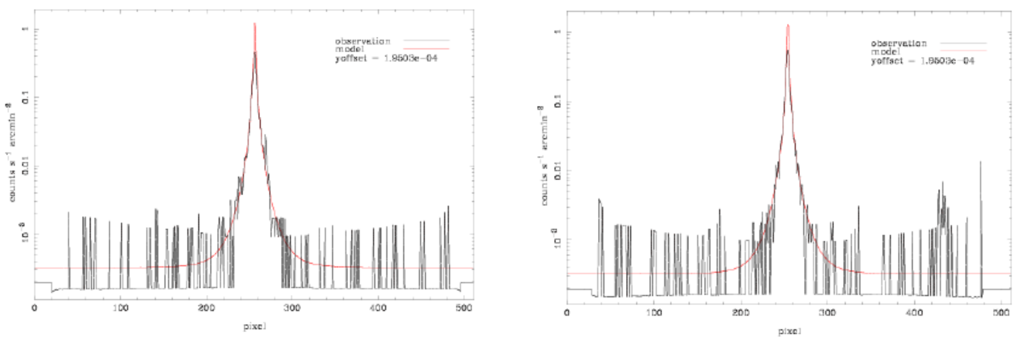

a) b)

Figure 2.7: Cross-section cuts of the A478 X-ray image (see figure 2.6). a) Cross-section cut along the x-direction. b) Cross-section cut along y-direction. The red curve corresponds to the best fit Sérsic model (Magnard 2002).

of the X-ray emission allows us to use temperature profiles defined by Eqs. (1.71) and (1.72) together with the Sérsic parameters already found without any further iteration.

2.4 Error estimation

The error bar associated to every model parameter obtained by FIT, is computed by the MINOS function of MIGRAD (see James 1994, and references therein). If n is the number of free parameters of the problem, once MIGRAD has found a minimum in this n-D parameter space, the MINOS function proceeds then to estimate the corresponding error bars. The method used by MINOS gives asymmetric error bars. If η is the parameter being considered (in our case $\eta = \nu, a, n_{e0}$) and σ_η^{pos} and σ_η^{neg} their associated positive and negative errors, we will consider as the parameter error bar the quantity $\sigma_\eta = max(\mid \sigma_\eta^{neg} \mid, \sigma_\eta^{pos})$. To find the errors σ_η^{pos} and σ_η^{neg}, the program makes the parameter η vary, minimizing at every step the function given by Eq. (2.4) with respect to the other n-1 parameters. If C_0 is the minimum value of Eq. 2.4 with respect to the other n-1 parameters, the minimization process is halted once the two values of η at which $C = C_0 + Err$ are found. In the case of a "negative-log-likelihood" function, as it is our case, the value of Err corresponding to one standard deviation is $Err = 0.5$ (see James 1994).

The error bars on a physical quantity (e.g., specific entropy, dynamical mass or potential energy) depending on the model parameters are obtained by means of Monte Carlo simulations. Every parameter η was modeled by a gaussian distribution with σ equal to the corresponding σ_η deviation. The distributions for every parameter are then used to compute the resulting distribution of the physical quantity and the corresponding 1σ error, for each cluster (see Demarco et al. 2003).

2.5 Summary of results and discussion

The details concerning the calculations of gas and dark matter density profiles, dynamical mass and temperature profiles and the different correlations between cluster specific entropy, mass and potential energy are fully presented in the next chapter. Here I will just summarize the main results of the present work accompanied with some important remarks.

Our analysis of the sample of 24 nearby clusters of galaxies show that:

- The Sérsic profile can also be used to describe the gas density distribution of the ICM, being a good alternative to the popular isothermal β-model. Note that a Sérsic profile does not require an isothermal ICM.

- At first order, the integrated specific entropy of the gas is nearly the same among the clusters. The same conclusion is obtained for the dark matter. This result agrees very well with the constant specific entropy among cluster ellipticals found by Lima Neto et al. (1999).

- At second order, the integrated specific entropy of the gas correlates with the logarithm of the gas mass. In an analogous way the specific entropy of the dark matter correlates with the logarithm of the dark matter mass. Such a result also agrees very well with a similar correlation found in cluster ellipticals and simulated galaxies (Márquez et al. 2000, 2001).

- The cluster potential energy and dynamical mass correlates with each other. This correlation follows closely the theoretical self-similar relation $U \propto M^{5/3}$ introduced in section 2.1. This behavior is also seen in real ellipticals (Márquez et al. 2001) and reproduced by numerical simulations (Lanzoni 2000; Jang-Condell & Hernquist 2001).

The correlations found in this analysis indicate the existence of an "entropic line" for galaxy clusters (see Magnard 2002), in analogy to elliptical galaxies. The existence of both an entropic surface and a potential energy-mass surface in the Sérsic parameter space for galaxy clusters implies that these objects can be considered as a single-parameter family, described by one of the Sérsic parameters only (e.g. Márquez et al. 2001).

The importance of the correlations found here resides in the fact that they are probably the result of the physics ruling cluster formation. A correlation between the global specific entropy and the mass keeps some information on the various events affecting the thermodynamical history of clusters. Following the results from simulated elliptical galaxies (Márquez et al. 2000), the observed variation of integrated specific entropy with dynamical mass in clusters suggests that dissipation-free merging processes between DM halos are of importance in such a relation, because of their impact on the final total mass and on the amount of entropy produced during the cluster formation. Dissipating processes in clusters may also play a role as generators of entropy. These mainly correspond to Bremsstrahlung emission ($L \propto M^{4/3}$) and non-gravitational processes affecting the intra cluster gas. Violent merger events can be accompanied by an important dissipation of energy and creation of entropy, while minor mergers can be translated in an adiabatic accretion of matter without a significant production of entropy. These energy losses, however, are all negligible compared to the cluster gravitational energy. Thus the value of the slope in the specific entropy-mass relation reflects the impact of such processes on the cluster history. Clusters with higher global specific entropy could have undergone more episodes of hierarchical merging through their histories, thus becoming more massive.

On the other hand, considering the collapse of matter to form a virialized gravitational system, the correlation between the potential energy and the total mass of the final structure is a natural consequence of the conservation of energy and mass during its formation. A self-similar relation defined by $U \propto M^{5/3}$ is expected from theory (see Márquez et al. 2001) and we show that it is indeed also followed by our observed galaxy clusters. Note that merging events and energy losses affecting the integrated specific entropy are however small enough as to allow conservation of mass and energy.

All these results strongly suggest that the formation processes affecting galaxies and clusters of galaxies are quite similar regardless the scale involved.

In the following chapter I present the full paper "A study of dark matter halos and gas properties in clusters of galaxies from ROSAT data" by R. Demarco, F. Magnard, F. Durret & I. Márquez (Demarco et al. 2003) where a complete analysis and the entire set of results from the data introduced previously in this chapter are presented.

Chapter 3

Dark matter and gas structure in clusters

Paper accepted in Astronomy & Astrophysics (A&A, 407, 437. 2003)

A&A 407, 437–451 (2003)
DOI: 10.1051/0004-6361:20030864

Astronomy & Astrophysics

A study of dark matter halos and gas properties in clusters of galaxies from ROSAT data*

R. Demarco[1,2], F. Magnard[2], F. Durret[2], and I. Márquez[3]

[1] ESO-European Southern Observatory, Karl-Schwarzschild Str. 2, 85748 Garching b. München, Germany
[2] Institut d'Astrophysique de Paris, CNRS, 98bis Bd Arago, 75014 Paris, France
[3] Instituto de Astrofísica de Andalucía (C.S.I.C.), Apartado 3004 , 18080 Granada, Spain

Received 30 January 2003 / Accepted 28 May 2003

Abstract. Self-gravitating systems such as elliptical galaxies appear to have a constant integrated specific entropy and obey a scaling law relating their potential energy to their mass. These properties can be interpreted as due to the physical processes involved in the formation and evolution of these structures. Dark matter halos obtained through numerical simulations have also been found to obey a scaling law relating their potential energy to their mass with the same slope as for ellipticals, and very close to the expected value predicted by theory. Since the X-ray gas in clusters is weakly dissipative, we test here the hypothesis that it verifies similar properties. Comparable properties for the dark matter component are also investigated.
With this aim, we have analyzed ROSAT-PSPC images of 24 clusters, and fit a Sérsic law to their X-ray surface brightness profiles. We found that: 1) the Sérsic law parameters (intensity, shape and scale) describing the X-ray gas emission are correlated two by two, with a strong correlation between the shape and scale parameters; 2) the hot gas in all these clusters roughly has the same integrated specific entropy, although a second order correlation between this integrated specific entropy and both the gas mass and the dynamical mass is observed; 3) a scaling law links the cluster potential energy to its total mass, with the same slope as that derived for elliptical galaxies and for dark matter halo simulations. Comparable relations are obtained for the dark matter component. All these correlations are probably the consequence of the formation and evolution processes undergone by clusters of galaxies.

Key words. cosmology: theory – cosmology: dark matter – galaxies: clusters: general – X-rays: galaxies: clusters

1. Introduction

Clusters of galaxies are known to be the largest gravitationally bound objects in the Universe. The amplification of primordial density fluctuations by gravity is thought to be the origin of structure formation, however the details of the formation process are not yet well understood and the study of the structure and properties of dark matter halos and of the intra cluster plasma in virialized systems can give important clues to understand the physics involved in the formation and evolution of galaxy clusters. Nowadays, these studies have undergone great improvements with the developement of advanced observational facilities and techniques, together with the progress of numerical simulations.

Many works have been developed during the last decades on this respect. Secondary infall and the effects of this process on the cluster structure were discussed by Gunn & Gott (1972), and self-similar solutions for dark matter halos and gas were studied in numerical simulations carried out e.g. by Fillmore & Goldreich (1984), Bertschinger (1985), Teyssier et al. (1997) and Subramanian (2000). Cold Dark Matter (CDM) studies based on high-resolution N-body simulations performed by Navarro et al. (1996, 1997) suggest a cuspy and universal dark matter (DM) density profile in galaxies and clusters of galaxies, independent of mass scale and cosmology; this result is contradicted by Jing & Suto (2000). However, some important observational facts seem not to be reproduced by these studies: numerical simulations based on the CDM scenario predict density profiles with steep inner slopes which fail to reproduce the rotation curves of low surface brightness (LSB) galaxies (Flores & Primack 1994; Moore et al. 1999). Although other works claim that cuspy DM profiles are consistent with the available data for dwarfs and LSB galaxies (van den Bosch & Swaters 2001), microlensing studies towards the center of our galaxy also support the incompatibility between CDM simulations and observational evidence (Binney & Evans 2001). To explain the discrepancy concerning the central slopes of DM halos (Navarro et al. 1997; Moore et al. 1999), the lack of sufficient resolution in the central regions of simulated halos has been proposed; Point Spread Function (PSF) effects together with insufficient resolution on galaxy rotation curves (van den Bosch & Swaters 2001) may be also at the origin of the discrepancy between models and observations.

Send offprint requests to: R. Demarco, e-mail: demarco@iap.fr
* Based on data obtained from the public archive of ROSAT at the Max-Planck-Institut für Extraterrestrische Physik.

Observations in the X-ray band provide valuable information on the hot Intra Cluster Medium (ICM). A popular model used to fit the spatial distribution of the X-ray gas is the so called β-model (Cavaliere & Fusco-Femiano 1976; Sarazin 1988) which assumes an isothermal ICM. However, this model may not be good enough to describe the cluster gas component, since the isothermality of the ICM is still rather controversial. Cooling flows are known to produce a drop of the gas temperature towards the center of the cluster; besides, outside the cooling flow region things are still not clear. Temperature profiles based on ASCA (White 2000) and ROSAT (Irwin et al. 1999) data were found to be consistent with the isothermal hypothesis. On the other hand, Markevitch et al. (1998) found from ASCA observations that cluster temperatures decrease significantly with radius. Irwin & Bregman (2000) analysed BeppoSAX data and claimed a slight rise in cluster temperature with radius, a result which is at odds with De Grandi & Molendi (2002), who found that for a set of 21 clusters the temperature profile has a clear isothermal core (excluding the cooling flow region) followed by a rapid radial decline. Note that such a core is consistent with Chandra observations of cooling flow clusters, where the temperature profile rises rapidly with radius, then remains approximately constant out to ~0.8 Mpc (Allen et al. 2001b). Finally, XMM-Newton observations e.g. of Coma (Arnaud et al. 2001) and Abell 1795 (Tamura et al. 2001) show small but significant radial variations of the temperature. Numerical simulations seem to confirm a decline of temperature profiles with radius, but are not able to reproduce the flatness of these profiles in the innermost regions (Frenk et al. 1999; Loken et al. 2002). This disagreement may be due to additional physical processes that must be taken into account in future numerical simulations. Another point is that a single β value cannot always fit the X-ray surface brightness profile of clusters (Allen et al. 2001a,b; Hicks et al. 2002).

The ICM density and temperature distributions are of fundamental importance because they can be used to determine the specific entropy distribution of the ICM, thus providing important information to understand nongravitational internal and external processes that may contribute to the ICM thermal history, such as external preheating and energy injection through supernova-driven galaxy winds (Brighenti & Mathews 2001; Dos Santos & Doré 2002). Non-gravitational processes may be responsible for the observed breaking of the self-similar relation between X-ray luminosity and temperature predicted by theory (Arnaud & Evrard 1999; Rosati et al. 2002 and references therein) and for the so called Entropy Floor (Ponman et al. 1999; Helsdon & Ponman 2000; Lloyd-Davies et al. 2000).

With the assumption that the X-ray plasma in clusters of galaxies is weakly dissipative, clusters considered as self-gravitating systems are likely to verify properties similar to those recently found in elliptical galaxies, considered as self-gravitating systems. Namely, the optical surface brightness profiles of elliptical galaxies can be fit by a Sérsic law (Sérsic 1968; Caon et al. 1993; Ciotti & Bertin 1999):

$$\Sigma(s) = \Sigma_0 \ \exp\left[-\left(\frac{s}{a}\right)^{\nu}\right] \tag{1}$$

characterized by three parameters: Σ_0 (intensity), a (scaling) and ν (shape). For a sample of 132 ellipticals belonging to three galaxy clusters, the Sérsic parameters were found to be correlated two by two, and in the three-dimensional space defined by these three parameters they are located on a thin line. These properties have been interpreted as due to the fact that, to a first approximation, all these elliptical galaxies have the same specific entropy (entropy per unit mass) (Gerbal et al. 1997; Lima Neto et al. 1999; Márquez et al. 2000), and that a scaling law exists between the potential energy U and the mass M for these galaxies: $U \propto M^{1.72\pm0.03}$ (Márquez et al. 2001). Each of these relations defines a two-manifold in the $[\log\Sigma_0, \log a, \nu]$ space. The thin line on which the galaxies are distributed in this space is the intersection of these two two-manifolds. Such relations are most probably a consequence of the formation and evolution processes undergone by these objects, since theory predicts $U \propto M^{5/3}$ under the hypothesis that energy and mass are conserved (Márquez et al. 2001).

Interestingly, numerical simulations of cold dark matter haloes in two different mass ranges lead to a similar scaling law between the potential energy and mass of the haloes. In the mass range $4\times10^5 \leq M \leq 4\times10^8\ M_\odot$ (unvirialized clusters), Jang-Condell & Hernquist (2001) find a relation consistent with $U \propto M^{5/3}$, while in the mass range $10^{12} \leq M \leq 10^{15}\ M_\odot$ (virialized clusters) Lanzoni (2000) finds $U \propto M^{1.69\pm0.02}$.

In this work, we present a study aimed at testing whether results similar to those found in elliptical galaxies can also be obtained for galaxy clusters, based on an accurate modeling of the cluster X-ray surface brightness. We use a de-projection of the Sérsic profile (Eq. (1)) to obtain the gas and DM density distributions, temperature profiles, dynamical mass distributions and estimations of the integrated specific entropies of the gas and DM components for a set of 24 nearby galaxy clusters and a group. Interesting correlations between physical quantities are found, comparable to those observed in elliptical galaxies, which can give important clues to understand better the formation and evolution of galaxy clusters. This paper is structured as follows: our sample is described in Sect. 2; the calculations of the physical quantities used in this paper are presented in Sect. 3; the method used to determine the gas density profile from the X-ray surface brightness is described in Sect. 4; the methods used to derive the temperature profile and the dark matter distribution are explained in Sect. 5; results are presented in Sect. 6 and conclusions in Sect. 7.

2. The sample

We have retrieved data taken with the PSPC-B camera of ROSAT from the ROSAT archive at MPE. The energy range considered is 0.44−2 keV, corresponding to the four energy bands $R4$ to $R7$ (Snowden et al. 1994). These bands were chosen in order to avoid the low signal to noise ratio in the lower bands due to the high absorption by the hydrogen column. The spatial resolution of the PSPC is 25″ and its energy resolution corresponds to 0.43% at 0.93 keV. We selected observations with the longest exposure times and where the cluster showed a regular shape, with no obvious mergers and a

Table 1. Cluster sample and observational data from the literature.

Cluster	z	Exp. time (s)	T_0 (keV)	$L_X(10^{44}$ erg s$^{-1})$
A85	0.0518	10 240	$6.20^{+0.40}_{-0.15}$	$19.52^{+1.35}_{-1.35}$
A478	0.0881	21 969	$6.90^{+0.35}_{-0.35}$	$32.00^{+4.08}_{-4.08}$
A644	0.0704	10 246	$6.59^{+0.17}_{-0.17}$	$18.92^{+2.17}_{-2.17}$
A1651	0.0860	7429	$6.10^{+0.20}_{-0.20}$	$18.78^{+2.21}_{-2.21}$
A1689	0.1810	13 957	$9.02^{+0.40}_{-0.30}$	$55.73^{+8.92}_{-8.92}$
A1795	0.0631	26 172	$5.88^{+0.14}_{-0.14}$	$25.42^{+1.47}_{-1.47}$
A2029	0.0765	12 550	$8.47^{+0.41}_{-0.36}$	$41.93^{+2.96}_{-2.96}$
A2034	0.1510	8952	7.00	6.86
A2052	0.0348	6211	$3.10^{+0.20}_{-0.20}$	$4.27^{+0.34}_{-0.34}$
A2142	0.0899	6186	$9.70^{+1.30}_{-1.30}$	$61.12^{+3.95}_{-3.95}$
A2199	0.0299	40 999	$4.10^{+0.08}_{-0.08}$	$7.09^{+0.25}_{-0.25}$
A2219	0.2250	11 200	$12.40^{+0.50}_{-0.50}$	$64.56^{+6.96}_{-6.96}$
A2244	0.0970	2963	$8.47^{+0.43}_{-0.42}$	$25.32^{+2.14}_{-2.14}$
A2319	0.0559	3169	$9.12^{+0.15}_{-0.15}$	$39.74^{+2.17}_{-2.17}$
A2382	0.0648	17 444	2.90	0.91
A2390	0.2310	10 335	$11.10^{+1.00}_{-1.00}$	$63.49^{+14.87}_{-14.87}$
A2589	0.0416	7289	$3.70^{+1.30}_{-0.70}$	$3.42^{+0.38}_{-0.38}$
A2597	0.0852	7163	$4.40^{+0.40}_{-0.70}$	$15.37^{+1.79}_{-1.79}$
A2670	0.0761	17 679	$4.45^{+0.20}_{-0.20}$	$4.97^{+0.92}_{-0.92}$
A2744	0.3080	13 648	$11.00^{+0.50}_{-0.50}$	$62.44^{+14.41}_{-14.41}$
A3266	0.0594	13 547	$8.00^{+0.30}_{-0.30}$	$16.48^{+0.64}_{-0.64}$
A3667	0.0552	12 560	$7.00^{+0.60}_{-0.60}$	$22.70^{+4.20}_{-4.20}$
A3921	0.0960	11 997	$4.90^{+0.55}_{-0.55}$	$10.92^{+1.52}_{-1.52}$
A4059	0.0460	5439	$3.97^{+0.12}_{-0.12}$	$5.78^{+0.54}_{-0.54}$
HCG62	0.0137	19 639	$1.1^{+0.05}_{-0.05}$	0.12

For A2034 and A2382, the temperatures and X-ray luminosities were taken from Ebeling et al. (1996) who do not provide error bars.

smooth light curve (no strong scattered solar X-ray contamination). We thus built a sample of 24 clusters (see Table 1) with redshifts ranging between 0.01 and 0.3. Redshifts were taken from the SIMBAD data base (except for A2199 for which the redshift was obtained from Wu et al. 1999), and gas temperatures and luminosities from Wu et al. (1999), except for A2034 and A2382 for which temperatures were taken from Ebeling et al. (1996). We assume $H_0 = 50$ km s^{-1} Mpc^{-1}, $\Omega_0 = 1$, and $\Lambda = 0$ throughout this analysis. In order to increase the range in T_X, in particular to include cooler systems when drawing the $L_X - T_X$ relation, we intended to add several groups to our sample of clusters. However, we only included in our sample the group HCG 62, the one with the longest exposure time and best signal to noise ratio (we also tried to include HCG 94, but discarded it because of its signal to noise ratio). More groups will be considered in forecoming works.

The data reduction was done using the software developed by Snowden et al. (1994). The routines in the software provide the best available modeling and subtraction of various non-cosmic background components and corrections for exposure, satellite wobbling, vignetting and variations of detector quantum efficiency. A flat-field correction of the images was applied and the non-extended sources were masked, except the cluster centers. The whole procedure was carried out only in clusters without strong scattered solar X-ray contamination; for each cluster, we checked the light curves in the 4 energy bands considered, and all those with count rate peaks larger than 3 counts s^{-1} in their light curves were excluded.

3. Estimating physical quantities

3.1. Gas density profile

The observed X-ray emission of the ICM is directly related to the gas distribution in the dark matter halo gravitational potential. Thus, in order to compare theory with observations, a description of the gas distribution is needed. Using a parameter-dependent model for the gas density profile, it is possible to re-construct the 3D X-ray emission of the cluster which, once projected and compared to the observations (Sect. 4), will allow us to derive the best set of values for the model parameters. We have chosen a 3D deprojection of a Sérsic profile (Sérsic 1968) to describe the gas distribution in clusters. This choice was motivated by the fact that we already used this profile to fit the optical surface brightness of elliptical galaxies, and computed all the physical quantities needed here, such as the entropy, potential energy, etc., as a function of the three Sérsic parameters (see Márquez et al. 2001 and references therein). Note that from a mathematical point of view, since the Sérsic profile has three parameters instead of two (compared to other models as for instance the β-model), the fitting process is more flexible. Besides, the fact that the volume integral of this profile does not diverge at large radii allows us to compute important quantities such as the total mass, potential energy and entropy of the system without any extra mathematical requirement such as a cutoff radius, for instance. Note also that the Sérsic law (Eq. (1)) is a non-homologous generalization of the de Vaucouleurs $R^{1/4}$ profile (de Vaucouleurs 1948). The 3D deprojection of such a profile corresponds to a generalized form of the Mellier-Mathez profile (Mellier & Mathez 1987) given by:

$$\rho_{\rm gas}(r) = \rho_0\ (r/a)^{-p}\ \exp[-(r/a)^{\nu}] \tag{2}$$

where ρ_0 is the volume gas density associated to the central column density Σ_0 and the parameters p and ν are related by the numerical approximation (Márquez et al. 2001):

$$p \simeq 1.0 - 0.6097\nu + 0.05563\nu^2 \tag{3}$$

which gives the best approximation to the Sérsic law when Eq. (2) is projected. The Sérsic profile defined by Eq. (1) corresponds to a surface mass density while Eq. (2) is the volume mass density. The condition that the mass obtained by integrating Eq. (1) must be equal to the mass obtained by integrating Eq. (2) implies:

$$\rho_0 = \frac{1}{a}\,\Sigma_0\,\frac{\Gamma(\frac{2}{\nu})}{2\,\Gamma(\frac{3-p}{\nu})} \tag{4}$$

where $\Gamma(a)$ is the complete gamma function defined by $\Gamma(a) = \int_0^\infty x^{a-1}{\rm e}^{-x}{\rm d}x$.

3.2. Dark matter distribution and dynamical mass

Once the gas distribution is known, a reasonable hypothesis can be used to derive the dark matter distribution in the cluster. Previous works on X-ray clusters suggest a power law relation between the distributions of dark matter and gas (e.g. Gerbal et al. 1992; Durret et al. 1994). We will assume here a relative distribution of the DM and gas of the form $\rho_{\rm DM}/\rho_{\rm gas} = R(r)$, where $R(r)$ is a power law of the form:

$$R(r) = \kappa\left(\frac{r}{a}\right)^{-\alpha}\cdot \tag{5}$$

Under this hypothesis, the dark matter also follows a Sérsic law: it decreases exponentially above a certain radius and its asymptotic behavior towards the cluster centre is a power law of slope $p' = -(p+\alpha)$. The values for κ, assuming $\alpha = 0.25$ are given in Table 2 (see Sect. 4).

Using Eqs. (5) and (2), the total amount of mass contained within a spherical region of radius r is given by the integral:

$$\begin{aligned} M_{\rm Dyn}(r,\kappa,\alpha) &= \int_0^r \left[\kappa\left(\frac{u}{a}\right)^{-\alpha} + 1\right]\rho_{\rm gas}(u)4\pi u^2{\rm d}u \\ &= \frac{4\pi\rho_0 a^3}{\nu}\left\{\kappa\,\gamma\left[\frac{3-(p+\alpha)}{\nu},\left(\frac{r}{a}\right)^{\nu}\right] + \gamma\left[\frac{3-p}{\nu},\left(\frac{r}{a}\right)^{\nu}\right]\right\} \end{aligned} \tag{6}$$

where $\gamma(a,z)$ is the incomplete gamma function defined by $\gamma(a,z) = \int_0^z x^{a-1}{\rm e}^{-x}{\rm d}x$.

3.3. Gas temperature profile

An important point in our study is to compute the temperature distribution of the ICM. This can be achieved by estimating the gas density profile, obtained by fitting the observations, and assuming that clusters of galaxies are systems in a nearly hydrostatical equilibrium sate. A hypothesis on the state equation of the ICM gas is also needed. An ideal gas state equation can be considered as a good approximation, although its application to self-gravitating systems has been questioned in the past (see Bonnor 1956 and references therein).

Therefore, the equation of hydrostatical equilibrium:

$$\nabla P(r) = -G\frac{M_{\rm Dyn}(r)}{r^2}\rho_{\rm gas}(r) \tag{7}$$

is then combined with the equation of state for the hot intracluster plasma:

$$P(r) = \frac{\rho_{\rm gas}(r)}{\mu m_{\rm p}}k_{\rm B}T_{\rm gas}(r) \tag{8}$$

to provide the following equation from which the ICM temperature as a function of radius $T_{\rm gas}(r)$ can be derived once the gas number density as a function of radius $n_{\rm gas}(r)$ is known:

$$M_{\rm Dyn}(r) = -\frac{k_{\rm B}}{\mu m_{\rm p}G}r^2\left\{T_{\rm gas}(r)\frac{{\rm d}\ \ln[n_{\rm gas}(r)]}{{\rm d}r} + \frac{{\rm d}T_{\rm gas}(r)}{{\rm d}r}\right\} \tag{9}$$

where G is the gravitational constant, $k_{\rm B}$ is the Boltzman constant, μ is the plasma molecular weight (we assume $\mu = 0.6$ for the ICM) and $m_{\rm p}$ the proton mass. The electron number density and the gas mass density are related by $n_{\rm gas}(r) = \rho_{\rm gas}(r)/(1.14\ m_{\rm p})$. The gas temperature profile can be obtained as a function of κ and α by replacing Eqs. (6) and (2) into Eq. (9), and performing a Gauss-Laguerre integration of the latter. The solution is of the form:

$$T(r,\kappa,\alpha) = \left(\frac{w}{\nu a}\right)\left(\frac{r}{a}\right)^{p}{\rm e}^{\left(\frac{r}{a}\right)^{\nu}}t(r,\kappa,\alpha) \tag{10}$$

where $w \equiv 4\pi\,G\,\frac{\mu m_{\rm p}}{k_{\rm B}}\,\frac{\rho_0 a^3}{\nu} = 1.54\times 10^{38}\left(\frac{\rho_0 a^3}{\nu}\right)$ m keV, and

$$\begin{aligned} t(r,\kappa,\alpha) = \int_{\left(\frac{r}{a}\right)^{\nu}}^{\infty} &\left\{\kappa\gamma\left[\frac{3-(p+\alpha)}{\nu},x\right]\right. \\ &\left. + \gamma\left[\frac{3-p}{\nu},x\right]\right\}x^{-\frac{(p+\nu+1)}{\nu}}{\rm e}^{-x}{\rm d}x. \end{aligned} \tag{11}$$

Equation (10) will be used together with a model for the hot plasma spectrum to derive the best set of values for κ and α, in agreement with quantities already observed in clusters of galaxies such as their mean X-ray temperature and luminosity and their baryonic mass fraction (see Sect. 5).

3.4. Potential energy and specific entropy

Changing the upper limit of the integral in Eq. (6) to ∞ we obtain the total dynamical mass:

$$M_{\rm Dyn} = \frac{4\pi\rho_0 a^3}{\nu}\left\{\kappa\,\Gamma\left[\frac{3-(p+\alpha)}{\nu}\right]+\Gamma\left(\frac{3-p}{\nu}\right)\right\}. \tag{12}$$

The total potential energy of the cluster is given by:

$$U_{\rm pot} = G\frac{M^2_{\rm Dyn}}{R_{\rm g}} \tag{13}$$

where the gravitational radius $R_{\rm g}$ is defined by $R_{\rm g} = a\,R^*_{\rm g}$, where a is the scale parameter and $R^*_{\rm g}$ is a dimensionless radius given by the numerical approximation:

$$\ln(R^*_{\rm g}) \simeq \frac{0.82032 - 0.92446\ \ln(\nu)}{\nu} + 0.84543$$

(Márquez et al. 2001).

In spite of the X-ray emission, which is responsible in many cases for cooling flow processes affecting the equilibrium state of the cluster in the inner regions, we may consider clusters as structures where dissipating processes are negligible compared to their gravitational energy, thus settling into a nearly thermodynamic equilibrium at large scale. This can be inferred by a simple order of magnitude calculation: the potential energy of a cluster of mass $\sim 10^{15}$ $M_\odot$ and radius ~ 1 Mpc is about 8×10^{64} ergs. The energy lost through X-ray emission during a Hubble time ($\sim 2\times10^{17}$ s) by a cluster of X-ray luminosity $\sim 10^{45}$ erg s^{-1} is around 3×10^{62} ergs, a value which is almost 300 times smaller than its potential energy. We can therefore estimate the gas entropy of such a configuration.

The specific entropy of the intra-cluster gas can be computed from the distribution function in the phase space, $f(x, v)$, of the gas particles using the microscopic Boltzmann-Gibbs definition:

$$s = -\frac{\int f\ \ln(f)\ {\rm d}^3x\ {\rm d}^3v}{\int f\ {\rm d}^3x\ {\rm d}^3v} \tag{14}$$

where the Boltzmann constant is $k_{\rm B} = 1$. Note that this expresion gives us the specific entropy of the entire system (gas or DM) because the integration covers the total volume in phase space. This definition then corresponds to an integrated specific entropy, and it will be referred to as "global" specific entropy. It is important to say that when we use the words "integrated" or "global" for the specific entropy, we are referring to this definition applied to the gas or DM separately and not to the sum of these two components.

To find the distribution function some simplifying hypotheses are needed. The first one is that our system is spherically symmetric, and the second one is that the velocity dispersion of the gas particles is isotropic (we neglect any possible rotation of the gas). Thus the distribution function f, depending explicitly only on the total energy, can be obtained from the density profile by an Abel inversion (Binney & Tremaine 1987). In this way, $f = f(\rho)$ and the integrated specific entropy can be computed numerically as a function of the Sérsic parameters only, providing a way to estimate the integrated specific entropy of the ICM from its surface brightness fit. It is important to emphasize here that the Boltzmann-Gibbs definition of the specific entropy makes no assumption on the equation of state, in particular the ideal gas equation for the ICM, and no assumption either on the validity of a hydrostatic equilibrium state of the system; this definition is therefore a general one since it only assumes spherical symmetry and an isotropic velocity dispersion tensor. Since the method we present here, based on the cluster X-ray surface brightness fitting, provides a good constrain on the gas density profile, this density profile, together with Eq. (14) can be used to obtain a good estimate of the global ICM specific entropy.

The specific entropy can also be obtained from the following set of equations (Balogh 1999):

$$s(r) = c_v\left\{\ln\left[\frac{2\pi(\mu m_{\rm p})^{8/3}K_0(r)}{h^2}\right]+\frac{5}{3}\right\} \tag{15}$$

and

$$K_0(r) = \frac{k_{\rm B}T_{\rm gas}(r)}{\mu m_{\rm p}\rho_{\rm gas}(r)^{2/3}} \tag{16}$$

where c_v is the specific heat capacity at constant volume of the plasma. These widely used equations require, however, the following assumptions on the ICM: the gas is considered to be monoatomic and the equation of state for an ideal gas is supposed to hold. By knowing the ICM density and temperature distributions, Eqs. (15) and (16) can then be used (see Sect. 6.3) to compute the gas specific entropy profile for each cluster. Gas density profiles are obtained from the X-ray surface brightness fit (see Sect. 4) while temperature profiles are derived by assuming both the hydrostatic equilibrium condition and the ideal gas state equation for the ICM, as explained before. Since the physical quantities involved here are intensive, these equations cannot be integrated to derive the integrated specific entropy of the gas, and Eq. (14) will have to be used for this purpose.

The entropy is of fundamental importance to understand the effects of non-gravitational processes on the thermodynamical history of clusters. Previous studies refer to the gas entropy at $0.1r_{\rm vir}$, where $r_{\rm vir}$ is the cluster virial radius (e.g. Ponman et al. 1999; Lloyd-Davies et al. 2000), while in this work we estimate the gas specific entropy for the entire cluster. Our calculations take into account all possible sources of heating and cooling, regardless of the distance to the centre, thus providing a good quantitative basis to which models can be compared in order to disentangle the different processes that affect the internal energy of the ICM during its history since the earlier epochs of the cluster formation.

We also notice that our assumption concerning the $\rho_{\rm DM}/\rho_{\rm gas}$ ratio (Eq. (5)) implies that the resulting DM density distribution is also Sérsic-like, with a central density distribution described by a power law varying as $r^{-(p+\alpha)}$. Under the hypothesis already stated concerning the distribution function of particles in phase space, we can in principle also compute the integrated specific entropy of the DM halo by using Eq. (14) and the DM density profile. Therefore the DM specific entropy is calculated numerically from the equation:

$$s = -\frac{1}{M}\int_0^{\Psi(0)}\frac{{\rm d}M}{{\rm d}\epsilon}\ln f(\epsilon){\rm d}\epsilon\ , \tag{17}$$

which can be derived from Eq. (14), and where ϵ represents the binding energy, M the total halo mass, and Ψ the relative gravitational potential (see Magnard 2002).

4. Fitting method and density profile

Finding the gas density profile amounts to deriving the best set of values for the Sérsic parameters. This has required to fit the ROSAT images by a pixel-to-pixel method, which creates a three-dimensional model of the X-ray emission which is then projected by integration along the line of sight, taking into account the energy response and the point spread function of the detector. The result is a synthetical image which can be compared to the observation, and the best set of Sérsic parameters is obtained by successive iterations. The gas density profile defined by Eq. (2) is used to model the bremsstrahlung emission, and the free-bound and bound-bound X-ray emissions are taken into account. The code computes the X-ray emissivity ϵ_ν in every point; it is then projected to obtain the surface brightness. This projected image is then convolved with the ROSAT point spread function (PSF), which varies as a function of position (and energy) on the detector. We have used in our fits a FWHM of 2 pixels which corresponds to the central PSPC PSF.

The cluster redshift and the mean gas temperature are required as input parameters. To obtain an initial guess for the free parameters in Eq. (2) we fit a Sérsic profile (Eq. (1)) to the X-ray surface brightness of each cluster. In order to stay as close as possible to our hypothesis of spherical symmetry, we selected clusters presenting the most round and uniform projected X-ray emission. However, this emission is not perfectly circular and due also to the fact that what we observe is always a projection on the plane of the sky of a three dimensional structure, we decided to take into account during the fitting process the ellipticity of the projected emission supposing also that all the clusters are oblate spheroids, i.e., that the third axis along the line of sight is a major axis. If a is the semi–major axis, which also corresponds to the scale parameter in the Sérsic profile, and b is the semi–minor axis, we define the ellipticity of the projected X-ray emission by $e = \sqrt{1-(b/a)^2}$. The ellipticity and semi-major axis position angle of the X-ray distribution are thus considered as free parameters for the fit and given as inputs for the code. The gas was assumed to be isothermal as a first approximation.

After obtaining the initial guesses for each free parameter, we use these values together with Eq. (2) to make a new synthetic image, then compare it to the actual ROSAT image. The parameter values are then changed and the comparison process is repeated iteratively, until it finds the 3D X-ray emission which best fits the surface brightness profile of the observation when projected. The fitting process is carried out with the MIGRAD method in the CERN MINUIT library (James 1994). In this process, the gas temperature is kept constant, as a first approximation. The exact shape of the temperature profile is not crucial when finding the set of values for the parameters, because the emissivity does not have a strong dependence on temperature as compared to its dependence on density; indeed, we find that modifying the temperature profile changes the values of the Sérsic parameters by at most a few percent, as explained in Sect. 5.

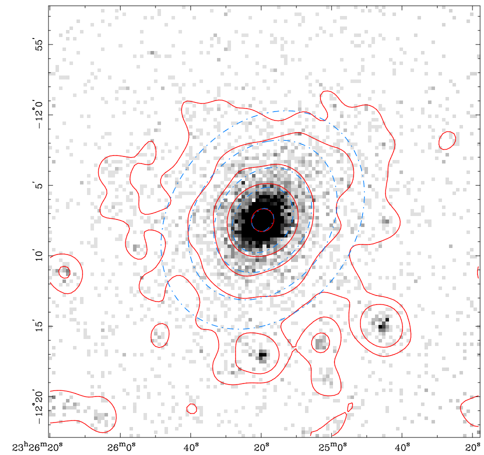

Fig. 1. Comparison of our best model of the X-ray surface brightness (dot-dashed ellipses) with the corresponding ROSAT image for the cluster A2597. The X-ray iso-contours are 0.5, 1, 3, 10 and 100 times the background; they were made after smoothing the original image with a Gaussian kernel of $\sigma = 3.2$ pixels.

The fitting process directly gives us the best estimates for the semimajor axis a and shape parameter ν. However, the central electronic number density n_{e0} given by the fit is not accurate enough, and is estimated by another method (see Sect. 5).

We evaluated errors with the MINUIT error function MINOS, which calculates parameter errors taking into account both parameter correlations and non-linearities. Resulting errors correspond to a 1σ deviation.

All the equations presented in Sect. 3 refer to spherical symmetry, for which we had to define an equivalent scale parameter, a_{eq} in order to go from the oblate geometry considered in the fit to the spherical geometry of the model. This new scale is defined as $a_{eq} = (a^2 b)^{1/3}$ and will be used instead of a to compute the specific entropy, the dynamical mass and the potential energy of a spherically symmetric X-ray region.

We show in Fig. 1 a comparison of our best fit Sérsic model of A2597. The good fit of the cluster surface brightness can clearly be seen, confirming the capability of the Sérsic profile to reproduce the cluster X-ray emission.

5. Gas temperature and dark matter to gas ratio

The fitting process described above provides the best values of a_{eq} and ν for a given gas temperature profile, assuming as a first approximation that each cluster has an isothermal ICM, and then obtaining, through an iterative procedure, the best compatible gas density and non-isothermal temperature profiles, assuming hydrostatic equilibrium and spherical symmetry.

Table 2. Best fit values for the Sersic parameters of the ICM, κ from Eq. (5), and radius r_{200} within which the mean density is 200 times the critical density of the Universe.

Cluster	ν	$a_{\rm eq}$ (kpc)	$n_{\rm e0} \times 10^{-3}$ (cm^{-3})	κ	r_{200} (kpc)
A85	0.55 ± 0.01	260 ± 5	5.72 ± 0.11	7.17 ± 0.32	2714
A478	0.50 ± 0.01	143 ± 4	18.51 ± 0.52	7.04 ± 0.42	2607
A644	0.82 ± 0.01	389 ± 6	3.58 ± 0.06	7.19 ± 0.21	2421
A1651	0.74 ± 0.02	385 ± 9	3.57 ± 0.11	6.59 ± 0.25	2453
A1689	0.58 ± 0.01	198 ± 9	14.26 ± 0.82	7.90 ± 0.35	2594
A1795	0.54 ± 0.00	164 ± 2	12.30 ± 0.23	7.64 ± 0.21	2462
A2029	0.49 ± 0.01	151 ± 4	16.63 ± 0.52	8.65 ± 0.43	2946
A2034	1.00 ± 0.03	811 ± 18	1.72 ± 0.04	3.58 ± 0.43	2450
A2052	0.47 ± 0.01	100 ± 5	11.70 ± 0.72	9.90 ± 0.67	1930
A2142	0.81 ± 0.01	528 ± 6	3.86 ± 0.05	4.26 ± 0.50	2824
A2199	0.60 ± 0.00	180 ± 1	6.82 ± 0.06	9.42 ± 0.20	2142
A2219	0.85 ± 0.02	689 ± 15	3.40 ± 0.08	4.04 ± 0.24	2887
A2244	0.56 ± 0.02	237 ± 17	6.38 ± 0.68	13.05 ± 0.70	3039
A2319	0.80 ± 0.01	755 ± 13	1.86 ± 0.04	5.13 ± 0.10	3294
A2382	1.17 ± 0.04	831 ± 19	0.49 ± 0.01	6.61 ± 0.66	1900
A2390	0.59 ± 0.02	313 ± 16	8.61 ± 0.48	5.13 ± 0.62	2658
A2589	0.72 ± 0.02	312 ± 8	2.31 ± 0.07	9.25 ± 1.73	2008
A2597	0.39 ± 0.01	37 ± 4	71.44 ± 46.76	12.42 ± 1.60	2035
A2670	0.52 ± 0.03	215 ± 27	4.05 ± 0.74	11.44 ± 0.58	2331
A2744	1.35 ± 0.07	877 ± 25	2.26 ± 0.07	4.82 ± 0.29	2506
A3266	1.18 ± 0.01	935 ± 7	1.22 ± 0.01	5.66 ± 0.20	2973
A3667	0.89 ± 0.01	990 ± 9	1.07 ± 0.01	3.29 ± 0.36	2723
A3921	0.81 ± 0.02	653 ± 15	1.41 ± 0.04	3.66 ± 0.50	2090
A4059	0.64 ± 0.01	233 ± 8	4.34 ± 0.18	8.46 ± 1.02	2033
HCG62	0.36	22	17.4	36.9 ± 1.63	–

In order for the $n_{\rm e0}$ normalization to give the observed number of counts, we first computed the cluster flux F, after substraction of point sources and background (obtained by the 2D fit). The masked source pixel counts were set to the mean value taken within ellipses. Then $n_{\rm e0}$ was chosen so that a bremsstrahlung XSPEC model convolved by a hydrogen column absorption would give the same flux as seen by ROSAT:

$$F = \frac{3.02 \times 10^{-15}}{4\pi d_{\rm L}^2} \int n_{\rm e} n_{\rm I} {\rm d}V$$
$$= \frac{3.02 \times 10^{-15}}{4\pi d_{\rm L}^2} \frac{2^{2+\frac{2p-3}{\nu}}}{\nu} a^3 {n_{\rm e0}}^2 \pi \Gamma\left[\frac{3-2p}{\nu}\right]$$

where $d_{\rm L}$ is the luminosity distance to the cluster, and n_I is the number density of plasma ions.

Equations (10) and (11) provide the ICM temperature profiles as families of solutions depending on the parameters κ and α. Since these are found to be different from those assumed to estimate the Sérsic parameters, the fitting process must be repeated, using the new temperature profile, in order to obtain a new set of parameters for each cluster, until convergence.

We tested on one cluster (A2029) the effect of a temperature gradient on the gas density profile from distances close to $r_{\rm eff}/4$ outwards, where $r_{\rm eff}$ corresponds to an effective radius which contains half of the cluster gas mass. For this, we did a second fit of the surface brightness of A2029 using a new temperature profile given by a power law of the form $T(r) = T_0(r/r_{\rm eff})^\beta$ where $r_{\rm eff} \simeq 2800$ kpc. T_0 was set in order to have a non-weighted mean temperature equal to the mean cluster temperature (Table 1) and we considered the cases $\beta = -0.5$ and -1. After the first iteration, the values found for $n_{\rm e0}$, $a_{\rm eq}$, and ν remained almost unchanged for both values of β: the scale and shape parameters changed by about 1%, and the central electronic density by 4% with respect to the isothermal fit.

We therefore decided to keep the Sérsic values given by the original fit as the definitive ones. Equation (10) can be rewritten in the form $T(r,\kappa,\alpha) = \kappa T_1(r,\alpha) + T_2(r)$. We produced a set of $T_1(r,\alpha)$ profiles corresponding to values of α between 0 and 2 with steps of $\Delta\alpha = 0.1$. These curves together with their corresponding $T_2(r)$ profiles and an adequate set of values for κ were used to find which combination of κ and α gives the closest values to the observed global temperatures and luminosities (Ebeling et al. 1996; Wu et al. 1999), and baryon mass fractions (Arnaud & Evrard 1999; Mohr et al. 1999; Schindler 1999). These quantities are evaluated as follows. The two profiles $n_e(r)$ and $T(r, \kappa, \alpha)$ plus the hypothesis of a gas metallicity equal to $0.3\,Z_\odot$ (see Renzini 1997) and the emission process determine the cluster X-ray emission. We used the XSPEC software to simulate the corresponding spectra with a bremsstrahlung emission model (to be coherent with the emission model used in the fitting program). We summed up the spectra from shells of constant electronic density and temperature over radius, considering only the volume intersected by the ROSAT observation cylinder. The spectrum obtained is then convolved with a photoelectric absorption model and with the ROSAT response function to produce the simulated spectrum. A fit is then performed on this spectrum to derive the X-ray temperature and luminosity (the metallicity and hydrogen column density are fixed).

The set of κ and α has to produce L_X and T in agreement with the observed data within errors. Moreover, the gas mass fractions should stay inside the observed limits. So we performed a minimization of the distance between the observed data and the predictions from our model. We found that the best α is often very close to zero, which is not in good agreement with results obtained from numerical simulations by Teyssier (2002) which show a $\rho_{\rm DM}/\rho_{\rm g}$ ratio varying globally as $r^{-0.25}$; besides our values of α are not well constrained. We therefore chose to impose $\alpha = 0.25$; κ was then recomputed to give luminosities and temperatures as close as possible to the observations.

To each temperature profile $T(r, \kappa, \alpha)$ corresponds a couple of simulated observational parameters $(T_{\rm sim}, L_{\rm sim})$. The value of κ is constrained by imposing these parameters to be close (within error bars) to the real observational values. The gas mass fraction is checked to be compatible with the isothermal hypothesis.

6. Results

6.1. Mass distributions and parameter correlations

The 3D gas density profiles were computed with Eq. (2) for all the clusters in our sample, using the sets of parameters obtained from the surface brightness fitting process (described in Sect. 4) of the PSPC images and listed in Table 2. By means of Eq. (5), the corresponding DM distribution can be recovered. In Fig. 2 we show the 3D gas and DM density profiles for every cluster divided by the critical density of the Universe at the cluster redshift (e.g., Ettori et al. 2002): $\rho_c(z) = 3H^2(z)/(8\pi G)$, where the Hubble constant at redshift z is defined by $H(z) = H_0\sqrt{\Omega_m(1+z)^3 + 1 - \Omega_m}$.

Both DM and gas distributions are Sérsic-like, implying that the corresponding profiles decrease exponentially outwards above a certain distance from the cluster centre; on the other hand, when r goes to zero they follow a power law in radius with a logarithmic slope tending asymptotically to $-p(\nu)$ for the gas and to $-(p(\nu) + \alpha)$ for the DM.

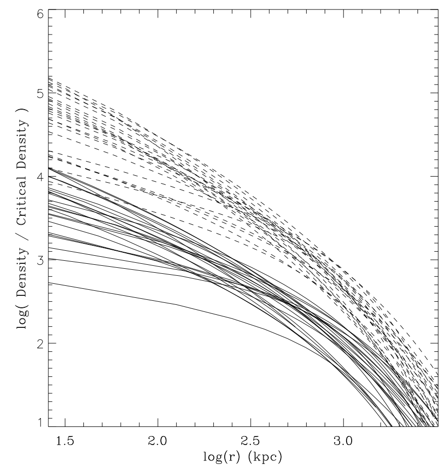

Fig. 2. 3D deprojected gas (full lines) and dark matter (dashed lines) density profiles divided by the critical density of the Universe at the cluster redshift.

The values for κ, obtained as described in Sect. 5, are in most cases smaller than 10, while the value for α was fixed to 0.25 (see above). Although DM halos are denser than the ICM gas, as implied by the κ factor and the asymptotic slope difference α, the general shapes of both profiles look quite similar, implying that dark matter and gas are distributed in a comparable way. This effect is a natural consequence of the hypotheses and conditions imposed to our model. However such a behaviour seems to be the case for massive systems (like those in our sample – see total masses in Table 3), as shown by observations of galaxy clusters at moderate and high redshifts (Schindler 1999). The gas would be accreted into the forming structure and once the system reaches a relaxed state, the gas just accommodates into the halo potential. This is true at the scale of massive galaxy clusters where the potential well is deep enough to prevent the gas from expansion due to non-gravothermal processes. In this case, both dark matter and gas present similar distributions in contrast with what is observed in smaller systems such as groups of galaxies and even galaxies, where the gas can produce extended cores as result of energy injection due to supernova explosions or shock winds (Bryan 2000; Bower et al. 2001; Brighenti & Mathews 2001). It is also important to mention that Eq. (5), based on galaxy cluster observations, may no longer be valid for low mass systems such as groups of galaxies, in which case our DM model would be inappropriate to describe groups.

The averaged gas density profile for our set of 24 galaxy clusters is well fit by a Sérsic profile with parameters: $\rho_0 = 7.4 \times 10^{-24}$ kg m^{-3}, $a_{\rm eq} = 367$ kpc and $\nu = 0.56$. The latter gives $p(\nu) = 0.67$ which makes the corresponding DM density profile vary as $r^{-0.92}$ when r goes to zero. This central

Table 3. Gas and dynamical masses, potential energy, central gas column density and integrated specific entropy for gas and DM as derived from Sérsic parameters.

Cluster	$M_{\rm gas}(\times 10^{14}\ M_\odot)$	$M_{\rm Dyn}(\times 10^{15}\ M_\odot)$	$U_{\rm pot} \times 10^{58}$ (kg m^2 s^{-2})	Σ_0 (kg m^{-2})	Gas Spec. Entr.	DM Spec. Entr.
A85	5.11 ± 0.41	2.59 ± 0.35	0.78 ± 0.20	0.36 ± 0.01	204.3 ± 0.18	206.1 ± 0.91
A478	4.98 ± 0.56	2.29 ± 0.35	0.72 ± 0.21	0.68 ± 0.03	204.1 ± 0.24	205.7 ± 1.00
A644	1.80 ± 0.13	1.18 ± 0.16	0.39 ± 0.10	0.26 ± 0.01	201.3 ± 0.15	203.7 ± 0.87
A1651	2.53 ± 0.29	1.46 ± 0.24	0.46 ± 0.14	0.27 ± 0.01	202.3 ± 0.25	204.4 ± 0.98
A1689	4.11 ± 0.85	2.35 ± 0.52	1.05 ± 0.41	0.65 ± 0.05	203.3 ± 0.43	205.3 ± 1.22
A1795	3.10 ± 0.20	1.63 ± 0.20	0.45 ± 0.10	0.50 ± 0.01	203.0 ± 0.14	204.9 ± 0.88
A2029	6.14 ± 0.69	3.26 ± 0.46	1.26 ± 0.31	0.66 ± 0.03	204.6 ± 0.25	206.5 ± 1.00
A2034	4.44 ± 0.44	1.79 ± 0.42	0.64 ± 0.29	0.23 ± 0.01	203.1 ± 0.22	204.6 ± 0.93
A2052	1.67 ± 0.38	0.95 ± 0.21	0.13 ± 0.05	0.32 ± 0.02	202.4 ± 0.49	204.3 ± 1.31
A2142	5.11 ± 0.22	2.17 ± 0.40	0.94 ± 0.35	0.38 ± 0.01	203.4 ± 0.09	205.0 ± 0.80
A2199	1.27 ± 0.04	0.86 ± 0.08	0.18 ± 0.03	0.28 ± 0.01	201.2 ± 0.07	203.5 ± 0.79
A2219	8.55 ± 0.85	3.56 ± 0.75	2.17 ± 0.89	0.42 ± 0.01	204.4 ± 0.22	205.9 ± 0.94
A2244	3.92 ± 1.45	3.33 ± 1.15	1.53 ± 0.88	0.36 ± 0.05	203.7 ± 0.75	206.4 ± 1.60
A2319	7.45 ± 0.62	3.64 ± 0.63	1.79 ± 0.61	0.26 ± 0.01	204.5 ± 0.19	206.4 ± 0.90
A2382	0.96 ± 0.01	0.67 ± 0.11	0.11 ± 0.03	0.06 ± 0.01	200.4 ± 0.22	202.9 ± 0.91
A2390	9.06 ± 2.17	3.72 ± 1.01	1.78 ± 0.85	0.62 ± 0.05	205.0 ± 0.51	206.5 ± 1.31
A2589	0.97 ± 0.12	0.73 ± 0.11	0.13 ± 0.04	0.15 ± 0.01	200.6 ± 0.28	203.2 ± 1.00
A2597	2.30 ± 2.14	1.26 ± 1.13	0.22 ± 0.49	0.78 ± 0.52	203.1 ± 1.69	204.9 ± 1.94
A2670	2.86 ± 2.09	2.03 ± 1.35	0.46 ± 0.59	0.22 ± 0.05	203.6 ± 1.24	206.0 ± 2.18
A2744	4.00 ± 0.52	2.20 ± 0.47	1.36 ± 0.55	0.26 ± 0.01	202.3 ± 0.28	204.4 ± 0.95
A3266	3.33 ± 0.11	2.03 ± 0.31	0.92 ± 0.28	0.17 ± 0.01	202.4 ± 0.07	204.7 ± 0.77
A3667	6.93 ± 0.31	2.52 ± 0.57	0.83 ± 0.38	0.19 ± 0.01	204.4 ± 0.10	205.7 ± 0.81
A3921	3.53 ± 0.40	1.34 ± 0.31	0.29 ± 0.13	0.17 ± 0.01	203.1 ± 0.25	204.5 ± 0.98
A4059	1.24 ± 0.20	0.80 ± 0.14	0.15 ± 0.05	0.22 ± 0.01	201.2 ± 0.34	203.5 ± 1.09

slope for the DM halo is shallower than the self-similar solution for spherical collapse in an expanding universe found by Bertschinger (1985) ($\rho \propto r^{-2.25}$), than the asymptotic behaviour found by Moore et al. (1999) in their numerical simulations ($\rho \propto r^{-1.5}$) and than the NFW (Navarro et al. 1996, 1997) universal density profile. However it is steeper than the $\rho \propto r^{-0.75}$ critical solution found by Taylor & Navarro (2001) for galaxy-sized CDM halos based on the study of their phase-space density distribution. This critical solution can be interpreted as a maximally "mixed" configuration, where the phase-space distribution across the system is the most uniform one compatible with a monotonically decreasing density profile and with the power-law entropy distribution. This configuration would be the result of non-spherically symmetric formation processes through hierarchical merging. Mass shells are continuously mixed and the density profiles tend to be shallower than the NFW profile at the center, converging to the $\rho \propto r^{-0.75}$ distribution for maximal mixing (Taylor & Navarro 2001).

One important advantage of the Sérsic density profile is that its volume integral converges when integrated up to infinity, making it thus possible to determine the total cluster mass, and the potential energy and entropy of the system without introducing a cutoff radius, in contrast to the popular β-model, for instance. Total dynamical masses can thus be computed (see Eq. (12)) and the resulting values for all clusters are given in Table 3.

Figure 3 shows the resulting cumulative dynamical mass profiles for every cluster as obtained by means of Eq. (6) with the corresponding Sérsic parameters. Every profile has been normalized to the corresponding cluster total mass, $M_{\rm dyn}$ (see Eq. (12)), and the radial coordinate has been normalized to the corresponding cluster r_{200} radius, which is defined as the radius within which the mean density is 200 times the critical density of the universe, ρ_c, as defined above. In general, we can define a radius r_Δ within which the mean density is Δ times ρ_c and r_Δ can be obtained from the relation $M(r < r_\Delta)/(4\pi r_\Delta^3/3) = \Delta\rho_c$). The averaged cumulative dynamical mass distributions show a logarithmic slope $\mathrm{d}\log M/\mathrm{d}\log r \sim 1$ at $r \sim 0.7\ r_{200}$. Further out this slope decreases rather fast. According to our model, the cumulative mass profiles converge only around $r \sim 10\ r_{200}$, but

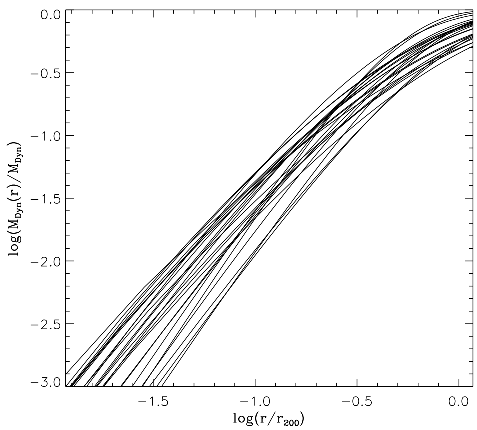

Fig. 3. Synthetic cumulative dynamical mass profiles normalized to the corresponding total integrated cluster mass $M_{\rm Dyn}$. The radial coordinate is normalized to the cluster r_{200} radius.

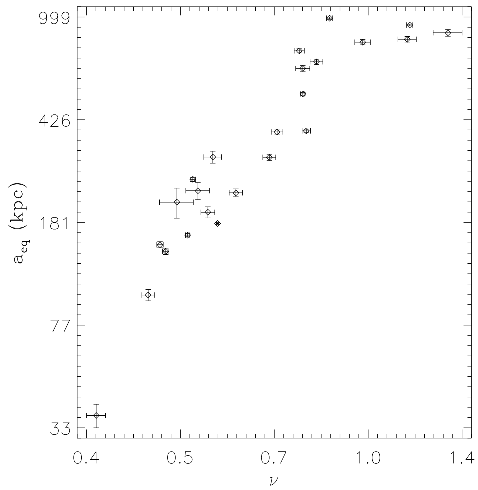

Fig. 4. Correlation between the density profile parameters $a_{\rm eq}$ and ν.

the mass variation is only of a factor of two, going from $M \sim 10^{15}$ $M_\odot$ at $\sim r_{200}$ to $M \sim 2 \times 10^{15}$ $M_\odot$ at ~ 10 r_{200}.

The analysis by Ettori et al. (2002) of BeppoSAX data includes some clusters of our sample. They estimate masses for $\Delta = 1000$ and 2500, by using either a NFW or a King profile for the total mass distribution. Comparing our results with theirs for the same clusters, we see that our mass estimates, derived from the Sérsic profile for these two values of Δ within the same r_Δ radii as indicated in their Table 2 are in quite good agreement. In most cases, our masses differ by about 10% or less, with differences reaching about 20% for a few cases. These differences are likely to be due to the use of different functional forms (the Sérsic, NFW and King models) to describe the mass profile. Moreover, from our sample we find in average $r_{200} \sim 2.5 \pm 0.4$ Mpc (see Table 2). These values are about 78% of those found in numerical simulations by Navarro et al. (1996) for cluster sized systems of comparable masses. Moreover, we note that the values of our scale parameter $a_{\rm eq}$ are comparable to those of the scale radius $r_{\rm s}$ of the NFW profile for similar mass ranges. In this way, we obtain in average $a_{\rm eq}/r_{200} \sim 0.12$ in good agreement with the value of $r_{\rm s}/r_{200} \sim 0.14$ (Navarro et al. 1996), the difference being of only 14%. We can therefore say that the Sérsic profile is able to describe the mass distribution in clusters in as much the same way as other models as the NFW and King models, the differences being due to the mathematical natures of the models.

Based on a de-projected Sérsic model for the gas density profile, the best set of values of $n_{\rm e0}$, $a_{\rm eq}$ and ν for each cluster is given in Table 2. These three parameters are displayed two by two in Figs. 4–6. A clear correlation between the shape (ν) and scale ($a_{\rm eq}$) parameters is seen, while the correlations we find for $\Sigma_0 - \nu$ and $\Sigma_0 - a_{\rm eq}$ (Σ_0 being obtained from ρ_0 by using Eq. (4)), are clear but show a somewhat larger scatter. Note that these three correlations have shapes similar to those found in elliptical galaxies. This may indicate, as for ellipticals, the existence of an entropic line on which galaxy clusters lie, in which case the correlation shown in Fig. 4 may just be the projection of this isentropic relation on the $\log(\nu) - \log(a_{\rm eq})$ plane. In the case of elliptical galaxies, this entropic line was interpreted as the intersection of two surfaces in the [$\log \Sigma_0$, log a, $\log \nu$] space: the entropic surface and the energy-mass surface (Márquez et al. 2001). In this work, we find that these two surfaces exist for our galaxy clusters as well, and these clusters are also located on a line corresponding to the intersections of the two surfaces (see Sect. 6.5). A complete discussion on this point will be presented in a forecoming paper (Magnard, in preparation). It is worth noting that, although from the mathematical point of view no correlation between the model parameters is expected, the fact that we observe such correlations probably indicates that they are due to the physics underlying the X-ray emission distribution.

6.2. Temperature profiles

We show in Fig. 7 the 3D non-weighted temperature profile for every cluster in our sample, calculated with the parameters given in Table 2 and normalized to the corresponding median temperature from the literature (see Table 1). As for the total mass profiles, the radial coordinate has been normalized to the corresponding cluster r_{200} radius. All the profiles are very similar: they slightly increase from the center, then remain approximately constant to finally decrease at large radii. The mean temperature profile is consistent with an almost isothermal distribution for radii smaller than 0.25 r_{200} ($\sim$625 kpc), in agreement with other works (Allen et al. 2001; De Grandi & Molendi 2002), followed by a rapid decrease for radii larger than 0.25 r_{200}, with a logarithmic slope of the order of -0.6 for

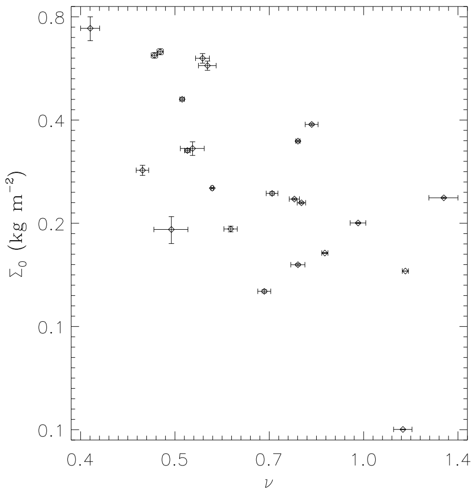

Fig. 5. Correlation between the density profile parameters Σ_0 and ν.

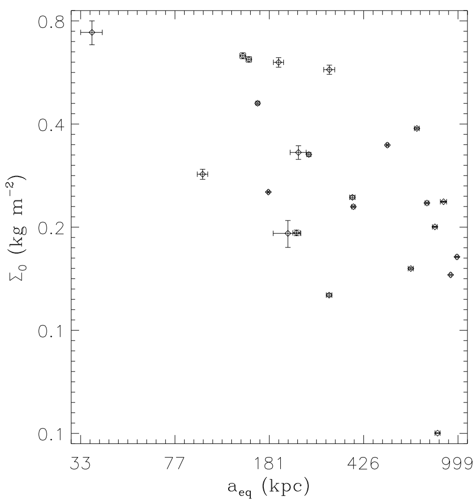

Fig. 6. Correlation between the density profile parameters Σ_0 and $a_{\rm eq}$.

radii around 0.63 r_{200}. This decrease results to be quite similar to the slope of −0.64 found by De Grandi & Molendi (2002) at radii larger than ~750 kpc for their mean temperature profile, taking into account the cooling and non-cooling flow clusters of their sample. The results of Markevitch et al. (1998) based on ASCA observations show similar trends for the temperature distribution. The characteristic central drop we obtain in our temperature profiles is due to the mathematical properties of

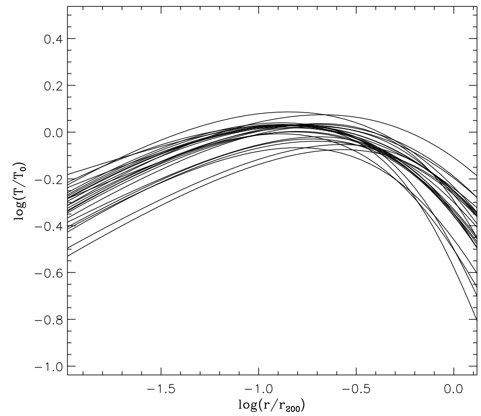

Fig. 7. Synthetic 3D temperature profiles calculated from Eqs. (10) and (11) with the values of κ given in Table 2. The temperature is normalized to the global cluster temperature and the radial coordinate is normalized to the cluster r_{200} radius.

the density profile rather than to a real physical effect, but the lack of resolution of the PSPC impedes from properly addressing this issue, and we cannot tell anything about the temperature distribution within the central cooling flow region.

In Fig. 8 we show the re-projected emission weighted temperature profile for every cluster, defined by:

$$T_{\rm ew}(R) = \frac{\int n_{\rm e}^2(r) T(r) {\rm d}z}{\int n_{\rm e}^2(r) {\rm d}z}. \qquad (18)$$

The $L_X - T_X$ relation derived from our calculations is shown in Fig. 9. Our power law fit (excluding HCG 62) is $L_X \propto T_X^{2.65\pm0.17}$; the exponent is in agreement with Markevitch (1998), who finds $L_X \propto T_X^{2.64\pm0.27}$, but our line is shifted towards higher luminosities. This shift is probably due to the fact that we include the central region in our luminosity evaluation, while Markevitch excises it.

6.3. ICM and DM specific entropies

The global specific entropy $s_{\rm gas}$ of the ICM is given in Table 3. It is found to vary very little from one cluster to another, as for the specific entropy of stars in elliptical galaxies (Márquez et al. 2001 and references therein). This is, however, a first order behavior. Numerical simulations of elliptical galaxies formed in a hierarchical merging scheme, show that their specific entropy varies a little with mass, most probably due to merging processes (Lima Neto et al. 1999; Márquez et al. 2000). The situation is not different in galaxy clusters. We show in Fig. 10 that the global specific entropy of the ICM and the gas mass are indeed clearly correlated, although this is a second order effect (about 2%), small compared to the dominant relation $s_{\rm gas} \sim$ constant that we observe. The difference with elliptical galaxies is that the slope in Fig. 10 is steeper than for

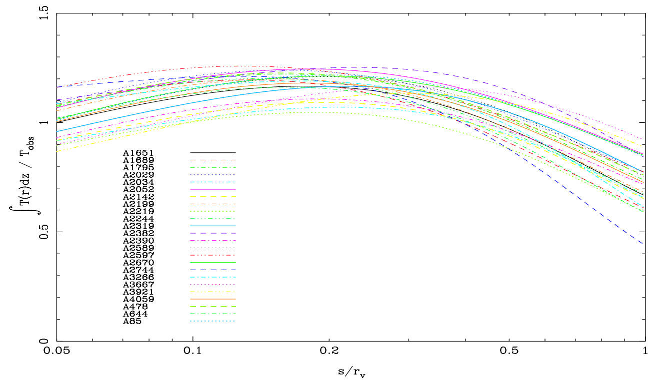

Fig. 8. Re-projected emission weighted temperature deduced from our model. The projected radii s are normalized to the corresponding $r_v = r_{200}$ radii, and the temperatures are normalized to the observed isothermal temperatures.

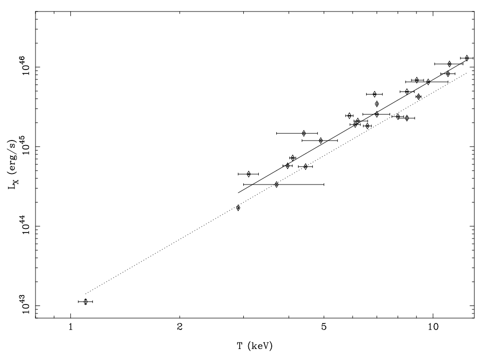

Fig. 9. Relation between L_X and T_X. The point at the lower left corner corresponds to the group HCG 62. The solid line shows the best fit (see text) and the dotted line is the fit found by Markevitch (1998).

ellipticals: if we write $s_{\rm gas} = s_0 + \beta \ln(M_{\rm gas})$, our best fit to the data gives $\beta = 1.86 \pm 0.15$ compared to $\beta \simeq 1$ for ellipticals (with s_0 constant). The error bars correspond to 1σ deviations and were computed from the parameter errors given by MINOS and by means of Monte Carlo simulations. Every parameter was modeled by a gaussian distribution with σ equal to the corresponding 1σ deviation from MINOS. These distributions were then used to derive the total mass and specific entropy distributions and the corresponding 1σ errors for each cluster. For the linear fit we used a linear least-squares approximation in one dimension, taking into account the error bars in both directions at the same time. A comparable relation is found between the integrated specific entropy $s_{\rm gas}$ of the ICM and the dynamical mass of the cluster, with a somewhat steeper slope of 2.67 ± 0.12. In our fitting of the cluster X-ray surface brightness we have also taken into account the cluster center, thus our estimation of the gas specific entropy necessarily takes into account the effects of the central cooling flow. This information is integrated together with the other non-gravitational thermal processes affecting the intra cluster gas.

The integrated specific entropy of the X-ray gas is displayed in Fig. 11 as a function of the observed isothermal gas temperature. The entropy appears to increase with the temperature, consistently with a power law (the best fit to our data is shown in Fig. 11 and corresponds to $s_{\rm gas} \propto T^{4.92}$). However, the dispersion is quite large. Note that such a relation has already been observed by Ponman et al. (1999) and Lloyd-Davies et al. (2000), and predicted by gravitational simulations (Borgani et al. 2001; Muanwong et al. 2002). The only group shown in this plot does not exhibit a significant entropy floor, but other groups need to be added. It would be important to get a good evaluation of this entropy floor as it is a strong constraint on the non-gravitational energy injection (Lloyd-Davies et al. 2000).

The derived gas density and temperature profiles can be used to compute the gas specific entropy profile for each cluster by using Eqs. (15) and (16).

The $K_0(r)$ profiles are shown in Fig. 12, where the radial coordinate is normalized to the r_{200} radius. All these profiles are consistent with a gas specific entropy increasing with radius, indicating that the gas has been heated by shock fronts at successive epochs when collapsing into the cluster potential well, before being virialized. Thus, the specific entropy profile provides useful information about the ICM thermal history. Some of the profiles flatten towards the center below 0.8 r_{200}, while others correspond to power laws throughout. The average of the profiles defined by Eq. (16) has a logarithmic slope $\mathrm{d}\log K_0/\mathrm{d}\log r \sim 1$ at about 0.6 r_{200} and it is in agreement with results obtained by Tozzi & Norman (2001) who studied the effect of an entropy excess in the ICM gas before accretion into the DM halo. No entropy core is present, perhaps due to the effect of central cooling, although this could also be due to the mathematical nature of the profiles derived from the Sérsic model. In general our profiles are in agreement with external heating models for rich clusters (Tozzi et al. 2000;

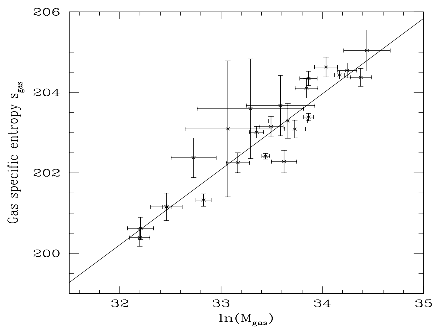

Fig. 10. Relation between the gas integrated specific entropy, $s_{\rm gas}$ and the gas mass. The best fit line is indicated (see text).

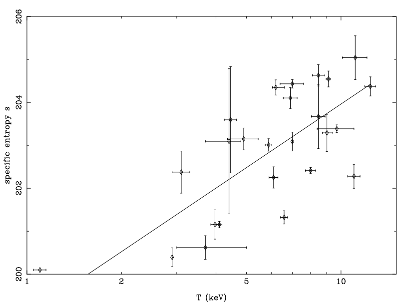

Fig. 11. Relation between the gas integrated specific entropy and the mean gas temperature taken from the literature (see text). The point at the lower left corner corresponds to the group HCG 62.

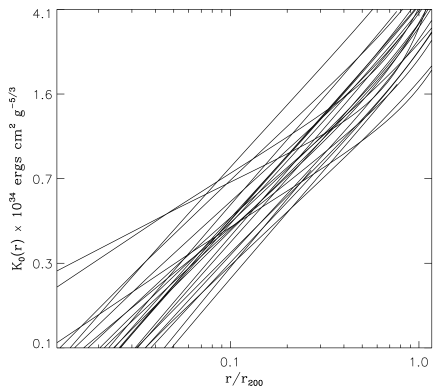

Fig. 12. K_0 profiles based on density and temperature models.

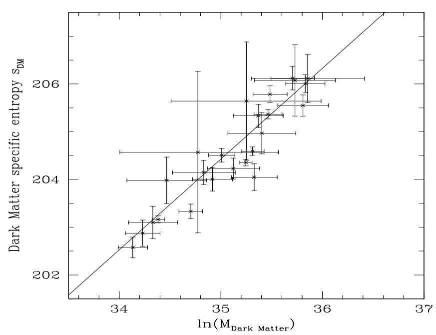

Fig. 13. Relation between the dark matter integrated specific entropy and mass. The best fit line is indicated (see text).

Tozzi & Norman 2001). However, we notice that the $K_0(r)$ profiles obtained from our density and temperature distributions are about a factor of 7 larger than those inferred by Tozzi & Norman (2001). This is probably just due to a normalization effect related to the way the density and temperature are computed; it is mainly the entropy variations that are a reliable physical quantity.

The assumed relation (5) between the dark matter and gas densities allows us to also compute the global dark matter entropy (see Table 3) numerically from Eq. (17), which comes out directly from the definition given in Eq. (14). The corresponding entropy-mass relation thus found for the dark matter is very close to that obtained for the gas, with $\beta \simeq 1.90 \pm 0.17$ as seen in Fig. 13.

6.4. Potential energy – mass relation

The relation between the dynamical mass and potential energy, previously shown for elliptical galaxies (Márquez et al. 2001) and in numerical simulations (Lanzoni 2000; Jang-Condell & Hernquist 2001), is displayed in Fig. 14 for our set of clusters. If we write it as $\ln(U_{\rm pot}) - I \ln(M_{\rm dyn}) =$ const, the best fit to our data imply $I = 1.68 \pm 0.08$, in excellent agreement with the theoretical value of $5/3$. The error bars and linear fit are computed in the same way as explained in the previous section.

6.5. Discussion

The correlations presented in the previous sections between the mass, potential energy and integrated specific entropy, confirm the existence of an entropic surface, $s(\Sigma_0, a, \nu) - \beta \ln(M(\Sigma_0, a, \nu)) =$ const (see Eq. (14)), and a potential energy-mass surface, $\ln(U_{\rm pot}(\Sigma_0, a, \nu)) - I \ln(M_{\rm dyn}(\Sigma_0, a, \nu)) =$ const, in the Sérsic parameters space, remarkably similar to the case of elliptical galaxies (Márquez et al. 2001). Indeed, we observe the clusters in our sample to be located at the intersection of these two surfaces, indicating the existence of an "entropic line" for galaxy clusters (see Magnard 2002). We have checked by simulations that this line is also recovered for a random set of values of the Sérsic parameters, suggesting the possibility that this relation could be a consequence of the model assumed

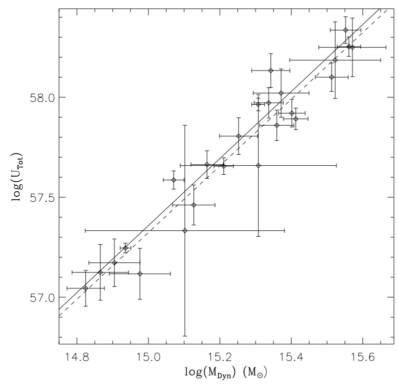

Fig. 14. Relation between the dynamical mass and the potential energy. The solid line corresponds to the best fit to the data and the dashed line is the theoretical slope of $I = 5/3$ defined by the relation $\ln(U_{\rm pot}) - I\ \ln(M_{\rm dyn}) = {\rm const}$.

to describe the final viralized system (in our case a Sérsic profile). However, the fact that a Sérsic profile reproduces very well the X-ray surface brightness of clusters, and hence the gas distribution of the ICM, supports the idea that the physical processes operating during the formation and evolution of galaxy clusters, which are of course responsible for the final structure reached by the ICM and DM halo, are indeed at the origin of the entropic line. To confirm this, the same method as in this work, but with different models for the gas density profile should be used. Moreover, the existence of both an entropic surface and a potential energy-mass surface for galaxy clusters implies that these objects can be considered as a single-parameter family, described by one of the Sérsic parameters only (e.g. Márquez et al. 2001). Interestingly, analogous correlations have been obtained for galaxy clusters by Fujita & Takahara (1999). The importance of the above mentioned correlations resides in the fact that they are probably the result of the physics ruling cluster formation. A correlation between the global specific entropy and the mass conserves information on the various events affecting the thermodynamical history of clusters. The observed variation of $s_{\rm gas}$ with dynamical mass in clusters suggests that dissipating processes in clusters play an important role as generators of entropy. These mainly correspond to Bremsstrahlung emission ($L \propto M^{4/3}$) and cooling flows. Merging processes between clusters are of importance in such a relation, because of their impact on the final total mass and on the amount of entropy produced during the cluster formation. Violent merger events can be accompanied by an important dissipation of energy and creation of entropy, while minor mergers can be translated in an adiabatic accretion of matter without a significant production of entropy. These energy losses, however, are all negligible compared to the cluster gravitational energy. Thus the value of the slope β in the specific entropy-mass relation reflects the impact of such processes on the cluster history. Clusters with higher global specific entropy could have undergone more episodes of hierarchical merging through their histories, thus becoming more massive.

On the other hand, considering the collapse of matter to form a virialized gravitational system, the correlation between the potential energy and the total mass of the final structure is a natural consequence of the conservation of energy and mass during its formation. A self-similar relation defined by $U \propto M^{5/3}$ is expected from theory (see Márquez et al. 2001) and we show that it is indeed also followed by our observed galaxy clusters.

All these results strongly suggest that the formation processes affecting galaxies and clusters of galaxies are quite similar regardless the scale involved.

7. Conclusions

We have shown in the present work that the Sérsic profile can be used as a good tracer of the matter distribution in clusters, under the assumption that clusters are well relaxed structures, as it was the case in elliptical galaxies. Its mathematical properties make it an interesting and useful tool that can be employed to explore the physics of relaxed systems, although any other appropriate profile can be used. The density profiles obtained here reproduce well the X-ray surface brightness profiles of the ROSAT PSPC images. The asymptotic behaviour of these profiles towards the cluster center turns out to be shallower than the NFW profile, but still within the limits predicted by numerical simulations concerning the central slope of galaxy-sized DM halos. Temperature profiles derived here (considering the hydrostatical equilibrium hypothesis for the cluster structure) are in agreement with other works. We estimate the integrated specific entropy content for galaxy clusters and our specific entropy profiles are consistent with the predicted shape of the entropy distribution for massive clusters, obtained by simulations which take into account pre-heating and cooling processes.

We have shown that both for the gas and for the dark matter the integrated specific entropy and the potential energy have behaviors comparable to those observed for stars in elliptical galaxies: the integrated specific entropy is constant to first order and in reality increases slightly with mass as a logarithmic function, while the potential energy scales with mass as a power law. Note that the index of this power law is close to the theoretical value of 5/3 for elliptical galaxies and clusters. This strongly suggests that all these self gravitating systems behave similarly, even though they may have very different masses and thermodynamical histories. Elliptical galaxies could then be considered as scaled down versions of galaxy clusters (Moore et al. 1999). Moreover, integrated specific entropy-mass and potential energy-mass correlations should be the result of the formation history of the clusters. Heating mechanisms and merger events play an important role here and total mass and energy are conserved during the whole formation process of the final virialized structure.

It would be interesting to apply the Sérsic model to high redshift galaxy clusters in order to test the possible evolution of the scaling relations found in this work. The use of Chandra and XMM-Newton data will be crucial in these kinds of studies due to their higher resolution and sensitivity compared to ROSAT. We also note that a similar analysis could be carried out in samples of synthetic clusters derived from numerical simulations.

Acknowledgements. We are very grateful to Daniel Gerbal, G. B. Lima Neto, G. Mamon and S. Dos Santos for many enlightening discussions. R.D. acknowledges many interesting discussions with Raphaël Lescouzères.

References

Allen, S., Ettori, S., & Fabian, A. 2001a, MNRAS, 324, 877
Allen, S., Schmidt, R., & Fabian, A. 2001b, MNRAS, 328, L37
Arnaud, M., Aghanim, N., Gastaud, R., et al. 2001, A&A, 365, L67
Arnaud, M., & Evrard, A. 1999, MNRAS, 305, 631
Balogh, M. L., Babul, A., & Patton, D. R. 1999, MNRAS, 307, 463
Bertschinger, E. 1985, ApJS, 58, 39
Binney, J., & Evans, N. 2001, MNRAS, 327, L27
Binney, J., & Tremaine, S. 1987, Galactic Dynamics (Princeton University Press)
Bonnor, W. B. 1956, MNRAS, 116, 351
Borgani, S., Governato, F., Wadsley, J., et al. 2001, ApJ, 559, L71
Bower, R. G., Benson, A. J., Lacey, C. G., et al. 2001, MNRAS, 325, 497
Brighenti, F., & Mathews, W. 2001, ApJ, 553, 103
Bryan, G. 2000, ApJ, 544, L1
Caon, N., Capaccioli, M., & D'Onofrio, M. 1993, MNRAS, 265, 1013
Cavaliere, A., & Fusco-Femiano, R. 1976, A&A, 49, 137
Ciotti, L., & Bertin, G. 1999, A&A, 352, 447
de Vaucouleurs, G. 1948, Ann. Astrophys., 11, 247
De Grandi, S., & Molendi, S. 2002, ApJ, 567, 163
Dos Santos, S., & Doré, O. 2002, A&A, 383, 450
Durret, F., Gerbal, D., Lachièze-Rey, M., Lima Neto, G. B., & Sadat, R. 1994, A&A, 287, 733
Ebeling, H., Voges, W., Böhringer, H., et al. 1996, MNRAS, 281, 799
Ettori, S., De Grandi, S., & Molendi, S. 2002, A&A, 391, 841
Fillmore, J., & Goldreich, P. 1984, ApJ, 281, 1
Flores, R., & Primack, J. R. 1994, ApJ, 427, L1
Frenk, C. S., White, S. D. M., Bode, P., et al. 1999, ApJ, 525, 554
Fujita, Y., & Takahara, F. 1999, ApJ, 519, L51
Gerbal, D., Durret, F., Lima Neto, G. B., & Lachièze-Rey, M. 1992, A&A, 253, 77
Gerbal, D., Lima Neto, G. B., Márquez, I., & Verhagen, H. 1997, MNRAS, 285, L41
Gunn, J., & Gott, J. R. III 1972, ApJ, 176, 1
Helsdon, S. F., & Ponman, T. J. 2000, MNRAS, 315, 356
Hicks, A., Wise, M., Houck, J., & Canizares, C. 2002, ApJ, 580, 763
Irwin, J. A., Bregman, J. N., & Evrard, A. E. 1999, ApJ, 519, 518
Irwin, J. A., & Bregman, J. N. 2000, ApJ, 538, 543
James, F. 1994, CERN Program Library Long Writeup D506
Jang-Condell, H., & Hernquist, L. 2001, ApJ, 548, 68
Jing, Y. P., & Suto, Y. 2000, ApJ, 529, L69
Lanzoni, B. 2000, Ph.D. Thesis, Université Paris 7
Lima Neto, G. B., Gerbal, D., & Márquez, I. 1999, MNRAS, 309, 481
Lloyd-Davies, E. J., Ponman, T. J., & Cannon, D. B. 2000, MNRAS, 315, 689
Loken, C., Norman, M. L., Nelson, E., et al. 2002, ApJ, 579, 571
Magnard, F. 2002, Ph.D. Thesis, Université Paris 6
Markevitch, M., Forman, W. R., Sarazin, C. L., & Vikhlinin, A. 1998a, ApJ, 503, 77
Markevitch, M. 1998b, ApJ, 504, 27
Márquez, I., Lima Neto, G. B., Capelato, H., Durret, F., & Gerbal, D. 2000, A&A, 353, 823
Márquez, I., Lima Neto, G. B., Capelato, H., et al. 2001, A&A, 379, 767
Mellier, Y., & Mathez, G. 1987, A&A, 175, 1
Mohr, J. J., Mathiesen, B., & Evrard, A. E. 1999, ApJ, 517, 627
Moore, B., Quinn, T., Governato, F., Stadel, J., & Lake, G. 1999, MNRAS, 310, 1147
Muanwong, O., Thomas, P. A., Kay, S. T., & Pearce, F. R. 2002, MNRAS, 336, 527
Navarro, J., Frenk, C., & White, S. 1996, ApJ, 462, 563
Navarro, J., Frenk, C., & White, S. 1997, ApJ, 490, 493
Ponman, T. J., Cannon, D. B., & Navarro, J. F. 1999, Nature, 397, 135
Renzini, A. 1997, ApJ, 488, 35
Rosati, P., Borgani, S., & Norman, C. 2002, ARA&A, 40, 539
Sarazin, C. 1988, X-Ray Emission from Clusters of Galaxies (Cambridge University Press)
Schindler, S. 1999, A&A, 349, 435
Sérsic, J. L. 1968, Atlas de Galaxias Australes, Observatorio Astronómico de Córdoba, Argentina
Snowden, S. L., McCammon, D., Burrows, D. N., & Mendenhall, J. A. 1994, ApJ, 424, 714
Subramanian, K. 2000, ApJ, 538, 517
Tamura, N., Kaastra, J. S., Peterson, J. R., et al. 2001, A&A, 365, L87
Taylor, J. E., & Navarro, J. F. 2001, ApJ, 563, 483
Teyssier, R., Chièze, J.-P., & Alimi, J.-M. 1997, ApJ, 480, 36
Teyssier, R. 2002, A&A, 385, 337
Tozzi, P., Scharf, C., & Norman, C. 2000, ApJ, 542, 106
Tozzi, P., & Norman, C. 2001, ApJ, 546, 63
van den Bosch, F. C., & Swaters, R. A. 2001, MNRAS, 325, 1017
White, D. 2000, MNRAS, 312, 663
Wu, X.-P., Xue, Y.-J, & Fang, L.-Z. 1999, ApJ, 524, 22

Chapter 4

Galaxy spectroscopy

In this chapter I will talk about the study of galaxy spectra and the spectroscopic data reduction process. This is the basis for the analysis and interpretation of the data I will discuss in chapter 5 and which constitutes the main topic of my thesis work.

Spectroscopy is the most powerful tool of astrophysics, allowing, for example, to compute distances to galaxies and study the properties of their stellar contents as well as the internal dynamics of cluster galaxies. The photons coming from the astronomical source of interest can be separated according to their energy by the means of instruments called spectrographs. The resulting "image" is something that astronomers call the spectrum of the source or more technically speaking its Spectral Energy Distribution (SED). In the following sections I will describe shortly the most important spectral features of galaxy spectra according to galaxy-type (see section 1.3.1). I will concentrate on the spectral features of "normal", non-active galaxies. I will discuss about photometric properties of galaxies and finally I will talk about technical issues concerning the observation of galaxy spectra and their reduction before using them to estimate physical quatities such as the galaxy redshift. All these concepts and technical issues will be applied to the study of galaxies in distant clusters, as I will discuss in chapter 5.

4.1 Galaxy Spectra

The SED of a given galaxy is the result of combining the flux at every wavelength emitted from each of its components: stars and gas. The spectrum of a galaxy can be thus quite complex since it will be the reflection of the different types of stars in different number fractions living in the galaxy, together with all the interactions of the stellar light with the surrounding medium (and, in principle, the medium between us and the source too). Recognizing and analysing spectral features in galaxy spectra represents a fundamental issue in cosmology. Spectral features can be used to estimate the redshift to the galaxy and thus its distance. Moreover, the presence or absence of specific features can be used as an indication of the morphological type of the galaxy. In addition to this, the integrated galaxy spectrum constitutes a powerful diagnosis of the stellar populations as well as a tracer of galaxy evolution.

4.1.1 Stellar spectra

Before describing the general characteristics of galaxy spectra, it is suitable to start by quickly reviewing the main characteristics of stellar spectra (see e.g., Binney & Merrifield 1998 for a detailed description). Stars can be classified into spectral types which are ordered according to temperature. These types are designated as O, B, A, F, G, K, M, R, N and S and are subdivided into subtypes ranging from 0 to 9. The first types correspond to hot and blue young stars and the last types contain cooler and redder old stars. The range in temperature goes from about 50000 K in the case of hot O stars to around 3000 K in the case of S stars. Our Sun, for instance, is a G2 star with a temperature of 5500 K. This classification scheme is defined by the variation with temperature of typical absorption features in the stellar spectra. In general terms, the hot spectral classes (O, B and A) are characterized by the appearance of ionized atom lines such as e.g. HeII, MgII, SiII, SiIII and SiIV. Cooler spectral types, on the other hand, show a marked presence of lines from neutral atoms, and absorption bands from molecules appear strongly in M-type stars. Important lines, as I will show below, are the Ca II K(λ3933) and H(λ3968) lines and the Hydrogen Balmer lines (as e.g. H_α (λ6563), H_β (λ4861), H_γ (λ4340) and H_δ (λ4101)). The Ca lines are strongly dominant in cool G- and K-type stars. On the other hand, Balmer absorption features are more dominant in hot, young stars, attaining a maximum strength in A0 type stars and decreasing in strength toward cooler types. Other classifications such as the MK system (see e.g., Binney & Merrifield 1998) takes into account not only temperature but also luminosity, defining thus five luminosity classes. In this classification, our Sun is a star belonging to the class V, which corresponds to the luminosity class of main-sequence (MS) stars. Table 4.1 summarizes the main physical characteristics of MS (class V) stars.

4.1.2 SED models

The compilation of stellar libraries and evolutionary population synthesis models offer the possibility of decomposing the overall galaxy spectrum and studying its evolution with cosmic time (e.g., Silva & Cornell 1992; Bruzual & Charlot 1993; Fioc & Rocca-Volmerange 1997; Poggianti et al. 1999;

Stellar type	O5	A0	G2	K5	M5
M ($M_\odot$)	60	2.9	1.0	0.67	0.21
$\mathbf{L}_V$ ($\mathbf{L}_{V\odot}$)	8×10^5	50	1.0	0.15	0.01
Temperature (Kelvin)	44500	9520	5860	4350	3240
Life time (Gyr)	10^{-3}	0.5	10	40	2000
B-V color	-0.33	-0.02	0.65	1.15	1.64

Table 4.1: Main characteristics of some representative main sequence (MS) stellar types as in Rich (2001). The life time on the MS corresponds to the time necessary to burn the hydrogen in the stellar core (~10% of the total hydrogen) at a roughly constant luminosity. See also Binney & Merrifield (1998).

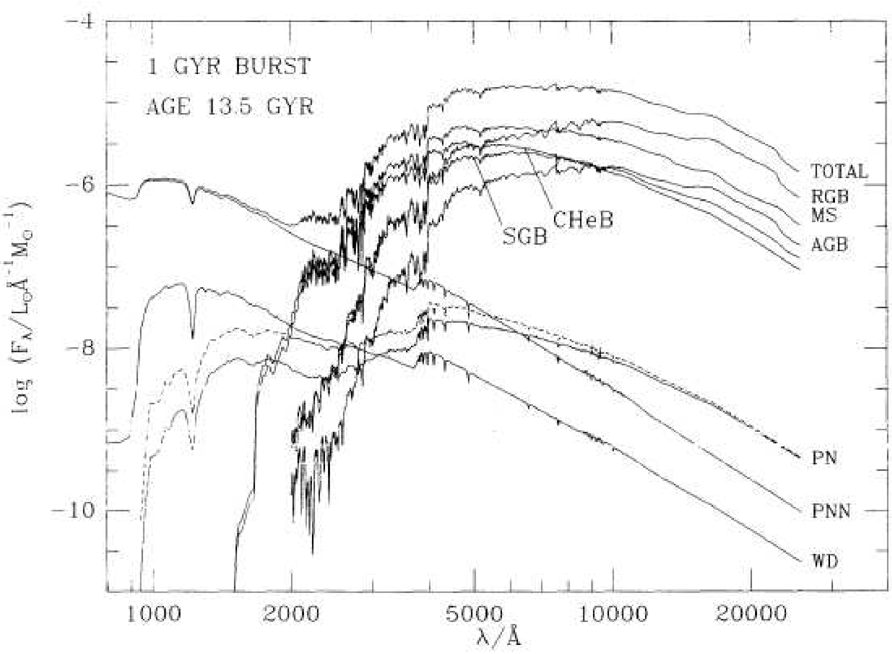

Figure 4.1: Contribution of different groups of stars to the total Spectral Energy Distribution (SED) of a 1 Gyr burst population with a Salpeter (Salpeter 1955) IMF observed at an age of 13.5 Gyr (from Bruzual & Charlot 1993). Stars have been arranged in the following groups: main-sequence (MS), subgiant branch (SGB), red giant branch (RGB), asymptotic giant branch (AGB), core He burning (CHeB), planetary nebulae (PN), bare PN nucleus (PNN) and white dwarfs (WD).

Le Borgne et al. 2003). For instance, Fig. 4.1 illustrates how different stellar groups produce the overall SED of a 1 Gyr burst population at an age of 13.5 Gyrs (Bruzual & Charlot 1993). More than half of the light at wavelengths greater than 4000 Å is produced by red giant stars, whereas MS and subgiant stars, of G- and K-type, dominate the light between 3000 and 4000 Å. With only one initial 1 Gyr burst, the young high-mass MS stars of O- to A-type have disappeared by 13,5 Gyrs. The spectrum blueward of 2000 Å is entirely dominated by low-mass post-AGB stars. The SED shown in figure 4.1 may be a good representation of the spectrum of an early-type galaxy.

The evolution with time of such a model can be followed by mean of evolutionary population synthesis models. Figure 4.2 shows an example of the evolution with time of a model spectrum produced by an initial stellar burst of 1 Gyr of duration followed by passive evolution. The time is indicated on the left hand side of each spectrum. At an age of 0.4 Gyr, the SED is dominated by the strong UV continuum and a number of strong emission lines, both produced by the initial burst of stars and consistent with a high Star Formation Rate (SFR). At about 1.4 Gyrs, the UV continuum has decreased significantly (indicating the decrease in the SFR) and the Balmer absorption features, due to the presence of young MS stars (with temperatures at which most of the hydrogen is in its n=2 state), are strong. Afterward, these lines will decrease in strength and the overal spectrum will get dominated by the light of red, low mass MS stars and red giants, becoming a typical elliptical galaxy spectrum.

It is important to say that this evolution may also be a function of the environment. Real galaxies may evolve differently depending on whether they are in clusters or in the field.

The inclusion of gas and dust in models of spectral evolution is an important factor. Early-type galaxies have a low fraction of cold gas, although ellipticals can have extended, hot X-ray emitting gas (see e.g., Braine, Henkel & Wiklind 1997, and references therein). Late-type Spiral galaxies have large fractions of neutral gas (e.g. HI, OI) as well as regions with ionized gas (e.g. HII, OII, OIII). For example, HII regions are normally associated to very young and massive stellar populations, and constitute the birthplaces of stars. The UV flux coming from just born massive stars ionize the surrounding medium producing, by subsequent recombination, characteristic emission lines in the integrated galaxy spectrum. This can be seen in the initial starburst phase shown in figure 4.2. In the optical band the most common emission lines are those of the Hydrogen Balmer series and Oxygen. Emission lines such as OII (λ3727) and H_α (λ6563) are indicators of on-going star formation processes. The UV continuum in the galaxy

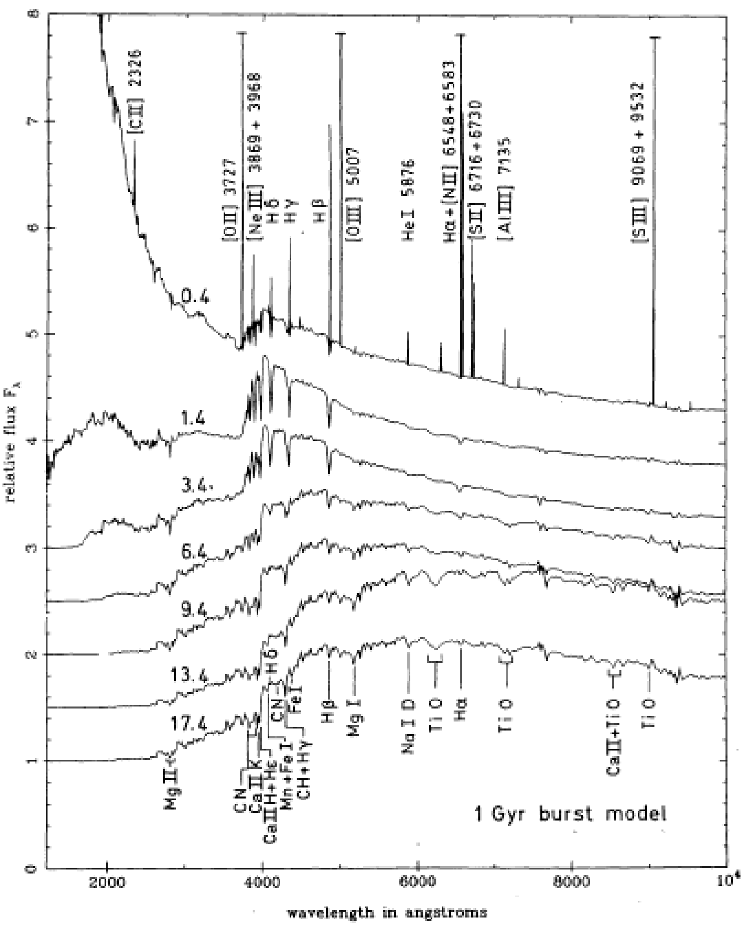

Figure 4.2: Evolution with time of the Spectral Energy Distribution of a model caracterized by an initial burst of τ=1 Gyr, followed by passive evolution. The time is indicated on the left hand side of each spectrum and spectral features are labeled (taken from J. Schombert's lectures. URL: http://zebu.uoregon.edu/~js/lectures/st_pop/page_9.html).

SED will be determined by the emission coming from O, B and A stellar populations mainly. This UV continuum together with emission lines can be used as tracers of the SFR in galaxies (e.g., Kennicutt 1983; Donas & Deharveng 1984; Kennicutt et al. 1992a). However, any measurement of the UV continuum and the equivalent witdth (EW) of emission lines must take into account the effects of dust and gas absorption, in the galaxy itself and along the line of sight between us and the source (e.g., Calzetti, Kinney & Storchi-Bergmann 1994; Madau et al. 1996). Metals present in the stellar atmospheres and in the interstellar medium of a galaxy are efficient in absorbing UV photons. The dust will absorb the line emission and the continuum more strongly in the UV, reemitting this radiation in the infrared (IR). The observable effect would be a decrease of the UV flux of the galaxy and an excess of emission at IR wavelengths.

4.1.3 Spectral features and galaxy type

General characteristics of the integrated spectra of galaxies correlate with morphological galaxy-type (see e.g., Kennicutt 1992b). This is the result of the relation between the main structural components of a galaxy, the bulge and the disk, and the stellar population present in these structures. The bulge is dominated by old ($\sim$ 10 - 40 Gyr), cool ($\sim$ 5900-4400 Kelvin) K and G stars, whereas the disk, where spiral arms are located, is inhabited by young (10^{-3}- 4 Gyr), hot ($\sim$ 50000 - 6500 Kelvin) O - F stars. The bulge-to-disk ratio of the galaxy will therefore determine its overall spectrum.

Early-type galaxy spectra

In general, today early-type galaxies (ellipticals and S0) do not show the presence of emission lines, in clear contrast to late-type galaxies. This is an indication of no star-forming activity in these systems, in consistency with the considerably low amount of gas present in ellipticals and the lack of gas in the disk of S0s. These galaxies also do not show clear signature of Balmer absorption features, in particular H_δ, indicating the lack of young (few Gyrs), massive stars. Massive MS stars are short-lived objects (see table 4.1). At the typical ages of local early-type galaxies, this population has basically died out, and the lack of star formation activity reinforces the predominance of the old and red population. The light of early-types is therefore dominated by G- and K-type stars, in particular low-mass MS stars and red giants (e.g., Bruzual 1983). These populations contribute greately to the strength of the CaII K(λ3933) and H(λ3968) lines, some of the main characteristics of early-type SEDs. Figure 4.3 shows a typical elliptical galaxy template, obtained by combining observed spectra in the optical and UV (see Kinney et al. 1996, and references therein, for details on how this template was made). The K and H absorption features of Ca

II are clearly visible, as well as other features such as MgI ($\lambda3834$), the G band ($\lambda4304.4$) produced by the CH molecule, Mg_b ($\lambda5175$) and Na ($\lambda5892$). Note the absence of strong Balmer features.

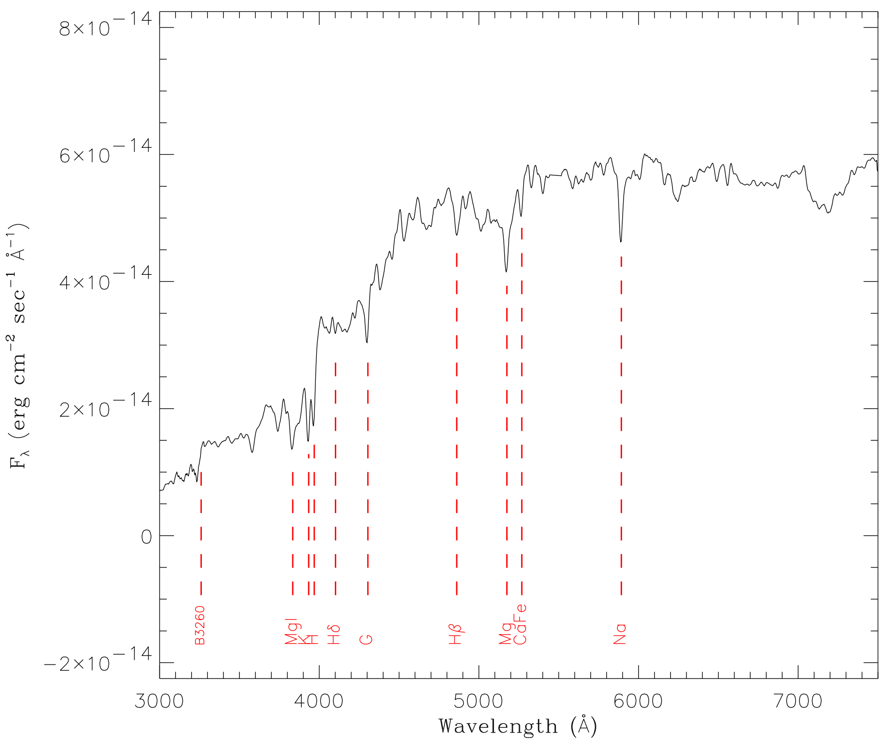

Figure 4.3: Elliptical galaxy SED template (from Kinney et al. 1996). This template has been determined by ground-based optical observations and UV observations from space (see Kinney et al. 1996 for details). A number of metalic absorption features, as the CaII K and H lines can be seen, as well as the charateristic 4000 Å break. Note that absorption Balmer lines do not show significant strength.

But the most typical feature of early-type galaxies is the strong drop off in flux around 4000 Å (e.g., Dressler & Shectman 1987b; Poggianti & Barbaro 1997, and references therein), usually called the "4000 Å Break" . This jump in the SED is characteristic of cool (G and K) stars and is the result of the absorption produced by the Ca II H and K features followed at shorter wavelengths by an apparently lowered continuum, in reality made up of many blended iron and other lines (see Emerson 1996). This discontinuity can be quantified by measuring the ratio of mean fluxes in two windows above and below 4000 Å. The mean observed value in nearby early-type galaxies is of the order of 2. The 4000 Å Break is quite sensitive to the presence of young and hot stars (Dressler & Shectman 1987b; Poggianti & Barbaro 1997), which increase the UV flux in the spectral region below 4000 Å. This explain why this feature becomes weaker and weaker as we move to late-type spirals and irregular galaxies. For stars with ages greater than about 2 Gyrs, the 4000 Å Break becomes sensitive to metallicity, increasing with metallicity and age (see Poggianti & Barbaro 1997). Another break at 3260 Å can also be seen in the SED of early-types.

All the above describes well the average population of local elliptical in clusters. Secondary star formation activity has been observed in field ellipticals at redshifts greater than 0.3 and up to $z \sim 0.6$ (see Treu et al. 2002), indicating differences in the stellar contents of early type galaxies in different environments at different lookback times.

Late-type galaxy spectra

The spectrum of Sa galaxies is quite similar to that of Ellipticals and S0 galaxies. Their bulge component still dominates, and signatures of weak emission lines and an increase of the UV continuum are due to on-going star formation and young stellar populations in the disk. Balmer absorption lines start to be visible, although rather weak. As we move to later-type spirals, the central bulge becomes smaller and the disks with spiral arms start to dominate. Balmer absorption features, as H_δ (λ4101), becomes stronger, indicating the presence of young stars formed in some burst which ended some 1 - 2 Gyrs ago (Dressler & Gunn 1983; Poggianti & Barbaro 1997). Emission line EWs increase, and the strength of the 4000 Å jump decreases considerably due to the UV flux at wavelengths shorter than 4000 Å from young O to F stars. Figure 4.4 shows the SED of a typical Sc galaxy (see Kinney et al. 1996). The 4000 Å Break has been completely suppressed and many strong emission lines are visible, indicating clear on-going starburst processes in the spiral arms. Some Balmer lines, observed as absorption features in earlier types, have here become emission lines. In the optical, these emission lines correspond to [OII] (λ3727), H_β (λ4861), [OIII] (λ4959 and λ5007), H_α+[NII] (λ6563) and [SII] (λ6717 and λ6731). In contrast to the red continuum of early-types, the continuum of late spirals is blue. The spectrum of Irregular (Im) galaxies is similar to Sc spirals although it can be even bluer at wavelengths below 4000 Å. Although the H_δ feature is a sign of relatively young stellar populations living in a galaxy, it cannot be used as a pure age indicator because it is also affected by the age-metallicity degeneracy problem (Poggianti & Barbaro 1997). Another important spectral feature, characteristic of late-type galaxies is the so called "Balmer Break". This discontinuity is due to the large cross-section for photoionization of hydrogen in the n=2 state, typical of young A stars with temperatures of about 10000 K (see Emerson 1996). Closely spaced lines near the ionization threshold at λ=3700 Å (Balmer limit) contribute greatly to the observed jump.

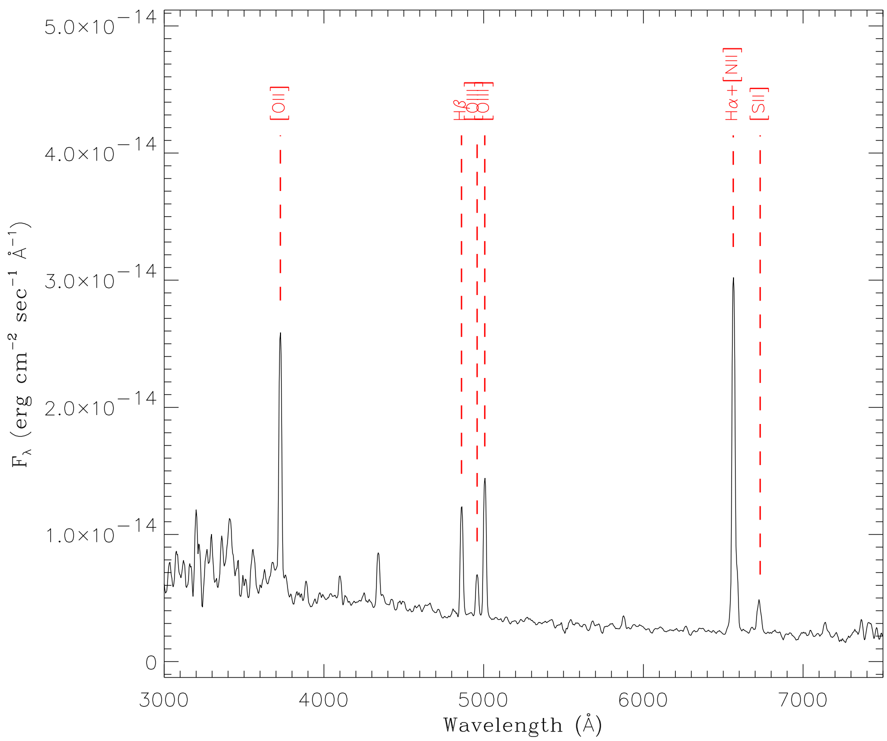

Figure 4.4: Sc galaxy SED template (from Kinney et al. 1996). This template has been determined by ground-based optical observations and UV observations from space (see Kinney et al. 1996 for details). This spectrum shows Balmer lines in emission, clear indication of star-forming activity in this type of galaxies. The high UV flux coming from the young stellar population has completely suppressed the 4000 Å Break.

The above picture suggests that late-type Spirals and Irregular galaxies have been forming stars since they were formed down to the present time.

Feature	**Wavelength (Å)**	**Feature**	**Wavelength (Å)**
B3260	3260.0	H_β	4861.3
[OII]	3727.3	[OIII]	4958.9
MgI	3834.0	[OIII]	5006.8
CaII K	3933.7	Mg_b	5175.4
CaII H	3968.5	Na	5892.5
B4000	4000.0	H_α	6562.8
H_δ	4101.7	[NII]	6583.6
G	4304.4	[SII]	6717+6731.3

Table 4.2: Main spectral features in galaxy spectra. Quoted values correspond to rest frame values. B4000 is the 4000 Å Break whereas B3260 is a spectral break at 3260 Å.

Early-type galaxies, on the contrary, seem to transform most of their gas into stars on timescales much less than the age of the universe. Figure 4.5 shows a comparison between SEDs of different galaxy types. The spectra are those presented in Bolzonella, Miralles & Pelló (2000). They correspond to the combined spectra of local galaxies obtained by Coleman, Wu & Weedman (1980), extended into the UV and infra-red (IR) spectral regions by means of the Galaxy Isochrone Synthesis Spectral Evolution Library (GISSEL; Bruzual & Charlot 1993). The changes in relative flux, when moving from one galaxy type to another, are evident. This figure clearly illustrates the correlation between morphological galaxy type and the shape of the corresponding integrated SED. The stark increase of UV flux due to young stars is the main feature in Sbc, Scd and Im galaxies, the latter being the bluest. Early-types are, as I have already commented, very well characterized by their strong 4000 Å break with most of their flux being emitted in the red and IR spectral windows. Since most of the light in Ellipticals and S0 galaxies is radiated at wavelengths longer than the 4000 Å Break, the use of red and IR filters to study their properties are of great importance. Red and IR light comes from the bulk (the most common and long-lasting) of their stellar population, being a good tracer of the total mass contained in stars and being insensitive to the star formation history of the galaxy, which varies depending on the environment and possible interactions. This is quite important when studying galaxy evolution from redshift $z \sim 1$ down to $z = 0$, as I will discuss later.

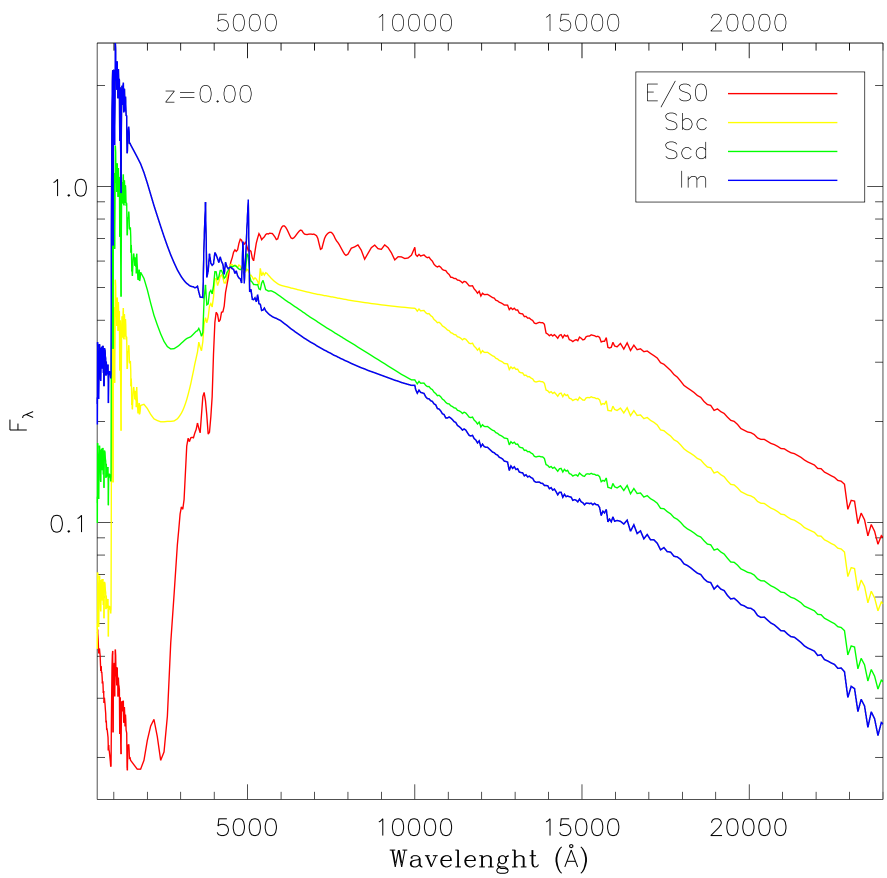

Figure 4.5: Comparison between the SEDs of different galaxy types. These templates are presented by Bolzonella, Miralles & Pelló (2000) and correspond to the observed galaxy SEDs of Coleman, Wu & Weedman (1980), extended to the UV and IR by the Galaxy Isochrone Synthesis Spectral Evolution Library (GISSEL) of Bruzual & Charlot (1993). The changes in the relative flux when going from one galaxy type to another indicates the difference of stellar populations of every galaxy type.

4.1.4 Spectrophotometric properties of galaxies

In this section I will shortly review basic concepts on photometry that will be useful to understand photometrical properties of galaxies, which is of great importance in the study I will present in chapter 5. To begin, let us consider an object of intrinsic luminosity L. If the object is at a distance d from us, the flux we receive from the source will be $f = L/(4\pi d^2)$. In astronomy, the apparent brightness of an object is expressed in terms of its apparent magnitude. Physiological studies have shown that equal steps of brightness sensed by the eye correspond fairly well to equal ratios of flux, i.e., the response of the eye to a luminous stimulus is logarithmic. The system of astronomical magnitudes is defined in such a way that if m_1 is the magnitude of a source with observed flux f_1 and m_2 is the magnitude of a source with observed flux f_2, then the difference in magnitude will be:

$$\Delta m = m_1 - m_2 = -2.5 log_{10} \left(\frac{f_1}{f_2} \right) \tag{4.1}$$

In general, the total (bolometric) luminosity of a source is difficult to measure, and astronomers normally observe sources by using filters which select light within a determined wavelength range. A given set of filters with specific characteristics can be used to define a photometric system. Some of the most commonly used broad band systems are the Johnson-Morgan-Cousins (UBVRI; e.g., Bessel 1990, and references therein), the Thuan-Gunn (e.g., Schneider, Gunn Hoessel 1983), the WFPC2 and SDSS (see e.g., Fukugita, Shimasaku & Ichikawa 1995; Binney & Merrifield 1998, and references therein). Table 4.3 gives the most important characteristics of the standard filters in the UBVRI system. Figure 4.6 shows the set of B,V,R and I FORS Bessel filters and the near-IR J, H, and K_s SOFI filters overlaid on the SED of the Elliptical template shown in figure 4.5. Another photometric system that is normally found in the literature is the AB system (see Oke & Gunn 1983). This system is defined in such a way that the magnitude AB of a source with specific flux $f(\nu)$ calibrated in $erg\ s^{-1}\ cm^{-2}\ Hz^{-1}$ is $AB = -2.5 log_{10}(f(\nu)) - 48.60$. The value of the constant is chosen such that AB=V for an object with a flat spectrum.

If $S_\xi(\nu)$ is the response of the standard ξ-band (ξ=U, B, V, R, I, etc.) filter-photometer combination and $f(\nu)$ is the flux of the astronomical object, then the observed flux of the source, averaged over the standard photometric band ξ, will be:

$$f_\xi = \frac{\int_0^\infty S_\xi(\nu) f(\nu) d\nu}{\int_0^\infty S_\xi(\nu) d\nu} \tag{4.2}$$

Thus, the observed magnitude ξ of an object in the ξ-band will be:

Filter	λ_{eff} **(Å)**	$\Delta\lambda$ **(FWHM; Å)**	**M (sun)**	A/A$_V$
U	3650	660	5.61	1.531
B	4450	940	5.48	1.324
V	5510	880	4.64	1.0
R	6580	1380	4.42	0.748
I	8060	1490	4.08	0.482
J	12000	2130	3.64	0.282
K	21900	3900	3.28	0.112

Table 4.3: Main charactersitics of the standard filters in the UBVRI system. The fourth column gives the absolute magnitude of the sun in the corresponding filter and the last column gives the band's extinction coefficient relative to that of the V band (Binney & Merrifield 1998; Rich 2001).

$$\xi = -2.5log_{10}(f_\xi) + C_\xi \tag{4.3}$$

where C_ξ is a constant called zero-point, whose value depends on the photometric system employed. Astronomers define the absolute magnitude M_ξ of a source of intrinsic luminosity L as the observed magnitude of the source at a distance of 10 pc, in the band ξ. Then if ξ is the observed magnitude of an object at a distance d from us, astronomers define the distance modulus of the object as $\xi - M_\xi = 5log_{10}(d) - 5 + A_\xi + K_\xi + E_\xi$. The A_ξ term is the extinction coefficient of the band ξ (see table 4.3), which decreases towards longer wavelengths, and has a typical value of $A_V \sim 0.1$ mag for extragalactic sources in directions perpendicular to the galactic plane. The K_ξ term corrects the effects due to the redshift in the case of distant sources and is called the k-correction. The E_ξ term take into account changes in galaxy luminosity due to the evolution in time of the SED and is called e-correction. This corrections depend on the SED of the source, the bandpass, and redshift (Poggianti 1997, and references therein). The "color" of an object is defined as a difference of magnitudes in two different bands. If $\xi 1$ and $\xi 2$ are two different bandpasses with $\lambda_{eff,\xi 1} < \lambda_{eff,\xi 2}$, then the "color", or color index, of the object in those bands is:

$$\xi 1 - \xi 2 = -2.5 \left\{ \frac{\int_0^\infty S_{\xi 1}(\nu) f(\nu) d\nu}{\int_0^\infty S_{\xi 2}(\nu) f(\nu) d\nu} \right\} \tag{4.4}$$

Multi band photometry offers a very efficient way to obtain a rough description of the SED of a large number of objects at the same time. In practice, the magnitude and colors of a source are determined in the following way. Images of the target object are taken with different filters. The

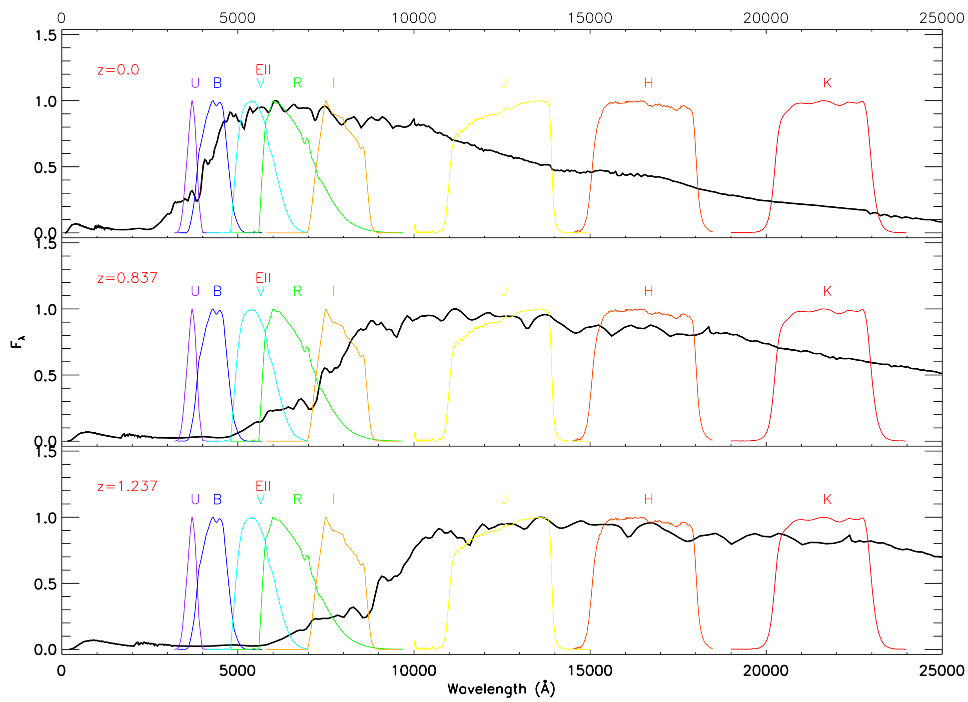

Figure 4.6: The E/S0 spectrum shown in Fig. 4.5 (Coleman, Wu & Weedman 1980; Bolzonella, Miralles & Pelló 2000) at three different redshifts (without evolution). The upper panel shows the early-type SED at $z = 0$ (rest frame). The middel panel shows the spectrum a redshift $z = 0.837$ and the bottom panel show the same spectrum at $z = 1.237$. The set of B,V,R and I FORS Bessel filters and the near-IR J, H, and K_s SOFI filters are also shown.

total number of counts within a given aperture centered in the object of interest is computed. The contribution from the background is obtained by summing up the number of counts within an annulus concentric to the aperture. The difference of both numbers will give the number of counts coming from the object within the given aperture. Observations of photometric standard stars are used to calibrate these number counts into physical flux units. Once the flux is obtained, Eq. (4.3) is used to compute the magnitude of the object in the given image, i.e., in the given filter. Differences of magnitudes in defferent filters will give the color index of the object (see Eq. 4.4). The total magnitude of an extended object, such as a galaxy, is not a well defined quantity, since galaxies have no clear edges and therefore their total magnitude will depend on the choice of the aperture size. Moreover, computing the value of the zero-point is a crucial step. Colors, on the other hand, are just differences in magnitudes, and they can be computed within fixed apertures, in which most of the galaxy light is contained.

For known redshift objects, by just looking at their colors one can have, at a first glance, a rough idea of the galaxy type, and of the kind of dominant stellar population living in the galaxy. At the same given redshift, early-type galaxies are always redder than late-type. For instance, nearby ($z \leq 0.025$; Kennicutt 1992b) ellipticals show colors $B-R$ and $U-V$ of the order of 1.6, whereas nearby Scd galaxies show $U-V$ colors around 0.4 (Fukugita, Shimasaku & Ichikawa 1995, and references therein).

The typical $U-V$ colors in local ellipticals are due to their strong 4000 Å break, as can bee seen in the top panel of figure 4.6 and as was discussed before. In the case of local late-type spirals, the presence of a young stellar population will increase the UV flux at wavelengths shorter than the 4000 Å break, therefore reducing its strength and producing bluer colors, i.e., smaller $U-V$ values. The change in color of a given galaxy type as a function of redshift is illustrated in figure 4.7. These color-color tracks have been computed for E/S0, Sbc, Scd and Im galaxies by using the Coleman, Wu & Weedman (1980) observed templates of local galaxies, without evolution of the SED as a function of z. $B-R$ and $R-K$ colors have been computed for every template in the range $0.1 \leq z \leq 2$, with steps of $\Delta z = 0.1$. Filled circles indicate colors at $z = 0.5$, 0.8, 1.0 and 1.5. Fig. 4.7 shows a problem of degeneracy between color and galaxy type. As it can be seen, the $B-R$ colors of high redshift ($z \sim 1.5$) E/S0 galaxies can be well reproduced by late-type galaxies at lower redshift. In an analogous way, Scd galaxies between $0.8 < z < 1.5$ can well mimic the $R-K$ color of early-types at $z \sim 0.5$. This problem can be solved by taking into account two colors at the same time, as it is shown. More refined models that take into account evolutionary effects in the SED of every galaxy type with z

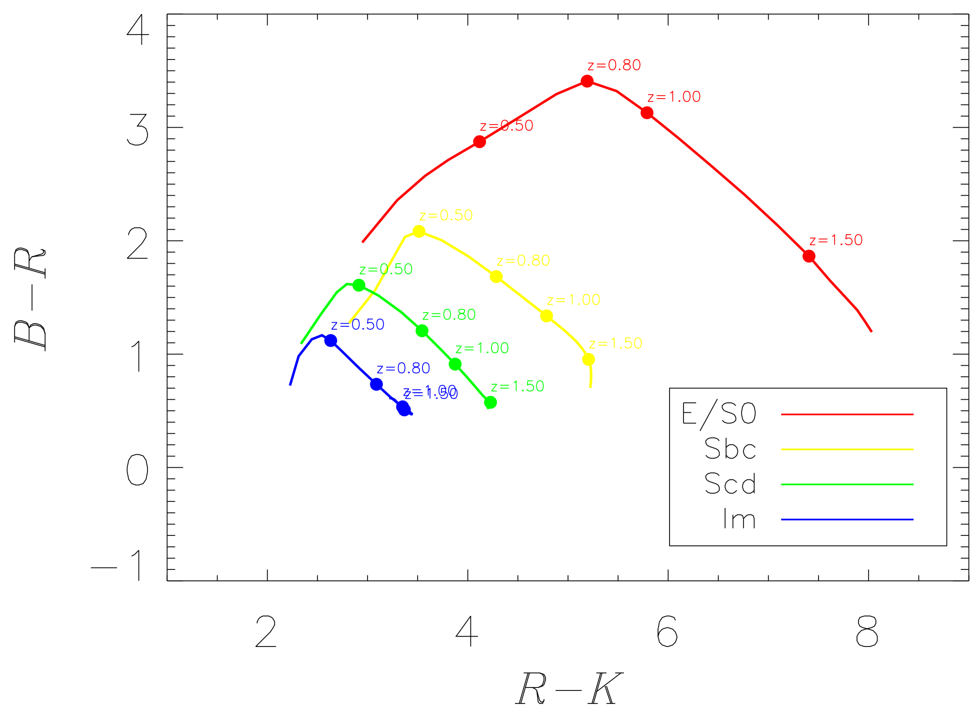

Figure 4.7: The different lines indicate the variation with redshift of the B-R and R-K colors of galaxies of different type. The spectra used to compute the color-color tracks are those from Coleman, Wu & Weedman 1980. The optical bandpasses used to compute magnitudes are from Keck, whereas the IR K-band filter is from SOFI (NTT). No evolution of the galaxy spectra is considered.

can give more accurate predictions. While at low redshifts differences in the color-color plane may be not very large ($\Delta(B-R) \sim \Delta(R-K) \sim 1$ mag) among galaxy types, at high redshifts the difference between Elliptical and late-type galaxies becomes significant, specially due to the $R-K$ color ($\Delta(R-K) \geq 3$). Thus, color-color diagrams together with an accurate modeling of SEDs of galaxies can be used as a powerful method to select determined types of galaxies at high redshifts (e.g., Steidel et al. 1999; Stevens & Lacy 2001), as I will show in chapter 5. The changes for E/S0 galaxies in color-color space can be also visualized by looking at the different panels in figure 4.6. Top pannel corresponds to a rest-frame SED. The middel pannel show the same spectrum at $z = 0.837$ and the bottom panel shows the same spectrum at $z = 1.237$. The different colors of a given galaxy contain the information on its relative flux at different wavelengths. By fitting its photometry with that of an adequate template SED, physical quantities of the galaxy can be measured. One of them is its redshift. The redshift obtained by fitting the broad band photometry of a galaxy is called **photometric redshift**. This technique concentrates on broad features, such as the 4000 Å break and the overall shape of the spectrum. An advantage of photometric redshifts is that, since they depend on photometric data, they represent an efficient way to obtain many redshifts with relatively short observing times. Moreover it offers the possibility of estimating the redshifts of faint galaxies, close to the spectroscopic limit, where spectroscopic redshifts can be hard to obtain. However, accurate photometric redshifts require accurate photometry, and this represents a serious limitation compared to spectroscopic redshifts. Typical uncertainties of photometric redshifts are $\sigma_z \sim \pm 0.1$ (see e.g., Massarotti et al. 2001), whereas spectroscopic redshifts uncertainties are $\sigma_z \sim \pm 0.001$. Moreover an appropriate model for the observed source spectrum is required. Works describing and using the photometric redshift technique include Benítez (2000), Bolzonella, Miralles & Pelló (2000), Fernández-Soto (2001), Rudnick et al. (2001), Chen et al. (2003).

4.2 Multi Object Spectroscopy

In this section I am going to explain in some detail technical issues related to the analysis of spectroscopy data, which has been the most important part of my thesis work. Spectroscopy is the most powerful tool of astrophysics to learn the physics of distant objects, spite of the difficulty of performing this kind of observation on faint objects. A good and efficient use of spectroscopy requires to have a knowledge of some global characteristics of the system under study, such as its broad band colors, and the use of a number of technical procedures in order to get the best results. The complexity of spectroscopy is high, however, it can lead to surprising results.

The spectroscopic work I will present below is one of the major parts of one of the most extensive survey carried out in two distant clusters (see chapter 5). For example, in order to well characterize the dynamical state of a cluster of galaxies as well as performing a complete analysis of its galaxy populations, observing as many galaxies as possible, in the most efficient way, is crucial. The **Multi-Object Spectroscopy** (MOS) technique offers the possibility of fulfilling these goals. In what follows I will describe the most important aspects of data reduction and analysis when dealing with MOS spectroscopy. Although the discussion I will present below is based on a particular instrument-telescope configuration, the general procedure is a standard one, that can be applied to any MOS data.

4.2.1 VLT+FORS spectroscopy

The spectroscopic observations and corresponding data reduction I will start discussing now are the base for the research work I will present in chapter 5. All the spectroscopic observations were carried out on Paranal Observatory, northern Chile, with the Very Large Telescope [1] (VLT). The VLT is a set of 4 Unit Telescopes (UTs) of 8.2 m aperture each (see left picture in Fig. 4.8). Mounted at the Cassegrain focus of a UT, the FOcal Reducer and low dispersion Spectrograph (*FORS*; Appenzeller & Rupprecht, 1992) was chosen as the ideal instrument to carry out our spectroscopic campaign. There are two such instruments currently in operation: FORS1 and FORS2 (see right picture in Fig. 4.8). Detailed information on both instruments can be found at http://www.eso.org/instruments/fors1/. Both FORSs operate in the range between 3300 Å and 11000 Å. Two spatial resolutions and hence field sizes can be selected by exchanging the collimators. The resulting field of view is 6.8' × 6.8' with the standard resolution (SR) collimator. With the high resolution (HR) collimator the field of view reduces to 3.4' × 3.4' for the FORS1 Tektronix CCD detector and 4.2' × 4.2' for the FORS2 MIT CCD mosaic. All our observations were conducted in SR mode, which corresponds to a pixel scale of $\sim 0''.2/pix$ with FORS1 and $\sim 0''.25/pix$ with FORS2 (in SR the default readout mode has been binned 2×2 pixels). The frames obtained with FORS1 have a typical size of 2080 × 2048 pixels. In the case of the FORS2 mosaic detector, a frame is composed by two 2k × 4k MIT CCDs sections separated by a gap of 480 μm (see Fig. 4.11). Both upper and lower detectors have a size of 2048 × 1034 pixels, and the center of the field of view will be at ~260 pixels on the y-axis of the upper "master" CCD for unbinned SR mode.

[1]The Very Large Telescope (VLT) on Paranal observatory, Chile, is directed and operated by the European Southern Observatory (ESO). ESO is an intergovernmental, European organisation for astronomical research, whose headquarter is in Garching, near Munich, Germany.

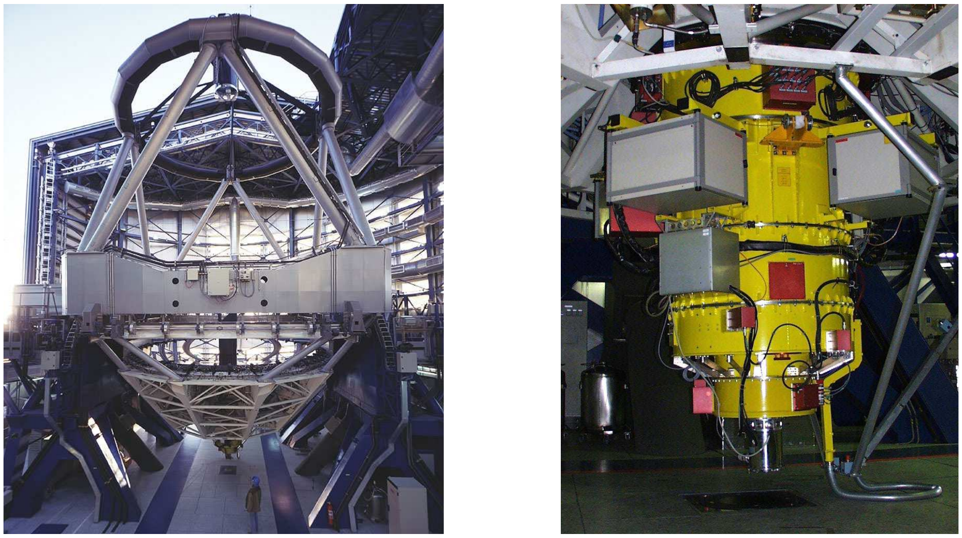

a) b)

Figure 4.8: a) The 8.2 m unit telescope (UT) at Paranal observatory, Chile. The telescope has an alt-azimuth mount as well as two Nasmyth foci, one Coude focus and one Cassegrain focus. b) The spectrograph FORS placed in the Cassegrain focus of a UT.

The current FORS2 MIT CCD mosaic is in operation since March 22, 2002. Before that, a detector as the one of FORS1 was in place. The new mosaic detector has the great advantage of being more optimized in the IR than the former detector. A comparison of the quantum efficiency (QE) between both the older and the current FORS2 CCDs is shown in figure 4.9. At wavelengths longer than ~ 7000 Å the improvement is notorious. At 8000 Å, for instance, the QE of the current mosaic detector is about 30% higher with respect to the old detector. This has represented a very significant improvement in the quality and deepness of our more recent data compared to the one obtained before the upgrade. This confirms the good capabilities of FORS2 to study high redshifts galaxies.

From the set of grisms available with FORS, we have used two: the 150I and the 300I. The choice of the grism is based on the target selection criteria, and therefore depends on the characteristics of the target and on the scientific goal of the observations. I will go back to this point later in chapter 5. The response curve of both grisms is shown in figure 4.9. The main characteristics of each grism are summarized in table 4.4.

In general, every grism has an associated order-separating filter, which is intended to avoid contamination in the spectrum due to the second order. These filters have also the disadvantage of intruducing a sharp cutoff

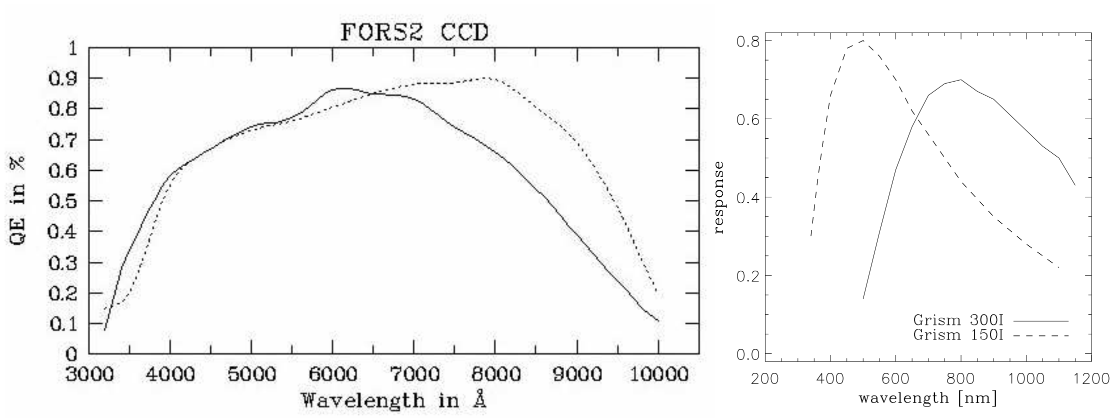

a) b)

Figure 4.9: a) Improvement of the FORS2 CCD MIT mosaic detector compared to the former detector. The solid line indicates the quantum efficiency (QE) of the old CCD while the dashed line clearly shows the enhancement in the detector response at wavelengths greater than 7000 Å. For instance, the QE at 8000 Å increased by about 30% with the upgrade. b) Comparison between the grisms 150I and 300I is presented. The 300I grism has a better response over 7000 Å.

Grism	λ_{cent} (Å)	range (Å)	dispersion (Å/pix)
FORS1			
150I	7200	3300 - 6500	5.52
300I	8600	6000 - 11000	2.59
FORS2			
150I	7200	3300 - 6600	6.9
300I	8600	6000 - 11000	3.24

Table 4.4: Main characteristics of grisms 150I amd 300I, corresponding to the standard resolution (SR) mode. The spectral range quoted for every grism corresponds to the first order for a slit located in the center of the field. In the case of the grism 150I, the red end of the range corresponds approximately to the wavelength at which the second order overlap occurs.

at the blue end of the spectral range. Being aware of possible 2nd order contamination, in most of the exposures we decided not to use such a filter in order to gain spectral coverage in the blue region. The most important and crucial part is to define the target candidates, i.e., objects on which one should put a slit. This selection will depend, as already mentioned, mainly on the photometric characteristics of the objects to be observed. The existence of other kind of data, as for example X-ray, or just visual inspection can be used to drive the final selection. The scientific objects that I was interested in and the appropriate selection criteria associated to them will be treated in detail in section 5.2.3. Multi-Object Spectroscopy observations with FORS can be carried out in two different modes [2]. The first mode, called MOS as well, is available with both FORS1 and FORS2. This mode consists in a movable blade system, which provides a maximum number of up to 19 slits per mask. Another mode, only available with FORS2 is the so called MXU mode. MXU is an acronym for Mask eXchange Unit, storage unit holding up to 10 masks and built into the top section of FORS2. The masks are laser-cut black painted stress relieved invar sheets of 0.21 mm thickness. The importance of the MXU mode is that it allows to have up to about 40 slits per mask, which turns out to be very useful to study galaxy clusters, for instance. These masks are prepared with the help of a special software, FIMS [3] (FORS Intrumental Mask Simulator), developed at the European Southern Observatory (ESO). The mask design requires the use of input images with an astrometric accuracy better than 1/6 of the slit width all over the field of view. Typical slit widths are of the order of 1 arcsecond. Therefore, the use of pre-imaging obtained with FORS is highly recommended. Images of the region of the sky of interest obtained with other instruments have to be registered onto the FORS pre-image previous to the use of FIMS.

FIMS is then employed to create a file containing the position and the dimensions of every slit. This file will be used to create physically the masks at the observatory. The graphical interphase of FIMS displays the image of the scientific target and overlays the exact position of the slits on it. The images are oriented with the North up and the East to the left. The mask layout can be rotated and shifted in any direction in order to optimize the number of slits according to the distribution of the target candidates. The final orientation and position of the mask, however, has to be set at the beginning, since it is impossible to change it during the positioning of the slits. The mask desing includes the selection of reference stars and some reference slits. Figure 4.10 shows two examples of masks as displayed with FIMS. The image on the left shows a typical MOS mask whereas that on the right shows a typical MXU design.

[2]see FORS1+2 user manual for details (http://www.eso.org/instruments/fors1/userman/index.html).
[3]see FIMS manual for more details (http://www.eso.org/instruments/fors1/userman/index.html).

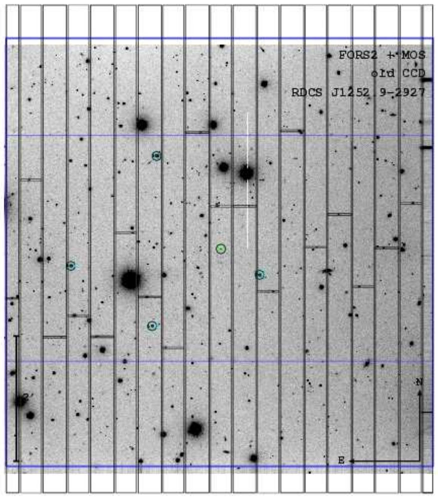

a)

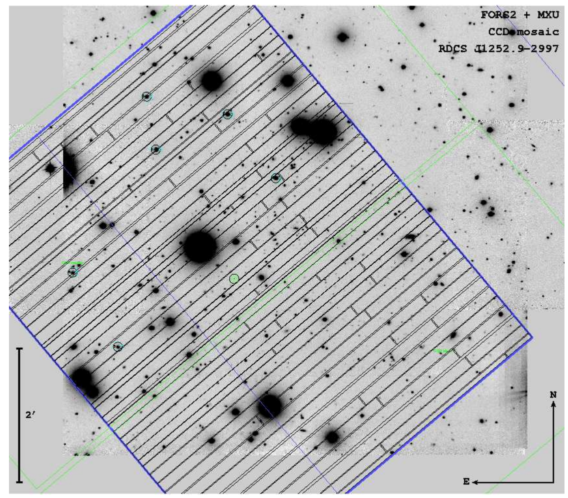

b)

Figure 4.10: This figure shows the final design of two masks, as shown with FIMS. Both layouts are displayed on top of the image used to position the slits. The image astrometric accuracy has to be better than 1/6 of the slit widths. Typical slit widths are of the order of 1". a) The design corresponds to a MOS mask with 18 slits. b) Final design of a MXU mask with 44 slits. Circles in both overlays indicate reference stars.

The observations can be executed in Visitor Mode (VM) or Service Mode (SM) at the VLT. A special software called p2pp [4] (Phase 2 Proposal Preparation), developed at ESO, is used by the astronomer, in which are all the requirements for the observation: coordinates, exposure time, grisms, filters and mask must be provided. One observation consists in a set of scientific and calibration frames. A scientific frame (SCI) is an exposure taken on the target object, in our case a mask on cluster galaxies, as it comes out of the telescope. These raw images have to be corrected before they become scientifically useful. The corrections of the images are done by using BIAS, and spectroscopic dome FLAT exposures, taken with an identical setup as the one used to acquire the SCI image and during the same night of observation. Spectroscopic data also requires the observation of calibraton lamps (WAVE) and spectro-photometric standards (STDs) in order to calibrate the spectroscopic data in wavelength and flux, respectively. There are two sets of WAVE frames, one associated to the SCI images and other associated to the STD images. The details of the correction and calibration of spectroscopic data are explained below.

[4] see http://www.eso.org/observing/p2pp/

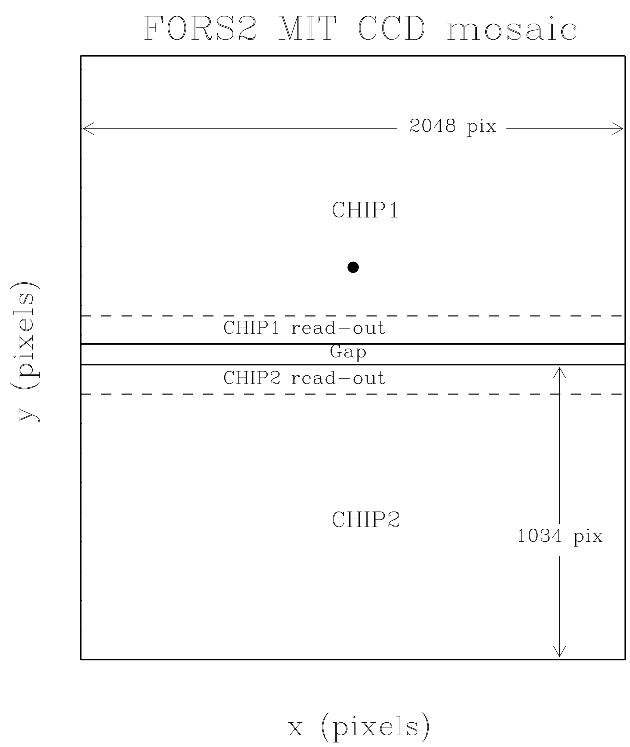

Figure 4.11: Schematic FORS2 2k×4k MIT CCD layout. The detector consists in two chips of 2048×1034 separated by a gap of 480 μm. The pixel size is 15 μm which, in standard resolution mode, projects to 0".25 on the sky. Readout positions are as shown in the figure. The point on the upper "master" chip indicates the center of the field of view, which is located about 260 pixels from the lower edge of the chip.

4.2.2 Data Reduction

Learning the secrets (at least some of them) of the spectra reduction work was one the main tasks of my training on galaxy spectroscopy data analysis. In this section I will concentrate on the reduction of FORS2 data (FORS1 data can be treated in a very similar manner) and I will describe the characteristics and use of a dedicated software I developed at ESO to reduce spectra taken with FORS. This software uses IRAF [5] procedures and specific shell scripts. The first steps in the treatment of the data, as executed by the software, are:

1. All the frames are separated into two main categories: SCIENCE and STANDARD. The first one contains all the SCI exposures together with the associated sets of BIAS, FLAT and WAVE frames. The second category contains the observations of spectro-photometric standards (STDs) and the associated BIAS, FLAT and WAVE frames. Every image in each category is separated according to its chip ID (CHIP1 or CHIP2; see Fig. 4.11). Finally, images are grouped according to mask ID, in order to separate the different masks.

2. The overscan correction is performed on every frame, regardless of category or type. This procedure consists in subtracting the readout level which is measured from the readout regions of every chip. The readouts for FORS2 are shown in Fig. 4.11. After this, the BIAS in every category are separated by chip ID and combined to produce an upper and lower master BIAS (MBIAS).

3. In both categories, every FLAT is bias-corrected by subtracting the corresponding MBIAS frame (upper or lower). Taking into account the mask ID and chip ID, the FLATs are combined to produce upper and lower master FLATs (MFLATs).

4. Once MBIAS and MFLATs are available in every category, SCI, STD and WAVE frames can finally be calibrated. If $IMAGE_{raw}$ represents any uncalibrated SCI, STD or WAVE image of any chip ID, then the final calibrated image, $IMAGE_{calib}$, will be obtained as:

   $$IMAGE_{calib} = \frac{IMAGE_{raw} - MBIAS}{MFLAT}$$

   This is done for both chip IDs separately in both categories. In the SCIENCE category different masks are processed with their corresponding MFLAT frames.

[5] Image Reduction and Analysis Facility. See http://iraf.noao.edu/iraf-homepage.html.

5. Finally, both CHIP1 and its corresponding CHIP2 are merged to form a single frame. This is procedure is carried out automatically with the FSMOSAIC tool of FIMS.

The final result of the steps above mentioned is shown in figure 4.12. The image to the left shows a corrected FORS1 (or the former FORS2) MOS frame. The image to the right, on the other hand, shows a corrected FORS2 MXU exposure. The fact that the MXU mode provides a larger number of slits compared to the MOS mode can clearly be seen. The gap of the CCD MIT mosaic once the two chips are merged (see also Fig. 4.11) can also be seen.

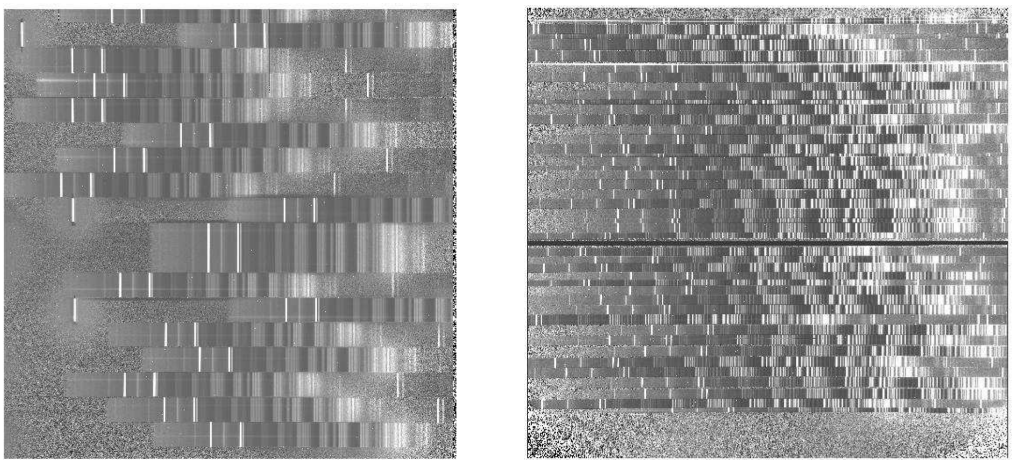

a) b)

Figure 4.12: a) Final processed MOS frame. b) MXU final processed and merged image. Both MOS and MXU exposures have been BIAS and FLAT corrected and correspond to the same designs shown in Fig. 4.10.

The next stage is the extraction of the spectra. Let us supose that we have observed only one mask and that N exposures were obtained. By using the information in the header of the images, the position of every slit on the MXU mask can be computed and all the slits extracted automatically. For every slit, there will be N slit frames that will have to be combined. One of such extracted slit frames is shown in figure 4.13. In the figure, the dispertion axis is horizontal and the spatial axis vertical. The object spectrum can be seen at the middle of the slit, while the arrow indicates the 6300 Å sky line as a reference. By using standard IRAF tasks, the software does the sky subtraction, the fringe suppression, the registration and final combination of all N slit frames. The fringing pattern created by the interference of bright OH sky lines within the detector has a major impact in the red part of the spectrum beyond 7500 Å. In order to remove this effect, several exposures with offsets along the slit (dithering) are needed. The fringe suppresion routines implemented in the software are those in BOGUS [6], a piece of IRAF software developed by D. Stern, A.J. Bunker and S.A. Stanford. Although in the former FORS2 detector the fringing contamination was quite significant, in the new FORS2 MIT CCD mosaic the fringe amplitude has been found to be $\sim 5\%$ in the worst cases. In our data, the fringing of FORS2 spectra is hardly visible. A final reduced slit ready for the extraction of the object spectrum is shown in figure 4.14. The 6300 Å sky line residual is indicated as reference and the presence of an [OII] emission line in the spectrum of the object is visible.

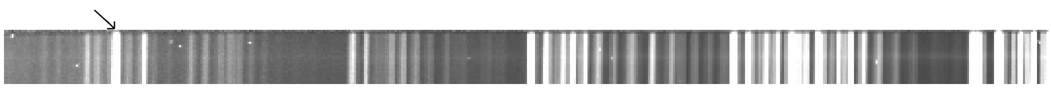

Figure 4.13: Typical slit frame stracted from a multi-object mask. The dispersion axis is horizontal and the spatial axis vertical. The trace of the galaxy can be seen in the middle of the slit, under the dominant sky contamination. The arrow to the left shows the 6300 Å sky line as a reference. The wavelength range shown here is 6050-8500 Å.

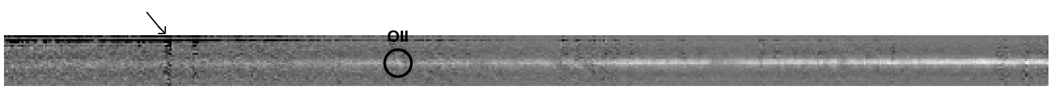

Figure 4.14: Final slit frame after sky substraction, fringe suppression and combination of dithered exposures corresponding to the same object in figure 4.13. The portion of spectrum shown here covers a spectral range from $\sim$ 5900 to 8400 Å. The residuals of the sky line at 6300 Å are indicated with an arrow. An emission line feature in the galaxy spectrum, due to [OII](λ3727), is visible at about 6850 Å. At a first glance one can see the decrease in flux towards the blue part of the spectrum, suggesting an early type for the galaxy.

The extraction of the trace of the object in the slit shown in figure 4.14 requires to fit the center of the object's spatial profile along the dispersion

[6]BOGUS is available on line at http://zwolfkinder.jpl.nasa.gov/s̃tern/homepage/bogus.html

axis. In general, the trace of the object is not parallel to the theoretical dispersion axis. This can be due to distortions produced by the optical system and by differential atmospheric refraction effects. A polynomial fit is performed to determine the trace position, and the resulting solution is then applied to extract the object spectrum and the calibration arc spectrum from the corresponding WAVE slit. The calibration arc spectrum associated to the object in figure 4.14 is shown on the left in figure 4.15. To the right, the corresponding identification atlas is shown. By comparing the observed arc spectrum with the one in the reference atlas, the transformation that allows to go from pixel coordinates to wavelengths can be computed. This dispersion solution is then applied to the corresponding extracted spectrum in order to calibrate it in wavelength. Typical rms residuals values obtained for the dispersion solution are 0.07 Å. Differences between the actual dispersions and the values quoted in the last column of table 4.4 are between 1% and 2%.

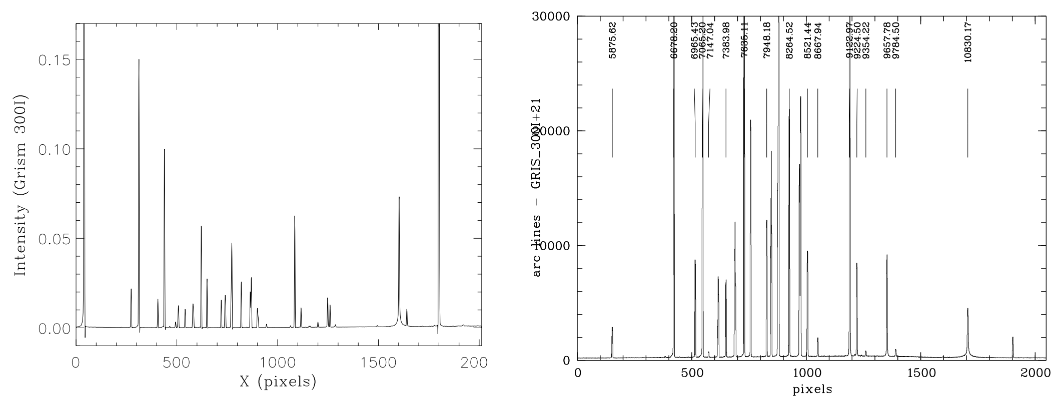

a) b)

Figure 4.15: a) Calibration arc spectrum taken with the 300I grism and a ArHeNe lamp. The x-axis is in pixels. b) Identification spectrum for the 300I grism showing Argon, Helium, and Neon lines. The comparison between both spectra allows to find the dispersion solution, which gives the transformation from pixel coordinates to wavelength coordinates. A polynomial solution, with rms residuals of ~ 0.07 Å is applied to the stracted spectrum in order to calibrate it in wavelength.

The next stage in the data reduction corresponds to the calibration in flux of the scientific spectrum. Spectroscopic observations of spectrophotometric standards are then used to accomplish this task. Some stars observed in our program are Feige56, Feige110, LTT7379 and LTT7987

(Hamuy et al. 1992, 1994)[7]. The software carries out the reduction of the spectro-photometric standad spectrum in the same way as with the scientific targets. The trace of the standard is extracted and wavelength calibrated. After this, the spectrum is compared to tabulated data for the same star, which contains its observed flux in units of $erg\ cm^{-2}\ s^{-1}$ Å^{-1}. Here, the airmass at mid-exposure of the observed standard and the appropriate extinction correction are used to compute a sensitivity function. Every scientific spectrum is then devided by the corresponding sensitivity function to obtain the final flux calibrated SED. An absolute flux calibration of the data is always difficult to obtain; however, in our case, we are interested only in a relative flux calibration. Figure 4.16 shows the final extracted wavelength and flux calibrated spectrum of Fig. 4.14. The already observed [OII](λ3727) emission line can clearly be identified in this spectrum. The prominent 4000 Å break together with the strong Ca II K (λ3934) and H (λ3969) absorption features are characteristic of an early type galaxy. The [OII] line would suggest that this object is an Sa galaxy, and that the [OII] emission would come from the disk surrounding the central bulge, where star formation takes place (the [OII] line is a tracer of the star formation activity in a galaxy).

4.2.3 Measuring redshifts

The final step in the data reduction process is to obtain the redshift of the object. Eq. (1.13) can be directly used to compute the redshift, for instance, of the object shown in Fig. 4.16. We only need to measure the observed wavelengths of some prominent features, in this case the Ca II lines or the [OII] line. The most direct way to obtain these numbers is by doing a gaussian fit of the line profile. The center of the gaussian is then used as the wavelength of the line. Measuring the wavelength of the [OII](λ3727) line and the Ca II K (λ3934) and H (λ3969) features in the spectrum of Fig. 4.16 gives respectively λ_{OII}=6849.6 Å , λ_K=7234.3 and λ_H=7299.2. Eq. (1.13) will thus yield $z_{OII} = 0.8377$, $z_K = 0.8391$ and $z_H = 0.8393$. The mean of these values turns out to be $\bar{z} = 0.8387$.

Another way to obtain the redshift of the same galaxy is by a cross-correlation technique (e.g., Tonry & Davis 1979). This technique assumes that the galaxy spectrum is the convolution of a stellar spectrum with a gaussian which describes the line of sight velocity dispersion of the galaxy stars. Cross-correlating a template spectrum with the galaxy spectrum then produces a function with several peaks. Stronger peaks indicate better correlation between the template and the observed spectra. Peaks in the cross-

[7]The complete list of spectro-photometric standard stars normally used with FORS2 can be found at http://www.eso.org/instruments/fors1/FORS2_Std.html

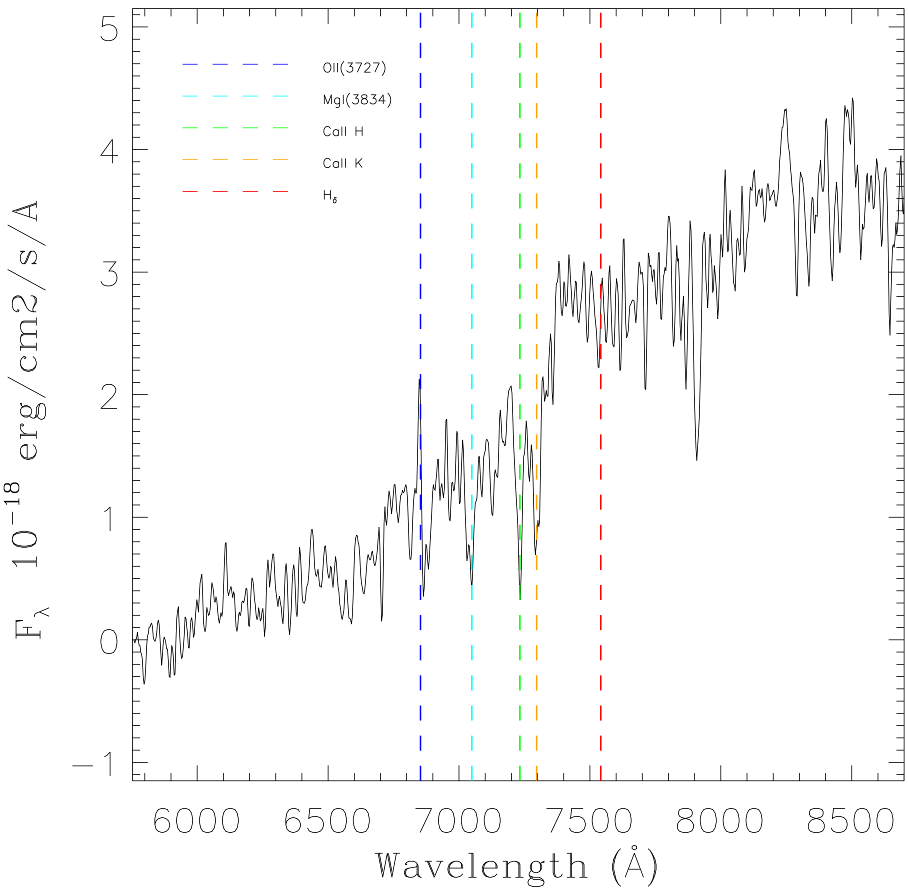

Figure 4.16: Final spectrum, calibrated in wavelength and flux. This spectrum corresponds to the object firstly shown in figure 4.13. Main spectral features are indicated. Note the OII (λ3727) line at $\sim$ 6850 Å indicating a redshift of $z \sim 0.838$. Ca II K (λ3934) and H (λ3969) lines and the 4000 Å break are clear.

correlation function are identified and fit by parabolas to obtain their position and width and hence the redshift and velocity dispersion of the galaxy respectively. In the present work, the elliptical and Sa templates of Kinney et al. (1996) have been the most used to estimate the galaxy redshifts.

Detailed information about CCD data reduction and spectroscopic data reduction using IRAF can be found in Wells (1994), Massey, Valdes & Barnes (1992) and Massey (1997).

Chapter 5

Galaxy populations in high-z clusters

How and when are galaxies formed? These are outstanding questions in modern cosmology. Throughout the previous chapters I have introduced the most important characteristics and properties of galaxies, without really developing the question of their formation and evolution. The present chapter is devoted to the study of galaxy populations in high redshift clusters of galaxies, the major part of my thesis work, aimed at addressing these questions and at casting some light in our understanding of galaxy evolution. As previously mentioned in chapter 1, X-ray surveys have a great impact in cosmology due to their ability in detecting distant clusters, key pieces in the study of the formation and evolution of structures in the universe. In the following sections I will present the science we have carried out so far on two of the most distant massive clusters of galaxies know to date in the southern sky, discovered in the ROSAT Deep Cluster Survey (RDCS; Rosati et al. 1995, 1998), from a multi-wavelength approach.

5.1 Observational background

Understanding the mass assembly history of galaxies is at present one of the hot topics in observational cosmology. The development of more advanced observational techniques and powerful telescopes are allowing the discovery of very distant galaxies (e.g. Steidel et al. 1996, 1999; Dey et al. 1998) and the obtaining of an unprecedented view of the galaxy populations in the distant universe ($z > 1$), a crucial step in the search for the epoch of the first light of galaxies. Part of the evidence indicating evolution in the populations of galaxies have already been introduced in section 1.3.1. Although there is a lot to be learned from late-type galaxies, of course, in what follows (and throughout the next sections in this chapter) I will concentrate the discussion on early-type galaxies, a class of objects that has been the subject of a great number of studies in the last decade since they are the most massive galaxies known and their stellar populations are old.

A comprehensive picture of the problem in question has to include the study of both galaxies in clusters and in the field. The distribution of galaxies out to $z \sim 2.5$ in the K20 survey (Cimatti et al. 2002a, 2002b) as well as the distribution of Extremely Red Objects (EROs; Daddi, Cimatti & Renzini 2000) favors Pure Luminosity Evolution (PLE) models for galaxy evolution, being in disagreement with the predictions of current hierarchical merging models. The surface density of EROs also indicates that the bulk of field ellipticals was already in place at least by $z = 2.5$. At higher redshift, red galaxies with $J - K > 1.7$ are observed to be strongly clustered at redshifts between 2 and 4, with $r_0 \sim 8h^{-1}$ Mpc (Daddi et al. 2003). Daddi and collaborators (2003) conclude that a direct evolutionary trend exists between this population of red galaxies at $z \sim 3$ on one side and EROS at $z \sim 1.5$ and local massive early-type galaxies on the other side. This indicates that early-type galaxies would be already formed by $z \sim 3$. The evolution of star formation in galaxies is another important issue. Local cluster early-types are characterized by old and evolved stellar populations, without signatures of recent star formation. This situation is observed to be however different in field early-type galaxies where evidence for recent star formation activity has been detected within $0.3 < z < 0.8$ (Menanteau, Abraham & Ellis 2001; Treu et al. 2002). Furthermore, early-type galaxies in local clusters show remarkable regularities in their spectro-photometric properties, as the fundamental plane (FP) and the color-magnitude (CM) diagram already introduced in section 1.3.1. Although the CM is characteristic of galaxies in clusters only, a FP for field ellipticals is also observed (e.g. Treu et al. 2001). All these observations indicate the impact of the environment on the observed properties of galaxies, and since clusters represent special regions in the universe and can be detected at high redshift they constitute ideal laboratories to study these environmental effects in the properties of galaxies.

5.1.1 Scenarios of galaxy formation and evolution

Let us shortly rewiew the two main scenarios of early-type galaxy formation and how the observed regularities in their properties, in particular the CM diagram, can be used to constrain these models. Following Bower et al. (1999), there are two main pictures that have been proposed to explain early-type galaxy formation: the so called Classical Model (e.g. Eggen, Lynden-Bell & Sandage 1962; Larson 1975; Arimoto & Yoshii 1987) and the Hierarchical Model based on CDM models (Kauffmann 1996; Kauffmann & Charlot 1998a, 1998b).

The Classical Model is illustrated in figure 5.1. The collapse of a proto gas cloud may be initially fragmented. Star formation goes quickly at the beginning and is unchecked until the first massive stars evolve to the supernova phase. Star formation can then continue only if the already formed dark matter halo is massive enough to retain the gas against the increasing pressure of supernova winds. The mass of the halo will thus determine how long the star formation activity will last until supernova winds have expelled all the gas, leaving a spheroidal star system. Eventually, a gas disc is subsequently accreted over a prolonged period if the galaxy resides in a low density environment (see Bower et al. 1999).

In the Hierarchical model also ilustrated in figure 5.1, on the other hand, there is no intrinsic difference between star formation occuring at different epochs. All galaxies are similar star forming systems in an equilibrium state between the inflow of gas and the rate at which it is either consumed or expelled out of the galaxy by supernova winds. The morphological appearance will change due to mergers of individual sub-components to form larger mass units, the environment playing an important role (see Bower et al. 1999).

As pointed out by Bower et al. (1999), the key difference between both models is that while morphology is set at an early time in the Classical model, morphology is a fluid quantity in the Hierarchical model that can change in both directions.

The patterns of regularities present in early-type galaxies at all redshifts represent fundamental characteristics that can be used to constrain the above mentioned scenarios. In particular the tight CM relation observed in local (Bower, Lucy & Ellis 1992; Terlevich, Caldwell & Bower 2001) and distant (Stanford, Eisenhardt & Dickinson 1998; Rosati et al. 1999; van Dokkum et al. 2001; Stanford et al. 2002; Blakeslee et al 2003; Lidman et al. 2003, and references therein) cluster early-type galaxies indicates that in clusters these galaxies are formed at redshifts even greater than $z = 2$, after an initial burst of star formation followed by PLE. The scatter about the CM relation and the slow steady evolution in the colours and luminosities of early-type galaxies are explained by the great age of the bulk of the stars, thus favoring the Classical picture presented above. The formation of early-types through mergers at redshifts below one as proposed in the Hierarchical model cannot be excluded by the observed CM relation in local clusters; however, the amount of merging and star formation that can take place are limited by the observed amount of scatter and the slope of the CM relation (Bower, Kodama & Terlevich 1998). In fact, the possibility that massive ellipticals are formed at redshifts well below 1 through merger events, in accordance with the Hierarchical picture, is also indicated by some observations (Van Dokkum et al. 1999), although in general this picture has recently been ruled out by the results from the K20 survey (Cimatti et al. 2002a, 2002b).

The CM relation represents a relation between the dynamical mass of a galaxy and the average metallicity of its stellar population (Faber 1973; Kodama & Arimoto 1997; Stanford, Eisenhardt & Dickinson 1998). In hi-

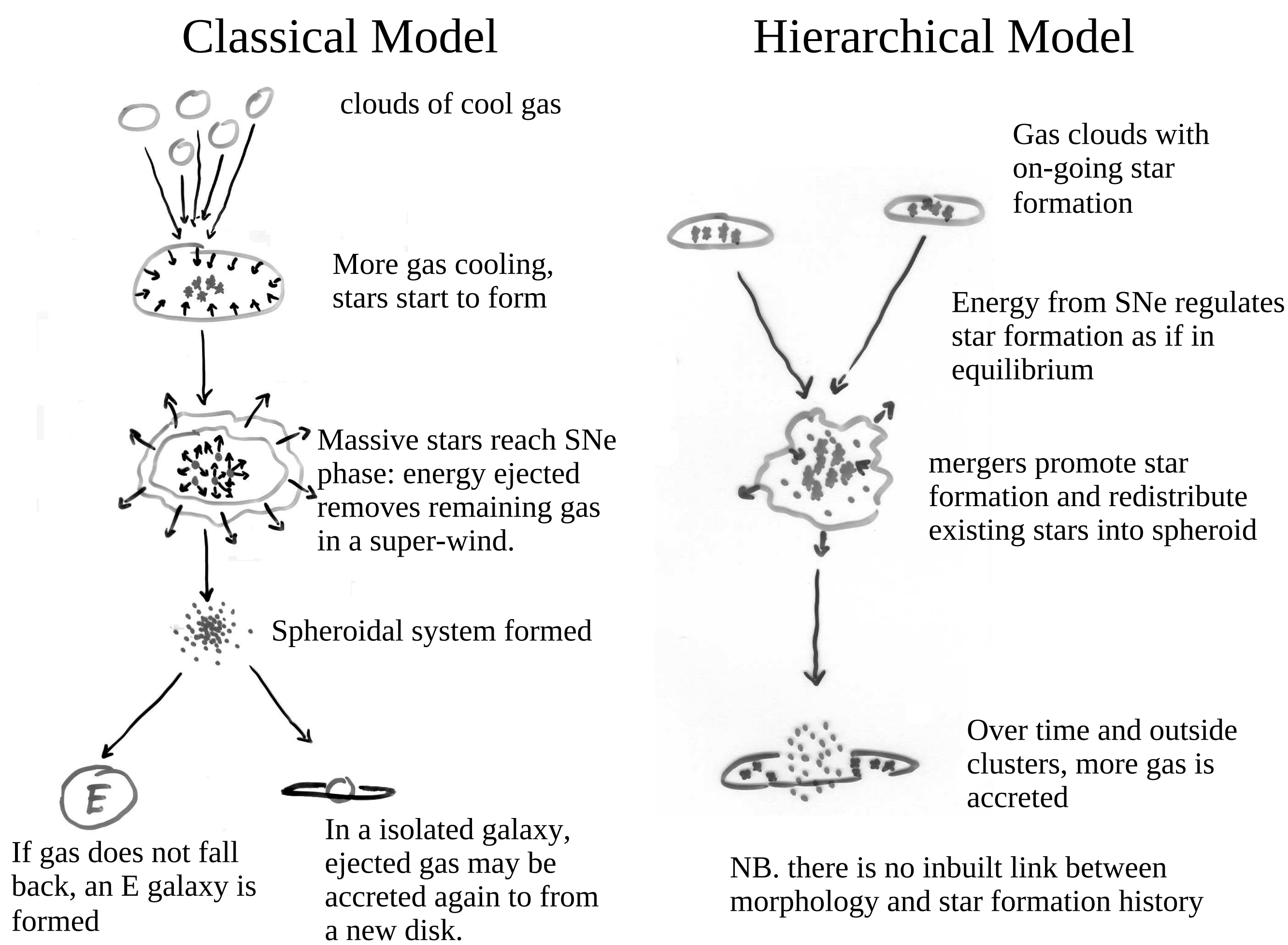

Figure 5.1: This figure shows the two dominant scenarios to describe early-type galaxy formation: the classical and the hierarchical model. In the Classical model, the spheroidal component is formed in a rapid phase at an early time, and the gas disc is subsequently accreted over a prolonged period if the galaxy resides in a low density environment. In the Hierarchical model, galaxies have no fixed morphology, but can cycle between the different morphological types depending on the number and strength of interactions and mergers (from Bower et al. 1999).

erarchical models, large ellipticals are formed from large spirals, which are better able to retain the metals that result from stellar evolution (Kauffmann & Charlot 1998b). Similarly, in the Classical model, larger ellipticals are better able to retain their metals. Although age differences can be used to explain the slope of the CM relation at low redshifts, the slope and the CM relation itself are lost by $z = 0.2$ (Kodama & Arimoto 1997) if age is the sole reason for the slope.

Studies of clusters up to $z \sim 1$ also show evolution in the galaxy LF (De Propris et al. 1999; Massarotti et al. 2003; Toft, Soucail & Hjorth 2003) and the FP (van Dokkum et al. 1998b, van Dokkum & Stanford 2003). Early-type galaxies in rich galaxy clusters are uniformly becoming both brighter and bluer as they become younger.

All these studies show that studying clusters at redshift similar or greater than 1 is the most direct means to make a significant step forward on the subject, providing conclusive tests for these competing scenarios. This has thus motivated the work that I will present in the following sections.

5.2 Scientific targets and data set

In the spirit of the last section, we have carried out an unprecedented and comprehensive spectroscopic and photometric survey with the ESO VLT of two of the most distant massive clusters known to date in the southern sky: RX J0152.7-1357 ($\alpha_{J2000} = 01^h52^m42^s$, $\delta_{J2000} = -13^o57^{'}00^{''}$) at $z = 0.837$ and RDCS J1252.9-2927 ($\alpha_{J2000} = 12^h52^m48^s$, $\delta_{J2000} = -29^o27^{'}00^{''}$) at $z = 1.237$. Both clusters were selected as extended X-ray sources in the ROSAT Deep Cluster Survey (RDCS, Rosati et al. 1995, 1998), which used a wavelet-based algorithm to detect and characterize X-ray sources in 180 ROSAT PSPC archival fields down to a limiting flux $f_{lim}(0.5 - 2\ keV) = 10^{-14} erg\ cm^{-2}\ s^{-1}$ (Rosati et al. 1998).

The VLT data has been obtained as part of the ESO Large Programe LP-166.A-0701 (P.I.: P. Rosati) and the ESO proposal 69.A-0683 (P.I.: P. Rosati), being supported by data coming from other ground and space based facilities. The data in hand for both clusters are summarized in table 5.1. Both clusters have been targeted with Chandra and XMM (Maughan et al. 2003; Rosati et al. 2004). Ground-based photometry in B, V, R, I, J and K have been obtained for RX J0152.7-1357 with Keck, VLT and NTT. On the other hand, the B, V, R, I, z, J and K photometry of RDCS J1252.9-2927 comes from VLT and NTT observations, where very deep imaging in J and K was obtained with ISAAC (Lidman et al. 2003) in very good seeing conditions. These observations are complemented by HST+ACS imaging over a 6'.5 $\times$ 6'.5 area in the r, i and z bands for RX J0152.7-1357 and in the i and z bands for RDCS J1252.9-2927 (see Blakeslee et al 2003). This impressive and large data set is delivering one of the most complete and

Cluster	z	X-ray Imaging	Optical and NIR imaging	Optical Spectroscopy
RX J0152.7-1357	0.837	Chandra (37 ks)	Keck+LRIS : B, V, R, I	VLT+FORS : 19h
			VLT+FORS : R	141 redshifts
			NTT+SOFI : J, K	78 members
			HST+ACS : r, i, z (27 orbits)	
RDCS J1252.9-2927	1.237	Chandra (190 ks)	VLT+FORS : B, V, R, I, z	VLT+FORS : 30h
		XMM (130 ks)	NTT+SOFI : J, K	205 redshifts
			VLT+ISAAC : J ($5\sigma_{lim}$: 25.7AB)	36 members
			: K ($5\sigma_{lim}$: 24.3AB)	
			HST+ACS : i, z (32 orbits)	

Table 5.1: Summary of the data in hand for RX J0152.7-1357 and RDCS J1252.9-2927 .

detailed view of high redshift clusters, a crucial step to understand galaxy formation.

5.2.1 Discovery observations

RX J0152.7-1357 was also discovered independently in the WARPS Survey (Ebeling et al., 2000) and reported in the Bright SHARC survey (Nichol et al. 1999, Romer et al. 2000). This is one of the most X-ray luminous clusters known in the Southern Sky at $z > 0.5$. First measurements with ROSAT and BeppoSAX gave an X-ray luminosity $L_X = (6.8 \pm 0.6) \times 10^{44} h_{50}^{-2} erg\ s^{-1}$ in the 0.5-2 keV band, a gas temperature of $kT \sim 6$ keV and a metallicity of $A \sim 0.5$ (Della Ceca et al., 2000). However, recent observations of this cluster with Chandra and XMM have revealed a complex structure of its ICM (see section 5.3.1) and allowed a more accurate determination of its temperature and metallicity (Tozzi et al. 2003).

RX J0152.7-1357 was spectroscopically confirmed with EFOSC1 at the ESO 3.60-m telescope at La Silla Observatory in November 1996. Spectroscopy of a small number of member galaxies gave a redshift of $z = 0.83$ (Della Ceca et al., 2000), placing RX J0152.7-1357 among the most distant clusters of galaxies known in the southern sky, akin to MS1054-03 (Donahue et al., 1998; van Dokkum et al., 1999).

RDCS J1252.9-2927 was discovered in the = 15.7 ksec ROSAT PSPC field with ID WP300093 at an off-axis angle of 13.9 with 31 net counts, corresponding to a flux of $(2.5 \pm 0.9) \times 10^{-14}$ erg cm^{-2} s^{-1} in the 0.5-2 keV band (see Fig. 5.3-a). A 30 minute I-band image obtained at the CTIO 4-m telescope with the Prime Focus camera in February 1997, revealed only a faint ($I \simeq 21.7$) galaxy pair very close to the X-ray centroid position. As part of a program to follow-up faint RDCS cluster candidates in the near-IR, J and K band imaging was obtained with the SOFI camera at the NTT in November 1998, which showed a clear overdensity of red galaxies with

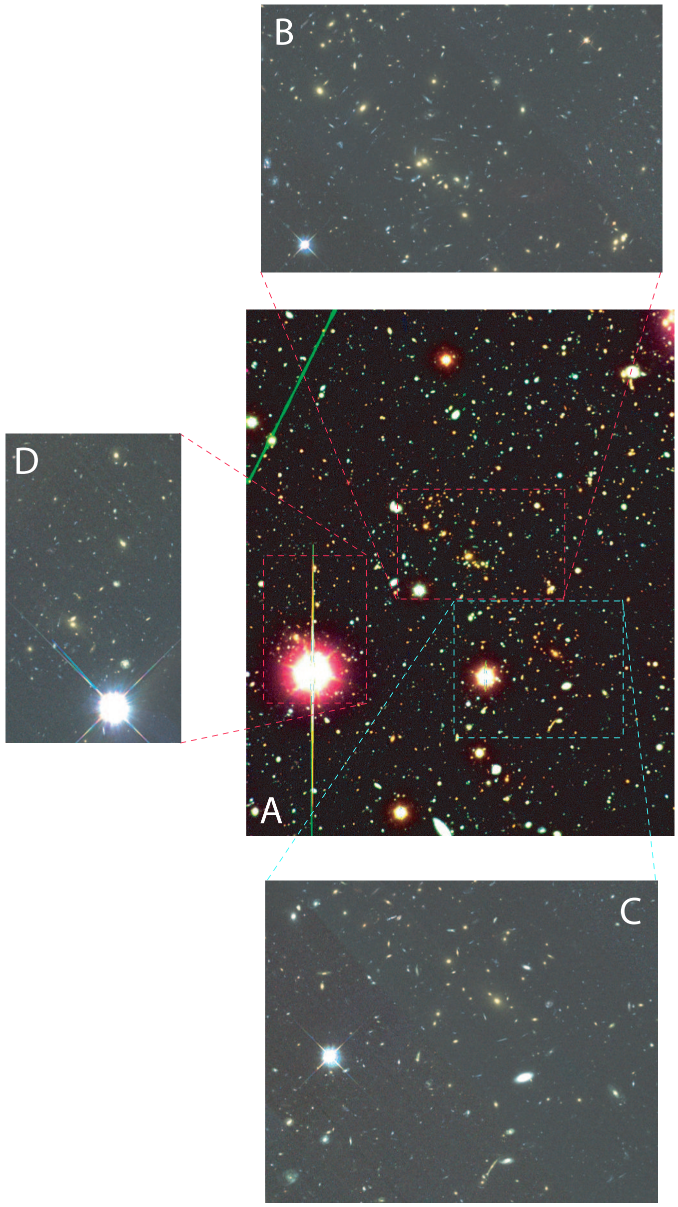

Figure 5.2: RX J0152.7-1357 ($z = 0.837$). A composite Keck image in V, R and I is shown in (A). The field of view is approximately 5 min $\times$ 6 min, and the three main clumps of the cluster are enclosed by the dashed boxes. Detailed views of the Northern, Southern and Eastern clumps are shown in (B), (C) and (D) respectively. These cutouts correspond to a composite HST+ACS image in r, i and z. The ACS data has been kindly provided by the ACS team.

$J - K \simeq 1.9$, typical of early type galaxies at $z > 1$ (see Lidman et al. 2003).

5.2.2 Multi-band imaging

Optical and Near-IR imaging

Optical imaging in different optical bandpasses as well as near-IR imaging have been obtained at VLT, NTT, Keck and HST.

In the case of RX J0152.7-1357 , the optical bands B, V, R and I were observed at *Keck* with the Low Resolution Imaging Spectrometer (*LRIS*; Oke et al., 1995). The seeing corresponding to each band was measured to be 0".86 in V, 1".19 in B, 1" in R and 0".73 in I. The LRIS images cover a region of $4'.9 \times 6'.54$ with a pixel scale of 0".21 pix^{-1}. On the other hand, the near-IR imaging was obtained at the NTT with SOFI. The J and K bands of SOFI were obtained in seeing conditions of 0".95 and 0".94 respectively. SOFI images cover a region of $4'.9 \times 4'.9$ with a pixel scale of 0".29 pix^{-1}. The LRIS and SOFI images thus provided the basis for the photometric catalog used during the subsequent study. The catalog was created with SExtractor (Bertin & Arnouts, 1996), obtaining aperture photometry in all the bands for 1494 objects. These magnitudes were then used to compute colors (see table 5.5). Additional imaging on RX J0152.7-1357 was obtained with FORS at the VLT in the R-band, covering a field of view of 6'.8 × 6'.8. Supporting all these ground based data, observations of RX J0152.7-1357 in the r, i and z bands with the Advance Camera for Surveys (ACS) aboard the Hubble Space Telescope (HST) have been conducted in the spring of 2002, completing a total of 27 orbits.

Observations of RDCS J1252.9-2927 in the optical have been carried out with FORS on the VLT, covering the B-, V-, R-, I- and z-bands. NTT+SOFI and VLT+ISAAC were used to obtain the near-IR imaging of the cluster. See Lidman et al. (2003; one of the papers in the next chapter) for details on the characteristics and reduction of the near-IR (SOFI and ISAAC) data. The remarkable point here is the exceptionally good quality of the ISAAC data: very deep imaging in J and K_s obtained in $\sim$ 0".4 seeing conditions. The deepness of the ISAAC images reaches 27.7 AB and 24.3 AB (5σ detection) in the J and K_s bands respectively. These observations are also complemented by HST+ACS imaging in the i- and z-bands obtained in 32 orbits during the spring of 2002 (see Fig. 5.4). The characteristics and details of these data are presented in Blakeslee et al. (2003; one of the papers in the next chapter).

X-ray imaging

The improved resolution of Chandra compared to other missions, represents a key ingredient in order to better map and study the structure of the

ICM in distant clusters and compare it with the observed optical galaxy distribution.

Previous images of RX J0152.7-1357 obtained with ROSAT and BeppoSAX (Della Ceca et al., 2000; Ebeling et al., 2000; Romer et al., 2000) first revealed the irregular shape of the X-ray emission suggesting the unrelaxed state of the cluster. However the limited resolution of these satellites could not show the details of the ICM structure and the possible existence of point sources in the cluster field of view. A 37 ksec Chandra pointing observation with the on-board Advanced CCD Imaging Spectrometer (ACIS) I array was performed on this cluster and for the first time, a detailed picture of the X-ray emission of RX J0152.7-1357 was achieved. A complete analysis of the Chandra data is presented in Maughan et al. (2003). Figure 5.7-a shows the Chandra X-ray image while the X-ray iso-contours are shown in Fig. 5.7-b. These contours correspond to 3, 5, 10, 20, and 30 σ over the X-ray background, obtained with a smoothing kernel of 4 arcsecs. The Chandra pointed observation has revealed with great detail the complex structure of the ICM of RX J0152.7-1357 : the emission is highly elongated in the northeast-southwest direction with two major merging clumps forming the central part of the cluster, and a secondary peak, unresolved by previous observations, at about 1 Mpc to the east of the central structure. The excellent resolution of Chandra also revealed the presence of four point sources, resolved for the first time, for which we also obtained spectroscopic information (see section 5.2.3). The two main X-ray peaks are separated by a projected distance of $\sim$ 1.6 arcmin (the centroids as estimated by Maughan et al. 2003 are listed in table 5.2). The third X-ray clump, visible to the east, is separated by $\sim$ 2'.4 from the central structure. At the cluster redshift, 1 arcmin corresponds to 450 kpc for a $\Lambda = 0.7$, $\Omega_M = 0.3$ and $H_0 =$ 70 km s^{-1} Mpc^{-1} universe. These substructures are a clear confirmation of the unrelaxed state of the cluster and of the complexity of its ICM. As pointed out by Maughan et al. (2003), the centroids of the X-ray northern and southern clumps present an offset with respect to the corresponding centroid for the galaxy distribution associated to these clumps; the direction of the offset suggest that both clumps are approaching each other and that the gas is being pushed back due to ram pressure. In addition, some evidence for a possible adiabatic shock front in between these clumps supports the picture that the substructures observed in RX J0152.7-1357 are in an on-going merging process.

X-ray observations of RDCS J1252.9-2927 have been obtained recently with both Chandra (ACIS-I detector) and XMM-Newton (EPIC and MOS detectors), as seen in Fig. 5.3. The details regarding the data obtained and the reduction procedures are presented in Rosati et al. (2004; see next chapter). Both imaging and spectroscopy have been obtained allowing a complete modeling of its X-ray surface brightness together with an unprecedented accuracy in the estimation of its temperature, metallicity, dynamical

Clump	α (J2000)	δ (J2000)	N	kT (keV)	z
North	$01^h\ 52^m\ 44^s.34$	$-13^o\ 57'\ 18''.86$	15	$5.5^{+0.9}_{-0.7}$	0.8377
South	$01^h\ 52^m\ 40^s.01$	$-13^o\ 58'\ 27''.27$	12	$5.2^{+1.1}_{0.9}$	0.8294
East	$01^h\ 52^m\ 52^s.42$	$-13^o\ 58'\ 5''.63$	8	...	0.8473

Table 5.2: Substructure in RX J0152.7-1357 . The temperatures are those in Maughan et al. 2003.

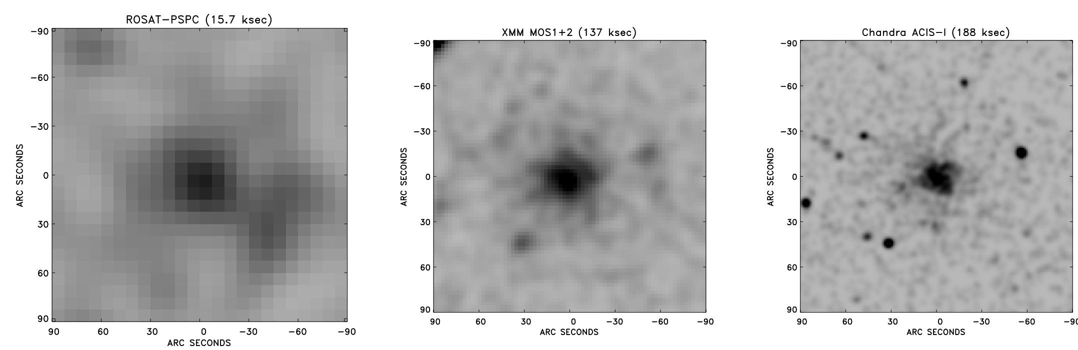

a) b) c)

Figure 5.3: X-ray observations of RDCS J1252.9-2927 (z = 1.237): a) 15.7 ksec exposure obtained with the ROSAT-PSPC. b) 137 ksec exposure obtained from combining XMM MOS1 and MOS2 data. c) 188 ksec exposure obtained with ACIS-I on-board Chandra. The field of view of each image is 180" × 180".

mass and redshift (see Rosati et al. 2004). In contrast to RX J0152.7-1357 , the X-ray surface brightness distribution of RDCS J1252.9-2927 is observed to be more regular, indicating a more advanced state of relaxation compared to RX J0152.7-1357 . Despite this, an E-W elongation in the galaxy member distribution has been identified (see section 5.4.1), coinciding with an apparent comet-like asymmetry of the X-ray emission. Although the relatively low photon statistics of the Chandra data prevent us from further speculating on the physical nature of this feature, this possible E-W elongation of the gas may suggest a more complex dynamical state of the cluster structure (see Rosati et al. 2004).

5.2.3 The spectroscopic survey

The major part of this thesis work has been the direct participation in the spectroscopic survey proposed in the ESO Large Program and follow-up proposal above indicated. The survey is aimed at the identification and confirmation of as many galaxy members as possible in each cluster. The main goals are to make a detailed characterization of the cluster galaxy populations as well as to perform an accurate dynamical study of these high-z clusters. The spectroscopic information is thus combined with high quality optical and near-IR photometry to deliver one of the most detailed views of the galaxy population in distant clusters ever seen. This huge collection of data makes possible to investigate the underlying stellar population of cluster galaxies, including both early-type and late-type systems, out to redshifts $z \sim 1.2$. This makes possible to study the CM relation at such large look-back times providing a robust test of the two afore mentioned scenarios (see section 5.1.1) and to study the population of star-forming members.

The main information concerning the spectroscopic survey on RX J0152.7-1357 and RDCS J1252.9-2927 is summarized in table 5.3. Our extensive spectroscopic survey on both clusters was carried out between December 1999 and February 2003 at the ESO VLT with FORS spectrographs (see section 4.2.1). The observations on RX J0152.7-1357 started in December 1999 and were concluded in August 2002, while the RDCS J1252.9-2927 campaign started in March 2001 and it was concluded in the February 2003 observing run. Observations were conducted in Visitor Mode (VM) and Service Mode (SM).

The strategy employed to select the targets was based on the available photometric data. Early-type galaxies in distant clusters are the reddest and brightest objects in distant clusters, which makes easy their identification. Hence, photometric redshift information as well as color-color diagrams (see section 4.1.4) were used to select early-type and emission line candidates mainly.

In the case of RX J0152.7-1357 , slitlets were placed on candidate objects

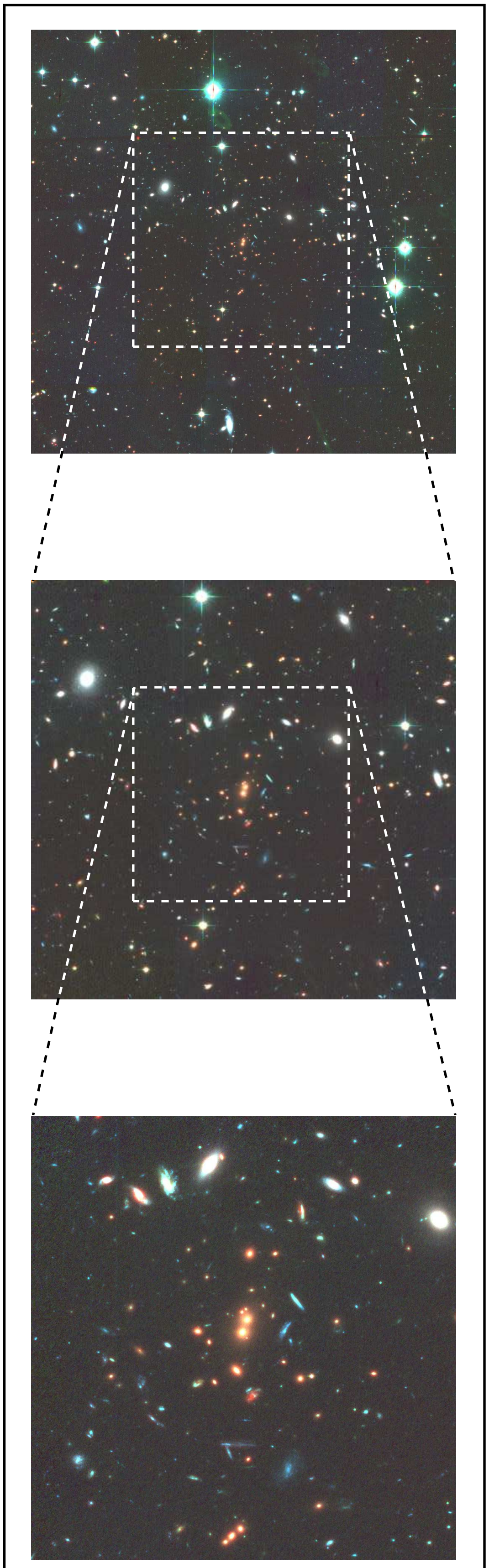

Figure 5.4: A zoom into the central region of RDCS J1252.9-2927 ($z = 1.237$). The field of view (fov) of the image on the top is 4' $\times$ 4', the fov of the middle image is 2' $\times$ 2' and the fov of the image on the bottom is 1' $\times$ 1'. At $z = 1.237$, 2' correspond to 1 Mpc. The color image used to produce this figure was obtained by combining VLT+ISAAC imaging in K_s (20 hr exposure in 0".4 seeing; Lidman et al. 2003) with HST+ACS imaging in i (20 orbits) and z (12 orbits) (Blakeslee et al. 2003). In each image the North is to the right and the East is up.

based on their photometric redshift and magnitude in the R band, taking into account a z_{phot}= 0.7-0.9 range and a limiting magnitude of R=24.

The color-color selection technique turned out to be extremely efficient in the case of RDCS J1252.9-2927 . Here (see Fig. 5.5) the selection of the spectroscopic sample was implemented in order not to introduce biases on the cluster galaxy populations, while minimizing the pollution by field galaxies. This was accomplished by targeting galaxies with $K_s < 21$, $J-K < 2.1$ and $R-K > 3$. Such criteria do not penalize cluster galaxies, since at $z = 1.24$ even the latest types are redder than $R-K = 3$ and early types are bluer than $J-Ks = 2.1$, however field contamination is significantly reduced. This primary selection was complemented by another one on the V-I vs I-z plane in order to improve the selection of Balmer-Break [OII] (λ3727) galaxies. The different color tracks in Fig. 5.5 correspond to different evolutionary models, computed with the most recent stellar library provided by Bruzual & Charlot. Single burst as well as exponential and constant SFR models are shown. The squares indicate spectroscopically confirmed non-emission line members. Circles indicate emission line [OII](λ3727) confirmed members. The emission line object in the upper right side of the plot corresponds to an object located in a region of shallower exposure, so the photometry is less accurate.

An adequate coverage of the $\sim$ 3500-4500 Å region in the rest frame of RX J0152.7-1357 and RDCS J1252.9-2927 (and thus an adequate coverage of the Balmer-break region) is provided by the 300I grism of FORS. At the redshift of the clusters, the Balmer-break is within the 7000-9000 Å range, which is well covered by the 300I grism (see figure 4.9-b). Although with a lower resolution, the 150I grism was also used in order to get coverage at wavelengths below 5000 Å of relatively bright field galaxies during bad seeing conditions. In most of the observations (see table 5.3) no order separation filters were used in order to get an extended coverage toward the blue part of the spectrum.

All the above is taken into account during the mask designing process (see section 4.2.1). Slit widths of 1", 1".2, and 1".4 were normally used, which give spectral resolutions of $\sim$ 13 Å, $\sim$ 16 Å, and $\sim$ 18 Å respectively for the 300I grism, and resolutions of $\sim$ 27 Å, $\sim$ 32 Å, and $\sim$ 38 Å respectively for the 150I grism. A total of 9 masks for RX J0152.7-1357 and 13 masks for RDCS J1252.9-2927 were prepared with FIMS (see section 4.2.1) as shown in table 5.3. During the observations, the telescope was adequately dithered in order to make possible the suppression of fringes on the spectra in the data reduction phase. The unfortunate small or non existing spatial offsets along the slit between exposures for the 7 first masks on RX J0152.7-1357 taught us the importance of this procedure: the presence of

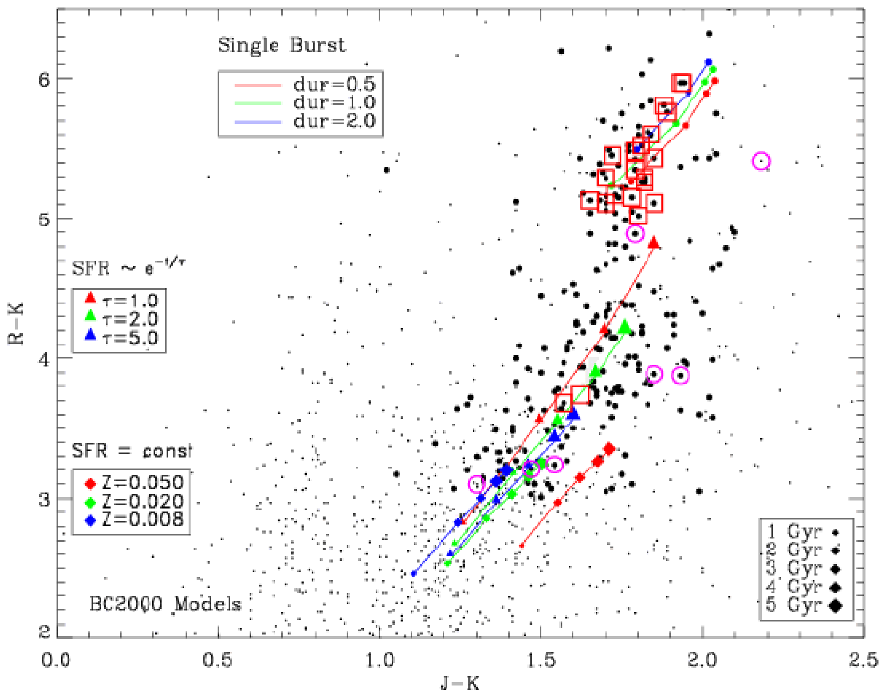

Figure 5.5: The selection of the spectroscopic sample for RDCS J1252.9-2927 ($z = 1.237$) was accomplished by targeting galaxies with $K_s < 21$, $J - K < 2.1$ and $R - K > 3$. This primary selection was complemented by another one on the V-I vs I-z plane in order to improve the selection of Balmer-Break [OII] ($\lambda 3727$) galaxies. The different color tracks in Fig. 5.5 correspond to different evolutionary models, computed with the Bruzual-Charlot stellar library. The squares indicate spectroscopically confirmed non-emission line members. Circles indicate emission line ([OII] $\lambda 3727$) confirmed members.

strong fringes made difficult the identification of spectral features beyond the 7000 Å. The telescope dithering and the suppression of fringes gave optimum results in the case of the last two masks on RX J0152.7-1357 and of the spectroscopy carried out on RDCS J1252.9-2927 . Once the data have been reduced as explained in Section 4.2.2, the identification of spectral features such as the [OII](λ3727) emission line, the CaII H and K absorption lines and the 4000 Å break is normally used to obtain the redshift of the targeted galaxies. Most of the redshifts were obtained by using the cross correlation technique described in section 4.2.3. In particular, I used the IRAF task XCSAO (Kurtz et al. 1992) to determine the redshifts. The typical formal errors in redshifts computed by this task are $\delta z \sim 3 \times 10^{-4}$ which corresponds to velocity errors of the order of 150 km s^{-1}. The observation more than once of some targets in different epochs and on different masks resulted to be useful in estimating the random error in our measurements. Typical values are $\delta z \sim 8 \times 10^{-4}$. A quality flag to every redshift measurement was assigned. This flag can have the values of 0, 1, 2 and 5. A quality flag 0 corresponds to objects with secure redshift, i.e, objects with a high correlation peak or clear spectroscopic features that allow an unambiguous determination of the object redshift. A quality flag 1 designates objects that have been targeted but no redshift could be determined (this is the case of very faint sources). Quality flag 2 are those objects with not secure estimation of the redshift, due to a poor correlation or weak spectral features that can be misidentified. A quality flag 5 is given to those objects that have been observed more than once and have more than one measurement of their redshift. This classification scheme is the one used for both RX J0152.7-1357 and RDCS J1252.9-2927 .

Cluster	Date	Telescope	Instrument	Grism/Filter	Exp. Time	No. Exp	Mask	Fims ID
c0152	Oct 00	UT2	FORS2	300I/none	1800	4	m1(MOS)	mos2.1.c0152
c0152	Oct 00	UT2	FORS2	300I/none	1800	4	m2(MOS)	mos2.2.c0152
c0152	Oct 00	UT2	FORS2	300I/none	1800	4	m3(MOS)	mos2.3.c0152
c0152	Oct 00	UT2	FORS2	300I/none	1800	8	m4(MOS)	mos2.4.c0152
c0152	Oct 00	UT1	FORS1	150I/none	1800	1	m5(MOS)	mos1.54.c0152Ivl
c0152	Dec 99	UT1	FORS1	300I/none	1800	2	m6(MOS)	mos1.23.C0152
c0152	Nov 01	UT4	FORS2	300I/none	1800	6	m7(MOS)	mos2.711.c0152Ivl
c0152	Aug 02	UT4	FORS2	300I/none	2030	4	m8(MXU)	mxu2.42.c0152Ivl
c0152	Aug 02	UT4	FORS2	300I/none	2030	6	m9(MXU)	mxu2.54.c0152vri
c1252	Mar 01	UT2	FORS2	300I/OG590	1500	1	m1(MXU)	mxu2.18
c1252	Mar 01	UT2	FORS2	300I/OG590	1800	9	m1(MXU)	mxu2.18
c1252	Mar 01	UT2	FORS2	300I/OG590	1800	8	m2(MXU)	mxu2.30
c1252	Mar 01	UT2	FORS2	300I/OG590	1800	1	m3(MXU)	mxu2.47
c1252	Mar 01	UT2	FORS2	300I/OG590	1500	1	m3(MXU)	mxu2.47
c1252	Apr 01	UT2	FORS2	300I/none	1800	9	m3(MXU)	mxu2.47
c1252	Mar 01	UT2	FORS2	300I/OG590	1200	5	m4(MOS)	mos2.1178
c1252	Mar 01	UT2	FORS2	150I/GG435	1800	2	m4(MOS)	mos2.1178
c1252	Mar 01	UT2	FORS2	150I/GG435	1500	1	m4(MOS)	mos2.1178
c1252	Mar 01	UT2	FORS2	150I/GG435	1200	1	m5(MOS)	mos2.1180
c1252	Mar 01	UT2	FORS2	150I/GG435	1800	2	m5(MOS)	mos2.1180
c1252	Apr 01	UT2	FORS2	300I/none	1800	9	m6(MXU)	mxu2.58
c1252	Apr 01	UT2	FORS2	150I/none	1800	4	m7(MOS)	mos2.1185

continues ...

Cluster	Date	Telescope	Instrument	Grism/Filter	Exp. Time	No. Exp	Mask	Fims ID
c1252	Apr 01	UT2	FORS2	150I/none	1800	4	m8(MOS)	mos2.1190
c1252	Apr 01	UT2	FORS2	150I/none	1800	2	m9(MOS)	mos2.1196
c1252	Apr 01	UT2	FORS2	300I/none	1800	5	m10(MXU)	mxu2.70
c1252	Oct 02	UT4	FORS2	300I/none	1799	1	m11(MXU)	mxu2.23.c1252mos
c1252	Feb 03	UT4	FORS2	300I/none	1200	11	m12(MXU)	mxu2.66.zk
c1252	Feb 03	UT4	FORS2	300I/none	1200	9	m13(MXU)	mxu2.69.zk

Table 5.3: Summary of spectroscopic observations.

5.3 Scientific results on RX J0152.7-1357 ($z = 0.837$)

5.3.1 Cluster structure

The above picture (see section 5.2.2) based on the projected X-ray emission of the ICM in RX J0152.7-1357 is also confirmed by the results of our spectroscopic survey. The 9 masks observed with FORS at the VLT have yielded 141 secure (quality flag 0) redshifts from which 78 correspond to cluster members within $0.81 < z < 0.86$ [1], confirming the excellent capabilities of VLT+FORS to carry out this kind of study on objects at large look-back time. The number of confirmed cluster members obtained in our spectroscopic survey is one of the largest obtained so far for a cluster of galaxies at high redshift, comparable to the number of confirmed members in MS1054-03, a cluster at redshift $z = 0.833$ (Donahue et al. 1998; Tran et al. 1999; van Dokkum et al. 1999). In addition to this, we have 12 objects at the cluster redshift which were classified as unsecure. The 78 secure cluster members are listed in table 5.5. Fig. 5.6-a shows the histogram (bin size of 0.004 in redshift) of all the secure redshifts obtained in our spectroscopic survey, where the main peak corresponds to RX J0152.7-1357 . A secondary peak in the redshift distrubution is clearly seen at $z \sim 0.64$, where 21 galaxies have been confirmed in the range $0.60 < z < 0.68$. Figure 5.6-b shows the histogram of the 78 cluster members, where the black dashed curve represents a gaussian fit to the total distribution of member galaxies. However a detailed analysis of the data shows that the total distribution of member galaxies is indeed not gaussian. The Shapiro-Wilk test rejected the null hypothesis of a Gaussian parent distribution, with a marginal significance at 92.4% confidence level (Girardi et al., in preparation). The mean redshift of the member distribution is $z = 0.837$, as computed by the biweight estimator (Beers et al. 1990), with a global velocity dispersion $\sigma_v = 1282^{+88}_{-77}$ km s^{-1} (Girardi et al., in preparation). The latter turns out to be the same (within the error bars) as the velocity dispersion measured by Tran et al. (1999) in MS1054-03. This velocity dispersion cannot however be directly used to infer the mass of the cluster by using the virial theorem (see section 1.4.1) because RX J0152.7-1357 is a not a virialized structure. A preliminary formal study of the substructure present in RX J0152.7-1357 has been carried out with the Dressler & Schectman test (Dressler & Schectman 1988), indicating the existence of substructure in the central region and to the east of it with significant probability (Girardi et al., in preparation). Based on the selection criteria indicated above, we have tried to cover uniformly the cluster field of view down to the faintest magnitudes, for which selection biases are not expected. This indicates that the evidence for substructure obtained from the galaxy distribution analysis is real.

Figure 5.6-b also shows the distribution of member galaxies within three

[1] The cluster is observed to be a well isolated structure within this redshift range.

different circular regions, which have been defined according to the three X-ray clumps observed by Chandra (see figure 5.7). The center of each region is listed in table 5.2 and the radii are 5".7, 4".2 and 5".7 for the Northern, Southern and Eastern clumps respectively. These radii have been adjusted in order to encompass most of the corresponding X-ray emission clump. The spectroscopic work on RX J0152.7-1357 has confirmed 15 cluster members belonging to the Northern Clump region, 12 objects with secure redshifts within the Southern Clump region and 8 galaxies at the cluster redshift in the Eastern Clump region.

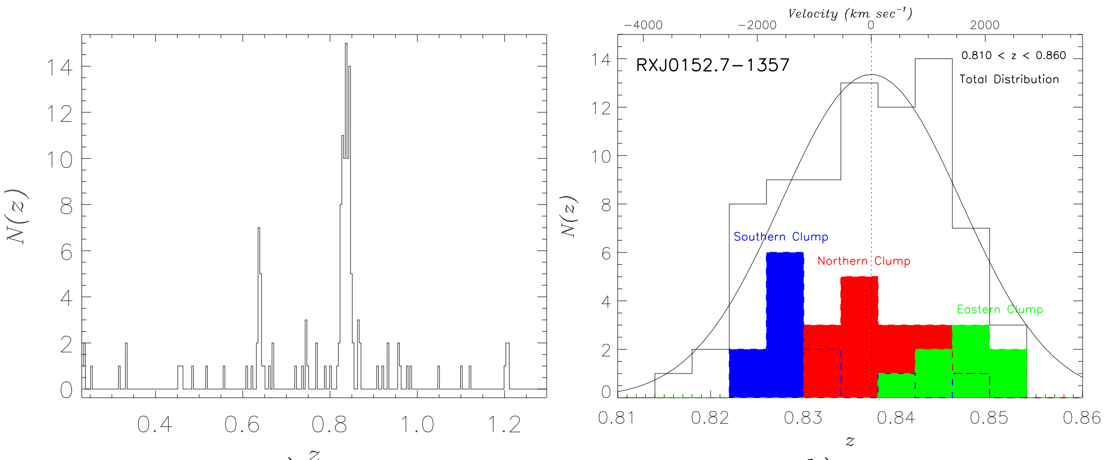

a) b)

Figure 5.6: a) Distribution of the 141 secure redshifts obtained. The main peak corresponds to RX J0152.7-1357 at $z = 0.837$, whereas the secondary peak corresponds to a concentration of 21 galaxies with secure redshift within the interval $0.60 < z < 0.68$. b) Redshift distribution of galaxy members in RX J0152.7-1357 . The color histograms show the distribution of galaxies in the three main clumps: North with 15 members, South with 12 members and East with 8 members. The solid line corresponds to the histogram of the whole set of 78 cluster members. The gaussian fits the overall distribution. The statistical analysis of the data gives a global velocity dispersion of $\sigma_v \sim 1300$ km/s and a median redshift of $z = 0.837$ (see text), with significant velocity substructure.

The projected distribution of secure cluster members, superposed on the Chandra iso-contours, is shown in figure 5.7-b. Member galaxies (filled circles) have been color-coded according to redshift as shown in the color table. The colors demonstrate the three dimensional structure of the cluster. The Southern Clump clearly is at a lower redshift compared to the other clumps, the structure to the East being the most distant among the three, as seen in figure 5.6-b. We conclude that the observed distribution of member galaxies in RX J0152.7-1357 reinforces the above picture shown by the X-ray emission. It is clearly elongated in a northeast-southwest direction, following the X-ray emission, with two merging clumps at the cluster center, in correspondence with the X-ray peaks (see figure 5.7). This suggests that RX J0152.7-1357 is a non-relaxed cluster of galaxies, still in formation through infall along filaments. The center of the Eastern Clump is dominated by galaxies with colors very similar to those of the cluster members, and might be a minor structure falling into the nascent cluster.

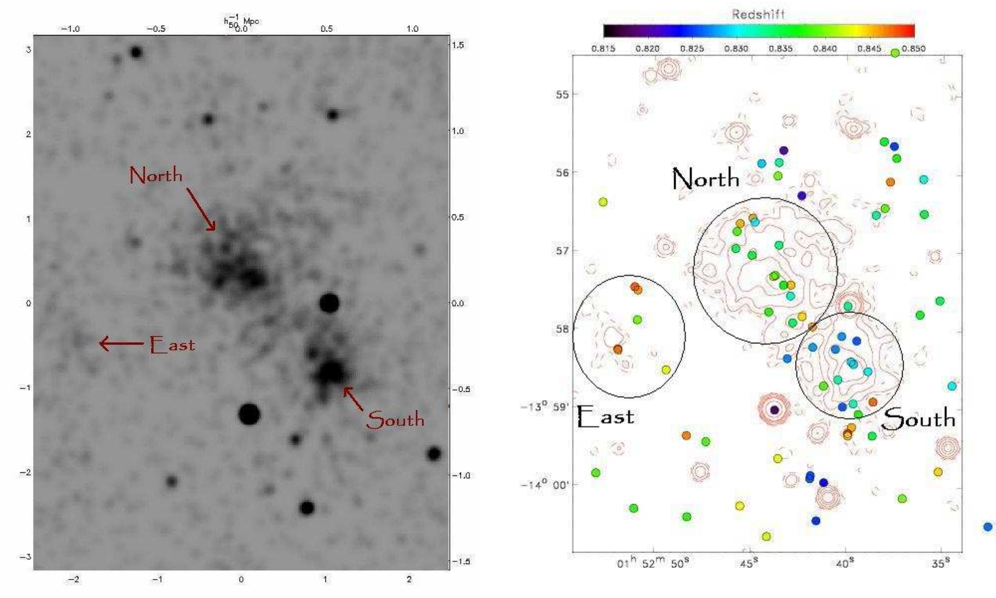

a) b)

Figure 5.7: X-ray and galaxy distributions in RX J0152.7-1357 ($z = 0.837$). The three main clumps in the X-ray and galaxy distributions are indicated by big circles and arrows and are called North, South and East. a) X-ray Chandra image of RX J0152.7-1357 . North is to the top and East is to the left. The two main X-ray blobs can clearly be seen, while the blob to the East presents a weaker intensity. X-ray point sources are also seen. b) The color circles are the 78 member galaxies as seen on the plane of the sky, and individual reshifts have been color-coded as shown in the color table. Chandra X-ray contours (3, 5, 10, 20 and 30 sigma over the background) are also overlaid on the galaxy distribution. From the colors it is clear that the southern clump is at lower redshift than the northern one, the clump to the East being the farthest. This picture indicates that RX J0152.7-1357 is a forming cluster in a merging phase.

ID	α (J2000)	δ (J2000)	R	B-R	R-K	z	Spec. Features
g63	01:52:40.915	-14:00:09.72	22.17	0.78	99.00	1.0027	MgII [OII]
g300	01:52:43.738	-13:59:01.39	21.03	0.15	3.15	0.8178	MgII
g557	01:52:39.780	-13:57:40.10	21.00	1.33	4.81	0.8692	MgII [OII] [OIII]
g1503	01:52:34.676	-13:59:30.54	....	....	....	0.7467	MgII [OIII]

Table 5.4: AGNs detected in the field of view of RX J0152.7-1357 . For the source ID g1503, Keck photometry is not available.

5.3.2 X-ray point sources

Previous observations of RX J0152.7-1357 performed with ROSAT and BeppoSAX (Della Ceca et al., 2000; Romer et al., 2000; Ebeling et al., 2000) were unable to show any possible X-ray point sources that might be contaminating the extended emission observed from the ICM, due to the limited spatial resolution of those satellites. In this respect, Chandra, offers new possibilities to the detection of point sources because of the enhanced spatial resolution of its detectors compared to those of previous missions.

The mask identified as m5 (see table 5.3) was observed in Visitor Mode in October 2000 with FORS1; this mask was designed to target the X-ray point sources resolved by the Chandra pointed observation of the cluster, and the grism 150I was used in order to get a greater wavelength coverage. The Chandra iso-contours as well as the X-ray point sources can be seen in figure 5.7. Only a single exposure of 1800 seconds was obtained, however with a good enough signal-to-noise to allow us to obtain the redshift of the X-ray sources along with several cluster members.

Table 5.4 summarizes the main data for these objects. The first column is the object ID in our photometric catalog. The second and third columns are the coordinates. The next three columns are the magnitude in the R band, the B-R color and the R-K color respectively. Column number seven is the redshift obtained in our spectroscopic follow-up and the last column corresponds to the spectral features identified in the spectrum. Figure 5.8 shows the spectrum of each X-ray point source after flux calibration. Telluric corrections were not applied. The four spectra show prominent and broad MgII emission lines characteristic of AGNs.

From the four AGNs, the one with ID=g300 is within the redshift range defining the cluster members, with a redshift of z=0.8178. It is located $\sim$ 1'.16 to the southeast of the Southern Clump brightest member (ID=g387). A second AGN, ID=557, presents a higher redshift of z=0.8692 which leaves it outside the range defining cluster membership, although its location on the plane of the sky is on the line dividing the two main interacting clumps, not far from both substructures. The other two AGNs are field objects.

It is interesting to note the presence of several AGNs in the cluster field of view and the fact that the two X-ray sources closest to the central region

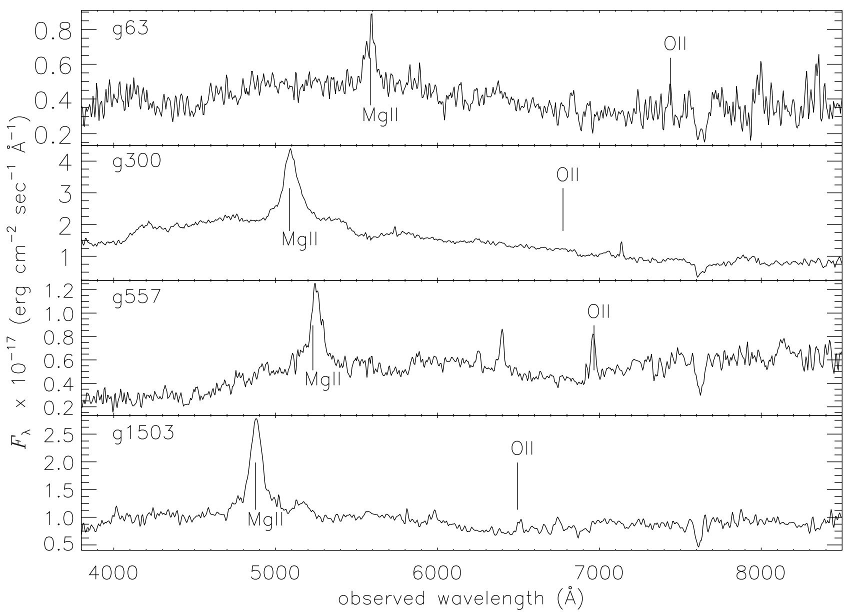

Figure 5.8: Spectra of four AGNs in the field of view of RX J0152.7-1357 . The ID of the AGN is indicated in the upper left corner of every plot. The MgII (λ2798) and [OII](λ3727) features are indicated. The redshift of the sources are, from top to bottom, 1.0027, 0.8178, 0.8692 and 0.7467. The source g300 ($z = 0.8178$) is a cluster member.

between the two main X-ray blobs, are also close in redshift. One of them (g300) is formally a cluster member and the other one (g557) is at a distance $\Delta z = 0.032$ from the median redshift of the cluster. These observations are thus consistent with the picture in which AGNs are considered as tracers of large scale structures in the universe (e.g., Gilli et al. 2003), however more AGN identifications around clusters are needed to firmly establish this.

5.3.3 The Color-Magnitude diagram in RX J0152.7-1357

The photometric catalog obtained for RX J0152.7-1357 from the LRIS and SOFI imaging (see section 5.2.2) is the one I used to compute the color-magnitude diagrams shown in figure 5.9. The photometry however is of inferior quality compared to the one obtained for RDCS J1252.9-2927 (Lidman et al. 2003; Blakeslee et al. 2003). The photometric catalog of the 78 cluster members is presented in table 5.5. The -1 values of the catalog correspond to objects which have a spectroscopic redshift but do not have photometry. This is due to the fact that the field of view delivered by the Keck images is smaller than the field of view of FORS and therefore, the photometric catalog does not cover the full area used for spectroscopy. Eleven out of the 78 member galaxies do not have color photometry, and therefore, the CM plot is limited to only the cluster members with available photometry.

The results are shown in figures 5.9 and 5.10. In all the CM diagrams shown in figure 5.9 a red sequence is well defined, in agreement with similar studies carried out in clusters a high redshift (e.g, Stanford, Eisenhardt & Dickinson 1998; Rosati et al. 1999; van Dokkum et al. 2001; Stanford et al. 2002; Blakeslee et al 2003; Lidman et al. 2003). In figure 5.10-a the R-K vs K CM diagram of the spectroscopic members is presented, while Fig. 5.10-b shows the V-R vs R-K Color-Color diagram of these objects. In both figures the filled red circles are non-emission line cluster members and filled green circles are emission line members.

Despite the scatter in the CM relation, which is in part due to the shallowness of our ground based photometry, a well defined red sequence can be seen at magnitudes brighter than 18 mag in the K-band. The HST+ACS photometry in 3 bands (r, i and z), already in hand, will be a substantial step forward in estimating more accurately the scatter and slope of the CM relation in RX J0152.7-1357 . Nevertheless, a rough linear fit of the data within the interval $14 < K < 18$ was computed and is indicated by the solid red line. Also plotted are the predicted CM relations at redshift $z = 0.8$ for passively evolving early-type galaxies formed at redshifts z_f=2, 3 and 5, computed by Kodama & Arimoto (1997) and kindly provided by T. Kodama. Despite the dispersion in the data points and the small separation between models, the linear fit and the distribution of the data on the bright part of the diagram are consistent with early-types in RX J0152.7-1357 being formed at redshifts similar or greater than 2. The existence of the red sequence at this redshift also supports the interpretation of the CM diagram as a correlation between galaxy mass and metallicity (Kodama & Arimoto 1997), and the population of objects with colors R-K $\sim$ 5, mainly dominated by k type galaxies, is consistent with PLE models of early-types formed at high redshift. An important point in favour of the Classical picture of galaxy formation (see section 5.1.1).

At this point, an interesting issue arises, which is the existence of about a tenth of galaxies with on-going star formation (clear emission lines in their spectra), located in the red sequence of the CM diagram. As an example, four of these galaxies are shown as filled blue circles in Figures 5.10-a and 5.10-b and their IDs in our photometric catalog are also indicated. These galaxies have red colors as it can be seen in Fig. 5.10-b. The fact that these [OII] red galaxies are close to the early-type galaxy sequence reinforces a formation redshift $z_f > 2$ for the bulk of the stellar population in their bulges.

5.3.4 Spectroscopic classification

The high quality spectra obtained for RX J0152.7-1357 with the VLT have allowed us to classify spectroscopically all 78 cluster members according to the classification scheme defined by Dressler et al. (1999, and references therein). This classification is based on the equivalent width (EW) of the [OII](λ3727) emission line and the EW of the H_δ(λ4101) line, both used as diagnostic spectral features of current and recent star formation in distant galaxy spectra respectively (see chapter 4). The classification consists of 10 spectroscopic classes: k, $k + a$, $a + k$, $e(c)$, $e(a)$, $e(b)$, $e(n)$, e, ? and CSB (photometrically defined starburst). A detailed description of every class as well as their physical interpretation is given by Poggianti et al. (1999). A representative spectrum of each class is shown in figure 5.11. The classification goes from early-type galaxies (corresponding to the k type) up to late-types (corresponding to starburst e(b) and e(n)).

At the cluster redshift of $z = 0.837$, the H_δ feature falls in the observer frame at λ=7534 Å, which is close to the telluric A band at $\lambda \sim$7600 Å. For this reason, a telluric correction was applied to the spectrum of each galaxy member. This correction was carried out with standard IRAF procedures. The resulting EWs and final classification of the 78 members are presented in table 5.5.

The resulting spectroscopic classification has then been combined with the color information available in order to investigate the correlations between galaxy color and spectral class. Also the distribution of the different spectral classes on the plane of the sky is studied. The main results are shown in figure 5.12.

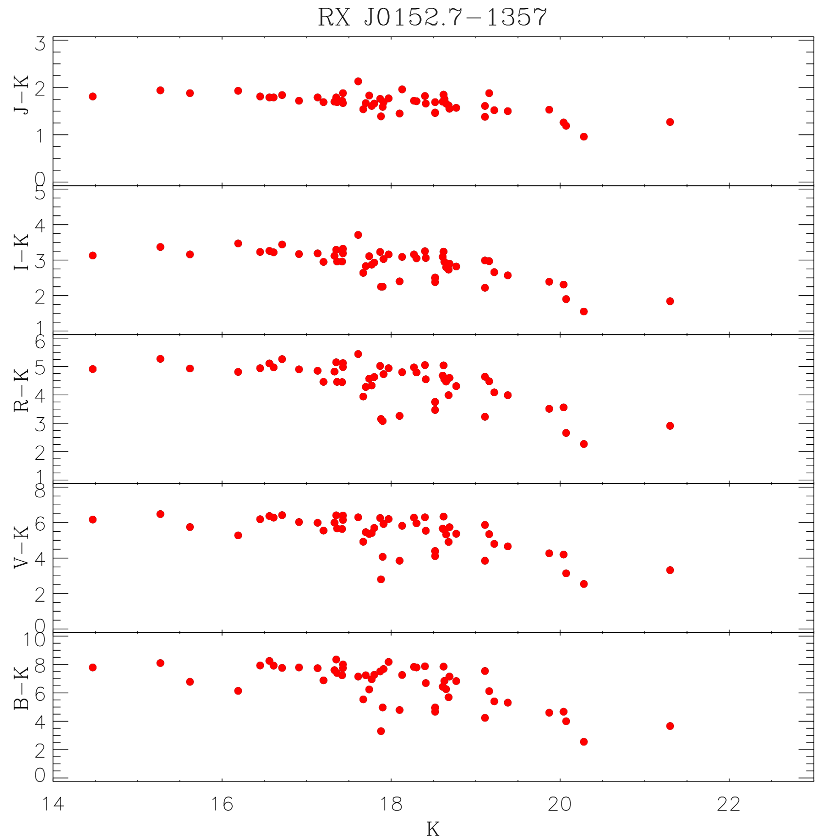

Figure 5.9: Color magnitude diagrams for the 78 spectroscopicaly confirmed galaxy members in RX J0152.7-1357 . A clear red sequence is seen in each diagram with the scatter around the sequence getting smaller toward the reddest colors.

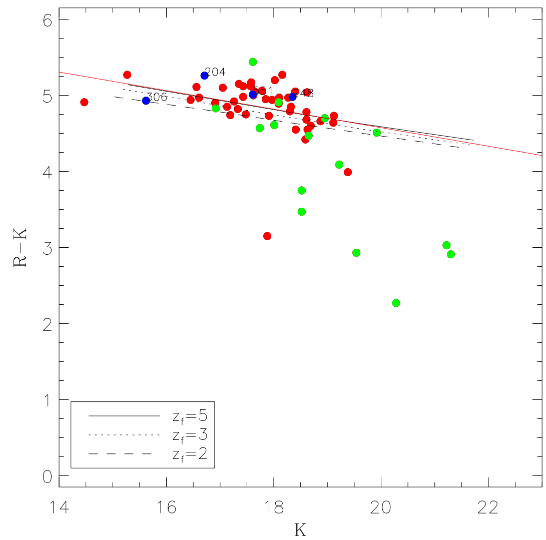

a)

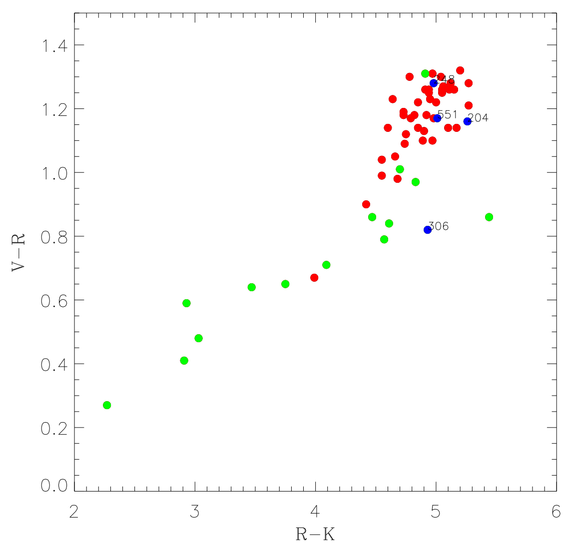

b)

Figure 5.10: a) R-K vs K color magnitude diagram for RX J0152.7-1357 spectroscopic cluster members. The filled red circles are non-emission line galaxies, filled green circles are emission line objects and filled blue circles correspond to the red emission line galaxies presented in section 5.3.4. The ID of each of these red emission line galaxies is indicated. The predicted CM relations at redshift $z = 0.8$ for passively evolving early-type galaxies formed at redshifts z_f=2, 3 and 5, computed by Kodama & Arimoto (1997) are also plotted. b) V-R vs R-K Color-Color diagram for RX J0152.7-1357 . Symbols are the same as in (a).

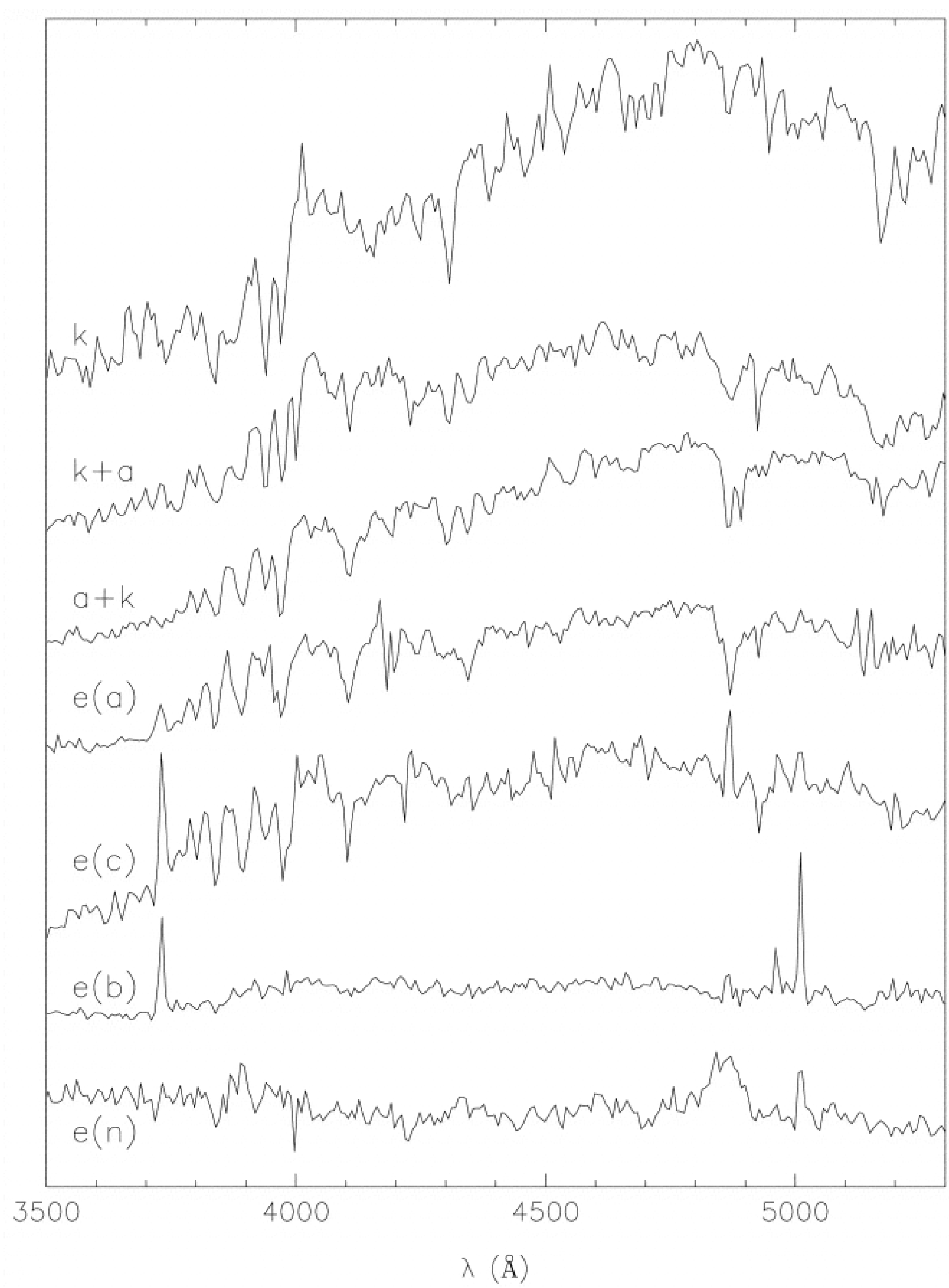

Figure 5.11: Representative spectra from each of the spectral classes in the classification scheme defined in Dressler et al. (1999). These spectra are plotted with arbitrary vertical scaling and in the rest frame (taken from Dressler et al. (1999)).

Gal ID	A.R. (J2000)	DEC (J2000)	R	B-R	V-R	V-I	R-I	R-J	R-K	z	E. L.	EW([OII])	EW(H_δ)	Class	Features
g18	01:52:41.551	-14:00:26.14	23.25	2.89	1.56	3.33	1.76	99.00	99.00	0.8249	1	-55.33	0	e(b)	[OIII]
g26b	01:52:48.293	-14:00:23.98	-1	-1	-1	-1	-1	-1	-1	0.8371	1	100000	0	e(n)	[OIII]
g47	01:52:45.535	-14:00:15.26	22.75	1.57	0.72	2.18	1.46	99.00	99.00	0.8436	1	-13.63	4.784	e(a)	MgI CaII [OIII]
g67	01:52:37.063	-14:00:08.60	22.50	0.85	0.55	1.59	1.04	1.57	99.00	0.8402	1	-1222.	0	e(b)	H_β
g85	01:52:41.894	-13:59:53.88	22.18	3.00	1.18	2.96	1.78	3.11	4.92	0.8258	0	0	0	k	MgI CaII
g113	01:52:41.165	-13:59:56.83	23.85	2.47	1.18	2.98	1.79	3.09	4.73	0.8237	0	0	3.829	k+a	CaII
g129	01:52:41.861	-13:59:51.43	23.17	2.81	1.22	2.97	1.75	3.23	4.85	0.8256	0	0	4.17	k+a	CaII
g131	01:52:51.912	-13:58:16.36	19.38	2.88	1.26	3.04	1.78	3.10	4.91	0.8436	0	0	0	k	MgI CaII
g144	01:52:35.189	-13:59:47.80	22.47	0.91	0.59	1.73	1.14	1.62	2.93	0.8446	1	-19.59	0.326	e	
g177	01:52:43.560	-13:59:38.62	23.12	1.79	0.86	2.53	1.67	2.81	4.47	0.8431	1	-12.17	3.399	e(c)	MgI CaII
g204	01:52:47.318	-13:59:26.09	21.97	2.50	1.16	2.98	1.82	3.42	5.26	0.8386	1	-17.95	1.657	e(c)	MgI CaII
g241	01:52:38.645	-13:59:20.69	23.66	2.81	1.30	3.10	1.80	3.19	5.04	0.8354	0	0	0	k	MgI CaII
g248	01:52:48.331	-13:59:21.55	23.33	2.96	1.28	3.04	1.76	3.26	4.98	0.8468	1	-20.99	1.961	e(c)	MgI CaII
g258	01:52:49.406	-13:58:31.15	20.54	2.83	1.21	3.11	1.90	3.33	5.27	0.8430	0	0	2.503	k	CaII
g267	01:52:39.914	-13:59:18.92	24.43	74.57	74.57	76.26	1.69	2.85	4.51	0.8497	1	-17.72	0	e	
g270	01:52:39.715	-13:59:14.17	23.05	1.71	0.86	2.58	1.73	3.31	5.44	0.8456	1	-38.01	0	e	
g295	01:52:39.377	-13:59:04.24	22.27	1.18	0.65	1.89	1.24	2.28	3.75	0.8374	1	-28.25	0	e	
g300	01:52:43.738	-13:59:01.39	21.03	0.15	-0.35	0.55	0.90	1.76	3.15	0.8178	1	0	0	e(n)	MgII (AGN)
g306	01:52:49.658	-13:58:28.02	20.55	1.85	0.82	2.59	1.77	3.05	4.93	0.8538	1	-25.07	1.603	e(c)	MgI CaII [OIII]
g327	01:52:40.200	-13:58:58.58	22.55	0.28	0.27	0.98	0.72	1.31	2.27	0.8258	1	-140.4	0	e(b)	H_β [OIII]
g332	01:52:39.646	-13:58:56.14	23.09	3.00	1.17	2.91	1.74	3.08	4.79	0.8322	0	0	1.913	k	MgI CaII
g347	01:52:38.609	-13:58:54.59	23.31	1.31	0.71	2.13	1.43	2.57	4.09	0.8474	1	-40.02	0	e(b)	CaII H_β [OIII]

continues ...

Gal ID	A.R. (J2000)	DEC (J2000)	R	B-R	V-R	V-I	R-I	R-J	R-K	z	E. L.	EW([OII])	EW(H_δ)	Class	Features
g377	01:52:41.189	-13:58:42.53	22.62	1.51	0.84	2.24	1.40	2.77	4.61	0.8390	1	-34.62	0	e	
g387	01:52:39.626	-13:58:25.86	21.67	3.14	1.26	3.11	1.85	3.32	5.11	0.8293	0	0	0	k	MgI CaII
g397	01:52:40.445	-13:58:37.70	23.45	2.82	1.25	3.05	1.80	3.23	5.05	0.8327	0	0	2.197	k	CaII
g418	01:52:38.875	-13:58:31.22	23.22	2.88	1.32	3.24	1.92	3.39	5.20	0.8299	0	0	0	k	CaII
g432	01:52:52.754	-13:58:23.81	22.99	2.81	1.18	2.99	1.81	2.95	99.00	0.8526	0	100000	1.349	k	MgI CaII
g439	01:52:39.763	-13:58:23.95	22.75	3.06	1.14	3.01	1.87	3.38	5.17	0.8294	0	0	2.356	k	CaII
g445	01:52:43.085	-13:58:21.76	22.91	3.24	1.26	3.04	1.78	3.17	4.94	0.8270	0	0	1.404	k	CaII
g468	01:52:40.579	-13:58:14.38	22.69	3.34	1.26	3.09	1.83	3.34	5.05	0.8272	0	0	1.855	k	MgI CaII
g491	01:52:41.762	-13:58:12.94	23.29	1.75	0.98	2.57	1.59	2.98	4.68	0.8278	0	0	0	k	MgI CaII
g498	01:52:39.470	-13:58:07.82	23.29	2.55	1.14	2.84	1.70	3.05	4.60	0.8258	0	0	4.065	k+a	MgI CaII
g513	01:52:40.250	-13:58:04.44	23.24	2.86	1.31	3.12	1.81	3.25	4.97	0.8275	0	0	0	k	MgI CaII
g543	01:52:50.914	-13:57:52.92	21.93	2.15	1.09	2.76	1.68	2.90	4.74	0.8397	0	0	0	k	MgI CaII
g547	01:52:41.784	-13:57:57.17	23.43	2.91	1.28	3.11	1.83	3.40	5.27	0.8460	0	0	0	k	CaII
g548	01:52:42.816	-13:57:54.22	23.07	2.58	1.10	2.86	1.76	3.26	4.97	0.8346	0	0	0	k	CaII
g551	01:52:36.170	-13:57:47.45	22.62	2.46	1.17	2.91	1.74	3.18	5.01	0.8362	1	-5.487	4.661	e(a)	MgI CaII [OIII]
g571	01:52:42.319	-13:57:49.43	22.84	3.18	1.27	3.09	1.82	3.29	5.06	0.8444	0	0	0	k	CaII
g595	01:52:44.069	-13:57:46.01	22.96	2.14	0.99	2.48	1.49	2.89	4.55	0.8377	0	0	3.229	k+a	MgI CaII
g598	01:52:39.929	-13:57:41.29	22.15	76.85	1.14	2.93	1.79	3.33	5.10	0.8332	0	0	0	k	CaII
g626	01:52:43.315	-13:55:41.92	23.18	2.29	1.04	2.64	1.60	2.79	4.55	0.8206	0	-3.603	2.838	e(c)	MgI CaII
g648	01:52:44.909	-13:56:34.12	23.65	1.80	1.01	2.55	1.55	3.03	4.70	0.8461	1	-484.8	0	e(b)	CaII [OIII]
g654	01:52:45.566	-13:56:38.26	22.55	2.88	1.28	3.09	1.80	3.24	5.12	0.8460	0	0	-100000	k	MgI CaII
g663	01:52:44.794	-13:56:37.10	23.75	2.90	1.23	2.88	1.65	3.03	4.64	0.8302	0	0	0	k	MgI CaII

continues ...

Gal ID	A.R. (J2000)	DEC (J2000)	R	B-R	V-R	V-I	R-I	R-J	R-K	z	E. L.	EW([OII])	EW(H_δ)	Class	Features
g679	01:52:45.792	-13:56:57.70	21.58	2.95	1.31	3.05	1.75	3.18	4.97	0.8342	0	0	0	k	MgI CaII
g688	01:52:43.534	-13:56:54.67	22.62	2.69	1.22	2.99	1.77	3.24	5.00	0.8339	0	0	0	k	CaII
g701	01:52:44.940	-13:57:02.66	21.39	2.99	1.25	2.96	1.71	3.13	4.94	0.8352	0	0	0.901	k	MgI CaII
g805	01:52:35.138	-13:57:36.47	23.37	1.32	0.67	2.09	1.42	2.49	3.99	0.8348	0	0	5.584	k+a	MgI CaII
g851	01:52:38.074	-13:55:34.57	22.31	1.67	0.79	2.25	1.46	2.74	4.57	0.8360	1	-5.748	4.505	e(a)	MgI CaII
g859	01:52:37.536	-13:54:26.17	22.68	2.92	1.15	2.98	1.84	99.00	99.00	0.8402	0	0	0	k	MgI CaII
g1006	01:52:41.762	-13:55:03.94	24.25	0.62	0.48	1.49	1.00	1.59	3.03	0.8503	1	-726.1	0	e(b)	H_β [OIII]
g1131	01:52:37.546	-13:55:38.06	24.21	0.75	0.41	1.49	1.07	1.64	2.91	0.8251	1	-1016.	0	e(b)	[OIII]
g1151	01:52:43.546	-13:55:51.17	23.39	2.48	1.30	3.03	1.73	3.03	4.78	0.8330	0	0	0	k	CaII
g1172	01:52:37.423	-13:55:47.21	22.23	2.74	1.12	2.83	1.71	3.05	4.75	0.8373	0	0	2.563	k	MgI CaII
g1184	01:52:44.465	-13:55:52.03	22.80	2.78	1.23	3.01	1.78	3.16	4.95	0.8288	0	0	1.091	k	MgI CaII
g1225	01:52:43.608	-13:56:01.54	23.53	3.01	1.05	2.77	1.72	3.02	4.66	0.8399	0	0	0	k	MgI CaII
g1226	01:52:36.010	-13:56:03.23	22.64	2.95	1.19	2.89	1.70	3.04	4.73	0.8310	0	0	3.233	k+a	MgI CaII
g1238b	01:52:37.833	-13:56:06.59	-1	-1	-1	-1	-1	-1	-1	0.8456	1	-89.85	0	e(b)	
g1258	01:52:38.021	-13:56:25.76	21.75	1.90	0.97	2.55	1.58	2.99	4.83	0.8392	1	-7.244	100000	e	MgI CaII
g1278	01:52:42.360	-13:56:16.51	21.98	2.89	1.14	2.80	1.66	3.06	4.85	0.8215	0	0	0	k	CaII
g1290	01:52:52.721	-13:56:22.74	21.99	1.20	0.64	1.73	1.09	1.78	3.47	0.8426	1	-18.82	2.779	e(c)	
g1338	01:52:38.482	-13:56:31.06	22.41	2.77	1.17	2.96	1.79	3.31	4.98	0.8331	0	0	0	k	CaII
g1367	01:52:35.974	-13:56:30.12	22.98	2.41	1.10	2.83	1.73	3.11	4.89	0.8352	0	0	2.252	k	MgI CaII
g1386	01:52:45.732	-13:56:44.41	23.00	2.93	1.31	3.06	1.75	3.11	4.91	0.8388	1	-5.882	100000	e	CaII
g1442	01:52:42.924	-13:57:33.62	22.50	3.20	1.26	3.11	1.86	3.36	5.15	0.8325	0	0	100000	k	MgI CaII
g1454	01:52:42.907	-13:57:25.20	23.01	1.54	0.90	2.25	1.36	2.75	4.42	0.8452	0	0	100000	k	MgI CaII

continues ...

Gal ID	A.R. (J2000)	DEC (J2000)	R	B-R	V-R	V-I	R-I	R-J	R-K	z	E. L.	EW([OII])	EW(H_δ)	Class	Features
g1465	01:52:43.296	-13:57:25.31	22.69	2.95	1.28	3.04	1.76	3.28	5.12	0.8365	0	0	2.963	k	MgI CaII
g1466	01:52:43.721	-13:57:18.00	22.15	2.78	1.18	2.89	1.70	3.12	4.82	0.8395	0	0	0	k	MgI CaII
g1467	01:52:43.819	-13:57:18.83	21.81	2.89	1.13	2.86	1.73	3.18	4.90	0.8412	0	0	1.332	k	MgI CaII
g1496	01:52:34.492	-13:58:41.75	-1	-1	-1	-1	-1	-1	-1	0.8300	1	-4.035	100000	e	MgI CaII
g1499	01:52:50.884	-13:57:30.05	-1	-1	-1	-1	-1	-1	-1	0.8462	0	0	0	k	MgI CaII
g1500	01:52:51.047	-13:57:27.54	-1	-1	-1	-1	-1	-1	-1	0.8477	0	0	1.903	k	MgI CaII
g1501	01:52:51.919	-13:58:15.31	-1	-1	-1	-1	-1	-1	-1	0.8473	0	0	3.103	k+a	MgI CaII
g1514	01:52:32.493	-14:00:29.41	-1	-1	-1	-1	-1	-1	-1	0.826	0	0	0	k	MgI CaII
g1519	01:52:39.921	-13:59:20.82	-1	-1	-1	-1	-1	-1	-1	0.8450	1	-83.64	0	e(b)	
g1530	01:52:50.992	-14:00:20.74	-1	-1	-1	-1	-1	-1	-1	0.8381	1	-129.5	0	e(b)	H_β [OIII]
g1531	01:52:52.952	-13:59:53.52	-1	-1	-1	-1	-1	-1	-1	0.8388	1	-107.3	0	e(b)	H_β [OIII]
g1532	01:52:44.135	-14:00:38.62	-1	-1	-1	-1	-1	-1	-1	0.8423	1	-12.38	0	e	MgI CaII H_β

Table 5.5: Spectro-photometric catalog for RX J0152.7-1357. The E.L. flag takes the values of 0 and 1 in the case of non-emission and emission line objects respectively. Equivalent Widths (EWs) are in Å and an absolute value of 10000 has been assigned to those features which either are outside the covered spectral range or a fair estimate of their EW could not be obtained. Spectral classes are those defined in Dressler et al. (1999). The last column indicates observed spectral features other than [OII] and H_δ. Unavailable magnitudes and colors have a -1 value.

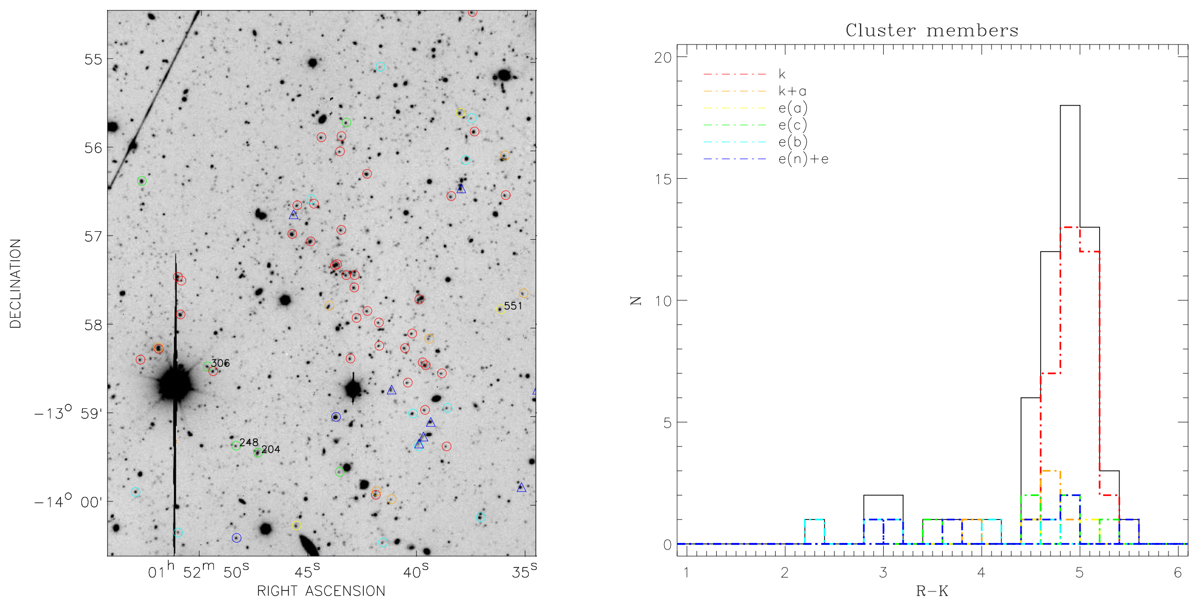

a) b)

Figure 5.12: Distribution of cluster members according to spectral class. a) Spatial distribution: the colors represent the different spectral types as defined in (b). Blue circles are "e(n)" galaxies and blue triangles are "e" galaxies. These two types together with the "e(a)", "e(b)" and "e(a)" types correspond to emission line galaxies (Dressler et al. 1999).The location of the 5 emission line red objects is indicated by their IDs. b) Color distribution: the different spectral classes are color-coded as indicated in the upper-left corner. The black histogram, corresponds to the total distribution.

A clear segregation in the spatial distribution of galaxies in RX J0152.7-1357 is seen. As shown in figure 5.12-a, the three main substructures are dominated by k type galaxies with a few $k+a$ objects. In addition to this, these galaxies have red R-K $\sim$ 5 colors, as seen in the color distribution of figure 5.12-b, being located also in the locus of the red sequence shown in figure 5.9. This information suggests an early formation epoch of the bulk of the galaxy populations within these substructures. On the other hand, the outer regions are populated mostly by galaxies with signature of recent and on-going star formation activity. These could be late-type field galaxies falling into the potential well of the nascent cluster. The view of RX J0152.7-1357 as a non-relaxed still forming cluster is thus reinforced.

The red galaxies with on-going star formation, introduced in the previous section, are mainly located in the outskirts surrounding the central main structure of RX J0152.7-1357 and they are seen to be as red as the brightest cluster early types. The four red emission line galaxies shown in Fig. 5.10 are also shown in figures 5.13 and 5.14, where the one-dimensional and two-dimensional spectra are displayed, together with a cutout of the galaxy taken from the ACS image. For each of these six galaxies, FORS spectroscopy has revealed a clear signature of [OII] (λ3727) which is an indicative of on-going star formation activity. The overall spectrum in each case is characteristic of galaxies belonging to the $k + a$ class to which the [OII] feature is superposed. In all these spectra, an H_δ feature has been identified, although a fair estimate of its EW was obtained only for 4 of them (see table 5.5). The most extreme case is the one of g306 (see Fig. 5.14-a), where [OIII] is also visible and the H_δ feature is quite notorious. All the spectra show a clear 4000 Å Break and are consistent with the observed red R-K colors.

All these characteristics indicate that these galaxies are the host of old stellar populations co-inhabiting with post-starburst populations of few Gyrs as suggested by the observed H_δ lines. At the same time, new stars are being formed as indicated by the [OII] emission lines. In order to have star formation, the presence of gas is required. This suggests the existence of disks surrounding the central regions of these galaxies. Here, the HST+ACS imaging has played a crucial role in unveiling the morphology of these objects. Some of these galaxies show indeed a clear spiral morphology (e.g., g204, g306 and g551), with clear arms and dust lanes in some cases, consistent with the observation of [OII]. However some others (e.g., g248; see Fig. 5.13-b) have an early-type morphology. No clear signs of a disk are observed.

This is the first time that such red star forming objects in a cluster are observed. In MS 1054-03 ($z = 0.83$) the existence of red mergers, mostly in the outskirts of that cluster, was reported by van Dokkum et al. (1999). However, in most of the mergers they do not observe evidence for the presence of gas to form a new disk, with only a 15% of the mergers having EW([OII]) larger than 5 Å. In our case, on the other hand, the observed red star forming galaxies have EW([OII]) > 5 Å. From all the objects located within one standard deviation above and below the locus defined by the red sequence, a 22% are emission line galaxies. There are no reasons to believe that our selection is biased against or in favour these red emission line galaxies. A possible explanation is that these galaxies in RX J0152.7-1357 are indeed the result of a merger between a bulge system, formed at a redshift greater than 2, and a disk system. However they are observed to be isolated and no signs of such a merging event is evident. This explanation turns out to be even more unlikely in the case of g248 (see Fig. 5.13-b), for example. Since these galaxies are located in the outer parts of the cluster, star formation in these systems could have been triggered by the interaction of these galaxies with the ICM during the possible infall of these systems into the cluster; however the fact that an old stellar population (red colors)

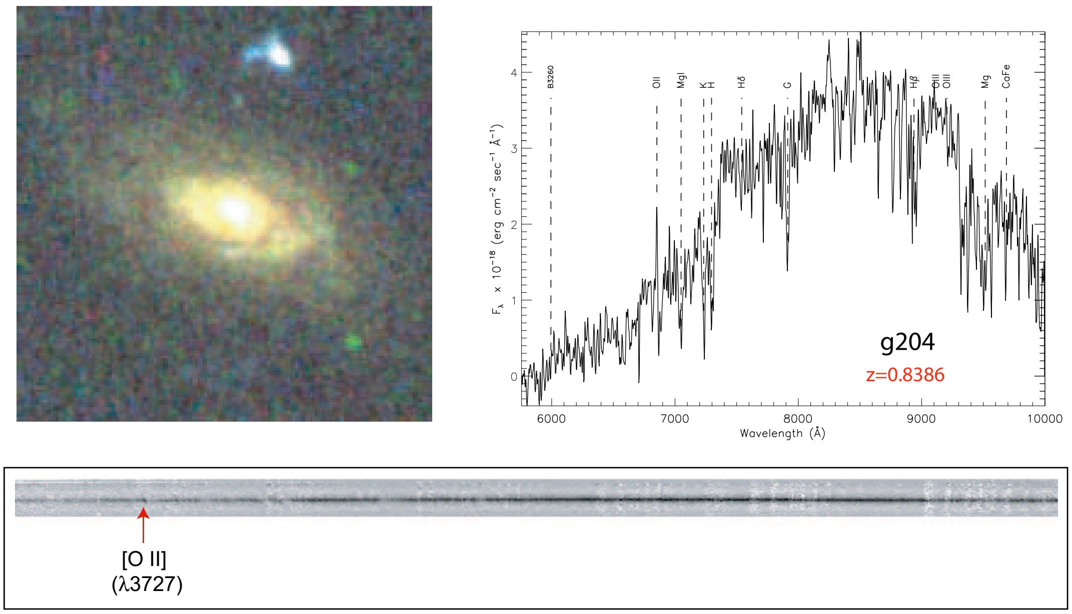

a)

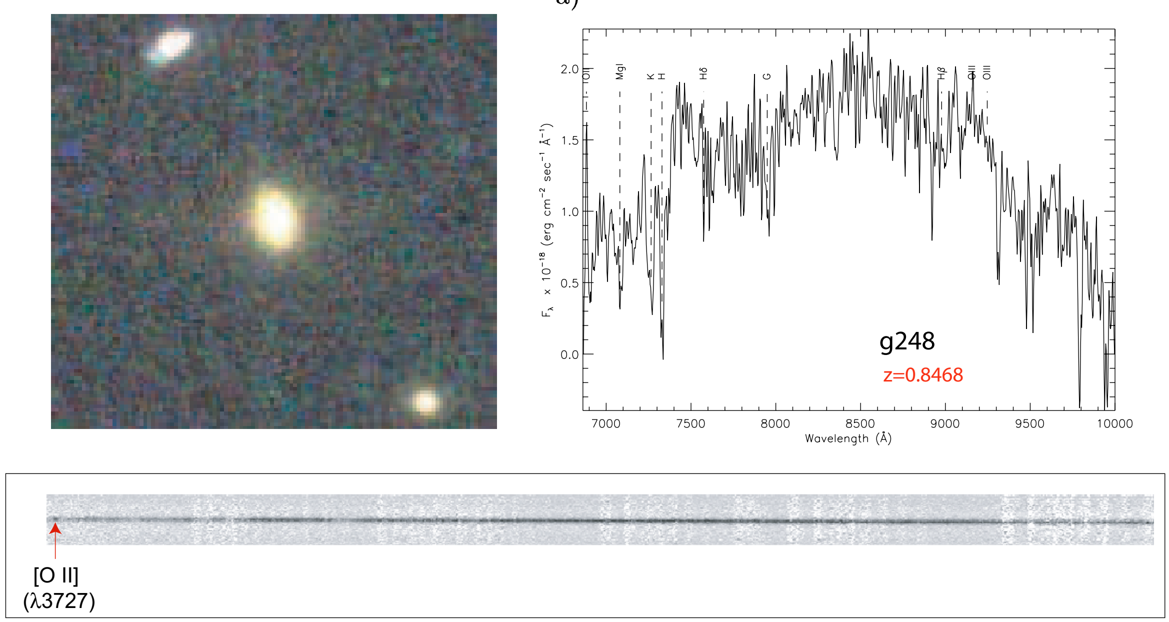

b)

Figure 5.13: Emission line galaxies with colors R-K > 4.75 in the sample of spectroscopic cluster members in RX J0152.7-1357 . Their spatial location is shown in Fig. 5.12-a and their spectro-photometric properties are presented in table 5.5. The cutout from the ACS color image (top-left), the one-dimensional (top-right) and the two-dimensional (bottom) spectra are shown. The drop in the red part of the spectral range of the continuum is possibly due to inaccuracies in the sensitivity function. Main spectral features are also indicated. a) Galaxy g204. b) Galaxy g248.

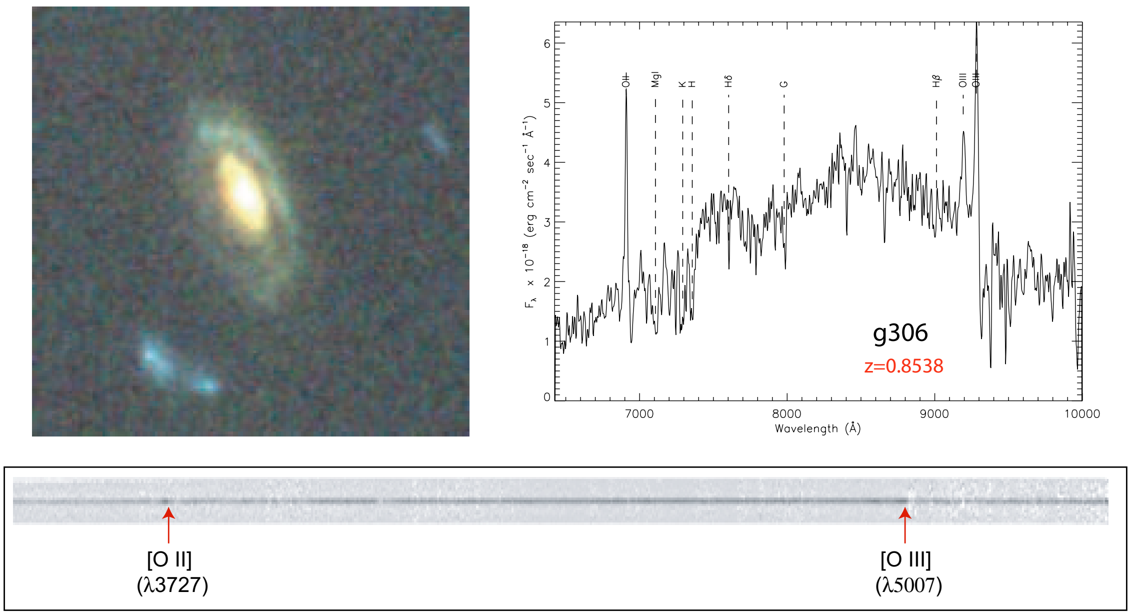

a)

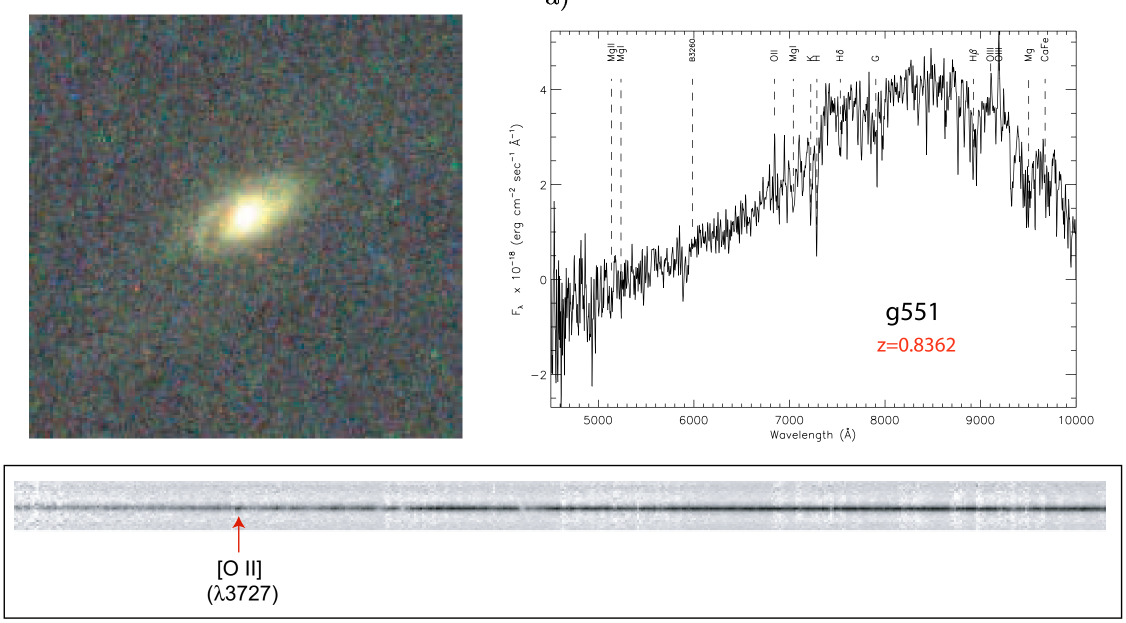

b)

Figure 5.14: Same as in figure 5.13. a) Galaxy g306. b) Galaxy g551.

is coexisting with gaseous disks with on-going star formation is a new result which requires further investigation.

5.4 Scientific results on RDCS J1252.9-2927 ($z = 1.237$)

In this section I will summarize part of the results obtained so far in the analysis of the data collected on RDCS J1252.9-2927 , one of the most distant clusters of galaxies known to date, concentrating more in the outcomes of the spectroscopic survey. The results from the X-ray observations with Chandra and XMM, including the ICM temperature and metallicity, cluster redshift and mass estimates, are presented in Rosati et al. (2004). The CM diagram of RDCS J1252.9-2927 from optical photometry with HST+ACS and near-IR photometry with the NTT and VLT are discussed in detail in Blakeslee et al. (2003) and Lidman et al. (2003) respectively. It is important to say that, due to the optical (i and z) bandpasses used in the ACS imaging, the CM diagram computed from these data turns out to be sensitive to the Balmer Break (at 3700 Å) and thus sensitive to changes in short time scale (few Gyrs) of the galaxy spectrum, due to possible star formation activity. The possible bias in the color of galaxies produced by these evolutionary effects are thus avoided by studing the CM relation at IR wavelengths (Lidman et al. 2003). Finally, the Luminosity Function of galaxies in RDCS J1252.9-2927 is presented in Toft et al. (2003). These papers are included in the next chapter.

5.4.1 Cluster structure

The efficient selection criteria of targets (see section 5.2.3 and figure 5.5) based on high quality imaging data has been a key piece in the success of our spectroscopic campaign. A total of 234 redshifts, from which 205 correspond to secure measurements, have been obtained with the 13 masks observed with FORS (see table 5.3) and one extra mask observed at Keck before the beginning of the ESO Large Program. This great effort has yielded to date 36 confirmed spectroscopic members in RDCS J1252.9-2927 ($z = 1.237$), the largest number of spectroscopic members discovered so far in a cluster of galaxies at such a large redshift. In comparison, on the two Lynx clusters (Rosati et al. 1999, Stanford et al. 2001) of the order of 20 members are known to date. Broad selection in color space (R-K vs J-K; see section 5.2.3) which reduced pollution without affecting completness. The secondary selection in V-I vs I-z allowed the discovery of 13 cluster members with strong [OII](λ3727) emission lines. Figure 5.15-a shows the histogram of RDCS J1252.9-2927 galaxy members. The median redshift of the distribution is $z = 1.237$ and the global velocity dispersion is 760^{+117}_{-69} km/s. The red area indicates the total distribution while the blue dashed one shows the distribution of star-forming members.

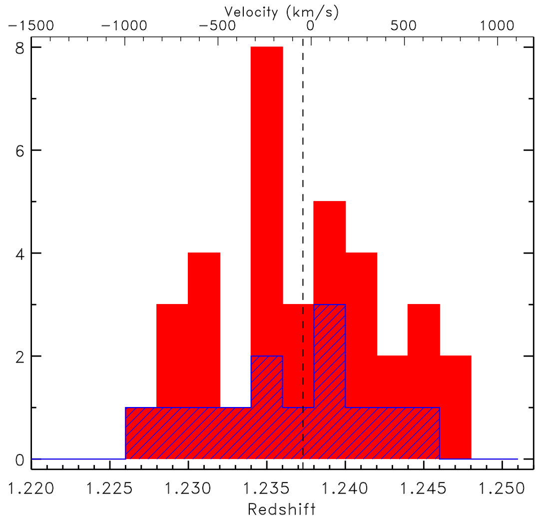

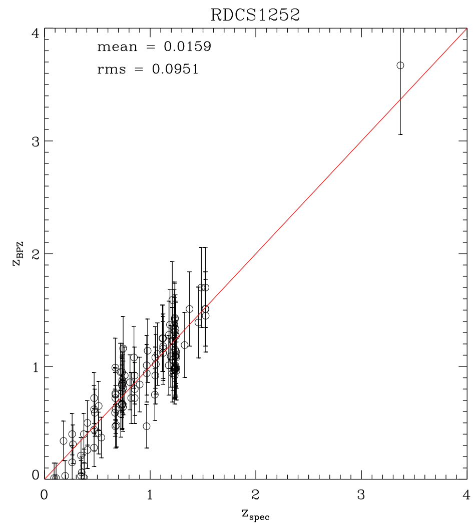

a) b)

Figure 5.15: a) Redshift distribution in RDCS J1252.9-2927 ($z = 1.237$). The median redshift of the distribution is $z = 1.237$ and the global velocity dispersion is 760^{+117}_{-69} km/s. The red area indicates the total distribution of members while the blue dashed one shows the distribution of star-forming members. b) Photometric vs spectroscopic redshifts. Photometric redshifts were obtained by following the Bayesian approach of Benítez (2000). The small scatter of the points confirms the good performance of the Bayesian Photometric Redshifts (BPZ) technique as well as the high quality of our ground-based photometry.

In Figure 5.16 we show RDCS J1252.9-2927 member distribution. The color circles are spectroscopic member galaxies as seen on the plane of the sky, and individual reshifts have been color-coded as shown in the color table. The overall shape of the distribution of the spectroscopically confirmed galaxy members is elongated in the East-West direction, although this is a mild effect, being more uniform compared to the galaxy distribution in RX J0152.7-1357 . This is an indication of a more advanced state of virialization of RDCS J1252.9-2927 ; however the possibility of having a cluster undergoing interaction through merging can not be completely ruled out.

The distribution of the star-forming galaxies is also displayed in Fig. 5.16. These objects are indicated by the red crosses on top of the circles. The outer regions of RDCS J1252.9-2927 are dominated by [OII] galaxies, supporting the picture of late-type galaxies from the field falling into the cluster potential. Here the HST+ACS imaging has revealed the morphology associated to these star forming galaxies. In general, a disk structure can be seen and some galaxies look like edge-on spirals. Although some emission line galaxies are observed within approximately 1 arcmin radius from the cluster center, the central region of RDCS J1252.9-2927 is dominated by early-type galaxies. Indeed, Figs. 5.15-a and 5.16 show that late-type systems are mostly missing in the center, in velocity space and spatial distribution, in agreement with the well known morphology-density relation (see section 1.3.1).

The excellent quality photometry obtained with our ground based imaging survey with FORS, ISAAC and SOFI (Lidman et al. 2003, Rosati et al., in preparation) has been used to derive accurate (rms ~ 0.095) photometric redshifts for all the sources in the RDCS J1252.9-2927 photometric catalog. The photometric redshifts has been computed by following the Bayesian approach presented in Benítez (2000). The comparison between photometric redshifts and spectroscopic redshifts is shown in figure 5.15-b. These photometric redshifts, calibrated with the available spectroscopy have been used to investigate the spatial distribution of the photometric cluster members (Toft et al. 2003; see paper in next chapter). The resulting light distribution is shown in figure 5.17 where the galaxy density contours are overlayed on the $\sim$ 4' $\times$ 4' mosaic K_s-band ISAAC image (Lidman et al. 2003). The contours are 2-12 times the density of galaxies in the HDFN with $K_s < 22.5$ and $0.935 < z_{phot} < 1.535$ (Fernández-Soto et al. 1999). We note that the density distribution of photometric cluster members also appears to be elongated in the East-West direction, in agreement with the distribution of the spectroscopic members. Inside the dashed circle of radius 65" (see Fig. 5.17) the contamination from field galaxies in the sample of photometric cluster members is estimated to be less than 25%. Within this circular region the LF of photometric cluster members in RDCS J1252.9-2927 is derived, which set independent constraints on the evolution of galaxy populations in clusters up to $z = 1.2$ (Toft et al. 2003; see paper in next chapter).

5.4.2 Constraining the evolution of early-type galaxies

The CM diagram in RDCS J1252.9-2927 and its implications on galaxy formation and evolution are fully discussed in Lidman et al. (2003) and Blakeslee et al. (2003) (see next chapter). Here I will just summarize the main new results.

Despite the high quality of the spectra obtained with the VLT of the galaxy population in RDCS J1252.9-2927 , a spectroscopic classification as the one applied to RX J0152.7-1357 is hard to achieve in this case, especially due to the difficulty in measuring directly the EW of the H_δ feature in the galaxy spectrum. Another alternative is to combine several spectra to produce a higher signal-to-noise one, and then try to recognize spectral features in the average spectrum.

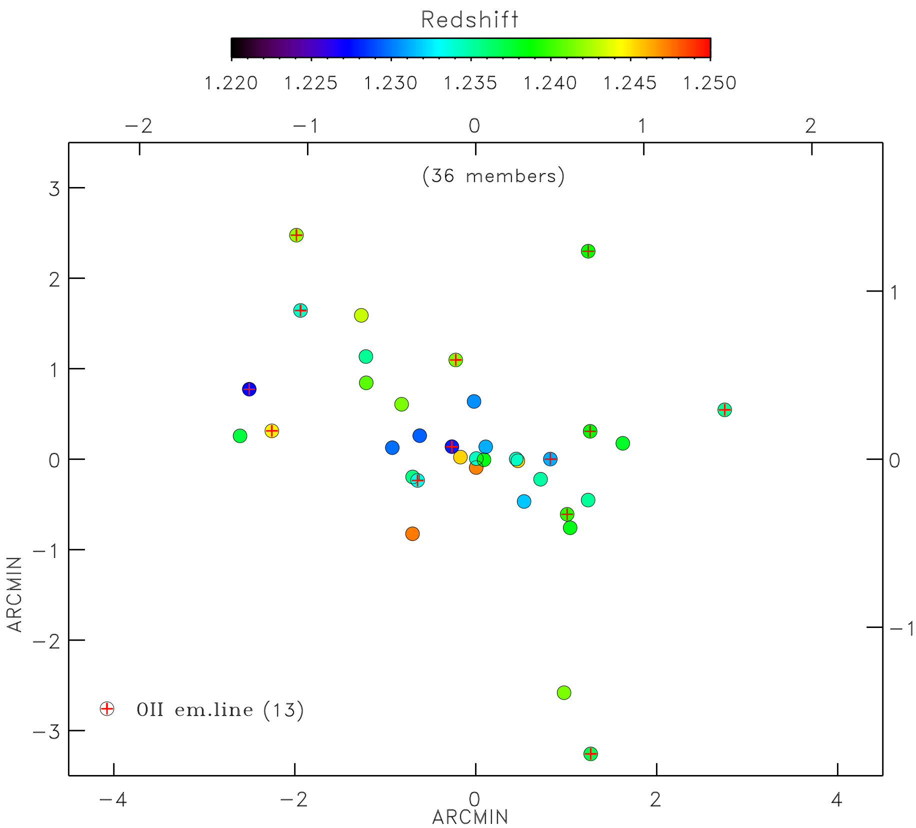

Figure 5.16: Color circles are the 36 spectroscopic member galaxies as seen on the plane of the sky. The median redshift of the member distribution is $z = 1.237$, and individual reshifts have been color-coded as shown in the color table. The overall shape of the galaxy distribution is elongated in the East-West direction. The global velocity dispersion of the cluster is σ_v $=760^{+117}_{-69}$ km/s. The red crosses on top of the circles indicate the 13 galaxies with [OII] emission lines.

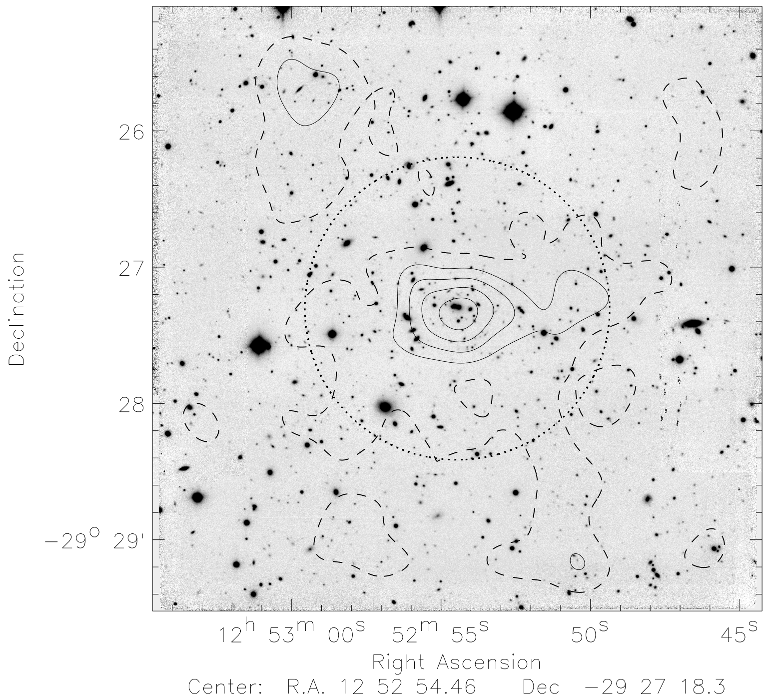

Figure 5.17: Contours of the smoothed density distribution of photometric cluster members in RDCS J1252.9-2927 . The contours are overlayed on the ~ 4' × 4' mosaic K_s-band ISAAC image (Lidman et al. 2003). The contours are 2-12 times the density of galaxies in the HDFN with $K_s < 22.5$ and $0.935 < z_{phot} < 1.535$ (Fernández-Soto et al. 1999). Dashed contours correspond to the minimum in density. Inside the dashed circle of radius 65" (see Fig. 5.17) the contamination from field galaxies in the sample of photometric cluster members is estimated to be less than 25% and within this circular region the LF of photometric cluster members in RDCS J1252.9-2927 is derived (Toft et al. 2003).

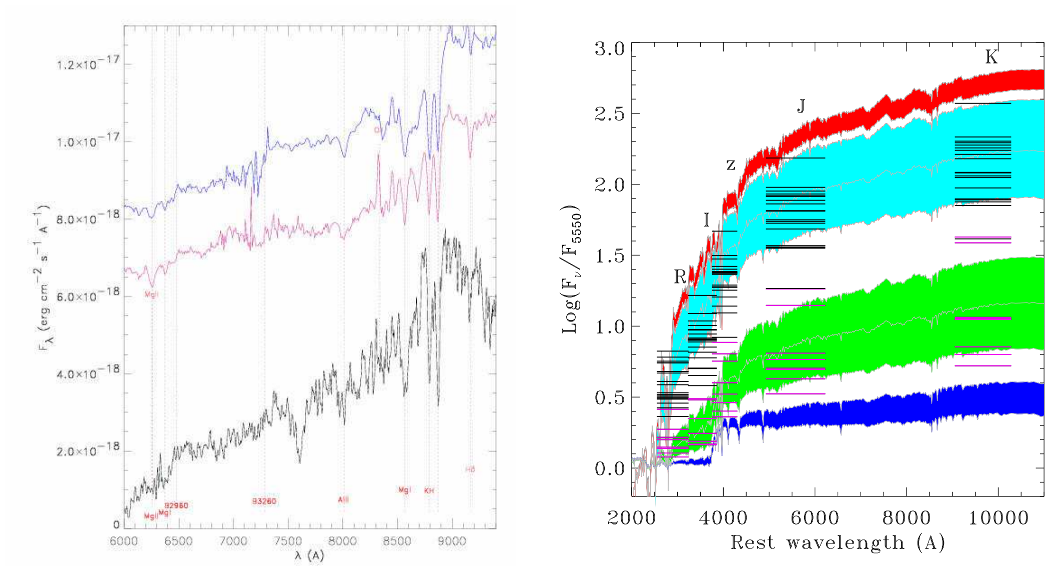

a) b)

Figure 5.18: Stellar populations in RDCS J1252.9-2927 galaxies. a) Stacked spectrum of the 10 brightest early-type member galaxies (bottom spectrum). The spectra of a local elliptical and an Sa galaxy (top and middle spectrum respectively) are also shown for comparison. A significant H_δ feature is observed, which indicates the existence of a relatively young (few Gyrs) stellar population inhabiting bright early type galaxies in RDCS J1252.9-2927 . No on-going star formation has been detected. b) The photometry of the RDCS J1252.9-2927 spectroscopic member galaxies is represented as horizontal bars. The black bars are non-emission line objects whereas the purple ones correspond to [OII] members. Bruzual-Charlot models are overplotted and are explained in the text.

In Figure 5.18-a I show the stacked spectrum of the 10 brightest early-type member galaxies (bottom spectrum). The spectra of a local elliptical and an Sa galaxy (top and middle spectrum respectively) are also shown for comparison. The important point here is the detection of a significant H_δ feature in the combined spectrum. As explained in chapter 4, this indicates the existence of a relatively young (few Gyrs) stellar population inhabiting bright early type galaxies, although no on-going star formation has been detected. This result is supported by the IR (Lidman et al. 2003) and ACS (Blakeslee et al. 2003) photometry which are best matched by models including stellar populations of few Gyrs at solar metallicity. The photometry of the RDCS J1252.9-2927 spectroscopic member galaxies is represented as horizontal bars in Fig. 5.18-b. The black bars are non-emission line objects whereas the purple ones correspond to [OII] members. Bruzual-Charlot models are overplotted. These represent galaxy spectra of different evolutionary histories at fixed solar metallicity. The 2 red and 3 cyan models correspond to stellar populations produced in a single burst followed by pure luminosity evolution (PLE). These models are characterized by two parameters: (burst duration (Gyr), age (Gyr)). From top to bottom these numbers are respectively (0.1,4), (0.1,3), (0.5,3), (2,3) and (2.5,3). The 3 green models are produced by star formation rates (SFR) with exponential decline. They are represented by two parameters: (the characteristic time τ (Gyr), age (Gyr)). From top to bottom these numbers are respectively (1,4), (1,3) and (2,3). Finally, the blue models are produced by constant SFR. They are characterized by the numbers: (the SFR ($M_\odot$/yr), age (Gyr)). From top to bottom these parameters are respectively (10,3) and (10,1). Solar metallicity is adopted in each model. The photometry of non emission line galaxies in RDCS J1252.9-2927 is well represented by single bursts with a duration between 0.5 and 2.5 Gyrs followed by PLE up to an age of 3 Gyr. On the other hand, the photometry of the star-forming galaxies is better reproduced by models invoking an exponential decline in the SFR up to an age of 3 Gyrs.

We conclude therefore that, for the first time, we have clear evidence that early-type galaxies in RDCS J1252.9-2927 are hosting young stars and that we are approaching the epoch of formation of the bulk of the stellar population in these galaxies. A formation redshift of $z_f \sim 3$ is required to reproduce the observations (Lidman et al. 2003).

5.5 Strong lensing features

Advance Camera for Surveys (ACS) observations are delivering an impressive view of the morphology of galaxies in the field of view of RX J0152.7-1357 and RDCS J1252.9-2927 . An example of this is shown in figure 5.19 for RX J0152.7-1357 and figure 5.4 for RDCS J1252.9-2927 . Clear strong lensing features can be seen in these images. We have an on-going program with VLT to target the strong lensing features observed in RX J0152.7-1357 , and the spectroscopic data should become available soon. I will report here on the spectroscopy carried out on the two arcs observed at about 16" to the south-west of the center of RDCS J1252.9-2927 . These arcs are shown in figure 5.20. These objects have the ID numbers g706 and g268 in our photometric catalog and we will refer to them as Arc A and Arc B respectively hereafter.

Arc A was observed three times during our spectroscopic campaign and Arc B twice, but only the improved efficiency in the red of the FORS2 CCD mosaic made possible to obtain the redshift for both arcs, after a 3 hr 40 min exposure for Arc A and a 3 hr exposure for Arc B. The resulting spectra are shown in figure 5.21. The blue spectrum shown on the upper part corresponds to the template used to cross correlate with the observed spectra. This template was kindly provided by Alice Shapley and is the composite spectrum of 199 Lyman Break Galaxies with strong Ly_α in absorption (Shapley et al. 2003). The cross correlation technique and the similarity of both spectra indicate that Arc A and Arc B are the images of the same galaxy at redshift $z = 3.36$ that is being lensed by the cluster potential well (see section 1.4.3). The first suggestion about the common nature of these arcs came from the similarities in the colors of both sources (see Fig. 5.20). Our spectroscopic analysis has confirmed this and now a modelling of the cluster structure based on the strong lensing modelling of the arcs is under way. This will give important constraints on the internal structure of the cluster and its DM distribution. The mass thus derived can be compared with dynamical measurements from the galaxy velocity dispersion and from the X-ray observations (Rosati et al. 2004).

5.6 Conclusions

In this chapter I have presented the main first results of an unprecedented study of the two most distant massive clusters in the southern sky: RX J0152.7-1357 ($z = 0.837$) and RDCS J1252.9-2927 ($z = 1.237$). The confirmation of 78 spectroscopic members in RX J0152.7-1357 and 36 spectroscopic members in RDCS J1252.9-2927 is the result of an extensive spectroscopic follow-up of both clusters and an efficient selection criterium based on the galaxy distribution in color space. The high quality of our spectroscopic data enables us to firmly characterize the underlying stellar populations of galaxies in these high redshift systems, thus allowing us to better constrain the mode and epoch of formation of cluster early types. X-ray (Maughan et al. 2003; Rosati et al. 2004), optical (Blakeslee et al. 2003) and near-IR imaging (Lidman et al. 2003), together with spectroscopic information, is providing a comprehensive picture of the internal structure and dynamics

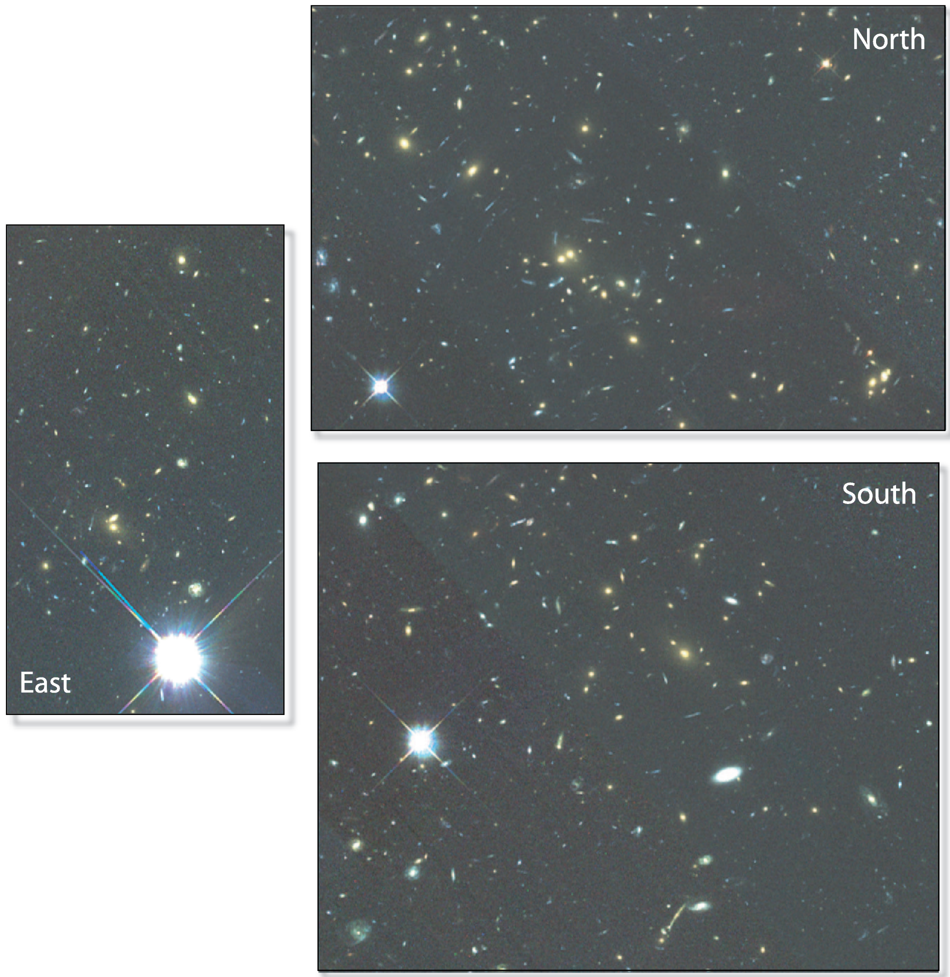

Figure 5.19: Strong lensing features in RX J0152.7-1357 . A detailed view of the three main structures in RX J0152.7-1357 is presented, showing a large number of strong lensing features in this cluster. Spectroscopy on the arcs is currently on-going and the determination of their redshift will set independent and strong constraints on the internal structure of the cluster. The color images shown here have been obtained by combining HST+ACS imaging in r, i and z (Courtesy of the ACS science team).

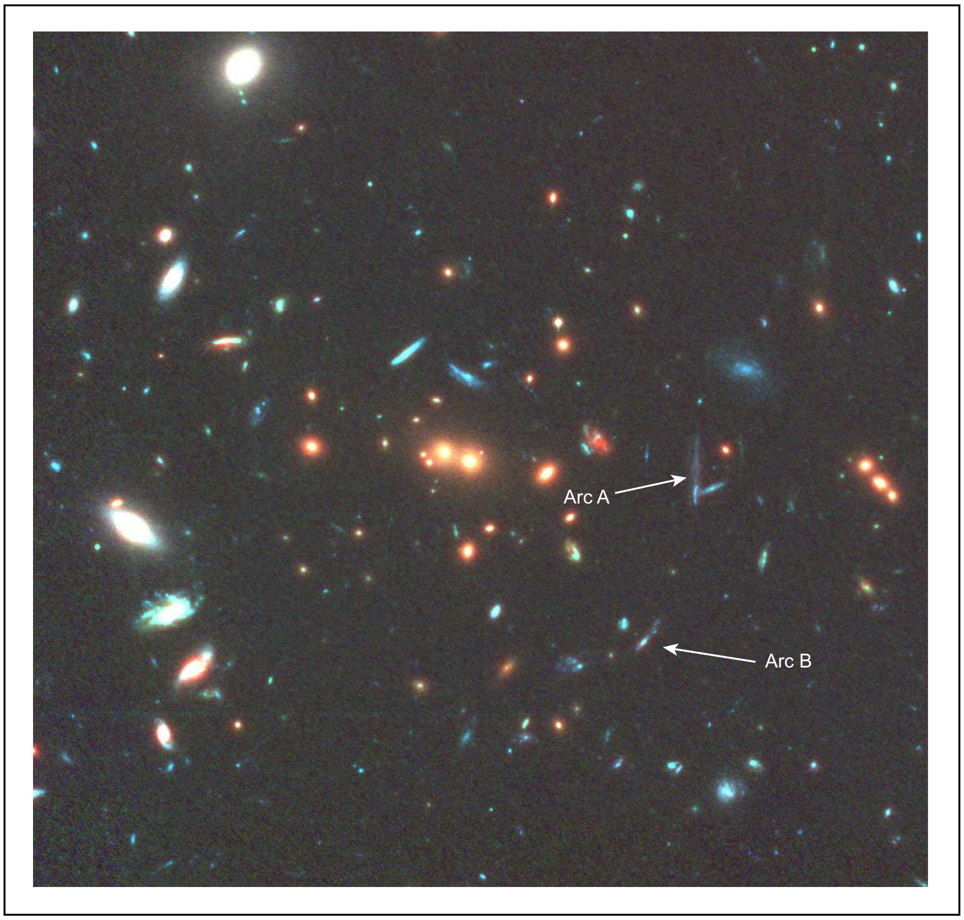

Figure 5.20: The central 1' $\times$ 1' field of view on RDCS J1252.9-2927 is presented. Two strong lensing features Arc A and Arc B are indicated. They are the images of the same galaxy at a redshift of $z = 3.36$ (see Fig. 5.21) and are located at about 16" to the south-west of the cluster center. The modeling of the cluster mass distribution based on this information is currently in progress. The color image shown here has been obtained by combining HST+ACS imaging in i and z (Courtesy of the ACS science team).

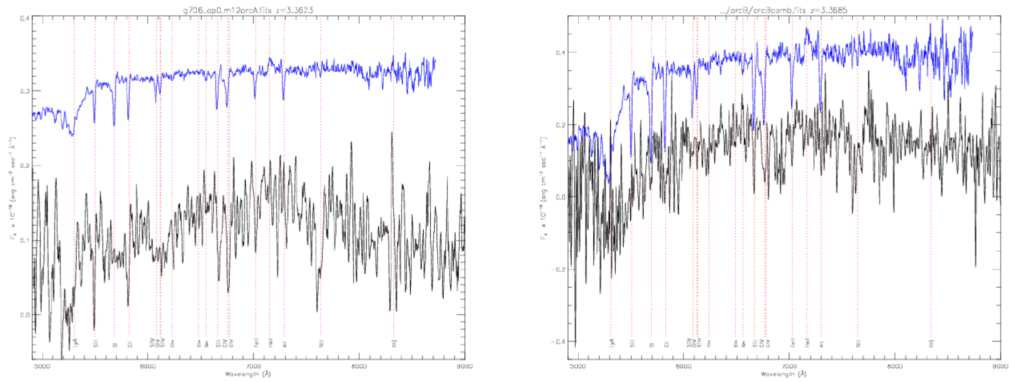

a) b)

Figure 5.21: The observed spectra for a) Arc A and b) Arc B. The blue spectrum shown on the upper part corresponds to the template used in the cross correlation, and is the composite spectrum of 199 Lyman Break Galaxies with strong Ly_{α} in absorption (Shapley et al. 2003). The cross correlation technique and the similarity of both spectra indicates that Arc A and Arc B are the images of the same galaxy at redshift $z = 3.36$. The main visible features are the Ly Break ($\sim$ λ1215.7), the SiII (λ1260.4, 1526.7) and CIV (λ1548.2, 1550.7) lines and the FeII (λ 1608.4) line.

of these clusters. Moreover, we are currently in the process of quantifying morphology with the ACS data in order to understand environmental effects on the galaxy population and evolutionary effects according to galaxy type.

In the case of RX J0152.7-1357 , we conclude that this system is clearly a dynamically young cluster. The filamentary structure observed in the RX J0152.7-1357 galaxy distribution agrees very well with the X-ray distribution (Maughan et al. 2003) of its ICM. There is strong evidence for significant substructure in this system (Girardi et al., in prep.), which supports the picture of a cluster in a merging phase. An important result is the discovery of about ten galaxies well within the cluster red sequence with on-going star formation. These galaxies are located in the outskirts of the cluster and their SEDs can be described as a E+A galaxy spectrum with [OII] superposed. The observed spectra and the red colors thus indicate the existence of old stellar populations and post starburst populations inhabiting these galaxies. The observed on-going star formation finds a natural, albeit surprising, explanation in the ACS images which show clear disks around red bulges in several cases. This new discovery requires further investigation.

RDCS J1252.9-2927 shows a well advanced state of relaxation, in spite of mild evidence for elongation in its galaxy and X-ray distribution. The analysis of all the photometric data in hand (Lidman et al. 2003, Blakeslee et al. 2003, Rosati et al., in preparation) shows that early type galaxies in clusters become bluer with increasing redshift. Models show that these colors are recovered if early-types are inhabited by young stellar populations of a few Gyrs. The formation redshift for these galaxies is inferred to be $z_f \sim 3$. Early-types would have thus been formed at this redshift by an initial burst followed by PLE, supporting the Classical model of early-type galaxy formation.

A detailed analysis of the dynamical mass of each cluster, based on the available spectroscopic data is under way. Mass estimates from X-ray observations with Chandra and XMM (Maughan et al. 2003; Rosati et al. 2004) show that RX J0152.7-1357 and RDCS J1252.9-2927 are indeed massive clusters at redshift $z \sim 1$. The existence of such massive structures at such high redshift reinforce the accumulated evidence that we are living in a low density universe. Model predictions indicate that the observation of a few very hot (T $\geq$ 8 keV) clusters at redshift greater than ~ 0.5 would rule out a $\Omega_M = 1$ cosmology (see Eke et al. 1998, and references therein). Nevertheless, the sample of distant hot (or massive) galaxy clusters known today is limited and future observations with Chandra and XMM should provide a conclusive answer to the issue.

Chapter 6

RDCS J1252.9-2927: an X-ray luminous, distant cluster

Paper accepted in The Astronomical Journal (AJ, Jan 2004)

TO APPEAR ON THE ASTRONOMICAL JOURNAL (JAN 2004)
Preprint typeset using LaTeX style emulateapj v. 11/12/01

CHANDRA AND XMM-NEWTON OBSERVATIONS OF RDCS1252.9–2927, A MASSIVE CLUSTER AT $z = 1.24$ [1]

P. ROSATI[2], P. TOZZI[3], S. ETTORI[2], V. MAINIERI[2,12], R. DEMARCO[2,11], S. A. STANFORD[4,5], C. LIDMAN[2], M. NONINO[3], S. BORGANI[6], R. DELLA CECA[7], P. EISENHARDT[8], B.P. HOLDEN[9], C. NORMAN[10]
[2]European Southern Observatory, Karl-Schwarzschild-Strasse 2, D-85748 Garching, Germany
[3]INAF, Osservatorio Astronomico di Trieste, via G.B. Tiepolo 11, I–34131, Trieste, Italy
[4]Department of Physics, University of California, Davis, CA 95616
[5]Institute of Geophysics and Planetary Physics, LLNL, Livermore, CA 94551
[6]Dip. di Astronomia dell'Università, via G.B. Tiepolo 11, I–34131, Trieste, Italy
[7]INAF, Osservatorio Astronomico di Brera, via Brera 28, I–20121, Milano, Italy
[8]Jet Propulsion Laboratory, Mail Stop 169-327, California Institute of Technology, Pasadena, CA 91109
[9]Lick Observatory, University of California, Santa Cruz, CA 95064
[10]Department of Physics and Astronomy, Johns Hopkins University, Baltimore, MD 21218
[11]Institut d'Astrophysique de Paris, 98bis Boulevard Arago, F-75014 Paris, France
[12]Dip. di Fisica, Università degli Studi di Roma Tre, I-00146 Roma, Italy

To appear on the Astronomical Journal (Jan 2004)

ABSTRACT

We present deep *Chandra* and *XMM-Newton* observations of the galaxy cluster RDCS1252.9–2927, which was selected from the ROSAT Deep Cluster Survey (RDCS) and confirmed by extensive spectroscopy with the VLT at redshift $z = 1.237$. With the *Chandra* data, the X-ray emission from the intra-cluster medium is well resolved and traced out to 500 kpc, thus allowing a measurement of the physical properties of the gas with unprecedented accuracy at this redshift. We detect a clear 6.7 keV Iron K line in the *Chandra* spectrum providing a redshift within 1% of the spectroscopic one. By augmenting our spectroscopic analysis with the *XMM-Newton* data (MOS detectors only), we significantly narrow down the 1σ error bar to 10% for the temperature and 30% for the metallicity, with best fit values $kT = 6.0^{+0.7}_{-0.5}$ keV, $Z = 0.36^{+0.12}_{-0.10} Z_\odot$. In the likely hypothesis of hydrostatic equilibrium, we measure a total mass of $M_{500} = (1.9 \pm 0.3)10^{14} h_{70}^{-1} M_\odot$ within $R_{\Delta=500} \simeq 536$ kpc. Overall, these observations imply that RDCS1252.9–2927 is the most X-ray luminous and likely the most massive bona-fide cluster discovered to date at $z > 1$. When combined with current samples of distant clusters, these data lend further support to a mild evolution of the cluster scaling relations, as well the metallicity of the intra-cluster gas. Inspection of the cluster mass function in the current cosmological concordance model $(h, \Omega_m, \Omega_\Lambda) = (0.7, 0.3, 0.7)$ and $\sigma_8 = 0.7 - 0.8$ shows that RDCS1252.9–2927 is an M^* cluster at $z = 1.24$, in keeping with number density expectations in the RDCS survey volume.

Subject headings: X-rays: galaxies: clusters — galaxies: clusters: individual (RDCS 1252.9-2927) — cosmology: observations

[1] Based in part on observations obtained at the European Southern Observatory using the ESO Very Large Telescope on Cerro Paranal (ESO program 166.A-0701).

1. INTRODUCTION

X-ray studies of galaxy clusters over the last decade have driven considerable observational progress in tracing the evolution of their global physical properties. Based on X-ray selected samples covering a wide redshift range, convincing evidence has emerged for modest evolution of both the space density of the bulk of X-ray clusters and their thermodynamical properties since $z \approx 1$ (see Rosati et al. 2002 for a review). With the advent of *Chandra* and *XMM-Newton* , and their unprecedented sensitivity and angular resolution, these studies have been extended beyond redshift unity and, in low redshift clusters, have revealed the complexity of the thermodynamical structure of the Intra-Cluster Medium (ICM) (e.g. Fabian et al. 2003b). Specifically, deep *Chandra* observations of the handful of clusters known to date at $z > 1$ (Stanford et al. 2001, 2002) have shown, for the first time at such large look-back times, the structure of the ICM at scales below 100 kpc and have allowed emission weighted temperatures to be measured. The new *Chandra* data have provided a crude determination of cluster scaling relations at large lookback times and a first study of their evolutionary trends (e.g. Holden et al. 2002, Vikhlinin et al. 2002, Ettori et al. 2003b). In more distant and complex systems, such as putative proto-clusters dominated by a powerful radio galaxy, *Chandra* deep pointings have only revealed non-thermal components in the diffuse plasma so far (Fabian et al. 2003a, Scharf et al. 2003). *XMM-Newton* observations of very distant clusters, although affected by source confusion in some circumstances, have the ability to collect a large number of photons, thus improving temperature determinations and allowing an estimate of the ICM metallicity (Hashimoto et al. 2002, Tozzi et al. 2003).

The discovery and the study of systems beyond redshift unity provides the strongest leverage for testing cluster formation scenarios. This, however, has been a challenging task with current X-ray searches due to the limited survey areas covered at faint fluxes. In this paper, we present *Chandra* and *XMM-Newton* observations of the fourth cluster at $z > 1$ discovered in the *ROSAT* Deep Cluster Survey (RDCS, Rosati et al. 1998) at the very limit of the *ROSAT* sensitivity: RDCS1252.9–2927 which has been confirmed at $z = 1.237$ with an extensive spectroscopic campaign carried out with the VLT. *Chandra* observations of the other three distant RDCS clusters, RDCS0910+5422 ($z = 1.10$), RDCS0848.9+4452 ($z = 1.265$), RDCS0848.6+4453 ($z = 1.273$) were presented in Stanford et al. 2002, 2001. We describe the optical and near-infrared data for RDCS1252 elsewhere (Rosati et al. in preparation, Lidman et al. 2003), while we focus here on the X-ray observations carried out with *Chandra* , augmented with a partial *XMM-Newton* data set. We derive physical parameters of the ICM and measure gas metallicity from the clear presence of the iron K line in the X-ray spectrum. We also derive the total mass of the cluster with a 16% accuracy by resolving the gas profile with the *Chandra* data and by combining *Chandra* and *XMM-Newton* spectra to improve the temperature determination. Our analysis takes advantage of the complementarity between the XMM and *Chandra* data sets: the superb angular resolution of *Chandra* is used to study morphological features of the ICM and to flag point sources contaminating the cluster emission, while the XMM data are used to boost the signal-to-noise of the diffuse component thus improving its spectral analysis. Overall, these data imply that RDCS1252.9–2927 is the most X-ray luminous and likely the most massive bona-fide cluster discovered to date at $z > 1$.

$H_0 = 70$ km s^{-1} Mpc^{-1}, $\Omega_m = 0.3$, $\Omega_\Lambda = 0.7$ are adopted throughout this paper.

2. OBSERVATIONS AND X-RAY DATA REDUCTION

2.1. *Discovery of RDCS1252.9–2927*

RDCS1252.9–2927 (hereafter RDCS1252 for brevity) was selected as an extended X-ray source (with a significance of 3.2σ) in the RDCS, which used a wavelet-based algorithm to detect and characterize X-ray sources in 180 ROSAT/PSPC archival fields down to $f_{\rm lim}$(0.5-2 keV)$= 10^{-14}$ erg cm^{-2} s^{-1} (Rosati et al. 1998). The source was found in the field with ROSAT ID WP300093 (exposure time = 15.7 ksec) at an off-axis angle of $13.9'$ with 31 net counts, corresponding to a flux of $(2.5 \pm 0.9)10^{-14}$ erg cm^{-2} s^{-1} in the 0.5-2 keV band. At fluxes $\sim 2 \times 10^{-14}$ erg cm^{-2} s^{-1}, the RDCS covers an effective area of 5 deg^2 and has maximum sensitivity for L^* clusters at $z \gtrsim 1$[2]. As a result, the four RDCS clusters at $z > 1$, with $L_X \lesssim L_X^*$, were found in the faintest flux bin (Rosati et al. 1999, Stanford et al. 02). A 30 minute *I*-band image obtained at the CTIO 4-m telescope with the Prime Focus camera in February 1997, revealed only a faint ($I \simeq 21.7$) galaxy pair very close to the X-ray centroid position. As part of a program to follow-up faint RDCS cluster candidates in the near-IR, *J* and *K* band imaging was obtained with the SOFI camera at the NTT in November 1998, which showed a clear overdensity of red galaxies with $J-K \simeq 1.9$, typical of early type galaxies at $z > 1$ (see Lidman et al. 2003). RDCS1252 has more recently been the core of a VLT Large Programme which included optical imaging with FORS2, deep near IR imaging with ISAAC (Lidman et al. 2003) and extensive spectroscopy with FORS2. Results from this program are described elsewhere; to date 36 cluster members have been confirmed with a median redshift of $z = 1.237$ and a velocity dispersion $\sigma_v \approx 800$ km/s.

2.2. *Chandra data*

RDCS1252 was observed with the *Chandra* ACIS–I detector in VFAINT mode in two exposures of 26 ks (Obs ID 4403) and 163 ks (Obs ID 4198). The data were reduced using the the CIAO software V2.3 (see `http://cxc.harvard.edu/ciao/`) starting from the level 1 event file. We used the tool `acis_process_events` with the `vfaint=yes` option to flag and remove bad X-ray events which are mostly due to cosmic rays. Such a procedure reduces the ACIS particle background significantly compared to the standard grade selection[3], whereas source X-ray photons are practically unaffected (only $\sim 2\%$ of them are rejected, independently of the energy band, provided there is no pileup). We also applied the correction to the charge transfer inefficiency to partially recover the original spectral resolution of ACIS–I. The data were filtered to include only the standard event grades 0, 2, 3, 4 and 6. We removed ~ 10 hot columns via visual inspection. We searched for flickering pixels (defined as those with more than two events contiguous in time, where a single time interval was set to 3.3 s), however most of them are already removed by the filtering of bad events for exposures

[2] We note that observations suggest $L_X^*(z=1) \simeq 10^{44}$ erg s^{-1}, in the 0.5-2 keV band (Rosati et al. 2002).

[3] see `http://asc.harvard.edu/cal/Links/Acis/acis/Cal_prods/vfbkgrnd/`

taken in VFAINT mode. We then applied a 3–σ clipping filtering of time intervals with high background levels using the script `analyze_ltcrv`, part of the CIAO distribution. The total effective exposure time is 188 ks after the application of this reduction procedure.

In Fig. 1, we show part of the ACIS-I field. The diffuse X-ray emission from the cluster is detected with a high signal-to-noise (S/N peaks to ~ 21 within a radius of $35''$), and can be traced out to $r = 59''$ (2σ above the background). The *Chandra* image (see bottom left of Fig. 1) immediately shows that point sources do not significantly contaminate the cluster emission, as it is sometimes the case (e.g. Stanford et al. 01). In most cases, sources close to the cluster core in projected distance have been found to be foreground or background AGN. In the RDCS1252 field we have only a few identifications of point sources to date (8 within a $6' \times 6'$ area), of which only one is at the cluster redshift (Fig. 1).

We performed the spectral analysis in two circular regions ($35''$ and $59''$ radii) around the centroid of the photon distribution after masking out point sources. In these apertures we detected approximately 850 and 1220 net counts in the 0.3–10 keV band. The background is obtained from a large annulus around the cluster position, after subtraction of point sources. The background photon file is scaled to the source file by the ratio of the geometrical area. We checked that variations of the background intensity across the chip do not affect the background subtraction, by comparing the count rate in the source and in the background at energies larger than 8 keV, where the signal from the source is null. The response matrices and the ancillary response matrices were computed for each exposure with the tool *acisspec* applied to the extraction regions. We applied the script `apply_acisabs` by Chartas and Getman to take into account the degradation in the ACIS QE due to material accumulated on the ACIS optical blocking filter since launch[4]. We manually decreased the effective area below 1.8 keV by 7% to homogenize the low–energy calibrations of ACIS–S3 and ACIS–I (see Markevitch & Vikhlinin 2001).

2.3. *XMM-Newton data*

The XMM–Newton observations were carried out in two epochs, on January 1 and 11 2003, for a total of $69.71 + 69.71 = 139.42$ ksec, using the European Photon Imaging Camera (EPIC) PN and MOS detectors (observation Id 0057740301/401). The PN data were negatively affected by one of the CCD gaps which fell on the outskirt of RDCS1252, making it difficult to extract regions for a merged MOS+PN spectroscopic analysis. After experimenting with different apertures, masking and background subtraction techniques, we decided to use the MOS1+MOS2 only for this analysis to avoid systematics which are at present not fully understood. Nonetheless, as shown below, data from the two MOS detectors significantly improved the signal-to-noise of the extracted spectra when combined with the *Chandra* data. We used the XMM Standard Analysis System (SAS) routines (SASv5.4.1) to obtain calibrated event files for the MOS1, MOS2 cameras. Time intervals in which the background was increased by soft proton flares were excluded by rejecting all events whenever the count rate exceeded 20 cts/100s in the 10–12 keV band for each of the two MOS cameras. The final effective exposure time amounts to 137 ks for the two MOS detectors. The spectrum was extracted from an aperture of $42''$ radius (see Fig. 1), which avoids all point sources clearly visible in the *Chandra* image. In this aperture, we measured 2110 MOS1+MOS2 net counts in the 0.5-8 keV band used for spectral fitting (1410 net counts in 0.5-2 keV band). Comparison of the *Chandra* and *XMM-Newton* images shows the well known complementarity of the two observatories: *XMM-Newton* has lower sensitivity to point sources and is prone to confusion, however its large collecting area yields high count rates on extended sources, much needed for spectroscopic analysis. *Chandra* allows ICM morphology and profiles to be studied even at these large redshifts, by separating the diffuse component from faint field sources.

3. RESULTS

3.1. *Spectral analysis*

The spectra are analyzed with XSPEC v11.2.0 (Arnaud 1996) and fitted with a single temperature MEKAL model (Kaastra 1992; Liedahl et al. 1995), where the ratio between the elements are fixed to the solar value as in Anders & Grevesse (1989). These values for the solar metallicity have recently been superseded by the new values of Grevesse & Sauval (1998), who used a 0.676 times lower Fe solar abundance. However, we prefer to report metallicities in units of the Anders & Grevesse abundances since most of the literature still refers to these old values. Since our metallicity depends only on the Fe abundance, updated metallicities can be obtained simply by rescaling by 1/0.676 the values reported in Table 1. We model the Galactic absorption with the tool `tbabs` (see Wilms, Allen & McCray 2000).

The fits are performed over the energy range 0.6–8 keV. We exclude photons with energy below 0.6 keV in order to avoid systematic biases in the temperature determination due to uncertainties in the ACIS calibration at low energies. We used three free parameters in our spectral fits: temperature, metallicity and normalization. We freeze the local absorption to the Galactic neutral hydrogen column density $N_H = 5.95 \times 10^{20}$ cm^{-2}, as obtained from radio data (Dickey & Lockman 1990), and the redshift to $z = 1.237$, as measured from the optical spectroscopy. Spectral fits are performed using the Cash statistics (as implemented in XSPEC) of source plus background photons, which is preferable for low signal–to–noise spectra. We also performed the same fits with the χ^2 statistics (with a standard binning with a minimum of 20 photons per energy channel in the source plus background spectrum) and verified that our best–fit model always gives a reduced $\chi^2 \sim 1$. All quoted errors below correspond to 1σ, or 68% confidence level for one interesting parameter.

The *Chandra* folded and unfolded spectra of RDCS1252 are shown in Fig. 2 for the larger aperture. A prominent Fe K is visible at $kT \simeq 3$ keV, which represents the first clear detection of an iron line from an ICM at $z > 1$. Using only *Chandra* data, the fit to the spectrum in the inner $35''$ radius gives a best fit temperature of $kT = 6.4^{+1.0}_{-0.8}$ keV, and a best fit metallicity of $Z = 0.47^{+0.21}_{-0.18} Z_\odot$. Our Fe K-line diagnostic is simpler and more robust than that based on the line–rich region around 1 keV, where the line emission is dominated by the L–shell transition of Fe, and the K–shell transitions of O, Mg, and Si. As a consistency check, if we leave free the Galactic absorption, we obtain a best fit value of $N_H = 2.9 \times 10^{20}$ cm^{-2}, with an upper limit of 6.3×10^{20} cm^{-2} at 1σ, thus consistent with the Galactic value of $N_H = 5.95 \times 10^{20}$ cm^{-2}. In this case, the best fit

[4] See `http://cxc.harvard.edu/ciao/threads/apply_acisabs/`

temperature is consistent (within 1σ) with the aforementioned best fit value. Interestingly, leaving the redshift free, a four parameter fit yields $z = 1.234^{+0.033}_{-0.035}$, which shows how accurately the redshift can be determined from the X-ray data alone due to the high signal-to-noise detection of the Fe line.

It is useful to repeat the analysis using the larger aperture to test systematic effects in the background subtraction. The fit to the spectrum extracted from the $59''$ aperture gives a temperature somewhat lower, $kT = 5.2^{+0.7}_{-0.6}$ keV, and a metallicity of $Z = 0.64^{+0.20}_{-0.18} Z_\odot$. The difference between the temperature measurement in the two apertures is not significant enough to be attributed to a temperature gradient. We also measured temperatures in two independent radial bins ($r < 35''$, $35'' < r < 59''$) and could find only weak evidence (1σ) of a temperature drop outward. The best fit redshift in this case is still consistent within 1σ with the spectroscopic redshift: $z = 1.27^{+0.02}_{-0.03}$. The spectral analysis of the *Chandra* data also yields a flux within the $59''$ aperture of 2.9×10^{-14} erg cm^{-2} s^{-1} in the 0.5-2 keV band, in good agreement with the ROSAT value. This corresponds to a luminosity of 1.9×10^{44} erg s$^{-1} h_{70}^{-2}$ in the rest frame 0.5-2 keV band, and a bolometric luminosity of 6.6×10^{44} erg s$^{-1} h_{70}^{-2}$. One can use the best fit β-model of the surface brightness profile described below to extrapolate these luminosities at larger radii. For example, values need to be multiplied by a factor 1.3 to encircle the flux within $r = 1$ Mpc (or $2'$).

Using the *XMM-Newton* data from the MOS detectors only, we extracted a spectrum in the energy range 0.5-8 keV (containing 2110 counts as opposed to 800 in the *Chandra* spectrum) and verified that the best fit temperature and metallicity are consistent, within 1σ, with the *Chandra* mesurements above. The XMM/MOS spectrum is shown in Fig. 3. To enhance the photon statistics, we performed a combined fit of the *Chandra* spectrum extracted from the $59''$ region, and the two MOS spectra from the 137 ksec *XMM-Newton* observations. Thus, we obtain a best fit temperature $kT = 6.0^{+0.7}_{-0.5}$ keV, and a best fit metallicity $Z = 0.36^{+0.12}_{-0.10} Z_\odot$. If we leave the redshift free, we obtain a best fit value of $z = 1.221^{+0.024}_{-0.017}$, i.e. within 1% of the spectroscopic redshift.

In Fig. 4, we show confidence contours in the $Z - kT$, $z - kT$ planes relative to the spectral fits discussed above. The combined *Chandra* and *XMM-Newton* analysis yields a temperature accuracy of 10%, which is unprecedented at these redshifts. We defer the analysis of extended and point sources from the full *XMM-Newton* data set, combined with *Chandra* and HST-ACS observations of the field (Blakeslee et al. 2003), to another paper (Mainieri et al. in preparation).

For completeness, we briefly report on the serendipitous group CXJ1252.6–2924 located at $12^h 52^m 34.2^s$ $-29°24'59''$ (J2000), $2.5'$ NW of RDCS1252 (see Fig. 1). Extracting a spectrum from the *Chandra* data with an aperture of $30''$ radius, we detect several low ionization metal lines. The best fit MEKAL model yields: $kT = 1.6^{+0.16}_{-0.31}$ keV, $Z = 0.42^{+0.33}_{-0.35} Z_\odot$, and a redshift $z = 0.32^{+0.02}_{-0.10}$. In this aperture, we measure 320 net counts, a flux of 8.7×10^{-15} erg cm^{-2} s^{-1} in the 0.5-2 keV band, corresponding to $L_X[0.5 - 2\,\mathrm{keV}] = 3.5 \times 10^{42}$ erg s^{-1}, and $L_{\rm bol} = 6.3 \times 10^{42}$ erg s^{-1}. Inspection of our CTIO I band image shows a galaxy group dominated by a luminous elliptical galaxy at the X-ray centroid.

3.2. *Mass determination*

The angular resolution provided by *Chandra* and the detection of the X-ray emission out to $1'$ (i.e. 0.5 Mpc) radius allows an accurate modeling of the gas profile of RDCS1252. This information, assuming hydrostatic equilibrium and isothermality of the gas, leads to a robust estimate of the total mass. The surface brightness profile is obtained from the exposure-corrected image by fixing the number counts per bin to 50 and is fitted with an isothermal $\beta-$model (Cavaliere & Fusco-Femiano 1976) providing a core radius of $79(\pm 13) h_{70}^{-1}$ kpc (or $9.5''$) and $\beta = 0.529(\pm 0.035)$ (see Fig. 5 and Ettori et al. 2003b for details). The model provides a reasonably good fit to the profile ($\chi^2 = 168$, with 156 degree of freedom), which does not require any further component (e.g. a double $\beta-$model) from a statistical point of view. We recover the gas density and total gravitating mass profile using analytic formula associated with the $\beta-$model: $n_{\rm gas} = n_{0,\rm gas}(1 + x^2)^{-3\beta/2}$ and $M_{\rm tot} = \frac{3\ \beta\ T_{\rm gas}\ r_c}{G \mu m_p} \frac{x^3}{1+x^2}$, where $x = r/r_c$, μ is the mean molecular weight in atomic mass unit (= 0.6), G is the gravitational constant, m_p is the proton mass; the central density, $n_{0,\rm gas}$, is obtained from the combination of the best-fit results from the spectral and imaging analyses as described in Ettori, Tozzi & Rosati (2003a). The errors are obtained from the distribution of the values after 1 000 Monte-Carlo simulations. We measure masses within the radius R_Δ encompassing a fixed density contrast, $\Delta_z = 500$ in an Einstein-de Sitter universe, with respect to the critical density, $\rho_{c,z}$, i.e. $\Delta_z = 3M_{\rm tot}(< R_\Delta)/(4\pi\rho_{c,z}R_\Delta^3)$. At $R_{500} = 536 \pm 40$ kpc, corresponding to an overdensity of 457 at the cluster redshift (or $\Delta = 500$ in an Einstein-de Sitter universe), we measure $M_{\rm gas} = (1.8 \pm 0.3)10^{13} h_{70}^{-5/2} M_\odot$ and $M_{500} = (1.6 \pm 0.4)10^{14} h_{70}^{-1} M_\odot$. These values are associated with the *Chandra* temperature measurement, $T_{\rm gas} = 5.2$ keV. If we take the best fit temperature of 6.0 keV from the combined *Chandra* and *XMM-Newton* analysis, the total mass scales up accordingly and the error bar decreases: $M_{500} = (1.9 \pm 0.3)10^{14} h_{70}^{-1} M_\odot$. In order to estimate the cluster virial mass, we can extrapolate our mass measurement to larger radii using a typical Navarro, Frenk & White profile with concentration $c = 5$. This yields $M_{\rm vir} \approx M_{\Delta=200} = 1.4 M_{500} = 2.7 \times 10^{14} h_{70}^{-1} M_\odot$. We also find a gas mass fraction $f_{\rm gas} = (0.10 \pm 0.04) h_{70}^{-3/2}$, consistent with other measurements in distant clusters (e.g. Ettori et al. 2003a).

4. DISCUSSION AND CONCLUSIONS

Taking advantage of the complementarity between *Chandra* and *XMM-Newton* observations, we have measured physical properties of RDCS1252 at $z = 1.237$ with unprecedented accuracy at these redshifts. The *Chandra* data allow the gas profile to be traced and modeled out to ~ 500 kpc, free of confusion from field sources, and therefore enables the mass to be accurately derived. By augmenting our spectroscopic analysis with the *XMM-Newton* data (MOS detectors only), we narrowed down the 1σ error bar to 10% for the temperature and 30% for the metallicity. In Table 1, we report a summary of the main physical properties of RDCS1252 measured from the X-ray data.

In Fig. 6, we show a color composite image of the field with overlaid *Chandra* contours. The color image combines deep near-infrared imaging with ISAAC and optical imaging with FORS at the VLT, with limiting AB magnitude of ~ 26 (Lidman et al. 2003, Rosati et al. in preparation). Cluster early type galaxies stand out as red objects which cluster strongly toward the centroid of the X-ray emission. The two central galaxies, which are $2''$ apart with Vega magnitudes $K \simeq 17.5$, lie near the peak of the X-ray emission. The overall distribution of cluster galaxies, well mapped by our spectroscopic and photometric redshifts, appear flattened along the E-W direction (Toft et al. in prep.). A close inspection of the *Chandra* data reveals an interesting feature in the X-ray surface brightness distribution of RDCS1252. In Fig. 5, the surface brightness profile azimuthally averaged in two separate sectors shows a discontinuity on the west side, at $r \approx 15''$ (or 125 kpc). This could be the origin of the relatively low β value (0.53) obtained by the King profile fit. A relatively sharp edge on the west side is visible in the raw *Chandra* image (Fig. 1), and is apparent in the adaptively smoothed X-ray color image (see upper right inset of Fig. 5), which is the composite of the three energy bands [0.5-1], [1-2], [2-7] keV. A close inspection of this image reveals a comet-like shape of the X-ray emission in the cluster core, a feature resembling the remarkable shock front discovered in the cluster 1E0657–56 at $z = 0.3$ (Markevitch et al. 2002), which is the result of a merging process of a cluster subclump. However, the relatively low photon statistics of the *Chandra* data prevent us from further speculating on the physical nature of this feature in RDCS1252. No major subclumps are visible in the distribution of the cluster galaxies, however we note the coincidence between the mild E-W asymetry of the gas and the E-W elongation of the cluster members. This could be the result of the infall of cluster galaxies along a major filament associated with a cold-front morphology of the gas due to the merger of a subclump just exiting the cluster core along the E-W direction.

The physical properties of RDCS1252, as derived from the *Chandra* data, help to constrain the high redshift end of cluster scaling relations and study their evolution. For example the $L_X - T$, $M - T$ relations, the entropy and metallicity of the ICM as function of redshift. We refer to the analysis of Ettori et al. (2003b), which used a sample of 26 clusters at $z > 0.4$, also including RDCS1252. We note here that the values of $L_{\rm bol}$ and T of RDCS1252 are consistent with the local $L - T$ relation measured by Markevitch (1998), and when combined with all the other data available on distant clusters in the *Chandra* archive, suggest only a mild positive evolution of the $L_X - T$ relation (see discussion in Ettori et al. 2003b and references therein). Our best fit value of the metallicity, $Z = 0.36^{+0.12}_{-0.10} Z_\odot$, lends further support to a lack of evolution of the ICM mean metallicity measured out to $z \simeq 1.3$ (see analysis by Tozzi et al. (2003), which did not include RDCS1252).

Overall, our analysis implies that RDCS1252 is the most X-ray luminous and likely the most massive bona-fide cluster discovered to date at $z > 1$. Despite the large look-back times probed by these observations, RDCS1252 appears already well thermalized, with thermodynamical properties, as well as metallicity, very similar to those of clusters of the same mass at low redshift. This is consistent with a scenario in which the major episode of metal enrichment and gas preheating by supernova explosions occurred at $z \sim 3$.

X-ray selected cluster surveys in the ROSAT era have led to routine identification of clusters out to $z \simeq 0.85$, with only a few examples at higher redshifts (Rosati et al. 1999, Ebeling et al. 2001, Stanford et al. 2002, Rosati et al. 2002). Although the redshift boundary for X-ray clusters has receded to $z = 1.3$ recently, a census of clusters at $z \simeq 1$ has just begun and the search for clusters at $z > 1.3$ remains a serious observational challenge. Extrapolating the RDCS yield to *XMM-Newton* or *Chandra* based serendipitous surveys now underway (e.g. Romer et al. 2001, Boschin 2002), one expects ~ 10 clusters as luminous as RDCS1252 in a 50 deg^2 area. An inspection of the underlying cluster mass function at $z = 1.24$ (e.g. Borgani et al. 2001), for our adopted cosmology and $\sigma_8 = 0.7 - 0.8$, shows that RDCS1252, with $M_{\rm vir} \sim 3 \times 10^{14} M_\odot$, could well represent a typical M^* cluster at these redshifts. Moreover, we note that the presence of such a cluster in the RDCS survey volume (see Fig.5 in Rosati et al. 2002) is in agreement with predictions based on the current cosmological concordance model (e.g. Bennett et al. 2003). Specifically, for the assumed cosmology and $\sigma_8 = 0.8$, we expect to find one cluster as massive as RDCS1252 or more in $1.5 \times 10^7 (h_{70}^{-1}{\rm Mpc})^3$ at $z \simeq 1.2$.

Using high-z radio galaxies as signposts for proto-clusters has been the only viable method so far to break this redshift barrier and push it out to $z \simeq 4$ (e.g., Venemans et al. 2002, Kurk et al. 2003). If there is an evolutionary link between these strong galaxy overdensities around distant radio galaxies and the X-ray clusters at $z \simeq 1.2$, viable evolutionary tracks should be found linking the galaxy populations in these systems, using their spectrophotometric and morphological properties. Recent follow-up *Chandra* observations of high redshift radio galaxies have revealed the presence of diffuse X-ray emission, in addition to a central point source (3C294 at $z = 1.786$: Fabian et al. 2003a; 4C41.17 at $z = 3.8$: Scharf et al. 2003). However, their spectral energy distribution and other energetic arguments indicate that the extended emission is likely non-thermal, and due instead to inverse Compton scattering of the CMB photons by a population of relativistic electrons associated with the radio source activity. The serendipitous detection of thermal ICM at $z > 1.5$ associated with $\sim L^*$ clusters remains extremely difficult, not only for the lack of volume in current X-ray surveys, but also for the severe $(1+z)^4$ surface brightness dimming which affects X-ray observations. These limitations will eventually be overcome by surveys exploiting the Sunyaev–Zeldovich (SZ) effect (e.g. Carlstrom et al. 2002), which will explore large volumes at $z > 1$. It is worth noting, however, that the current sensitivity of SZ observations is still not sufficient to detect any of the known X-ray clusters at $z > 1$, all having $L_X[0.5 - 2\,{\rm keV}] \lesssim 3 \times 10^{44}$ erg s^{-1}, such as RDCS1252. The current generation of large area optical surveys (e.g. using the z-band; Gladders & Yee 2000) remain a valid alternative to unveil a sizeble number of clusters at $z \sim 1$, while the next generation of large area surveys in the near-IR (e.g. Warren 2002) will push this boundary even further. Without a correspondingly large area X-ray survey, however, our ability to glean physical properties necessary to test structure formation scenarious, as well deriving cosmological parameters, will be rather limited.

The authors aknowledge support from NASA grant GO3-4166A. PR thanks the CXC for their prompt help in planning the *Chandra* observations. Part of this work was performed under the auspices of the U.S. Department of Energy by University of California, Lawrence Livermore National Laboratory under contract No. W-7405-Eng-48. CN acknowledges support under the ESO visitor program in Garching during the completion of this work. RDC acknowledges partial financial support from ASI (I/R/062/02).

REFERENCES

Anders, E., Grevesse, N. 1989, Geochimica et Cosmochimica Acta, 53, 197
Arnaud, K.A. 1996, "Astronomical Data Analysis Software and Systems V", eds. Jacoby G. and Barnes J., ASP Conf. Series vol. 101, 17
Bennet, C.L. et al. 2003, ApJ, in press
Blakeslee, J.P., et al. 2003, ApJ, in press
Borgani, S., Rosati, P. Tozzi, P., Stanford, S.A., Eisenhardt, P.E., Lidman, C., Holden, B., Della Ceca, R., Norman, C., Squires G. 2001, ApJ, 561, 13
Boschin, W. 2002, A&A, 396, 397
Carlstrom, J.E. 2002, ARA&A, 40,
Cavaliere, A., & Fusco Femiano, R. 1976. A&A, 49, 137
Dickey & Lockman, 1990, ARA&A, 28, 215.
Ebeling, H., Jones, L.R., Fairley, B.W., Perlman, E., Scharf, C., Horner, D. 2001, ApJ, 548, L23
Ettori, S., Tozzi, P., & Rosati, P. 2003a, A&A, 398, 879
Ettori, S., Tozzi, P., Borgani, S., & Rosati, P. 2003b, A&A, submitted
Fabian, A.C., Sanders, J.S., Crawford, C.S., Ettori, S. 2003a, MNRAS,341, 729
Fabian, A.C., Sanders, J.S., Allen, S.W., Crawford, C.S., Iwasawa, K., Johnstone, R.M., Schmidt, R.W., Taylor, G.B. 2003b, MNRAS, in press
Gladders, M.D., & Yee, H.K.C. 2000, AJ, 120, 2148
Grevesse, N., & Sauval, A.J. 1998, Space Science Reviews, 85, 161
Hashimoto, Y., Hasinger, G., Arnaud, M., Rosati, P., Miyaji, T. 2002, A&A, 381, 841
Holden, B.P., Stanford, S.A., Squires, G.K., Rosati, P., Tozzi, P., Eisenhardt, P., & Spinrad, H. 2002, AJ, 124, 33
Huo, Z., Xue, S., Xu, H., Squires, G., & Rosati, P. 2003, submitted
Kaastra, J.S. 1992, "An X–ray Spectral Code for Optically Thin Plasmas" (Internal SRON–Leiden Report, updated v2.0)
Lidman, C., Rosati, P., Demarco, R., Nonino, M., Mainieri, V. Stanford, S.A., & Toft, S. 2003, A&A, in press
Kurk, J.D., Pentericci, L., Röttgering, H.J.A., Miley, G.K. 2003, MNRAS, in press
Liedhal, D.A., Osterheld, A.L., Goldstein, W.H. 1995, ApJ, 438, L115
Markevitch, M. 1998, ApJ, 504, 27
Markevitch, M., & Vikhlinin, A. 2001, ApJ, 563, 95
Markevitch, M., Gonzales, A.H., David, L., Vikhlinin, A., Murray, S., Forman, W., Jones, C.,& Tucker, W. 2002, ApJ, 567, L27
Romer, K., Viana, P., Liddle, A.R., Mann, R.G. 2001, ApJ, 547, 594
Rosati, P., Della Ceca, R., Burg, R., Norman, C., Giacconi, R. 1998, ApJ, 492, L21
Rosati, P, Stanford, S.A., Eisenhardt, P.R., Elston, R., Spinrad, H., et al. 1999. AJ, 118
Rosati, P., Borgani, S., & Norman, C. 2002, ARA&A, 40, 539
Stanford, S.A., Holden, B.P., Rosati, P., Tozzi, P., Borgani, S., Eisenhardt, P.R., & Spinrad, H. 2001, ApJ, 552, 504
Stanford, S.A., Holden, B.P., Rosati, P., Eisenhardt, P.R., Stern, D., Squires, G., & Spinrad, H. 2002, AJ, 123, 619
Tozzi P., Rosati, P., Ettori S., Borgani, S., Mainieri V., & Norman, C. 2003, ApJ, in press
Scharf, C.A., Smail, I., Ivison, R., Bower, R.G., van Breugel, W., Reuland, M. 2003, ApJ, in press
Venemans, B.P., Kurk, J.D., Miley, G.K., Röttgering, H.J.A., van Breugel, W. et al. 2002, ApJ, 569, L11
Vikhlinin, A., VanSpeybroek, L., Markevitch, M., Forman, W.R., & Grego, L. 2002, ApJL, 578, 107
Warren, S.J. 2002, "Survey and Other Telescope Technologies and Discoveries", SPIE Conference series (astro-ph/0210231)
Wilms, J., Allen, A., & McCray, R. 2000, ApJ, 542, 914

TABLE 1
X-RAY PROPERTIES OF RDCS1252.9–2927 AT $z = 1.237$ *

RA	Dec	$L_{[0.5-2.0]}$ [a]	$L_{[bol]}$ [a]	T_x [b]	$Z_{\rm gas}$ [b]	$M_{\rm gas}$ [c]	$M_{\rm tot}$ [c]
J2000		10^{44} erg s^{-1}	10^{44} erg s^{-1}	keV	$Z_\odot$	$10^{13} M_\odot$	$10^{14} M_\odot$
$12^h52^m54.4^s$	$-29°27'17''$	$1.9^{+0.3}_{-0.3}$	$6.6^{+1.1}_{-1.1}$	$6.0^{+0.7}_{-0.5}$	$0.36^{+0.12}_{-0.10}$	$1.8^{+0.3}_{-0.3}$	$1.9^{+0.4}_{-0.4}$

*Adopted cosmology: $H_0 = 70$ km s^{-1} Mpc^{-1}, $\Omega_m = 0.3$, and $\Omega_\Lambda = 0.7$.

[a] Luminosity within an aperture of $60''$ (or 500 kpc)

[b] From combined *Chandra* and *XMM-Newton* spectral analysis

[c] Mass measured out to $R_{500} = 536 \pm 40$ kpc

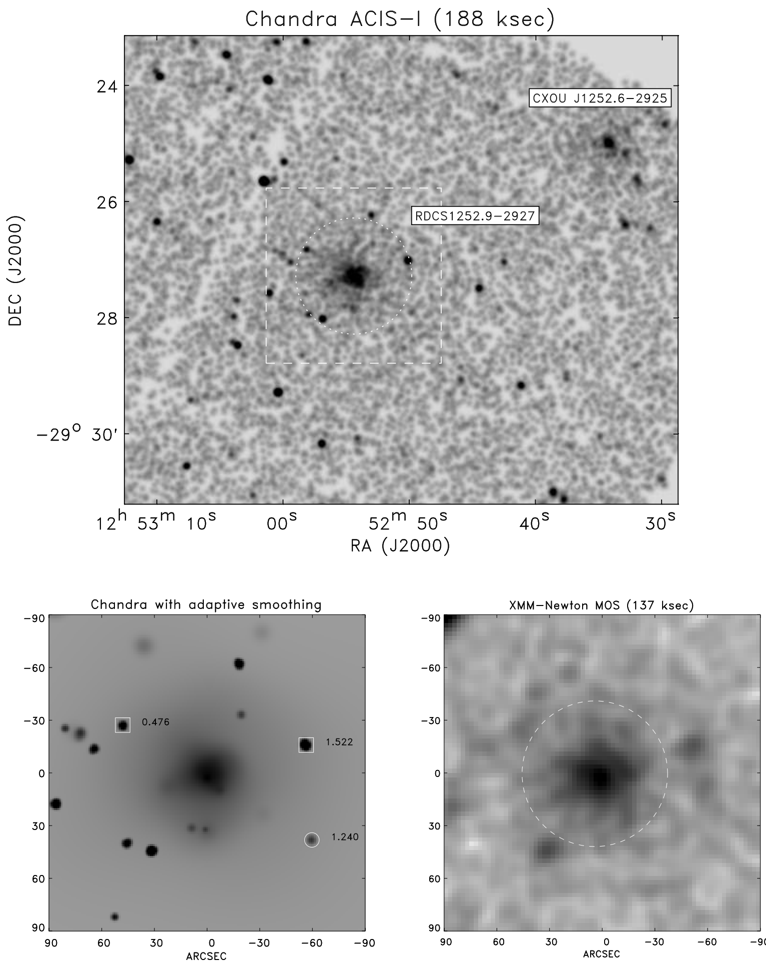

FIG. 1.— Top: Grey scale image of *Chandra* ACIS-I 188 ksec observations in the 0.5-2 keV band showing $9.6' \times 8.1'$ field around RDCS1252.9–2927 (a serendipitous low redshift group, CXOU J1252.6–2925, is also visible). The image has been smoothed by a gaussian with $\sigma = 2''$ and the grey-scale has a square root scaling; the dashed circle shows the $59''$ aperture used to extract spectra. The box marks a $3' \times 3'$ area around RDCS1252 shown in the bottom panels. Left: adaptively smoothed *Chandra* image in logarithmic scale. Sources with spectroscopic redshift are marked, the faint one (circle) is at the cluster redshift. Right: *XMM-Newton* MOS image (137 ksec) in the 0.5-2 keV band. The image has been smoothed by a gaussian with $FWHM = 9''$ and the grey-scale has square root scaling; the spectroscopic aperture of $42''$ radius is also shown.

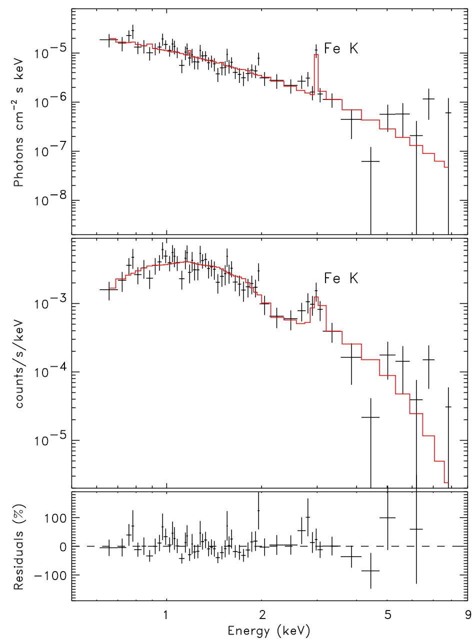

FIG. 2.— X-ray spectrum (data points) and best fit MEKAL model (solid line) from *Chandra* observations (188 ksec) of RDCS1252–2927 at $z_{spec} = 1.237$; from top to bottom: unfolded, folded spectrum and relative residuals; A clear redshifted Fe 6.7 keV line is visible. The spectrum is extracted from a 59″ radius region.

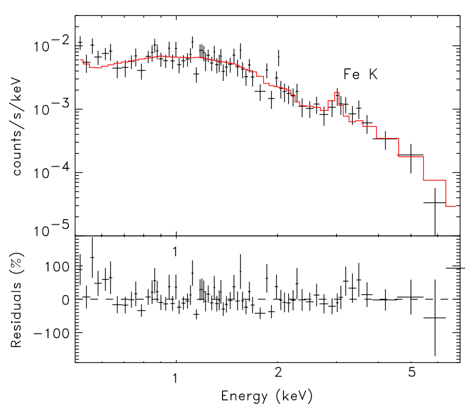

FIG. 3.— X-ray spectrum (data points) and best fit MEKAL model (solid line) from *XMM-Newton* observations (MOS detectors only, 137 ksec) of RDCS1252–2927. The spectrum is extracted from a 42″ radius region.

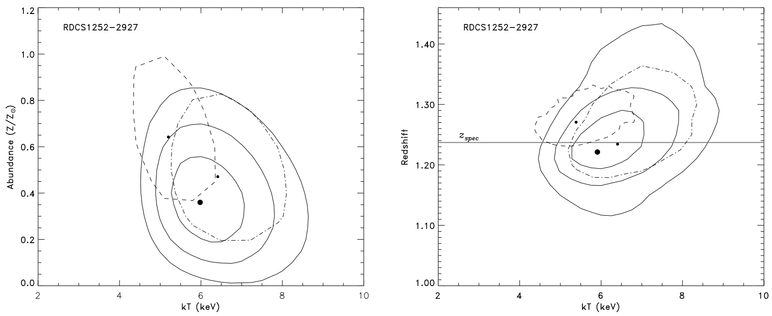

FIG. 4.— Left: best fit temperature and metallicity of the gas obtained by combining *Chandra* ACIS-I and *XMM-Newton* MOS data (solid contours for $1,2,3\sigma$ confidence levels for two interesting parameters). Dashed (dot-dashed) contours show the 1σ levels obtained from the *Chandra* data only, with apertures of $60''$ ($35''$) radius. Right: best fit redshifts and temperatures of the ICM, with the horizontal line marking the spectroscopic redshift based on 36 cluster members.

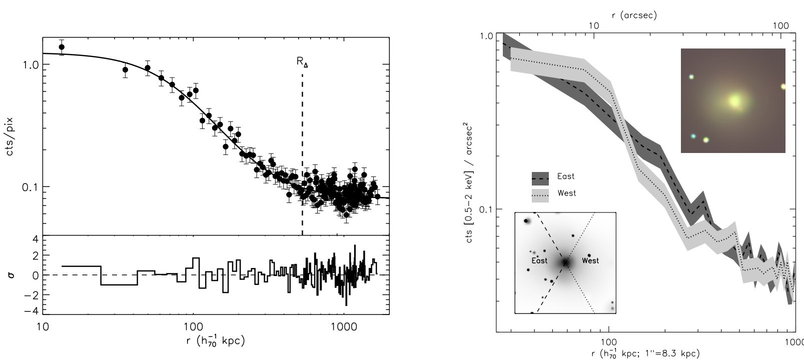

FIG. 5.— Left panel: surface brightness profile of RDCS1252.9–2927 with best fit β-model (solid line) and residuals. $R_\Delta = R_{500}$ indicates the radius within which the total and gas mass are calculated ($1'$ corresponds to 500 kpc at $z = 1.24$ for the adopted cosmology). Right panel: surface brightness profiles azimuthally averaged in two separate sectors over the area shown in the lower left inset; the shaded areas correspond to 1σ error bar. The upper right inset shows the adaptively smoothed, X-ray color image of the cluster core ($2' \times 2'$) showing the asymetric distribution of X-ray emission (see text).

See attached jpeg figure

FIG. 6.— Color composite image showing a $2' \times 2'$ field on RDCS1252.9–2927 at $z = 1.24$ with overlaid *Chandra* contours. The image combines optical and near IR bands from the FORS and ISAAC instruments on the VLT: $B+V$, $R+z$, and $J+K_s$. *Chandra* contours show the smoothed X-ray emission (with a gaussian FWHM of $5''$) at the levels of 3, 5, 10, 20 σ above the background.

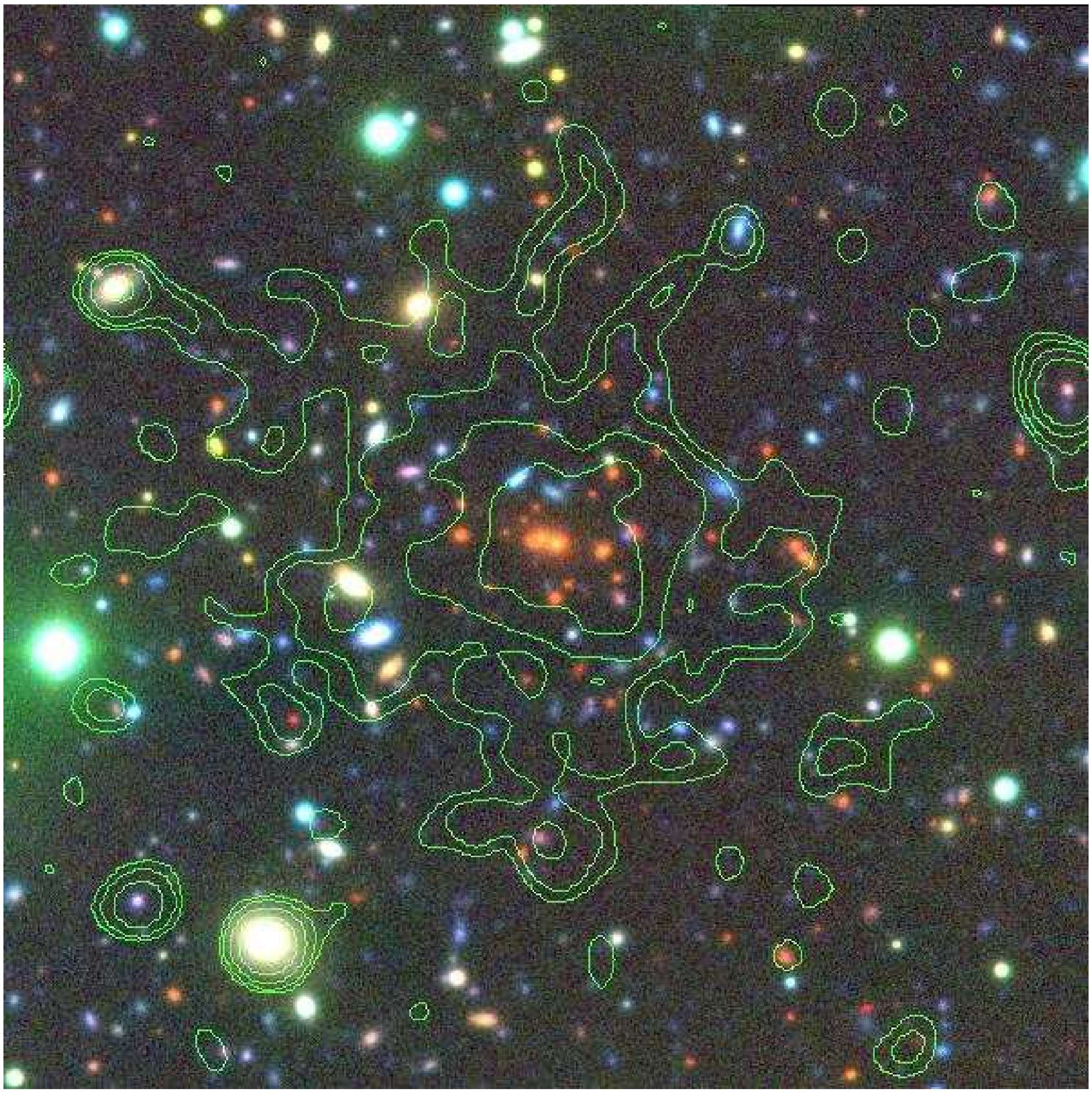

Figure 6.1: Fig. 6 in paper.

Paper accepted in Astronomy & Astrophysics (A&A, 2003)

Astronomy & Astrophysics manuscript no.
(will be inserted by hand later)

Deep near-infrared imaging of RDCS J1252.9-2927 at z=1.237

The colour-magnitude diagram ⋆

C. Lidman[1], P. Rosati[2], R. Demarco[2,3], M. Nonino[4], V. Mainieri[2], S. A. Stanford[5], and S. Toft[6]

[1] European Southern Observatory, Alonso de Cordova 3107, Casilla 19001, Santiago, Chile
[2] European Southern Observatory, Karl-Scwarzschild-Strasse 2, D-85748 Garching, Germany
[3] Institut d'Astrophysique de Paris, 98bis Boulevard Arago, F-75014 Paris, France
[4] Instituto Nazionale di Astrofisica, Osservatorio Astronomico di Trieste, via G.B. Tiepolo 11, I-34131, Trieste, Italy
[5] Department of Physics, University of California at Davis, 1 Shields Avenue, Davis, CA 95616, USA.
[6] Astronomical Observatory, University of Copenhagen, Juliane Maries Vej 30, DK-2100 Copenhagen, Denmark

Received Month DD, YYYY; accepted Month DD, YYYY

Abstract. We present deep SofI and ISAAC near-infrared imaging data of the X-ray luminous galaxy cluster RDCS J1252.9-2927. The ISAAC data were taken at the ESO Very Large Telescope under very good seeing conditions and reach limiting Vega magnitudes of 25.6 and 24.1 in the $J-$ and K_s-bands respectively. The image quality is 0.″45 in both passbands. We use these data to construct a colour-magnitude (C-M) diagram of galaxies that are within 20″ of the cluster center and brighter than $K_s = 24$, which is five magnitudes fainter than the apparent magnitude of a $L^\star$ galaxy in this cluster. The C-M relation is clearly identified as an over-density of galaxies with colours near $J - K_s = 1.85$. The slope of the relation is -0.05 ± 0.02 and the intrinsic scatter is 0.06 magnitudes with a 90% confidence interval that extends from 0.04 to 0.09 magnitudes. Both the slope and the scatter are consistent with the values measured for clusters at lower redshifts. These quantities have not evolved from $z = 0$ to $z = 1.24$. However, significant evolution in the mean $J - K_s$ colour is detected. On average, the galaxies in RDCS J1252.9-2927 are 0.25 magnitudes bluer than early-type galaxies in the Coma cluster. Using instantaneous single-burst solar-metallicity models, the average age of galaxies in the center of RDCS J1252.9-2927 is 2.7 Gyrs.

Key words. galaxies:clusters:general – galaxies:evolution – galaxies:formation – galaxies:photometry

1. Introduction

The tight relation between colour and apparent magnitude for early-type galaxies in massive galaxy clusters (the C-M relation) is seen at all redshifts, from the nearest clusters (Bower, Lucy & Ellis 1992) to the most distant clusters currently known (Rosati et al. 1999, Nakata et al. 2001; van Dokkum et al. 2001; Stanford et al. 2002; Blakeslee et al. 2003, hereafter BFP).

Observations show that although the zero-point of the C-M relation evolves considerably with increasing redshift (Aragón-Salamanca et al. 1993; Stanford et al. 1998, hereafter SED; van Dokkum et al. 2001; Stanford et al. 2002; BFP), the slope of the relation and the scatter about it appear to evolve very little (Ellis et al. 1997; SED, van Dokkum et al. 2000; BFP). However, for some clusters at $z \sim 1$, there is tentative evidence for a flattening in the slope (van Dokkum et al. 2001; Stanford et al. 2002).

Complimentary studies of clusters up to $z \sim 1$ show that significant evolution is also occurring in the galaxy luminosity function (De Propris et al. 1998; Massarotti et al. 2003; Toft, Soucail & Hjorth 2003) and the fundamental plane (van Dokkum et al. 1998, van Dokkum et al. 2003). Early-type galaxies in rich galaxy clusters are uniformly becoming both brighter and bluer as they become younger.

The monolithic collapse scenario of Eggen, Lynden-Bell & Sandage (1962) is an attractive framework to model the observations. In this scenario, the bulk of the stars form in a single burst over a relatively short period of time at redshifts greater than two (Ellis et al. 1997; Bower, Lucy and Ellis, 1992). Hence, the scatter about the C-M relation and the slow steady evolution in the colours and luminosities of early-type galaxies are explained by the great age of the bulk of the stars. Extensions to this model allow future merging and star formation, but the scatter in the C-M relation limits the amount of merging and star formation that can take place (Bower, Kodama & Terlevich 1998).

This picture of passively evolving, very old early-type galaxies in massive clusters should be compared to observations of moderately distant clusters ($z = 0.2$ to $z = 0.8$)

Send offprint requests to: C. Lidman: clidman@eso.org

⋆ Based on observations obtained at the European Southern Observatory using the ESO Very Large Telescope on Cerro Paranal (ESO program 166.A-0701(B)) and the ESO New Technology Telescope on Cerro La Silla (ESO program 61.A-0676(A)).

which show that the fraction of late-type, star-forming galaxies in massive clusters increases with redshift (Dressler et al. 1997; Couch et al. 1998, van Dokkum et al. 2000; Nakata et al. 2001), while the fraction of early-type galaxies does the opposite (Treu et al. 2003; van Dokkum et al. 2000). This picture should also be compared to semi-analytic and direct *N*-body numerical simulations which show that galaxy formation and evolution involves ubiquitous merging at all epochs (Kauffman and Charlot, 1998; Cole et al. 2000; Pearce et al. 2001). The simulations are able to reproduce the slope in the C-M relation and the scatter about it in present day clusters, although some difficulties, particularly at the high mass end, remain (Cole et al. 2000). At higher redshifts, the slope is predicted to flatten and the scatter is predicted to stay approximately constant, although there is a slight increase in the scatter at the bright-end of the C-M relation for clusters with $z > 1$ (Kauffman & Charlot, 1998; Ferreras & Silk 2000).

Thus, there are two quite distinct pictures for the formation of early-type galaxies. In hierarchical merger models, the bulk of the stars form in disk-like galaxies that later merge to become early-type galaxies. In monolithic collapse models, the bulk of the stars form in early-type galaxies and subsequent merging and star formation are limited. In both models, the C-M relation is fundamentally a relation between the dynamical mass of a galaxy and the average metallicity of the stellar population (Faber 1973). In hierarchical merger models, large ellipticals are formed from large spirals, which are better able to retain the metals that result from stellar evolution (Kauffman and Charlot 1998). Similarly, in monolithic collapse models, larger ellipticals are better able to retain their metals. Although age differences can be used to explain the slope of the C-M relation at low redshifts, the slope and the C-M relation itself are lost by $z = 0.2$ (Kodama & Arimoto 1997) if age is the sole reason for the slope.

The morphological evolution that is seen in hierarchical models can lead to a bias (the progenitor bias) in morphologically selected samples (van Dokkum et al. 2000; van Dokkum et al. 2001). The bias causes the progenitors of the youngest low-redshift ellipticals to drop out of morphologically selected high-redshift samples. Consequently, the C-M relation is similar to that of a single-age stellar population formed at very high redshift and the scatter in the relation is approximately redshift independent. The progenitor bias is implicitly included in the semi-analytical simulations described above and allows the star formation history of early-type galaxies in clusters to be considerably more varied than that in monolithic collapse models. The model predicts that the fraction of early type galaxies in clusters decreases with increasing redshift.

The importance of progenitor bias depends on the origin of the scatter in the C-M relation. If the scatter is entirely caused by age differences, then progenitor bias is important. If the scatter is partially caused by other effects, such as dissipationless merging with little subsequent star formation (van Dokkum & Ellis, 2003) or metallicity, then progenitor bias becomes less important and both the average age of the galaxies and the degree to which galaxies form coevally increase. The importance of progenitor bias also depends on the method used to derive C-M relations. C-M relations that are derived from morphological catalogues are more likely to be biased than C-M relations that are derived from photometric or complete spectroscopic catalogues.

Although hierarchical models have become the standard model for describing the formation of early-type galaxies in both cluster and field environments, these models are unable to describe all the observational data. Whereas the hierarchical merging model predicts a dramatic difference in the star formation histories of early-type galaxies in the field and in clusters (Diaferio et al. 2001), only small differences are inferred from observational data (Willis et al. 2002; Treu et al. 2002; Treu 2003; van Dokkum & Ellis 2003). More stringent tests of hierarchical models will come from observations of field and cluster galaxies beyond $z \sim 1$.

In this paper we describe deep near-infrared (NIR) observations of RDCS J1252.9-2927, an X-ray luminous cluster of galaxies at z=1.237 (Rosati et al. 2003). These observations allow us to construct a NIR C-M diagram of one of the most distant massive clusters known to an unprecedented depth and accuracy. Throughout this paper, we assume $\Omega_M = 0.3$, $\Omega_\Lambda = 0.7$ and $H_0 = 70$ km/s/Mpc. In this cosomology, $1'$ on the sky corresponds to approximately 0.5 Mpc at $z = 1.237$. Unless specified otherwise, all colours and magnitudes are on the 2MASS system.

2. Observations

2.1. SofI NIR imaging

As part of an NIR program to confirm high redshift galaxy clusters in the ROSAT Distant Cluster Survey (Rosati et al. 1998), RDCS J1252.9-2927 was observed during the nights of 1998 July 9th, 10th and 11th with SofI (Moorwood, Cuby & Lidman, 1998) on the ESO-NTT at the Cerro La Silla Observatory. SofI is equipped with a Hawaii 1024x1024 HgCdTe array, which, in the large field imaging mode, results in a pixel scale of $0''.29$ per pixel and a field of view of $4'.9$. The observations were done in J and K_s, which, at the redshift of the cluster, approximately correspond to the rest frame $V-$ and $z-$bands.

Individual exposures lasted 10 seconds in K_s and 20 seconds in J and six of these were averaged to form a single image. Between images, the telescope was offset by $10''$ to $30''$ in a semi-random manner.

The data were reduced in the standard way. From each image, the zero-level offset was removed, a flatfield correction was applied, and an estimate of the sky from other images in the sequence was subtracted. Images with the best image quality (better than 0.9") were then registered and combined. A summary of the data is given in Table 1. The central part of the SofI K_s band image is shown in Fig. 1.

The atmospheric conditions at the time the data were taken were very good. Zero Points (ZP) were derived by observing standards from the photometric catalogue of Persson et al. (1998). Several standards were observed during each night. The scatter in the J and K_s ZPs throughout the entire run were less than 0.02 magnitudes. The SofI J and K_s filters are a good match to those used in the LCO (Persson) system, so no colour corrections between the natural SofI system and the

Table 1. A summary of the observations taken with SofI. The image quality is derived from the FWHM of stellar objects in the combined images. The detection limit is the 5σ detection threshold over an 1.″4 diameter aperture, which is approximately twice the stellar FWHM.

Filter	Exposure (seconds)	Image Quality (″)	Detection Limit (Vega magnitudes)
K_s	5400	0.68	21.1
J	5040	0.72	22.5

LCO (Persson) system are made. However, we do transform the magnitudes and colours to the 2MASS system (Carpenter 2001)[1]. Since the 2MASS and LCO systems are very similar, the transformations are small.

We used the SExtractor software (Bertin & Arnouts 1996) to detect objects, to do the photometry and to classify sources as either point like or extended. The colours are derived from the flux within fixed apertures of 6 pixels (1.″73). A small correction (0.02 magnitudes) is applied to the J band data to account for the slightly poorer image quality. The total magnitude was estimated using the "BEST" magnitude in SExtractor. Since many of the sources in the center of the cluster are blended, the total magnitude was more often than not the corrected isophotal magnitude (Bertin & Arnouts 1996).

The flux of non-stellar sources are corrected for galactic extinction. Using $E(B-V) = 0.075$ (Bouwens et al. 2003), the corrections for J and K_s are 0.067 and 0.027 magnitudes respectively. Stellar sources are not corrected for galactic extinction.

About a dozen sources from the 2MASS point source catalogue are visible in the SofI images. The photometry for objects brighter than $J \sim 12.5$ and $K \sim 12$ in the SofI images is generally poor because of detector non-linearity. However, for fainter objects, we can make a comparison between SofI magnitudes and those in the 2MASS catalogue. The variance weighted differences between the magnitudes in the 2MASS catalogue and the SofI derived magnitudes for 9 objects in common is $\Delta J = -0.01$ and $\Delta K_s = 0.02$.

The C-M diagram of objects within 20″ of the cluster center is shown in figure 2. An over-density of galaxies with $J - K_s \sim 1.85$ is clearly seen in this diagram. Over the entire SofI image other populations can be identified. Stars have $J - K_s$ colours that vary between 0 and 1.0, with a well defined peak at $J - K_s = 0.8$, which corresponds to early M-dwarfs, and a less well defined peak at $J - K_s \sim 0.5$, which corresponds to mid-G-dwarfs.

The co-incidence of X-ray emission with two relatively bright galaxies ($K_s \sim 17.5$) and the distinctive sequence of galaxies with $J - K_s \sim 1.85$ showed that RDCS J1252.9-2927 was probably a distant, rich galaxy cluster worthy of a more detailed study. We therefore initiated a program to obtain deep NIR images with ISAAC (this paper), deep optical and comprehensive spectroscopic observations (Rosati et al. 2003, Demarco et al. 2003) and deep X-ray observations (Rosati et al. 2003).

[1] See also http://www.astro.caltech.edu/2mass.

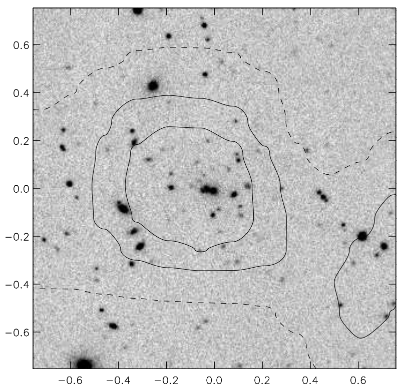

Fig. 1. The central part of the SofI K_s-band image. The 3, 5 and 7σ ROSAT X-ray contours are overlaid (Rosati et al. 1998). North is up and East is to the left. The image is 90″ on a side, which, for the adopted cosmology, is 0.75 Mpc at $z = 1.237$.

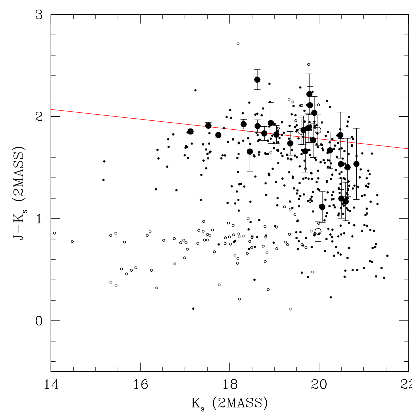

Fig. 2. The C-M diagram of objects in the SofI data. The large symbols are objects that are within 20″ of the cluster center and the small symbols are objects that are beyond 60″ of the cluster center. Objects that have been classified as stellar are plotted with open symbols and non-stellar objects are plotted with solid symbols. No classification is made for objects fainter than $K_s = 20$. The solid line is a fit to the C-M relation that was determined from the ISAAC data.

2.2. ISAAC NIR imaging

RDCS J1252.9-2927 was re-observed with ISAAC (Moorwood et al. 1999) on Antu (VLT-UT1) at the Cerro Paranal Observatory. The observations were done in service mode and the cluster was observed on 25 separate nights, stating on 2001 March 12th and ending on 2001 July 9th.

ISAAC, like SofI, is equipped with a Hawaii 1024x1024 HgCdTe array, which, in the S2 imaging mode, results in a pixel scale of 0.″1484 per pixel and a field of view of 2.′5. The cluster was imaged in J_s and K_s. The J_s filter is slightly narrower and redder than typical J filters and the blue edge of the filter is defined by the filter and not the atmosphere. This results in more stable photometry at the expense of introducing a small colour term.

We did not center the cluster within the ISAAC field of view. Instead we used a series of pointings which put the cluster into the four corners of the array. The resulting union of images covers a region which is slightly smaller than the region covered by the SofI data, but is significantly deeper and has significantly better image quality.

Individual integrations lasted 15 seconds in K_s and 30 seconds in J_s, and four of these were averaged to form a single image. Between images, the telescope was offset by 10″ to 30″ in a semi-random manner, and typically 30 to 40 images were taken in this way in a single observing block. In total, approximately 6 hours in both K_s and J_s were spent at each pointing. Since the cluster center was visible in all pointings, approximately 24 hours is spent on the cluster in both J_s and K_s.

In addition to these deep images, two additional regions that flank the eastern and western edges of the mosaic were observed so that potential cluster galaxies could be identified for later spectroscopic follow-up (Demarco et al. 2003). The total exposure time in each of the these flanking fields is 18 minutes, so the depth in these images considerably shallower that the depth obtained in the center of the mosaic. The details are given in Table 2.

The data were reduced in a similar way to that used for the SofI data, but with following additional steps.

- The difference in the relative level between odd and even columns was removed. The relative difference is a function of the average count level and it evolves with time.
- An electronic ghost, which is most easily seen when there are bright stars in the field of view, was removed.
- Sky subtraction is done with object masking. We used the XDIMSUM package for this step.
- Images were corrected for field distortion, which can amount to several pixels at the edges of the ISAAC field of view.
- Individual images were scaled to a common ZP before being combined.

The atmospheric conditions at the time the data were taken were very good. All but two of the nights were photometric and the image quality on the raw images varied between 0.″25 to 0.″8, with a median around 0.″45. Zero points were derived from the observations of photometric standards from the catalogue of Persson et al. (1998). The ISAAC $J_s - K_s$ colours were transferred to the LCO (Persson) system using the transformation

$$(J - K_s)_{\mathrm{LCO}} = 1.028 * (J_s - K_s)_{\mathrm{ISAAC}} - 0.011.$$

As with the SofI data, the colours and magnitudes were then transferred to the 2MASS system (Carpenter 2001) and only non-stellar sources are corrected for galactic extinction.

The ISAAC data were taken over a large number of nights and, consequently, the image quality over the entire mosaic is slightly variable. The dispersion in the image quality as measured from bright stars over the entire mosaic is about 8% in K_s and 5% in J_s. The median ellipticity is 0.05 and 0.03 for the K_s and J_s images respectively. In the central part of the mosaic, the uniformity of the PSF is considerably better, since the central part of the mosaic is common to all images.

We used the SExtractor software (Bertin & Arnouts 1996) to detect objects, to do the photometry and to classify sources as either point like or extended. The $J - K_s$ colour for objects in the central part of the mosaic are derived from the flux within fixed apertures of 6 pixels (0.″89 diameter). Since the image quality in the central part of the J_s and K_s ISAAC mosaics are very similar, there are no aperture corrections to the $J - K_s$ colours. The photometric errors were calculated independently, since the error in a fixed aperture is larger than the error that one would derive by multiplying the noise in a single pixel by the square root of the number of pixels in the aperture (Labbé et al. 2003).

The independently calibrated SofI images are used to check the photometric accuracy of the ISAAC data. The difference in the absolute calibrations are less than 0.02 magnitudes and the scatter in the $J - K_s$ colour of relatively bright objects ($K_s < 19$) is 0.02 magnitudes over a region that is within 30″ of the cluster center. The scatter increases to 0.03 magnitudes if all objects within the region covered in Fig. 3 are included. The scatter increases with increasing area because image quality becomes more variable as one moves away from the cluster center and all colour measurements are based on aperture magnitudes. Unless otherwise stated, we restrict the measurement of cluster properties in the analysis that follows to those galaxies that lie within 20″ of the cluster center. We also cross checked the photometry of the brightest cluster galaxies. Although there is significant dispersion in the total magnitude, about 0.15 magnitudes, the dispersion in the $J - K_s$ colour is less than 0.02 magnitudes and the mean difference is less than 0.01 magnitudes. The comparison between the independently calibrated SofI and ISAAC data and the comparison between objects in the SofI data and in the 2MASS catalogue suggest that the systematic error in our $J - K_s$ colours is no larger than 0.02 to 0.03 magnitudes.

The central 75″ of the ISAAC K_s band image is shown in Fig. 3. This images can be compared to the image taken with SofI (Fig. 1), and it demonstrates the increased depth and spatial resolution of the ISAAC data.

We mark the spectrally confirmed cluster members (Demarco et al. 2003) that lie fully within Fig. 3 with arrows. With the exception of one cluster galaxy, which has the morphology of an edge on spiral and [OII] emission, the morphologies of the spectrally confirmed cluster members are consistent with the morphologies of early-type galaxies. None of these galaxies show detectable [OII] emission (Demarco et al. 2003). For comparison, three spectrally confirmed field galaxies that lie with 20″ of the cluster center are circled. The colours and morphologies of these three galaxies are quite different to the

Table 2. A summary of the observations taken with ISAAC. The exposure times and detection limits of the mosaic refer to the central part of the mosaic, where the exposures are deepest. In other areas, the exposure time will vary from one quarter to one half of this depending on the overlap. The detection limit is defined as the 5σ detection threshold over an 0.″9 diameter aperture. The image quality is derived from the FWHM of stellar objects in the combined images.

Filter	Region	Exposure (seconds)	Image Quality (″)	Detection Limit (Vega magnitudes)
K_s	Mosaic	81990	0.45	24.1
J_s	Mosaic	86640	0.45	25.6
K_s	Eastern	1080	0.40	21.5
J_s	Eastern	1080	0.43	23.3
K_s	Western	1080	0.32	21.5
J_s	Western	1080	0.40	23.3

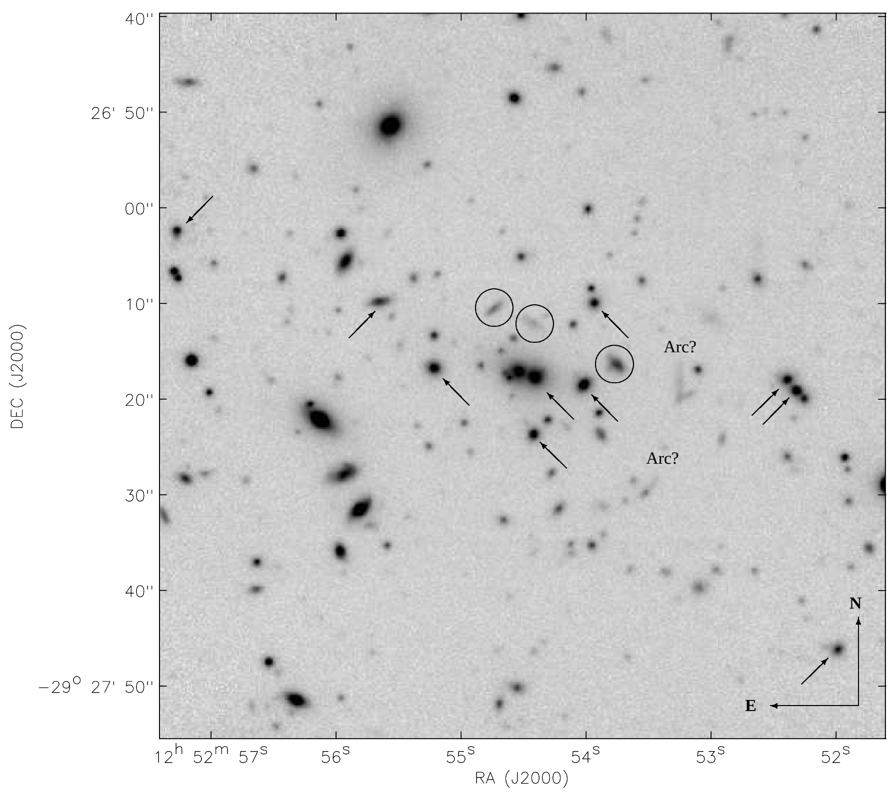

Fig. 3. The central part of the ISAAC K_s-band image. The image is 75″ on a side, which, in the adopted cosmology, corresponds to 0.67 Mpc at $z = 1.237$. The two galaxies near the center of the cluster are 1.″8 apart. Spectrally confirmed cluster members and field galaxies (Demarco et al. 2003) are marked with arrows and circles respectively. Two arc-like features are also marked.

colours and morphologies of the spectrally confirmed cluster members. One appears to be slightly disturbed edge-on spiral and the other two have highly irregular morphologies.

There appears to be two relatively red arc-like features about 20″ from the cluster center. Their shape and distance from the cluster are suggestive of giant gravitational arcs. However, higher resolution imaging and spectroscopy would be needed before conclusions could be drawn.

3. Results

3.1. The colour magnitude diagram

The ISAAC C-M diagram of objects within 20″ of the cluster center is shown in Fig. 4. Objects are plotted as solid symbols if they were classified as extended or as a star if they were classified as a point source. Objects fainter than $K_s < 21$ are not classified and are plotted as solid symbols. Unlike the C-M diagram that was derived from the SofI data (Fig. 2) and for reasons of clarity, objects outside this radius are not plotted. If they were, one would see a similar peak in the colours of stellar-like objects around $J - K_s \sim 0.8$.

Spectrally confirmed cluster members and field galaxies are marked with circles and crosses respectively. The field galaxies are also marked in Fig. 3, and all of them are morphologically distinct from the spectrally confirmed cluster members.

Galaxies that are within 20″ of the cluster center lie on a well defined C-M relation. The line in Fig. 4 is a fit to the galaxies within the blue rectangle (i.e. galaxies with $K_s < 21$, $J-K_s > 1.5$ and $J-K_s < 2.1$) and within 20″ of the cluster center. Even thought the fit has been done for galaxies brighter than $K_s = 21$, the upper envelope in the colour of galaxies that are as faint as $K_s = 24$ is defined by this relation. We also indicate, with boxes in Fig. 4, the location of five spectrally confirmed cluster galaxies that are more than 20″ form the cluster center but within the area bounded by Fig. 3. These cluster galaxies also lie on the C-M relation.

Recently, Labbé et al (2003) measured the galaxy number counts to very faint NIR magnitudes. We have used their results to estimate that, to $K_s = 21$, six field galaxies are expected within 20″ of the cluster center, which is considerably fewer than the 36 galaxies we do observe. We do not separate field and cluster galaxies when fitting the C-M relation, since the three spectrally confirmed field galaxies are already excluded by our colour cuts, i.e. they lie outside the blue rectangle in Fig. 4, and the remaining small number of unidentified field galaxies are unlikely to bias our fit.

The fit to the C-M relation was determined by adjusting the amount of intrinsic scatter that had to be added to the data until the reduced χ^2 was one. A floor to the error in the colour, as determined by comparing the colours of the brightest galaxies in the ISAAC and SofI data, was set to 0.02 magnitudes. Only those objects within the blue rectangle in Fig. 4 were used in the fit. Separate fits were done for regions of different radii centered on the cluster. In all cases, the dominant source of scatter is the intrinsic scatter. For completeness, we also report the fit to the slope of the C-M relation without adding additional scatter. The fits, the observed scatter and the inferred intrinsic scatter are reported in Table 3.

In measuring the intrinsic scatter, it is imperative that measurement errors are accurately estimated. We checked the accuracy of our measurement errors by adding artificial galaxies directly to the reduced data and by processing the artificial and real data in an identical manner. The errors estimated in this way are in excellent agreement with the errors that are estimated from the image noise. Representative error bars are plotted in lower part of Fig. 4 for galaxies with apparent magnitudes of $K_s = 18$, 19, 20 and 21.

We also used this technique to check for biases in the photometry. There is a tendency for the SExtractor BEST magnitude to miss an increasing fraction of the flux as objects become fainter. However, the error is less than 0.2 magnitudes over the magnitude range in which the fit to the C-M relation is done. Aperture magnitudes and the colours that are derived from them are unbiased.

The slope of the C-M relation is -0.05 magnitudes per magnitude, which is quite similar to the slope measured in clusters with redshifts up to $z \sim 0.9$ (SED). If the fit is done using aperture magnitudes instead of the total magnitudes, the slope steepens slightly, although the change is within the measurement error. The scatter about the relation is unchanged. If the fit was repeated just for the spectrally confirmed cluster galaxies that are marked in figure 3, the fitted slope and the measured scatter are also similar.

Recent observations of clusters above $z \sim 1$ have pointed to a possible flattening in the slope (van Dokkum et al. 2001; Stanford et al. 2002). We see no evidence for a flattening in the slope of the C-M relation in RDCS J1252.9-2927. The dotted line in Fig. 4 is how the C-M relation of the Coma cluster would appear if it were moved to the redshift of RDCS J1252.9-2927 (Rosati et al. 1999). Within the measurement uncertainties the slope for RDCS J1252.9-2927 is the same, but the $J-K_s$ colours of galaxies in RDCS J1252.9-2927 are on average 0.25 magnitudes bluer. This result is consistent with the trend seen in SED.

We estimate the intrinsic scatter to be 0.06 magnitudes with a 90% confidence interval from 0.04 to 0.09 magnitudes. This is similar to the scatter seen in clusters with redshifts up to $z \sim 0.9$ (SED). Even, if we have grossly overestimated the measurement errors, which is unlikely, the intrinsic scatter cannot be much larger than the measured scatter (0.06-0.08 magnitudes).

Within 20″ (0.16 Mpc) of the cluster center, 90% of galaxies brighter than $K_s = 21$, which is approximately 2.5 magnitudes fainter than the apparent magnitude of an $L^\star$ galaxy in this cluster (Toft et al. 2003) and 3.5 magnitudes fainter than the brightest cluster members, lie on the C-M relation. Three of the seven galaxies that do not lie on the sequence were found to be non-cluster members from follow-up spectroscopy. Of the other four, one is redder than the C-M relation and the other three are fainter than $K_s = 20$. There is no progenitor bias in the central regions of this cluster.

The average colour of a $L^\star$ galaxy in RDCS J1252.9-2927 is $J - K_s \sim 1.85$. This is similar to the colours measured for the early-type galaxies in RX J0848.9+4452 at $z = 1.26$

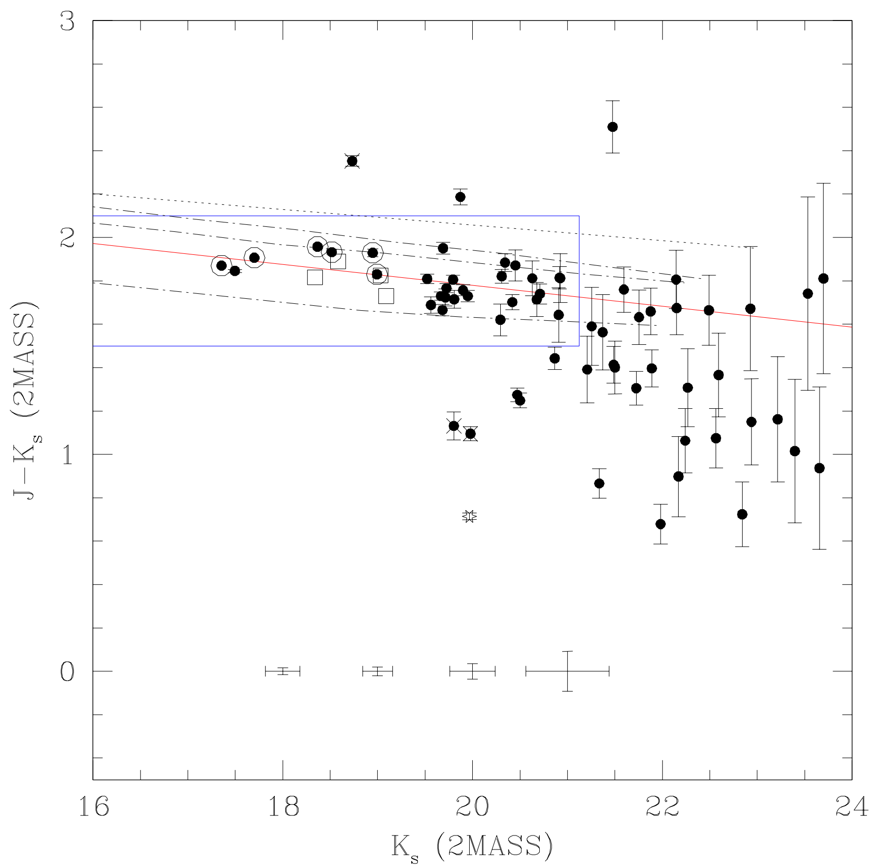

Fig. 4. The C-M diagram of objects within 20″ of the cluster center. The diagram is generated from the ISAAC data. The solid circles represent objects that have been classified as extended and the stellar symbol represents the object that was classified as a star. Spectrally confirmed cluster members are circled and spectrally confirmed field galaxies are marked with an "X". The solid red line is a fit to the C-M relation of galaxies within the blue rectangle (see text) and the dotted line is where the E/S0 sequence of the Coma cluster would lie if it were placed at z=1.24. The dot-dashed lines are monolithic collapse models (Kodama & Arimoto 1997). From top to bottom they represent formation redshifts of z = 2, 3 and 5. The error bars that are located near the bottom of the plot indicate the size of the colour and magnitude errors. Also plotted, as open squares, are the spectrally confirmed cluster members that are more than 20″ from the cluster center but within the field of view of Fig. 3.

(Rosati et al. 1999), which have $J - K \sim 1.85$ on the UKIRT system. However, the transformation between the UKIRT and 2MASS systems is uncertain, so it is not clear how comparable the average colour of galaxies in these two clusters are. Using the transformation equations in Hawarden et al. (2001), the colours agree very well, but using the transformation equations of Carpenter (2001), one would find that the early-type galaxies RX J0848.9+4452 are 0.1 magnitudes redder.

3.2. The epoch of galaxy formation

We have used the monolithic collapse models of Kodama and Arimoto (1997) to illustrate how the C-M relation changes with formation redshift. In these models, star formation occurs during gas infall and terminates when the energy from supernovae ejecta exceeds the binding energy of the gas. Larger galaxies are able to hold onto their gas longer, and, consequently, star formation occurs over a more extended period of time and they

Table 3. The fit to the C-M relation. Only objects within the blue rectangle of Fig. 4 are used in the fit.

Radius ($''$)	Number of Objects	Slope[1]	Slope[2]	Observed Scatter	Intrinsic Scatter	90% confidence region for intrinsic scatter
10	14	-0.046	-0.058 ± 0.017	0.066	0.060	0.039 to 0.091
15	19	-0.052	-0.055 ± 0.015	0.068	0.058	0.041 to 0.086
20	29	-0.046	-0.048 ± 0.015	0.082	0.070	0.052 to 0.093

Notes:
[1] No added scatter
[2] With additional scatter

have higher mean metallicities. Three models (with $z_f = 2{,}3$ and 5, where z_f is the redshift of formation) are plotted in Fig. 4 as the dot-dashed lines. They reproduce the measured slope very well and would suggest that the bulk of the stars in this cluster formed between $z = 2$ and $z = 3$.

We have also used the simple stellar population (SSP) synthesis models of Bruzual and Charlot (2003) to estimate the mean age and the age spread of galaxies in the center of RDCS J1252.9-2927. We use $J - K_s = 1.85$, which is the average colour of a $L^\star$ galaxy in the cluster, and a spread in colours from $J-K_s = 1.79$ to $J-K_s = 1.91$ to estimate the mean age and the age spread. If we assume that the spread in colours is entirely due to age difference, then, for instantaneous single-burst models with solar metallicity, a mean age of approximately 2.7 Gyrs and an age spread from 2.2 to 3.2 Gyrs are derived. These correspond to a mean formation redshift of $z_f = 2.8$ and a spread in formation redshifts from $z_f = 2.4$ to 3.6. The upper limits are highly uncertain. An increase of 0.01 magnitudes in $J - K_s$, which is smaller than our estimate of the systematic error, will move the upper limit beyond $z_f = 5$. The model colours in these simple models do not get much redder than $J - K_s = 1.93$ for solar metallicities.

If these models are allowed to evolve passively to $z = 0.5$, the corresponding scatter in $J - K_s$ evolves to less than 0.01 magnitudes, which is considerably less than the scatter measured in SED. However, we caution that there are differences in the way C-M relations in this paper and Stanford et al. have been built. The C-M relation in this paper is created from the central 0.33 Mpc of the cluster, whereas those of SED are created from larger areas. With additional optical and spectroscopic data on RDCS J1252.9-2927, one will be able to extend the area over which the C-M relation is derived so that a more robust comparison can be made.

Since the observed scatter in $J - K_s$ does not change from $z = 1.237$ to the present day, and since the scatter in SSP and monolithic collapse models should decrease as time goes on, it seems unlikely that the observed scatter in RDCS J1252.9-2927 is solely due to age differences. Alternative reasons for the scatter are metallicity variations at constant luminosity and/or dissipationless merging with little subsequent star formation. Such mergers may have already been identified in both cluster and field environments (vanDokkum et al. 1999; van Dokkum et al. 2001; van Dokkum et al. 2003).

If most of the scatter is due to metallicity differences, the mean age of formation does not change, but the range of redshifts over which galaxies would have formed narrows. If most of the scatter is due to dissipationless merging, then, in the monolithic collapse models of Kodama and Arimoto (1997), the mean age increases and the formation redshift is pushed higher, because galaxies will move left and down in the C-M diagram after the merging has taken place. The directions that galaxies move depend on the relative masses and metallicities of the progenitors.

The derived formation epoch is directly related to the assumed metallicity and the star formation history. If a lower metallicity was assumed, an earlier formation epoch would be derived. This is the well known age-metallicity degeneracy, and the NIR imaging data that is presented here cannot break the degeneracy. An advance in this area will require a comparison between deep spectroscopic data and the most recent stellar population synthesis models (Bruzual & Charlot 2003). However, in the SSP models that have been used here, the galaxies in RDCS J1252.9-2927 cannot be much metal poorer than solar, otherwise the formation epoch is pushed beyond the big bang. Additionally, the metallicity of the intra-cluster medium in this cluster is ~ 0.4 times solar (Rosati et al. 2003).

4. Conclusions

We have obtained very deep, $J-$ and K_s-band images of the X-ray luminous galaxy cluster RDCS J1252.9-2927 at $z = 1.237$ with ISAAC on the ESO VLT and with SofI on the ESO NTT. The data enable us to construct a $J-K_s$ versus K_s C-M diagram to $K_s = 24$, which is five magnitudes below $L^\star$ (Toft et al. 2003).

Galaxies within $20''$ of the cluster center define a tight C-M relation. The slope of the relation is -0.05 magnitudes per magnitude and is similar to the slope measured in clusters at lower redshifts (SED). This strengthens the hypothesis that the slope in the C-M relation is due to metallicity and not age. We see no evidence for a flattening in the slope as predicted in hierarchical models and tentatively observed in clusters at $z \sim 1$ (van Dokkum et al. 2001; Stanford et al. 2002).

More than 90% of the galaxies within $20''$ of the cluster center and brighter than $K_s = 21$ lie on the C-M relation. There is no progenitor bias in the centre of this cluster.

The intrinsic scatter in the $J - K_s$ colour of galaxies about the C-M relation in RDCS J1252.9-2927 is 0.06 magnitudes and is similar to the scatter measured in clusters from $z = 0$ to $z \sim 0.9$ (SED). Hence, the scatter has not evolved from $z = 1.24$ to the present day. This weakens the hypothesis that the scatter in the C-M relation is solely due to age. Dissipationless merging and metallicity variations at constant luminosity could also contribute to the scatter. We also see no evidence for increased scatter in the colours of galaxies at the bright end of the C-M relation.

Our results can be compared to those derived from high-resolution optical images of RDCS J1252.9-2927 that were taken with the Advanced Camera for Surveys on the Hubble Space Telescope in the F775W and F850LP filters. BFP find a tight C-M relation in the $i_{775} - z_{850}$ versus z_{850} C-M diagram, and they show that neither the slope of this C-M relation nor the scatter about it have evolved from $z = 0$ to $z = 1.24$. This concurs with the findings of this paper.

Using instantaneous, single-burst, solar-metallicity models, the average age of the bulk of the stars in the center of the cluster is 2.7 Gyrs. This corresponds to a formation redshift of $z_f = 2.8$. If the scatter about the CM relation is due to age, most of the galaxies in the center of this cluster were formed between $z = 2.4$ and $z = 3.6$.

Acknowledgements. This work would not have been possible without the dedicated efforts of ESO staff, both in Chile and Europe. We are grateful to Dr. Tadayuki Kodama for providing us with a copy of his models. We'd also like to thank Drs. Gustavo Bruzual and Stephane Charlot for providing us with a copy of their stellar evolution models prior to publication.

References

Aragón-Salamanca, A., Ellis, R. S., Couch, W. J., & Carter, D. 1993, MNRAS, 262, 764
Bertin, E. & Arnouts, S. 1996, A&AS, 117, 393
Bouwens. R. J., Illingworth, G. D., Rosati, P. et al. 2003, ApJ, in press
Bower, R. G., Lucey, J. R., & Ellis, R. S. 1992, MNRAS, 254, 601.
Bower, R. G., Kodama, T., & Terlevich, A. 1998, MNRAS, 299, 1193
Blakeslee, J. P., Franx, M., Postman, M. et al. 2003, ApJL, submitted (BFP)
Bruzual, G. & Charlot, S. 2003, MNRAS, in press
Carpenter, J. M. 2001, AJ, 121, 2581
Cole, S., Lacey, C. G., Baugh, C. M. & Frenk, C. S. 2000, MNRAS, 319, 168
Couch, W. J., Barger, A. J., Smail, I., Ellis, R. S., & Sharples, R. M. 1998, ApJ, 497, 188
Demarco et al. 2003, in preperation
De Propris, R., Stanford, S. A., Eisenhardt, P. R., Dickinson, M. & Elston, R. 1998, AJ, 118, 719
Diaferio, A., Kauffmann, G., Balough et al. 2001, MNRAS, 323, 999.
Dressler, A., Oemler, A., Couch, W. J., et al. 1997, ApJ, 1997, 490, 577
Eggen, O., Lynden-Bell, D. & Sandage, A. R. 1962, ApJ, 136, 748
Ellis, R. S., Smail, I., Dressler, A., et al. 1997, ApJ, 483, 582
Hawarden, T. G., Leggett, S. K., Letawsky, et al. 2001, MNRAS, 325, 563
Faber, S. M. 1973, ApJ, 179, 731
Ferreras, I. & Slik, J. 2000, ApJ, 532, 193.
Kauffmann, G. & Charlot, S. 1998, MNRAS, 294, 705
Kodama, T. & Arimoto, N. 1997, A&A, 320, 41
Labbé, I., Franx, M., Rudnick, G., et al. 2003, ApJ, 125, 1107
Massarotti, M., Busarello, G., La Barbera, F. & Merluzzi, L. 2003, A&A, 404, 75
Moorwood, A., Cuby, J.-G., & Lidman, C. 1998, ESO Messenger, 91, 9
Moorwood, A., Cuby, J.-G., Ballester, P., et al. 1999, ESO Messenger, 95, 1
Nakata, F., Kajisawa, M., Yamada, T., et al. 2001, PASJ, 53, 1139
Pearce, F. R., Jenkins, A., Frenk, C. S., et al. 2001, MNRAS, 326, 649
Persson, S. E., Murphy, D. C. Krzeminski, W., Roth, M. & Rieke, M. J. 1998, AJ, 116, 2475
Rosati, P., della Ceca, R., Norman, C., & Giacconi, R. 1998, ApJ, 492, L21
Rosati, P., Stanford, S. A., Eisenhardt, P. R., et al. 1999, AJ, 118, 76
Rosati, P. 2003, in preparation.
Rosati, P., Tozzi, P., Ettori, S. et al. 2003, submitted.
Stanford, S. A., Eisenhardt, P. R., & Dickinson, M. 1998, ApJ, 492, 461 (SED)
Stanford, S. A., Holden, B., Rosati, P. et al. 2002, AJ, 123, 619
Toft S., et al. 2003, in preparation
Toft, S., Soucail, G. & Hjorth, J. 2003, MNRAS, in press (astro-ph/0303066)
Treu, T. 2003, The Formation of Early-Type Galaxies: Observations to z=1. To appear in Clusters of Galaxies: Probes of Cosmological Structure and Galaxy Evolution, ed. J. S. Mulchaey, A. Dressler, & A. Oemler, Carnegie Observatories Astrophysics Series, vol 3 (astro-ph/0307281)
Treu, T., Stiavelli, M., Casertano, S. Møller & Bertin, G. 2002, ApJL, 564, L13.
Treu, T, Ellis, R. S., Kneib, J.-P., et al. 2003, ApJ, 591, 53
van Dokkum, P. G., & Franx, M. 2001, ApJ, 553, 90
van Dokkum, P. G. & Stanford, S. 2003, ApJ, 585, 78
van Dokkum, P. G. & Ellis, R. S. 2003, ApJL, 595, L53.
van Dokkum, P. G., Franx, M., Kelson, D. D. & Illingworth, G. D. 1998, ApJL, 504, L17
van Dokkum, P. G., Franx, M., Fabricant, D., Kelson, D. D. & Illingworth, G. D. 1999, ApJL, 520, L95
van Dokkum, P. G., Franx, M., Fabricant, D., Illingworth, G. D., & Kelson, D. 2000, ApJ, 541, 95
van Dokkum, P. G., Stanford, S. A., Holden, B. P., et al. 2001, ApJL, 552, L101
Willis, J. P., Hewett, P. C., Warren, S. J. & Lewis, G. F. 2002, MNRAS, 337, 953.

Paper accepted in The Astrophysical Journal Letters (ApJL, 596, 143. 2003)

TO APPEAR IN ApJ LETTERS, 20 OCTOBER 2003.
Preprint typeset using LaTeX style emulateapj v. 11/12/01

ADVANCED CAMERA FOR SURVEYS PHOTOMETRY OF THE CLUSTER RDCS 1252.9–2927: THE COLOR-MAGNITUDE RELATION AT Z = 1.24

JOHN P. BLAKESLEE[1], MARIJN FRANX[2], MARC POSTMAN[1,3], PIERO ROSATI[4], BRAD P. HOLDEN[5]
G. D. ILLINGWORTH[5], H. C. FORD[1], N. J. G. CROSS[1], C. GRONWALL[6], N. BENÍTEZ[1], R. J. BOUWENS[1],
T. J. BROADHURST[7], M. CLAMPIN[3], R. DEMARCO[4], D. A. GOLIMOWSKI[1], G. F. HARTIG[3], L. INFANTE[9]
A. R. MARTEL[1], G. K. MILEY[2], F. MENANTEAU[1], G. R. MEURER[1], M. SIRIANNI[1], R. L. WHITE[1,3]
To appear in ApJ Letters, 20 October 2003.

ABSTRACT

We investigate the color-magnitude (CM) relation of galaxies in the distant X-ray selected cluster RDCS 1252.9–2927 at $z=1.24$ using images obtained with the Advanced Camera for Surveys (ACS) on the *Hubble Space Telescope* in the F775W and F850LP bandpasses. We select galaxies based on morphological classifications extending about 3.5 mag down the galaxy luminosity function, augmented by spectroscopic membership information. At the core of the cluster is an extensive early-type galaxy population surrounding a central pair of galaxies that show signs of dynamical interaction. The early-type population defines a tight sequence in the CM diagram, with an intrinsic scatter in observed (i_{775}–z_{850}) of 0.029 ± 0.007 mag based on 52 galaxies, or 0.024 ± 0.008 mag for ~ 30 ellipticals. Simulations using the latest stellar population models indicate an age scatter for the ellipticals of about 34%, with a mean age $\tau_L \gtrsim 2.6$ Gyr (corresponding to $z_L \gtrsim 2.7$), and the last star formation occurring at $z_{\rm end} \gtrsim 1.5$. Transforming to rest-frame (U–B), we conclude that the slope and scatter in the CM relation for morphologically selected early-type galaxies show little or no evidence for evolution out to $z \approx 1.2$. Thus, elliptical galaxies were already well established in X-ray luminous clusters when the universe was a third of its present age.

Subject headings: galaxies: clusters: individual (RDCS 1252.9–2927) — galaxies: elliptical and lenticular, cD — galaxies: fundamental parameters — cosmology: observations

1. INTRODUCTION

Present-day cluster ellipticals are a remarkably well-behaved class of objects, with structural and chemical properties obeying simple power-law scaling relations. But this could not always have been the case in a hierarchical universe. While most galaxy formation models can be tuned to reproduce these relations at $z=0$, a more stringent test lies in reproducing their evolution with redshift. To this end, it is important to study rich clusters out to the highest redshifts, when fractional age differences among the galaxies were proportionately greater. In recent years, deep wide-field optical surveys and deep serendipitous X-ray surveys have uncovered significant numbers of rich galaxy clusters to redshift unity and beyond (see reviews by Postman 2002; Rosati 2003). These most distant, and most massive, of known gravitationally bound structures can then be studied in detail through targeted, high-resolution, follow-up optical and near-infrared observations.

We have undertaken a survey of rich galaxy clusters in the redshift range $0.8 < z < 1.3$ using the Advanced Camera for Surveys (ACS; Ford et al. 2002) on the *Hubble Space Telescope* (*HST*). The aim of this survey is to establish new constraints on the cluster formation epoch and the evolution of early-type galaxies. The first cluster observed, RDCS 1252.9–2927 (hereafter RDCS 1252) at $z=1.237$ (Rosati 2003; Rosati et al. 2003), was discovered as part of the ROSAT Deep Cluster Survey (Rosati et al. 1998) and is among the highest-redshift galaxy clusters with spectroscopic confirmation. This Letter presents the first results from our ACS cluster survey, focusing on the color-magnitude (CM) relation of the early-type galaxies in RDCS 1252. We adopt the best-fit WMAP cosmology: $(h, \Omega_m, \Omega_L) = (0.71, 0.27, 0.73)$ (Bennett et al. 2003), giving a scale of 8.4 kpc per arcsec at $z=1.237$.

2. OBSERVATIONS AND IMAGE REDUCTIONS

RDCS 1252 was observed in the F775W and F850LP bandpasses (hereafter i_{775} and z_{850}, respectively) with the ACS Wide Field Camera as part of the guaranteed time observation program (proposal 9290) during 2002 May and 2002 June. The observations were done in a 2×2 mosaic pattern, with 3 and 5 orbits of integration in i_{775} and z_{850}, respectively, at each of the four pointings. There was nearly $1'$ of overlap between pointings; thus, the core of cluster was imaged for a total of 12 orbits in i_{775} and 20 orbits in z_{850}.

The data were processed with the "Apsis" pipeline described by Blakeslee et al. (2003), with some recent updates. In particular, we used a version of the drizzle software (Fruchter & Hook 2002) supplied by R. Hook that implements the "Lanczos3" interpolation kernel (a damped sinc function). This kernel produces a sharper point spread function (PSF) and greatly reduces the noise correlation of adjacent pixels and the resulting "moire" patterns. Apsis also now removes discontinuities in the residual bias level at the amplifier boundaries, producing a more

[1] Department of Physics & Astronomy, Johns Hopkins University, Baltimore, MD 21218; jpb@pha.jhu.edu
[2] Leiden Observatory, P.O. Box 9513, 2300 Leiden, The Netherlands
[3] Space Telescope Science Institute, 3700 San Martin Drive, Baltimore, MD 21218
[4] European Southern Observatory, Karl-Schwarzschild-Str. 2, D-85748 Garching, Germany
[5] Lick Observatory, University of California, Santa Cruz, CA 95064
[6] Department of Astronomy & Astrophysics, The Pennsylvania State University, University Park, PA 16802.
[7] The Racah Institute of Physics, Hebrew University, Jerusalem 91904, Israel

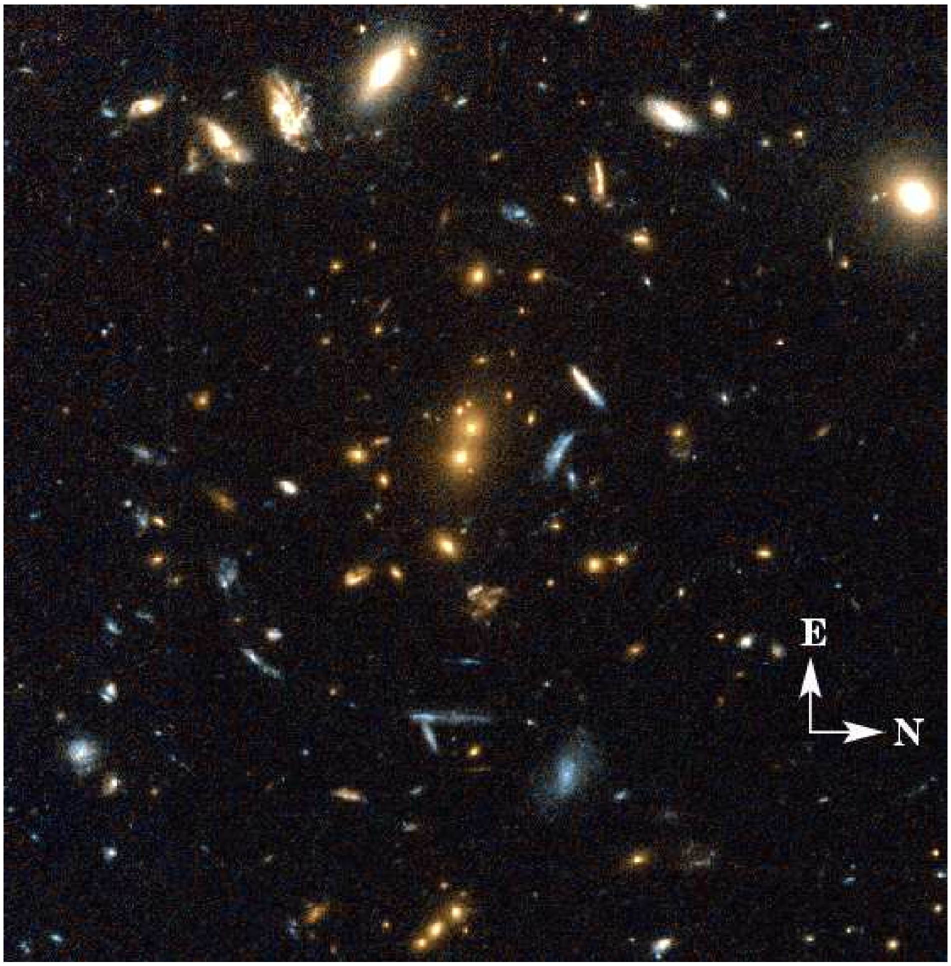

FIG. 1.— Color composite of the core region of RDCS 1252, constructed from our ACS/WFC F775W and F850LP images, shown in the observed orientation. The displayed field size is roughly $1'$ across, or less than 4% of the full mosaic.

uniform background. An earlier processing of these images has been used by Bouwens et al. (2003) for a study of the faint i_{775} dropout population at $z \sim 6$. We calibrate our photometry to the AB system using photometric zero points of 25.640 (i_{775}) and 24.843 (z_{850}). These are uncertain at the ~ 0.02 mag level, which has no effect on our conclusions. We adopt a Galactic reddening for this field of $E(i\text{–}z) = 0.041$ mag based on the Schlegel et al. (1998) dust maps.

3. OBJECT SELECTION AND PHOTOMETRY

Figure 1 shows the central $\sim 1'$ region of a color composite made from our reduced i_{775} and z_{850} images. A red galaxy population is clearly visible. The central pair of galaxies are separated by $1\farcs8$ (15 kpc) and are each of magnitude $z_{850} \approx 21$. We used SExtractor (Bertin & Arnouts 1996) in "dual-image mode" with low threshold and deblending settings to find objects in the reduced images and perform the initial photometry. SExtractor "MAG_AUTO" values were used for the total magnitudes. The (i_{775}–z_{850}) color effectively separates out evolved galaxies at $z \gtrsim 1$, and the cluster is obvious as a central concentration of galaxies with $0.80 < (i_{775}\text{–}z_{850}) < 1.05$. Figure 1b [removed from the ApJL version in order to meet the page limit] shows histograms of isophotal color within 3 different radii of the cluster center (defined midway between the two central galaxies) for galaxies with total z_{850} = 20–25 mag.

We selected an initial sample of 312 nonstellar objects with $z_{850} < 24.8$, in the broad isophotal color range $0.5 < (i_{775}\text{–}z_{850}) < 1.2$, and inside a radius of $1\farcm92$. Our goal is to study the early-type galaxy population in RDCS 1252, for which we have limited spectroscopic data, and these cuts are designed to select the vast majority of our target sample while reasonably limiting foreground/background contamination. The color selection is roughly 7 times broader than the full-width of the red sequence we find below. The radial cutoff corresponds to about 1.0 Mpc for both our adopted WMAP cosmology and an Einstein-deSitter cosmology with $h = 0.5$.

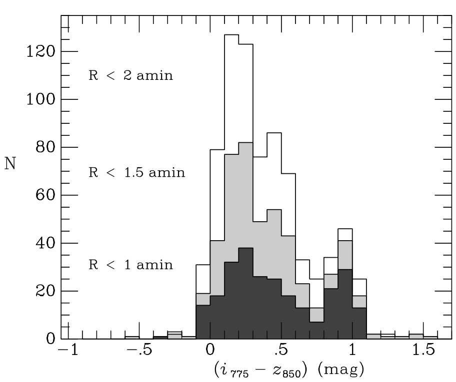

"FIG. 1b."— Histograms of (i_{775}–z_{850}) color for objects having $20 < z_{850} < 25$ and within the specified radii of the center of RDCS 1252. The cluster galaxies are near (i_{775}–z_{850}) = 0.95, and make up an increasing fraction of the objects within progressively smaller radii. [This figure was removed from the published version because of space limitations.]

Our final colors are measured within galaxy effective radii R_e to avoid biasing the CM slope due to color gradients. We follow the basic approach outlined by van Dokkum et al. (1998, 2000). We derive the R_e values using the program "galfit" (Peng et al. 2002) by fitting each galaxy to a Sersic model (convolved with the PSF), but constraining the n parameter such that $1 \leq n \leq 4$. Bright neighboring galaxies were fitted simultaneously. We note that subtraction of the model for the two central galaxies reveals evidence for interaction in the form of an S-shaped residual.

Next, we deconvolve i_{775} and z_{850} postage stamp images of each galaxy using the CLEAN algorithm (Högborn 1974) in order to remove the differential blurring effects of the PSF, which is ~ 10% broader in the z_{850} band. To reduce noise, the CLEAN maps are smoothed with a Gaussian of FWHM = 1.5 pix before adding the residual images to the maps to ensure flux conservation. We then measure the i_{775} and z_{850} magnitudes of each galaxy within a circular aperture of radius R_e, typically about 6 pix, or $0\farcs3$. We did not allow the radius to drop below 3 pix. Photometric errors were determined empirically from the pointing overlap regions. We reprocessed the 4 pointings separately and measured the color differences within R_e for 202 pairs of measurements for 74 different early-type galaxies (classifications described below) in the overlap regions. We then median-filtered to obtain the errors as a smooth function of magnitude. The error thus determined for single-pointing (i_{775}–z_{850}) measurements at z_{850} = 23 was 0.025 mag, rising to ~ 0.05 mag at z_{850} = 24.5.

Each galaxy in our initial sample was examined and morphologically classified, following a procedure similar to that of Fabricant et al. (2000). This was done independently of the profile fitting, but the types show a good correlation with Sersic n index. Here, we simply distinguish between E, S0, and later types, where the intermediate S0 class indicates the apparent presence of a disk without spiral or other structure. Full details on the classifications for a much larger sample, including the spatial distribution of the various types, will be presented by Postman et al. (2003, in preparation). About 180 galaxies in this field have measured redshifts, obtained with VLT/FORS (Rosati et al. 2003, in preparation), with 31 being cluster members. All galaxies in our initial sample classified as early-type, and not known to be interlopers from their spectra, are included in our CM analysis in the following section. Of the 31 known members, 22 are classified as early-type, and we include all of these in our analysis even though one (an S0) happened to lie beyond our 1 Mpc cutoff.

4. THE COLOR-MAGNITUDE RELATION AT $z = 1.24$

We fitted the early-type galaxy CM relations using simple linear least squares; other methods gave very similar results. We estimate the scatter from both the standard rms and the biweight scale estimator (Beers et al. 1990). No rejection was done in fitting subsamples composed of known members, the faintest of which has z_{850} = 23.48, or $\sim 0.5 L_B^*$. We also performed fits to samples with unconfirmed members, allowing us to go 1 mag further down the galaxy luminosity function. However, here we iterate to reject the 3-σ outliers, as these are likely to be interlopers: none of the 22 confirmed early-type members is more than 2.3-σ discordant. After the iterative rejection process, we find concordant scatters for those samples, and the rms and biweight estimator are the same to within ± 0.001 mag.

Figure 2 presents the CM relation for the RDCS 1252 galaxies. The fit to the full sample of early-type galaxies with $z_{850} < 24.5$ gives

$$(i\text{–}z) = (0.958 \pm 0.006) - (0.025 \pm 0.006)(z_{850} - 23)\,. \quad (1)$$

Other results are listed in Table 1. The mean locations of the CM relations for the elliptical and S0 subsamples agree to well within the errors, while the slopes are consistent at the 1.5-σ level. Eight known late-type members from Rosati et al. (2003, in preparation) for which we have photometry are bluer than the early-type galaxies by 0.25 mag, with a scatter of 0.14 mag about this offset, indicating young stellar populations. We find an intrinsic scatter $\sigma_{\rm int} = 0.023 \pm 0.007$ mag for the 15 confirmed elliptical members. For a limit of $z_{850} < 24.5$, we derive $\sigma_{\rm int} = 0.026$ mag for the clipped sample of 31 ellipticals and $\sigma_{\rm int} = 0.029$ for the 52 E+S0 galaxies. At this limit, the observational errors become dominant and classification is difficult, which could bias our $\sigma_{\rm int}$ estimates. For $z_{850} < 24.0$, still 3 mag down the luminosity function to about $0.3\,L^*$, we find $\sigma_{\rm int} = 0.024$ for 25 ellipticals (with no outliers).

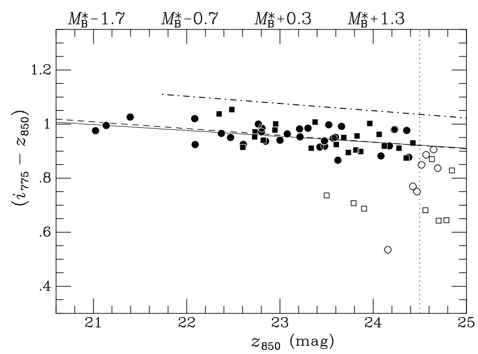

FIG. 2.— Color-magnitude diagram for early-type galaxies inside 1.′9 with $(i_{775}\text{–}z_{850}) > 0.5$, excluding spectroscopically known interlopers. Circles and squares represent ellipticals and S0s, respectively; solid symbols are used in the CM relation fits, while open symbols (all of which lack spectroscopic information) are rejected as outliers or as below the faint cutoff (indicated by the dotted line). Two representative fits are shown: the fit to the 15 elliptical members (solid line) and to the 52 early-type red-sequence galaxies. The approximate luminosity conversion for RDCS 1252 is shown at top, assuming the WMAP cosmology and −1.4 mag of luminosity evolution as described in the text, such that $M_B^* = -21.7$ (AB). The relation for the Coma cluster, transformed to these bandpasses at $z = 1.24$ (no evolution correction), is indicated by the dot-dashed line.

We estimate $M_B^* \approx -21.7$ AB for RDCS 1252, based on local surveys (Norberg et al. 2002), WMAP cosmology, and −1.4 mag luminosity evolution (Postman et al. 2001; van Dokkum & Stanford 2003). The correction from z_{850} to rest-frame B is +0.3 mag for an early-type spectrum. Thus the brightest cluster member at $z_{850} = 21.0$ corresponds to $\sim 4.8\,L_B^*$. The cluster red-sequence is about 0.1 mag bluer than predicted for non-evolving elliptical templates (Coleman et al. 1980; Schneider et al. 1983). For comparison, a Bruzual & Charlot (2003; hereafter BC03) solar metallicity model reddens by 0.11 mag and fades by 1.5 mag in aging from ~ 3 to ~ 11.5 Gyr. The present-day relation for the Coma cluster (transformed according to the relations given below) is also shown in Figure 2.

The tight CM relation allows us to constrain the scatter in early-type galaxy ages, subject to model uncertainties. The evolution in $(i_{775}\text{–}z_{850})$ at this redshift is complicated at young ages because z_{850} straddles the 4000 Å break and has its blue end near the Balmer jump at 3700 Å. The Balmer jump reaches a maximum at 0.5–1 Gyr, when the relative contribution from A stars is greatest, resulting in a red color at these ages. It is interesting that several of the S0s lie *above* the CM relation, possibly indicating ages < 1 Gyr. As the A star contribution lessens, the color quickly evolves towards the blue, reaching a local minimum near ~ 1.5 Gyr, before commencing a roughly monotonic reddening with age.

We have simulated the $(i_{775}\text{–}z_{850})$ colors of galaxies formed under two simple star formation models, similar to those used by van Dokkum et al. (1998). In Model 1, the galaxies form in single bursts randomly distributed over the interval $(t_0, t_{\rm end})$, where t_0 is set to the recombination epoch and $t_{\rm end} < t_z \equiv 5.1$ Gyr, the age of the universe at $z = 1.24$. In Model 2, galaxies form stars at constant rates between randomly selected times (t_1, t_2), where $t_0 < t_1 < t_2 < t_{\rm end}$. We vary $t_{\rm end}$ and at each step calculate colors and luminosities for 10,000 "galaxies" by interpolation and integration of the BC03 solar metallicity models. Assuming $\sigma_{\rm int} = 0.024$ mag for the ellipticals, Model 1 imples a minimum age $t_z\text{–}t_{\rm end} = 1.6$ Gyr, i.e., all galaxies finish forming at redshifts $z > z_{\rm end} = 1.9$; the mean luminosity-weighted age is $\tau_L = 3.3$ Gyr (corresponding to $z_L = 3.6$) with a scatter of 30%. Model 2 gives $t_z\text{–}t_{\rm end} = 0.53$ Gyr, $z_{\rm end} = 1.4$, and $\tau_L = 2.6$ Gyr (corresponding to $z_L = 2.7$) with 38% scatter. Thus, although some galaxies in Model 2 have formed stars recently, the mean ages are still high. Both models give a mean color $\langle i_{775}\text{–}z_{850}\rangle = 0.94$, similar to that observed.

For the S0s, we find $z_{\rm end} = 1.5$ for Model 1 and $z_{\rm end} = 1.3$, indicating recent star formation, and age scatters of 44–47%. Finally, we note that the 1996 version of the BC models would have predicted higher formation epochs, e.g., $z_{\rm end} > 2.5$ and $z_{\rm end} > 2.0$ for the ellipticals in Models 1 and 2, respectively, and an age scatter of only 20%, although the predicted color is then redder by 0.1 mag. Overall, we conclude that the ellipticals are an evolved population, with a mean age $\tau_L \gtrsim 2.6$, a minimum age $\sim 1 \pm 0.5$ Gyr, and an age scatter of (34 ± 15)%, where the error reflects uncertainty in $\sigma_{\rm int}$ and scatter in the models.

5. DISCUSSION

To enable comparison with previous work, we convert observed $(i_{775}\text{–}z_{850})$ quantities to rest-frame $(U\text{–}B)_z$ at $z = 1.24$. The models (BC03; Kodama et al. 1998) and empirical templates indicate $\Delta(U\text{–}B)_z = (1.8 \pm 0.4) \times \Delta(i_{775}\text{–}z_{850})$, where the error bar reflects the scatter in the models at the relevant ages and adds about 20% uncertainty to our transformed slope and scatter. Figure 3 uses this conversion, and other transformations from van Dokkum et al. (2000), to compare our results to some previous studies of the CM relation in intermediate-redshift clusters with *HST*, as well as the results of van Dokkum et al. 2001 on RX J0848+4453, the only cluster of comparable redshift to have its CM relation measured.

Linear fits to the data shown in Figure 3 yield slopes of -0.014 ± 0.010 and 0.003 ± 0.008 for the evolution in the absolute slope and the scatter, respectively. Thus, the scatter is constant, and there is at best marginal evidence for slope evolution, which indicates that the slope is due to a variation in metallicity, not age. Previous studies of cluster samples out to $z \sim 1$ have come to similar conclusions (e.g., Stanford et al. 1998; Kodama et al. 1998; van Dokkum et al. 2000). Van Dokkum et al. (2001) concluded that the slope at $z = 1.27$ was shallower than in the

Coma cluster. However, as shown in the figure, our slope measurement is consistent within the errors with both Coma and RX J0848+4453. Further studies of a diversity of clusters at similar redshifts are needed to explore this issue.

The lack of evolution in the CM relation scatter can be explained by progenitor bias (e.g., van Dokkum & Franx 2001): galaxies selected as early-type at any epoch will have old stellar populations, while the later-type progenitors of the youngest ellipticals today will not be selected. The result is an underestimate in the color scatter for the progenitors of modern ellipticals, and thus overestimated ages. An upper limit on the scatter for elliptical progenitors may be estimated from a fit to all confirmed RDCS 1252 members; the result is 3–4 times larger than for the early-type galaxies. A detailed study of the morphological fractions in RDCS 1252 (Postman et al. 2003, in preparation) should help illuminate the magnitude of this bias. We also note that the two central ellipticals themselves, based on their proximity and irregular isophotes, appear likely to undergo dissipationless merger to form a single $\sim 9L_B^*$ galaxy, similar to local cD galaxies.

We conclude that massive, evolved early-type galaxies were already present in rich clusters at z = 1.24. Our simple models imply mean luminosity-weighted ages of 2.6–3.3 Gyr, corresponding to formation at z = 2.7–3.6. However, the (i_{775}–z_{850}) color is not ideal for the redshift of RDCS 1252, being better suited to measuring the 4000Å break at $z \approx 1.1$. Combining our ACS data with deep, high-resolution near-IR imaging of this field (Lidman et al. 2003) will enable a more robust assessment of early-type galaxy ages. In addition, further studies of the CM relations and morphologies of galaxies in other $z \gtrsim 1$ clusters are needed to improve the constraints on the formation epoch of cluster galaxies and on the evolution of their stellar populations and structural properties.

ACS was developed under NASA contract NAS 5-32864, and this research has been supported by NASA grant NAG5-7697. The STScI is operated by AURA Inc., under NASA contract NAS5-26555. We thank our fellow ACS Team members for their help, Taddy Kodama for helpful discussions and models, and Stephane Charlot for the BC03 models.

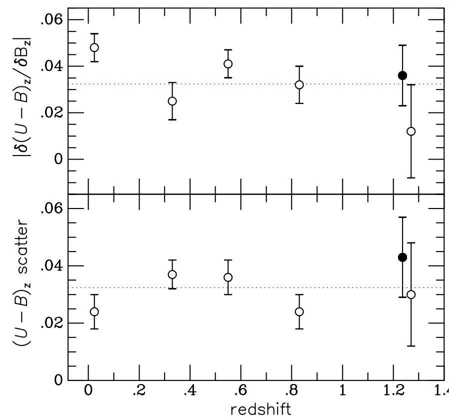

FIG. 3.— Slope (top) and scatter (bottom) of the rest-frame (U−B) CM relation as a function of redshift. The filled circle is from the present work; open symbols show results from, in order of increasing redshift, Bower et al. (1991); van Dokkum et al. (1998); Ellis et al. (1998); van Dokkum et al. (2000); and van Dokkum et al. (2001). The dotted lines indicate the average values.

REFERENCES

Beers, T. C., Flynn, K., & Gebhardt, K. 1990, AJ, 100, 32
Bennett, C. L. et al. 2003, ApJ, in press
Bertin, E. & Arnouts, S. 1996, A&AS, 117, 393
Blakeslee, J. P., Anderson, K. R., Meurer, G. R., Benítez, N., & Magee, D. 2003, ASP Conf. Ser. 295: ADASS XII, 257
Bouwens, R. J. et al. 2003, ApJ, in press (astro-ph/0306215)
Bower, R. G., Lucey, J. R., & Ellis, R. S. 1992, MNRAS, 254, 589
Bruzual A., G. & Charlot, S. 2003, MNRAS, in press (BC03)
Coleman, G. D., Wu, C.-C., & Weedman, D. W. 1980, ApJS, 43, 393
Ellis, R. S., Smail, I., Dressler, A., Couch, W. J., Oemler, A. J., Butcher, H., & Sharples, R. M. 1997, ApJ, 483, 582
Fabricant, D., Franx, M., & van Dokkum, P. 2000, ApJ, 539, 577
Ford, H. C. et al. 2002, Proc. SPIE, 4854, 81
Fruchter, A. S. & Hook, R. N. 2002, PASP, 114, 144
Högbom, J. A. 1974, A&AS, 15, 417
Kodama, T., Arimoto, N., Barger, A. J., & Aragon-Salamanca, A. 1998, A&A, 334, 99
Lidman, C. et al. 2003, A&A, submitted
Norberg, P. et al. 2002, MNRAS, 336, 907
Peng, C. Y., Ho, L. C., Impey, C. D., & Rix, H. 2002, AJ, 124, 266
Postman, M. 2002, ASP Conf. Ser. 268, 3
Postman, M., Lubin, L. M., & Oke, J. B. 2001, AJ, 122, 1125
Rosati, P., della Ceca, R., Norman, C., & Giacconi, R. 1998, ApJ, 492, L21
Rosati, P. 2003, in Clusters of Galaxies: Probes of Cosmological Structure and Galaxy Evolution (Cambridge: Cambridge Univ. Press), in press
Rosati, P. et al. 2003, AJ, submitted
Schlegel, D. J., Finkbeiner, D. P., & Davis, M. 1998, ApJ, 500, 525
Schneider, D. P., Gunn, J. E., & Hoessel, J. G. 1983, ApJ, 264, 337
Stanford, S. A., Eisenhardt, P. R., & Dickinson, M. 1998, ApJ, 492, 461
van Dokkum, P. G., Franx, M., Kelson, D. D., Illingworth, G. D., Fisher, D., & Fabricant, D. 1998, ApJ, 500, 714
van Dokkum, P. G., Franx, M., Fabricant, D., Illingworth, G. D., & Kelson, D. D. 2000, ApJ, 541, 95
van Dokkum, P. G., Stanford, S. A., Holden, B. P., Eisenhardt, P. R., Dickinson, M., & Elston, R. 2001, ApJ, 552, L101
van Dokkum, P. G. & Franx, M. 2001, ApJ, 553, 90
van Dokkum, P. G. & Stanford, S. A. 2003, ApJ, 585, 78

TABLE 1
RDCS 1252-2927 COLOR-MAGNITUDE RELATIONS

Sample	$z_{850}^{(\mathrm{lim})}$	N_r	N_c	Slope	σ_{bwt}[a]	σ_{bwt}[b]	σ_{int}
E[c].....	...	15	15	-0.022 ± 0.011	0.029	0.029 ± 0.005	0.023 ± 0.007
E+S0[c]..	...	22	22	-0.018 ± 0.013	0.038	0.038 ± 0.006	0.033 ± 0.007
E[d].....	24.0	25	25	-0.020 ± 0.009	0.033	0.033 ± 0.005	0.024 ± 0.008
E+S0[d]..	24.0	44	41	-0.025 ± 0.008	0.045	0.038 ± 0.004	0.029 ± 0.007
E[d].....	24.5	34	31	-0.019 ± 0.007	0.053	0.036 ± 0.005	0.026 ± 0.008
E+S0[d]..	24.5	58	52	-0.025 ± 0.006	0.054	0.039 ± 0.004	0.029 ± 0.007
S0[d]....	24.5	24	21	-0.042 ± 0.013	0.058	0.039 ± 0.006	0.032 ± 0.008

[a]Biweight scatter based on raw number of galaxies N_r.

[b]Biweight scatter based on N_c galaxies after 3-σ clipping.

[c]Spectroscopically confirmed members of specified type only.

[d]All red-sequence objects (known interlopers omitted) of specified type, $z_{850} < z_{850}^{(\mathrm{lim})}$ and within the area of analysis.

Paper submitted to Astronomy & Astrophysics (A&A)

Astronomy & Astrophysics manuscript no. lf1252˙2 October 7, 2003
(DOI: will be inserted by hand later)

K_s-band luminosity function of the $z = 1.237$ cluster of galaxies RDCS J1252.9−2927[⋆]

S. Toft[1], V. Mainieri[2], P. Rosati[3], C. Lidman[4], R. Demarco[5], M. Nonino[6], S. A. Stanford[7,8]

[1] Astronomical Observatory, University of Copenhagen, Juliane Maries Vej 30, DK-2100 Copenhagen Ø, Denmark
e-mail: toft@astro.ku.dk
[2] Max-Planck-Institut für extraterrestrische Physik, Postfach 1319, D-85748 Garching, Germany
[3] European Southern Observatory, Karl-Scwarzchild-Strasse 2, D-85748 Garching, Germany
[4] European Southern Observatory, Alonso de Cordova 3107, Casilla 19001, Santiago, Chile
[5] Institute d'Astrophysique de Paris, 98bis Boulevard Arago, F-75014 Paris, France
[6] Instituto Nazionale di Astrofisica, Osservatorio Astronomico de Trieste, via G.B. Tiepolo 11, I-34131, Trieste, Italy
[7] Department of Physics, University of California at Davis, 1 Shields Avenue, Davis, CA 95616, USA
[8] Institute of Geophysics and Planetary Physics, LLNL, Livermore, CA 94551, USA

the date of receipt and acceptance should be inserted later

Abstract. We derive the K_s-band luminosity function (LF) of the $z = 1.237$ massive X-ray luminous cluster of galaxies RDCS J1252.9−2927. Photometric redshifts, derived from deep multi-wavelength near infrared (NIR) and optical imaging data, and calibrated using a large subset of galaxies with spectroscopic redshifts, are used to separate the cluster galaxy population from the foreground and background field galaxy population. This allows for a simultaneous determination of the characteristic magnitude K_s^* and faint end slope α of the LF without having to make an uncertain statistical background subtraction. The derived LF is well represented by the Schechter function with $K_s^* = 18.54^{+0.45}_{-0.55}$ and $\alpha = -0.64^{+0.27}_{-0.25}$. The shape of derived LF is similar to that measured in local clusters at similar restframe wavelengths (in the z-band), but the characteristic magnitude is brighter by $\Delta M_z^* = -1.3 \pm 0.5$ magnitudes. The brightening of the characteristic magnitude, and lack of evolution in the shape of the bright end of the LF suggests that the massive cluster ellipticals that dominate the bright end of the LF were already in place at $z = 1.237$. The derived passive luminosity evolution is in agreement with the luminosity evolution derived from fundamental plane studies of clusters at similar redshifts and the evolution of the K-band LF of field galaxies to $z \sim 1$. Taken at face value the derived faint end slope is similar to the value measured at similar restframe wavelengths in the $z = 1$ cluster MG2016+112 and in clusters in the local universe, but due to the relatively large uncertainties, a modest evolution in the faint end slope between $z = 0$ and $z = 1.237$ is not ruled out.

Key words. galaxies: clusters: individual: RDCS J1252.9-2927 - galaxies: elliptical and lenticular, cD - galaxies: evolution - galaxies: formation -galaxies: luminosity function, mass function - cosmology: observations

1. Introduction

The galaxy luminosity function (LF) is a powerful tool for constraining models of galaxy formation and evolution. The LF of both field and cluster galaxies have been shown to be well represented by the Schechter function $\phi(m)\mathrm{d}m = n^*\left[10^{0.4(m^*-m)}\right]^{\alpha+1} e^{-10^{0.4(m^*-m)}}\mathrm{d}m$, where m^* is the characteristic magnitude of the distribution, α is the faint end slope, and n^* is a normalization constant describing the space density of galaxies.

The variation of the LF parameters with galaxy type (early-type/late-type), wavelength (UV, optical, near-infrared [NIR]) and environment (cluster versus field) and their evolution with redshift depends on the details of mass assembly and star formation and therefore provide strong constraints on galaxy evolution models.

At optical wavelengths, the local cluster galaxy LF has brighter m^* and flatter α than the field galaxy LF. While α measured in the field is approximately $\alpha \sim -1.25$ in all the optical bands, α in clusters become increasingly flatter toward the redder bands, gradually dropping from $\alpha = -1.40$ in the u-band to $\alpha = -0.58$ in the z-band (Goto et al. 2002), consistent with the hypothesis that clusters are composed of two distinct populations: a population of bright red early-type galaxies dominating the bright end and a population of fainter blue late-type galaxies (similar to typical field galaxies) dominating the faint end. In the Coma cluster there is a tendency for α to steepen with cluster centric distance, notably in the bluer optical bands, consistent with a star forming dwarf population that could be in

Send offprint requests to: S. Toft

[⋆] Based on observations obtained at the European Southern Observatory using the ESO Very Large Telescope on Cerro Paranal (ESO program 166.A-0101).

the process of being accreted from the field (Beijersbergen et al. 2002). Rich evolved clusters with cD galaxies tend to have flatter faint end slopes than poorer clusters, indicating a deficiency star forming dwarf galaxies in rich clusters (Lopez-Cruz et al. 1997; Driver & De Propris 2003).

While the variation in the LF parameters at optical wavelengths are sensitive to the star formation properties and morphological mix of the underlying galaxy population, the NIR LF is an excellent probe of the mass function of clusters. The K-band flux of a galaxy is a good tracer of its stellar mass (e.g. Madau et al. 1998) it is not very sensitive to star formation and attenuation by dust (compared to the optical band) and the k-corrections are fairly small and relatively independent of galaxy type even at high redshifts (e.g. Mannucci et al. 2001). The evolution of the mass function is directly predicted from galaxy formation and evolution models, making the K-band LF of field and cluster galaxies very useful for fundamental testing of the models.

Locally, the field galaxy K-band LF has been derived using the 2 Micron All Sky Survey (2MASS, Jarrett et al. 2000). Early-type and late-type field galaxies have similarly shaped LF but the early-types are brighter (more massive) and less numerous than the late-types (Kochanek et al. 2001). The evolution of the field galaxy K-band LF has been estimated in three broad redshift bins centered on $z = 0.5$, 1.0 and 1.5 using the K20 survey (Pozzetti et al. 2003). No evolution is found in α to $z = 1.0$, in the highest redshift bin the data are not deep enough to constrain it. The characteristic K-band magnitude of the galaxies in the $z = 1$ bin (which includes galaxies in the redshift range $0.75 < z < 1.3$) is consistent with a mild luminosity evolution in the K-band to $z \sim 1$ of $\Delta M^*_K = -0.54 \pm 0.12$. At $z = 1$, the bright end of the LF is still dominated by ellipticals, and only a small decrease in their space density is observed, indicating that the field ellipticals are largely in place at $z = 1$.

In a deep study of the LF of the Coma cluster, de Propris et al. (1998) find a characteristic magnitude $M^*_K = -24.02$ and a faint end slope of $\alpha = -0.78$. If they restrict the fit to "bright" galaxies ($M < M^* + 3$) they find $\alpha = -0.9$. de Propris et al. (1999) studied 38 clusters in the redshift range $0.1 < z < 0.9$ to look for an evolution in the K-band cluster LF. Their data was not deep enough to constrain the faint end slope , so they fixed it on the Coma cluster value $\alpha = -0.9$, and concentrated on searching for an evolution in the properties of the bright end. Using the same method as de Propris et al. (1999) the sample has subsequently been extended to include a few clusters in the redshift range $z = 1.0 - 1.2$ (Kodama & Bower 2003; Nakata et al. 2001). The conclusion from these studies is that the shape of the bright end of the K-band LF appears unchanged to $z = 1.2$ and the evolution of the characteristic K-band magnitude with redshift $K^*(z)$ is well described by passively evolving galaxies assembled at $z_f > 2$.

A high formation redshift is also inferred from the evolution of the colour magnitude (CM) relation of cluster early-types to $z \sim 1.3$ (Bower et al. 1992; Aragon-Salamanca et al. 1993; Stanford et al. 1998, 1997; Rosati et al. 1999; van Dokkum et al. 2001; Lidman et al. 2003). The simplest explanation for the evolution of the CM relation is the monolithic collapse models (e.g. Eggen et al. 1962) in which the bulk of stars are formed in a single short duration burst at high redshift and subsequently evolve passively, but it can be equally well explained by semi analytical hierarchical models (e.g. Kauffmann & Charlot 1998) in which the stars are formed in the disks of of late-type progenitors which later merge to form the elliptical galaxies, provided that the merging does not trigger significant star formation.

The K-band LF is predicted to evolve quite differently in the two formation scenarios, due to its close relationship with the evolution of the mass function.

If the galaxies were assembled at high redshift and subsequently evolved passively, as predicted by the monolithic models, we expect the characteristic magnitude to brighten with redshift (as a consequence of the passive evolution of the stars) but the shape of the LF to remain the same. If the galaxies were build up through continuous merging over a broader redshift interval as predicted in hierarchical models, we expect the shape of the LF to change with redshift to reflect the accretion history of the cluster and the merging history of the cluster galaxies. A deficiency of the brightest galaxies should appear as the the most massive galaxies break up into their progenitors, resulting in a steepening of the bright end of the LF with redshift. If small structures form first and subsequently merge to form larger structures, the faint end slope should steepen with redshift as galaxies break up into their progenitors. In many hierarchical models however, the cluster population grow by accretion of surrounding structures. The accretion history, and the mass spectrum of the accreted structures could influence the evolution of the LF. The Butcher-Oemler effect (Butcher & Oemler 1978) in intermediate redshift clusters is probably due to star formation in low mass galaxies which have been accreted from the field, induced by interaction with the cluster environment (Butcher & Oemler 1984; Fabricant et al. 1991; Smail et al. 1998; van Dokkum et al. 2000; de Propris et al. 2003). Such an accretion of primarily low mass galaxies could cause the faint end slope to decline with redshift, as a smaller number of low mass galaxies would have had time to be accreted onto the cluster environment at high redshift.

The apparent passive evolution of the bright end of the cluster LF to $z \sim 1$ is a challenge for hierarchical models which predict that the characteristic mass should be a factor of three smaller at $z \sim 1$ than at present (Kodama & Bower 2003). None of the studies mentioned above have been able to constrain the evolution of α. The first constraints on α at high redshift was derived by Toft et al. (2003) who simultaneously fitted K^* and α in the $z = 1$ cluster MG2016+112. The derived constraints on α are not strong ($\alpha = -0.60^{+0.39}_{-0.33}$), however it is important to keep it free in the fit since it is coupled to the derived value of K^* and its uncertainties. Furthermore it is noted that since α depends on wavelength, and the K-band corresponds roughly to restframe z-band at $z \sim 1$, the derived value should be compared to the local value measured in the z-band rather than in the K-band when studying evolutionary patterns.

In this paper, we derive firm constraints on K^* and α for the K-band LF of the massive, X-ray luminous cluster of galaxies RDCS J1252.9-2927 (Rosati et al. 2003b) at $z = 1.237$. We apply the method of Toft et al. (2003) to high quality multi-wavelength NIR and optical photometric data and extensive spectroscopic follow up observations covering a $4' \times 4'$ field around the cluster.

The outline of this paper is as follows: In §2 we give a brief introduction to the data and describe how cluster galaxies are separated from the field galaxy population using photometric redshifts, calibrated using the spectroscopic data. In §3 we derive the LF of the cluster galaxies, in §4 we compare to results from studies of lower redshift clusters to look for an evolution and compare it to model predictions, and in §5 we summarize and discuss the results. Throughout the paper we assume a flat cosmology, with $\Omega_m = 0.3$, $\Omega_\Lambda = 0.7$ and $H_0 = 70$ km s^{-1} Mpc^{-1}. Magnitudes are in the the Vega system.

2. Building a complete sample of cluster galaxies

The observational basis of this study consist of high quality multi-wavelength NIR and optical photometric data of a $4' \times 4'$ field around RDCS J1252.9-2927, supplemented by spectroscopic follow up observations, all obtained at the ESO Very Large Telescope (with the ISAAC, FORS1 and FORS2 instruments). The central part of the field was imaged for 24 hours in each of the NIR wavebands: J_s and K_s, and for approximately 1 hour in each of the optical wavebands: B, V, R, I and z. The full data set is described in detail in three companion papers: a paper describing the NIR data (Lidman et al. 2003) a paper describing the optical data (Rosati et al. 2003a) and a paper describing the spectroscopic data (Demarco et al. 2003).

To derive the luminosity function of the cluster galaxies in RDCS J1252.9-2927 we need a catalog of cluster galaxies which is complete to a certain magnitude. In Fig. 1 we plot a binned representation of the number of detected objects in the K_s-band as function of magnitude (Lidman et al. 2003). From visual inspection of the turnover magnitude in this figure we estimate that the K_s-band data are complete to $K_s = 22.5$. To build a sample of cluster galaxies which is complete to this magnitude, the redshift distribution of all galaxies in the field must be determined in order to separate the cluster galaxy population from the foreground and background populations of galaxies.

At faint magnitudes it is not feasible to obtain this solely through spectroscopic observations. Instead we take advantage of the extensive optical and NIR imaging data to derive photometric redshifts and calibrate and test these against a large subset of galaxies with spectroscopic redshifts.

2.1. Photometry and photometric redshifts

We used SExtractor (Bertin & Arnouts 1996) for object detection in each of the available wave bands, for computing magnitudes in apertures of 2″ and for cross-correlation of the resulting catalogues. The (3σ) limiting (Vega) magnitudes achieved for the imaging in 2″ apertures are: $B = 26.72$, $V = 26.76$, $R = 25.98$, $I = 25.68$, $z = 24.29$, $J_s = 23.90$, $K_s = 22.47$.

To obtain reliable colours we must take into account that the imaging in the different wavebands was obtained under different seeing conditions. To derive and apply these corrections we did the following: first, we computed magnitudes in apertures of 2″ in each of the available ("original") waveband images.

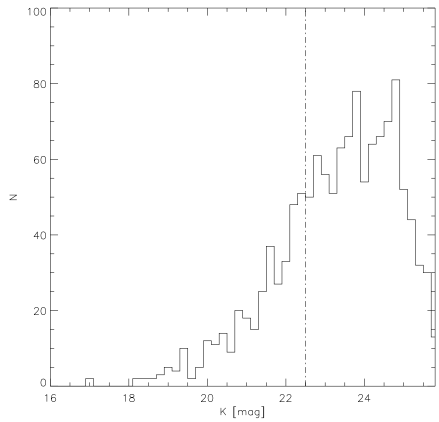

Fig. 1. Binned representation (bin size 0.2 mag) of the number of detected objects as a function of K_s-band magnitude. The data are estimated to be complete to $K_s = 22.5$.

We then degraded the point spread function (PSF) of the original images to match the worst seeing condition and recomputed the 2″ aperture magnitudes in the "degraded" images. The corrections to be applied to the "original" magnitudes was then derived by comparing the magnitudes derived for bright stellar objects in the "original" and the "degraded" images.

We used the Bayesian photometric redshift (BPZ) code of Benítez (2000) to derive photometric redshifts. The advantage of the Bayesian approach is the use of *a priori* probabilities by which it is possible to include relevant knowledge, such as the expected shape of redshift distributions and the galaxy type fractions, which can be readily obtained from existing surveys. For our study we used the same set of templates as those described in Benítez (2000): four Coleman et al. (1980) templates (E/S0, Sbc, Scd and Irr), and the spectra of two starburst galaxies in Kinney et al. (1996). We derived two interpolated SEDs between each pair of these spectral types. We used the priors derived by Benítez (2000) from the Hubble deep field north (HDFN) and Canada France redshift survey (CFRS) catalogues.

To quantify the reliability of the photometric redshift estimation we used a sample of secure spectroscopic redshifts from our campaign in this area (Demarco et al. 2003). In the region with multi-wavelength coverage described above, there are 120 such spectroscopically identified sources.

In Fig. 2 we plot z_{phot} versus z_{spec} for the spectroscopic sample. The photometric redshifts in general reproduce the spectroscopic redshift well but are systematically smaller. This is illustrated in Fig. 3 where we plot the distribution of deviations of the photometric redshifts from the spectroscopic redshifts. The (sigma clipped) mean of the distribution is $\langle z_{phot} - z_{spec} \rangle = -0.04$ and the standard deviation is $\sigma = 0.18$. If we restrict the analysis to the spectroscopic cluster mem-

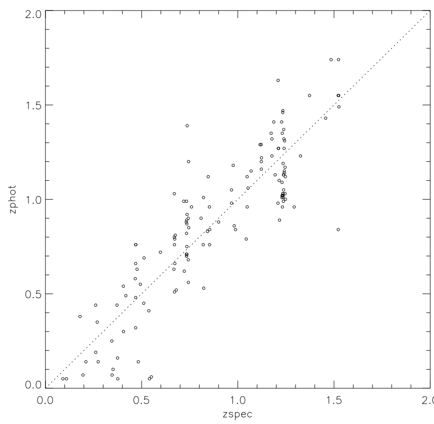

Fig. 2. Photometric redshift (z_{phot}) versus spectroscopic redshift (z_{spec}) for the full spectroscopic sample. Immediately recognizable is the cluster of galaxies at $z = 1.237$.

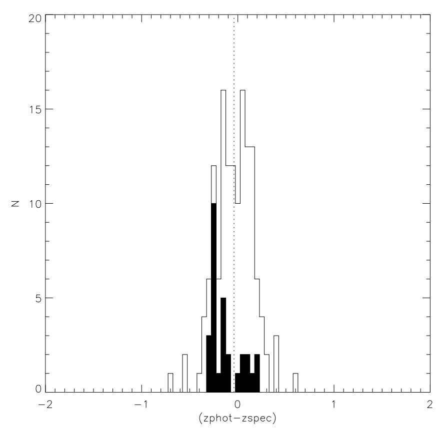

Fig. 3. Distribution of deviations of the photometric redshifts from the spectroscopic redshifts for the spectroscopic cluster member galaxies (filled histogram) and for the full spectroscopic sample (open histogram).

bers (the filled histogram in Fig. 3) the mean deviation is larger $\langle z_{phot} - z_{spec} \rangle = -0.13$ and the standard deviation is $\sigma = 0.16$. In Fig.4 we plot $\langle z_{phot} - z_{spec} \rangle$ as a function of redshift to investigate whether this is a consequence of a redshift dependent systematic photometric redshift error, which could be introduced by small errors in the photometric zero-points of one or more of the filters. No significant dependency on redshift is

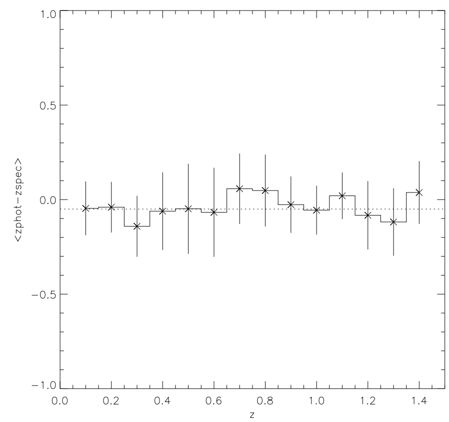

Fig. 4. Mean deviation of the derived photometric redshift from the spectroscopic redshift as a function of spectroscopic redshift, calculated in $\delta = 0.1$ bins. No significant dependency on redshift is observed. The dotted line marks the mean offset −0.04 of the full sample.

observed. In the following we add 0.04 to all the derived redshift to empirically correct for the systematic deviation.

To compare the photometric redshifts errors with those achieved in the literature we define for each object the reduced error in the photometric redshift estimation as $\delta_z = (z_{phot} - z_{spec})/(1 + z_{spec})$. For the full sample we achieve a mean offset $\langle \delta_z \rangle$=0.02 and an standard deviation of $\sigma(\delta_z)$=0.11. If we restrict our analysis to the cluster members we have $\langle \delta_z \rangle$=0.05 and $\sigma(\delta_z)$=0.09. The accuracy of our photometric redshifts are comparable to the accuracy achieved by Barger et al. (2003) in a similar Bayesian photometric redshift study of galaxies in the Chandra deep field north. For the HDFN, Benítez (2000) achieve a higher accuracy: $\sigma(\delta_z) = 0.06$, probably due to higher precession Hubble Space Telescope (HST) photometry.

2.2. The photometric cluster member sample

In this section we describe how the cluster galaxy population is separated from the foreground and background field galaxy population using the photometric redshift. We take into account the uncertainty in the photometric redshift estimation by allowing galaxies with photometric redshifts within Δz of the cluster redshift z_{cl} to be classified as "photometric members". The choice of Δz is a trade off between cluster galaxy completeness and field galaxy pollution. The interval must be sufficiently broad to include as many "real" cluster galaxies as possible and sufficiently narrow to minimize pollution from field galaxies. From Fig. 2-4 it can be seen that most cluster member galaxies at $z = 1.237$ are expected to have photometric redshifts in the range $|z_{phot} - z_{cl}| \leq 0.3$. Since we are aiming at building a sample of cluster galaxies which is complete to $K_s = 22.5$ we prioritize not to exclude any cluster members and choose

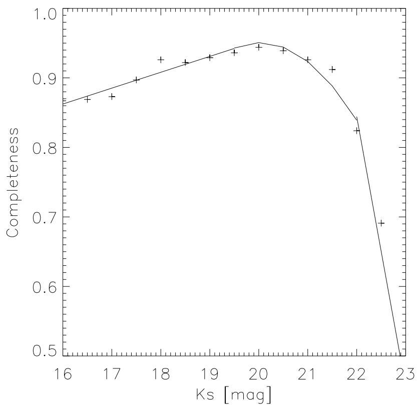

Fig. 5. Completeness function of the photometric member sample, calculated as the fraction of simulated z = 1.237 cluster galaxies recovered by the photometric redshift analysis as a function of magnitude.

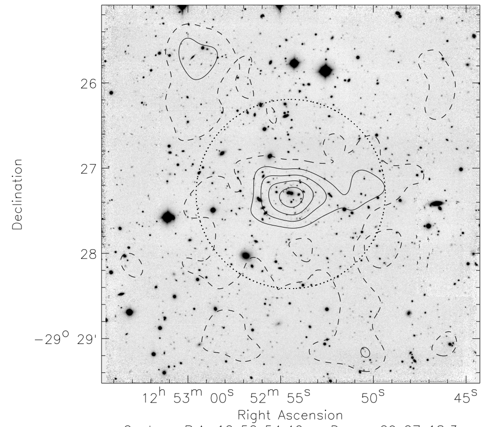

Fig. 6. Contours of the smoothed density distribution of photometric member galaxies overlayed on the ∼ 4′ × 4′ mosaic K_s-band ISAAC image (Lidman et al. 2003). The contours are 2 times (dashed line) and 4-10 times (full line) the density of galaxies in the HDFN with K_s < 22.5 and 0.935 < z_{ph} < 1.535 (Fernández-Soto et al. 1999). Inside the dotted circle with radius 65″ the contamination from field galaxies in the photometric member sample is 25%. This circle marks the aperture inside which we derive the cluster galaxy luminosity function of RDCS J1252.9−2927 in §3.

Δz = 0.3. In the following, galaxies with 0.935 < z_{ph} < 1.535 are thus classified as photometric members.

To estimate the "completeness function" of the photometric member sample (the fraction of z = 1.237 cluster galaxies recovered by the photometric redshift analysis in the Δz interval, as a function of magnitude) we did the following: for each δm = 0.5 mag bin in the observed range of magnitudes K_s = 16 − 23, we generated a catalog of 1000 galaxies at z = 1.237 as they would appear in a dataset with the same bandpasses and limiting magnitudes as the data of RDCS J1252.9-2927. The catalog was generated using the *make_catalog* code in the HYPERZ package (Bolzonella et al. 2000) and were drawn randomly from 7 template spectral types (E to Im). We then applied BPZ to the catalogs. In Fig. 5 we plot the fraction of input (z = 1.237) galaxies with derived photometric redshifts within 0.935 < z_{ph} < 1.535 as a function of K_s-band magnitude. Down to a magnitude of K_s = 21.5 about 90% of the galaxies are recovered. At K_s = 22.5 the recovery rate is 70%. The reason why BPZ appears to be performing slightly worse at the brightest magnitudes, compared to at fainter magnitudes, is that the simulated catalogs contain sizable fractions of bright late-type galaxies which are very rare at z = 1.237, and therefore are assigned small probabilities by BPZ, resulting in a some cases, in the most likely spectrum being a lower redshift spectrum of earlier type. The redshift evolution of the field galaxy luminosity function, and its cosmic variance is not known with sufficient accuracy to correctly incorporate the effects of pollution of field galaxies in the completeness function analysis. We return to the issue of field contamination in §2.3 and §3.

2.3. Spatial distribution of photometric member galaxies

To investigate the spatial distribution of the photometric members galaxies we constructed an image with the pixel value at the centroid of the photometric cluster members equal to one and the remaining pixel values equal to zero. This image was then smoothed with a Gaussian kernel with FWHM=60 pixels (∼ 8.″8). In Fig. 6 we overlay contours of the smoothed density distribution of the photometric member galaxies on the K_s-band image of the cluster. The contours are 2 − 10 times the density of galaxies in the HDFN with K_s < 22.5 and 0.935 < z_{ph} < 1.535 (Fernández-Soto et al. 1999).

There is a large concentration of photometric member galaxies in the central part of the field. In this region the photometric member sample must thus be dominated by cluster galaxies. The density of photometric members in the outer parts of the field is comparable to the density in the HDFN suggesting that field galaxy pollution could make a significant contribution to the photometric member sample in these regions. We discuss this further in §3

3. Luminosity function

We now have a sample of cluster galaxies which is complete to K_s = 22.5, or rather a sample which we know how to correct for incompleteness, and we can derive the K_s-band luminosity function of the cluster galaxies without having to make uncertain statistical corrections to account for foreground and background field galaxy contamination. The choice of Δz in §2.2 ensures that all spectroscopically confirmed cluster members are included in the photometric member sample. To take full advantage of the data we apply the maximum likelihood technique of Schechter & Press (1976) directly to the luminosity distribution of the cluster galaxies rather than doing a "least squares" fit to a binned representation. In this way we include the information that in many magnitude intervals no galaxies are found, and do not make the assumption of the χ^2 method that the underlying distribution is Gaussian. The "incompleteness" of the photometric redshift selection is taken into account through the completeness function shown in Fig. 5. This in turn leads to more realistic error bars. For more details of the method we refer to the appendix of Toft et al. (2003).

In §2.3 we argued that pollution from field galaxies in the photometric member sample could be significant in the outer parts of the $4' \times 4'$ field. The amount of pollution can be estimated from the subsample of photometric member galaxies with spectroscopic redshifts. The selection of the spectroscopic sample was designed not to introduce biases on the cluster galaxy populations, while minimizing the pollution of field galaxies. This was accomplished by targeting galaxies with $K_s < 21$, $J - K_s < 2.1$ and $R - K_s > 3$. Such criteria do not penalize cluster galaxies, since at $z = 1.237$ even the latest types are redder than $R - K_s = 3$ and early types are bluer than $J - K_s = 2.1$, however field contamination is significantly reduced.

In Fig.7 the bottom panel shows the contamination derived in apertures with increasing radius (centered on the cluster core). In the central parts of the field the contamination is modest. The pollution within 45″ is ∼ 10%, within 65″ it is ∼ 25%, and within 120″ it is 50%.

To investigate the effects of the pollution on our analysis we derived the luminosity function of the photometric member sample in apertures of increasing size. The top and middle panel in Fig.7 shows the variation of the luminosity function parameters with aperture radius.

There is a tendency for K_s^* to be slightly brighter and α to be slightly smaller (less negative) in apertures encompassing only the central regions where the contamination is small, compared to in larger apertures where the contamination is more pronounced, but the effect is barely significant since the error bars are larger in the smaller apertures due to the smaller number of galaxies. Part of the effect could be caused by intrinsic variation in the properties of the cluster galaxy LF with cluster centric distance, and part of it could be a consequence of field galaxy pollution. Since the effect is not statistically significant however, field galaxy pollution is not likely to significantly affect our results.

Based on Fig.7 we limit our cluster galaxy LF analysis to galaxies within 65″ of the cluster center, in order to maximize the number of galaxies while minimizing the pollution. The photometric member sample contains 100 galaxies within this distance, including 19 spectroscopically confirmed cluster members and 7 interlopers with spectroscopic redshifts different from z_{cl}. We remove the known interlopers from the sample and study the luminosity function of the remaining 93 galaxies in detail in the following.

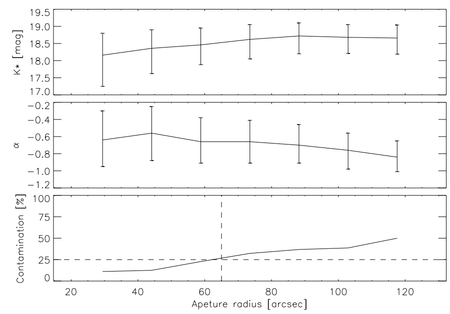

Fig. 7. The top and middle panel shows the K_s^* and α parameters of the LF of the photometric member galaxies derived in apertures of increasing size, centered on the cluster core. Note that the two parameters are not independent, so the error bars in the two plots are correlated. The bottom panel shows the contamination in apertures of increasing size estimated from the subsample of photometric member galaxies with spectroscopic redshifts. The contamination is calculated as the number of interlopers, i.e. photometric member galaxies with spectroscopic redshifts different from the cluster redshift (defined as $1.22 \leq z_{spec} \leq 1.25$), divided by the total number of photometric member galaxies with spectroscopic redshifts. Inside the aperture with radius 65″ (marked by the vertical dashed line), the contamination is 25%.

The Schechter function provides a good fit to the data. In Fig. 8 we plot $1 - 3\sigma$ likelihood contours of the two Schechter function parameters. There is some degeneracy between the two parameters, but we are able to put firm constraints on both the characteristic magnitude $K_s^* = 18.54^{+0.45}_{-0.55}$ and the faint end slope $\alpha = -0.64^{+0.27}_{-0.25}$. Such accuracy is unprecedented at these redshifts.

Since our analysis is based on photometric redshifts which can be sensitive to photometric errors, the results could potentially be affected by small changes in the photometry. To find out whether this is the case, we carried out a series of Monte Carlo simulations to investigate how sensitive the photometric redshift distribution is to the photometric errors. We generated 10 realizations of the full dataset, by randomly perturbing the photometry of the galaxies within their 1σ error bars. We then derived their photometric redshift distribution, defined a photometric cluster member sample, removed known interlopers and derived their LF in exactly the same way as for the original data set. The best fitting LF parameters of the perturbed datasets (represented by small symbols in Fig.8) all fall within the 1σ contour of the original dataset, indicating that the LF analysis is robust with respect to photometric perturbations, and that the effect of field galaxies scattering in and out of the Δz interval as the photometry is perturbed is small, otherwise we would expect to see larger variations in the LF parameters.

In Fig. 9 we plot the best fitting Schechter function and a binned representation of the data. For comparison, we plot the local z-band cluster and field galaxy LFs, rather than the local K-band cluster galaxy LFs, since the observed K_s-band corresponds roughly to restframe z-band at $z = 1.237$. Following the method of van Dokkum & Franx (1996) absolute z-band magnitudes M_z can be related to the observed K_s-band magnitudes through:

$$M_{z,AB} = K_{s,AB} - 5 * log(d_L/10) + 5log(1+z) + \beta(H-K)_{AB}, \quad (1)$$

where $z = 1.237$ is the redshift, d_L is the luminosity distance in parsecs and $\beta(H-K)_{AB}$ is a colour term to compensate for the fact that the redshifted z-band does not match the observed K_s-band exactly. The basic assumption made to derive this expression is that the flux at the redshifted z-band can be related to the observed H and K_s-band flux by $F_\nu(\nu_{z_{band}}(z)) = F_\nu(\nu_H)^\beta F_\nu(\nu_K)^{1-\beta}$. We adopt the value $(H-K)_{AB}(z = 1.25) = 0.57$ predicted by the passive evolution models of Kodama & Arimoto (1997) for an elliptical L^* galaxy formed at $z_f = 3$ (the mean formation redshift of cluster ellipticals derived from their CM relation, Lidman et al. 2003) and calculate $\beta = 0.35$ by assuming a simple power-law for the shape of the SED between ν_H and ν_K.

To further investigate the effect of field galaxy pollution on the results, we derived the LF of photometric members further away than 90″ from the cluster center, and found a fainter characteristic magnitude $K_s^* = 18.90^{+0.61}_{-0.95}$ and a steeper faint end slope $\alpha = -1.14^{+0.30}_{-0.32}$ than in the central region.

The LF of the photometric member galaxies in the central region of the cluster is very similar to the local cluster galaxy LF shifted to brighter magnitudes, while the LF of photometric member galaxies in the outer parts of the field is more similar to the local field galaxy LF. A likely explanation is that the photometric member sample at large distances from the cluster center becomes dominated by faint field galaxies, consistent with the conclusions from Fig.7.

Contamination from faint field galaxies is not likely to significantly affect the results derived for the cluster galaxy LF in the central part of the field, where the photometric member sample is dominated by bright galaxies, but we note that the main effect of such an contamination would be to overestimate the faint end slope, making the derived faint end slope a formal upper limit to the intrinsic faint end slope of the cluster galaxy LF.

4. LF evolution

From Fig.9 it can be seen that the characteristic magnitude of the restframe z-band LF at $z = 1.237$ is brighter than at $z = 0$. By transforming the observed K_s^* to M_z^* using Equation 1 a evolution of $\Delta M_z = -1.3 \pm 0.5$ mag is derived for the restframe z-band characteristic magnitude. The observed K_s^* can be converted to absolute (restframe) K_s-band magnitude by applying a k-correction:

$$M_{K_s} = K_s - 5 * log(d_L/10) - k_{K_s}(z = 1.237). \quad (2)$$

If we adopt the $k_{K_s}(z = 1.25) = -0.68$ for the k-correction (Mannucci et al. 2001) and compare to M_K^* derived locally in

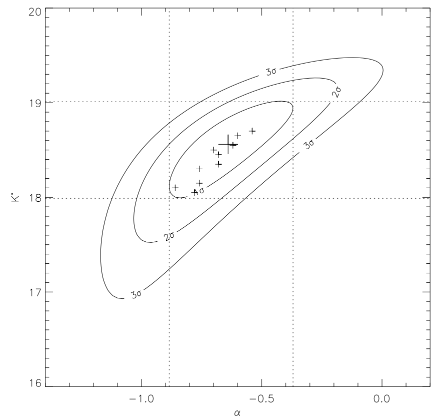

Fig. 8. Contour plot showing the constraints on the Schechter function parameters derived from the maximum likelihood analysis. The big cross marks the best fitting parameters, and the curves represent $1-3\sigma$ confidence levels. The small crosses marks the best fitting parameters for the catalogs with perturbed photometry (see text).

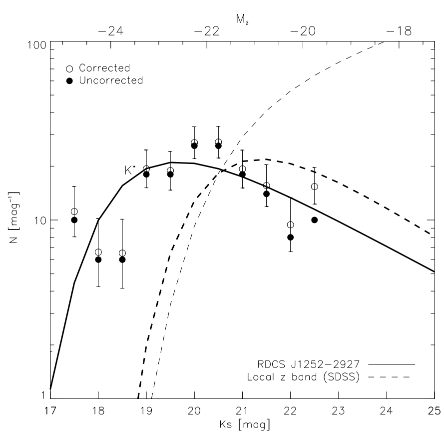

Fig. 9. The thick full curve is the K_s-band LF of the photometric member galaxies within 65″ of the cluster center, represented by the best fitting Schechter function, with parameters $K_s^* = 18.54^{+0.45}_{-0.43}$ and $\alpha = -0.64^{+0.27}_{-0.25}$. The thick dashed curve is the local z-band cluster galaxy LF which has $M_z^* = -22.36 \pm 0.06$ and $\alpha = -0.58 \pm 0.04$, and the thin dashed curve is the local z-band field galaxy LF which has $M_z^* = -22.34 \pm 0.06$ and $\alpha = -1.24 \pm 0.04$ (Goto et al. 2002). The filled symbols are a binned representation of the raw counts, while the open symbols have been corrected for the incompleteness of the photometric redshift selection, using the completeness function in Fig.5. The conversion between observed K_s-band magnitude and restframe z-band magnitude is given in the text.

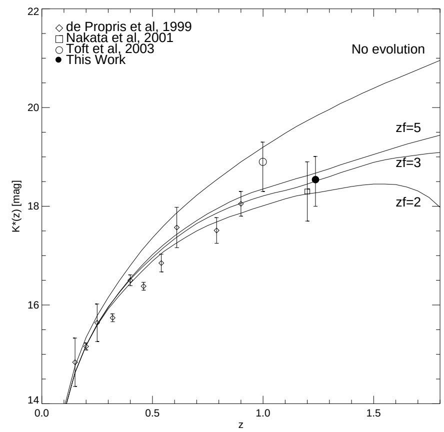

Fig. 10. Evolution of K_s^* with redshift. The curves represent the evolution of an L^* galaxy formed at $z_f = 2$, 3 and 5 predicted by the passive evolution models of Kodama & Arimoto (1997), normalized to the Coma cluster which have $K_s^* = 10.9$ (de Propris et al. 1998). The "no evolution" predictions are calculated using the k-corrections of Mannucci et al. (2001). The data points from the literature have been derived with a fixed $\alpha = -0.9$. (de Propris et al. 1999; Nakata et al. 2001) except for the $z = 1$ value which was was derived with α as a free parameter (Toft et al. 2003).

the Coma cluster, we derive an evolution in the restframe K-band characteristic magnitude of $\Delta M_K = -1.4 \pm 0.5$ mag (assuming that $M_K^* = M_{K_s}^*$), in agreement with the evolution derived in the restframe z-band. The errors quoted for ΔM_z and ΔM_K are dominated by the uncertainty in the derived K_s^*.

Taken at face value the observed faint end slope $\alpha = -0.64^{+0.27}_{-0.25}$ is similar to the value $\alpha = -0.60^{+0.39}_{-0.33}$ derived at similar restframe wavelengths (in the K_s-band) in the $z = 1$ cluster MG2016+112 (Toft et al. 2003), and the value $\alpha = -0.58 \pm 0.05$ derived (in the z-band) in local clusters (Goto et al. 2002), but due to the relatively large uncertainty in the high redshift values, we can not rule out modest evolution in α between $z = 0$ and $z \sim 1$.

In Fig.10 we compare the derived K_s^* with values derived for clusters at lower redshift and the predictions of passive evolution models for the evolution of an L^* galaxy formed at $z_f = 2$, 3 and 5 (Kodama & Arimoto 1997). The observed evolution of K^* to $z = 1.237$ is consistent with what is expected for a passively evolving population of galaxies formed at $z_f \gtrsim 2$.

5. Summary and discussion

In this paper we have taken advantage of an extensive NIR and optical dataset of the massive, X-ray luminous cluster of galaxies RDCS J1252.9-2927 to derive the first secure constraints on the shape of the K_s-band LF at $z > 1$. The LF was found to be well represented by the Schechter function over the observed range of cluster galaxy magnitudes: $K_s = [17.0 - 22.5]$.

We tested our analysis for the influence of photometric errors and pollution from field galaxies and found our results to be robust and relatively insensitive to the effects of field galaxy pollution in the central parts of the field where the constraints of the cluster galaxy LF is derived. The characteristic magnitude $K_s^* = 18.54^{+0.45}_{-0.55}$ is $\Delta M_z = 1.3 \pm 0.5$ magnitudes brighter than the characteristic magnitude measured for clusters in the local universe at similar restframe wavelengths (in the z-band).

This is consistent with studies of the fundamental plane in a cluster at similar redshift where a luminosity evolution of $\Delta M_B = -1.50 \pm 0.13$ was found in the restframe B-band (van Dokkum & Stanford 2003).

Apart from being shifted to systematically brighter magnitudes, the shape of the bright end of the LF at $z = 1.237$ appears similar to in the local universe. Since the K-band LF is a good tracer of the stellar mass function of the cluster galaxies, this suggests that the massive elliptical that dominate the bright end of the LF were already in place at $z = 1.237$. This is a challenge for hierarchical models which predict the bright end of the K-band LF to steepen and K^* to become fainter at high redshift as the massive galaxies break up into their progenitors. At $z \sim 1$ current hierarchical models predict the characteristic mass (closely related to the characteristic K-band magnitude) to be a third of that in the local universe (Kodama & Bower 2003), which is clearly not the case for RDCS J1252.9-2927.

The brightening of the characteristic magnitude, and lack of evolution in the shape of the bright end of the LF to redshift $z = 1.237$ is consistent with a simple formation scenario in which the massive elliptical galaxies that dominate the bright end of the K-band LF are passively evolving systems assembled at high redshift $z_f \simeq 3$.

This formation scenario is also in agreement with the observed properties of the CM-relation of elliptical galaxies in RDCS J1252.9-2927, which is identical to the CM relation found in local clusters in terms of slope and scatter, but bluer on average, consistent with old populations of stars formed at $2.7 < z_f < 3.6$ (Lidman et al. 2003; Blakeslee et al. 2003). From the evolution of the CM relationship alone it is not possible to distinguish between formation scenarios where the old stars are formed in monolithic collapse of the elliptical galaxies at high redshift, and scenarios where they are formed in the disks of less massive late-type galaxies which later merge to form the ellipticals, as long as the merging does not trigger significant star formation. From the lack of evolution in the shape of the bright end of the K-band LF we can however deduce that if the massive ellipticals in clusters formed through merging, it took place at higher redshifts ($z \gg 1$) than is predicted by current semi analytical models.

In the faint end of the LF we derive a slope $\alpha = -0.64^{+0.27}_{-0.25}$ which is similar to the slope measured at similar restframe wavelengths in the MG2016+112 cluster at $z = 1$ and in clusters in the local universe. The lack of evolution can be interpreted as lack of evolution in the stellar mass spectrum of the low mass galaxies that dominate the faint end of the K-band LF, consistent with a high formation-redshift/passive-evolution scenario similar to the one derived for the brighter cluster galaxies. However, due to the relatively large uncertainties involved, a modest evolution in α between $z = 0$ and $z = 1.237$

is not ruled out. Such an evolution is expected from hierarchical models, and from observational evidence such as the morphology-density relation (Treu et al. 2003), the Butcher-Oemler effect (Butcher & Oemler 1984; van Dokkum et al. 2000; Nakata et al. 2001) and the enhanced fraction of merging galaxies in intermediate and high redshift clusters (van Dokkum et al. 2000, 2001).

The results derived here for the evolution of the cluster galaxy K_s-band LF are similar to the results derived from the K20 survey for the evolution of the field galaxy K_s-band LF (Pozzetti et al. 2003). The magnitude of the luminosity evolution ($\Delta M_K = -1.4 \pm 0.5$ mag to $z = 1.237$) cannot be directly compared to the value derived in the field ($\Delta M_K = -0.54 \pm 0.12$ mag to $z = 1$, Pozzetti et al. 2003) since the latter is a mean value derived in a broad redshift interval, centered on a lower redshift, but we note that they are broadly consistent.

Acknowledgements. We thank T. Kodama for providing us with his elliptical galaxy evolution models and J. Hjorth for suggestions and discussions which helped improve the analysis and the presentation. This work was supported by the Danish Ground-Based Astronomical Instrument Center (IJAF). Support for SAS came from NASA/LTSA grant NAG5-8430, who is also supported by the Institute of Geophysics and Planetary Physics (operated under the auspices of the US Department of Energy by the University of California Lawrence Livermore National Laboratory under contract W-7405-Eng-48).

References

Aragon-Salamanca, A., Ellis, R. S., Couch, W. J., & Carter, D. 1993, MNRAS, 262, 764
Barger, A. J., Cowie, L. I., Capak, P., et al. 2003, AJ, 126, 632
Beijersbergen, M., Hoekstra, H., van Dokkum, P. G., & van der Hulst, T. 2002, MNRAS, 329, 385
Benítez, N. 2000, ApJ, 536, 571
Bertin, E. & Arnouts, S. 1996, A&AS, 117, 393
Blakeslee, J. P., Franx, M., Postman, M., et al. 2003, ApJ(in press)
Bolzonella, M., Miralles, J.-M., & Pell, R. 2000, A&A, 363, 476
Bower, R. G., Lucey, J. R., & Ellis, R. S. 1992, MNRAS, 254, 589
Butcher, H. & Oemler, A. 1978, ApJ, 219, 18
Butcher, H. & Oemler, A. 1984, ApJ, 285, 426
Cohen, J. G. 2002, ApJ, 567, 672
Coleman, G. D., Wu, C.-C., & Weedman, D. W. 1980, ApJS, 43, 393
de Propris, R., Eisenhardt, P. R., Stanford, S. A., & Dickinson, M. 1998, ApJ, 503, L45
de Propris, R., Stanford, S. A., Eisenhardt, P. R., & Dickinson, M. 2003, ApJ, 598
de Propris, R., Stanford, S. A., Eisenhardt, P. R., Dickinson, M., & Elston, R. 1999, AJ, 118, 719
Demarco, R., Rosati, P., Mainieri, V., et al. 2003, (in prep)
Driver, S. & De Propris, R. 2003, Ap&SS, 285, 175
Eggen, O. J., Lynden-Bell, D., & Sandage, A. 1962, ApJ, 136, 748
Fabricant, D. G., McClintock, J. E., & Bautz, M. W. 1991, ApJ, 381, 33
Fernández-Soto, A., Lanzetta, K. M., & Yahil, A. 1999, ApJ, 513, 34
Goto, T., Okamura, S., McKay, T. A., et al. 2002, PASJ, 54, 515
Jarrett, T. H., Chester, T., Cutri, R., et al. 2000, AJ, 119, 2498
Kauffmann, G. & Charlot, S. 1998, MNRAS, 294, 705
Kinney, A. L., Calzetti, D., Bohlin, R. C., et al. 1996, ApJ, 467, 38
Kochanek, C. S., Pahre, M. A., Falco, E. E., et al. 2001, ApJ, 560, 566
Kodama, T. & Arimoto, N. 1997, A&A, 320, 41
Kodama, T. & Bower, R. G. 2003, astro-ph/0308130
Lidman, C., Rosati, P., Demarco, R., et al. 2003, A&A(submitted)
Lopez-Cruz, O., Yee, H. K., Brown, J. P., Jones, C., & Forman, W. 1997, ApJ, 475, 97
Madau, P., Pozzetti, L., & Dickenson, M. 1998, ApJ, 498, 106
Mannucci, F., Basile, F., Poggianti, B. M., et al. 2001, MNRAS, 326, 745
Nakata, F., Kajisawa, M., Yamada, T., et al. 2001, PASJ, 53, 1139
Pozzetti, L., Cimatti, A., Zamorani, G., et al. 2003, A&A, 402, 837
Rosati, P., Mainieri, V., Demarco, R., et al. 2003a, (in prep)
Rosati, P., Stanford, S. A., Eisenhardt, P. R., et al. 1999, AJ, 118, 76
Rosati, P., Tozzi, P., Ettori, S., et al. 2003b, AJ(in press)
Schechter, P. & Press, W. H. 1976, ApJ, 203, 557
Smail, I., Edge, A. C., Ellis, R. S., & Blandford, R. D. 1998, MNRAS, 293, 124
Stanford, S. A., Eisenhardt, P. R., & Dickinson, M. 1998, ApJ, 492, 461
Stanford, S. A., Elston, R., Eisenhardt, P. R., et al. 1997, AJ, 114, 2232
Toft, S., Soucail, G., & Hjorth, J. 2003, MNRAS, 344, 337
Treu, T., Ellis, R. S., Kneib, J., et al. 2003, ApJ, 591, 53
van Dokkum, P. G. & Franx, M. 1996, MNRAS, 281, 985
van Dokkum, P. G., Franx, M., Fabricant, D., Illingworth, G. D., & Kelson, D. D. 2000, ApJ, 541, 95
van Dokkum, P. G. & Stanford, S. A. 2003, ApJ, 585, 78
van Dokkum, Stanford, S. A., Holden, B. P., Eisenhardt, P. R., Dickenson, M., & Elston, R. 2001, ApJ, 552, 101

Chapter 7

General conclusions and outlook

The work I have carried out during this thesis has allowed me to learn the "art" of spectroscopic data reduction as well as a number of analysis techniques for imaging and spectroscopic data. In addition, the broad range of astrophysical issues touched by the data sets used in this work has allowed me to learn and improve the astrophysical background necessary for the interpretation of these data. Specifically, I have become familiar with the treatment of Multi-Object Spectroscopy data from FORS at The ESO Very Large Telescope. Moreover, I have been able to learn the basic background related to X-ray imaging and apply this knowledge to the analysis of ROSAT/PSPC data in particular.

The spectroscopic work was carried out as part of a ESO Large Program devoted to carryed out an unprecedented spectro-photometric study of two of the most distant massive clusters of galaxies known in the southern sky: RX J0152.7-1357 at $z = 0.837$ and RDCS J1252.9-2927 at $z = 1.237$. These data are also supported by X-ray Chandra and XMM imaging as well as HST+ACS imaging on both clusters. This impressive collection of data constitutes one of the best and most complete ones available at present on two distant clusters of galaxies, and constitutes the raw material of the investigation presented in this thesis. A large fraction of the time has been devoted to putting together this massive data set, an effort which involved the preparation of observations, their execution, data reduction and calibration until a high quality final product was achieved. I believe that the first exciting results presented in this thesis are indicative of the quality and potential of this data set. They were obtained by only "scratching the surface" of it, and much more information will be gleaned as we further proceed into the analysis.

The X-ray work with the ROSAT imaging was devoted to the analysis of the X-ray surface brightness of 24 nearby ($0.01 < z < 0.3$) galaxy clusters, in order to better characterize their internal thermodynamical structure and set constraints on their evolution.

The main conclusions of the present thesis work can be summarized as follows:

The structure of nearby clusters

- Nearby clusters of galaxies in a well relaxed state are self-gravitational structures characterized by having an ICM specific entropy which, at first order, is nearly the same among clusters and, at second order, varies with the logarithm of the gas mass. A similar behavior is found for the Dark Matter component.

- This dependence between gas specific entropy and mass suggests that merging processes between DM halos play an important role in such a relation because of their impact on the final total mass and on the amount of entropy produced during the cluster formation. Dissipating processes (such as Bremsstrahlung emission) in clusters may also play a role as generators of entropy.

- The observed self-similar relation between potential energy and dynamical mass in nearby clusters indicates that total energy and mass are conserved during the whole formation history of the cluster. Merging events and energy losses affecting the integrated specific entropy are however small enough as to allow conservation of mass and energy.

- The observed specific entropy-mass and potential energy-mass relations in clusters have behaviors comparable to those observed for stars in elliptical galaxies. This strongly suggests that elliptical galaxies could be considered as scaled down versions of galaxy clusters.

Galaxy populations in high-z clusters

- RX J0152.7-1357 is a dynamically young cluster at $z = 0.837$ in an early merging phase. Seventy-eight spectroscopic cluster members have been confirmed giving a velocity dispersion of about 1300 km s^{-1}. The distribution of the cluster X-ray emission is well traced by that of the spectroscopic cluster members. Three main substructures in the distribution of the spectroscopic members can be identified. These substructures correspond to clear peaks in the X-ray emission.

- A clear segregation between early- and late-type galaxies is seen in RX J0152.7-1357 . The main central structures of the cluster are dominated by early-type galaxies while the outer regions of RX J0152.7-1357 show an important number of emission line star-forming galaxies. A surprising result was the discovery of cluster members belonging to the red sequence with on-going star formation, living in the outer regions of the cluster. Their location in the Color-Magnitude diagram is among the cluster early-types, suggesting a formation redshift greater than 2 for the stellar populations of their bulges. ACS imaging shows that, in several cases, conventional disks around red bulges are the place of the star forming activity, possibly induced by the interaction of the galaxy with the ICM. The coexistence of old and young stellar populations in a sizeable number of cluster galaxies, mostly placed in the outskirts of RX J0152.7-1357 , points toward a complex star formation history which requires further investigation.

- RDCS J1252.9-2927 is the most distant massive cluster known in the southern sky to date. The 36 spectroscopic members confirmed in this cluster give a median redshift of $z = 1.237$ and a velocity dispersion of $\sigma_v = 760^{+117}_{-69}$ km/s. 13 members with [OII] emission lines have been confirmed. The cluster center is dominated by early-type galaxies while the outer regions are dominated by emission-line galaxies. The morphology of the galaxy distribution is elongated in the E-W direction. This observation is supported by an asymmetry of the X-ray distribution also in the E-W direction suggesting a possible merging phase in the cluster. However we did not observe red emission line galaxies as in RX J0152.7-1357 .

- High quality optical and near IR VLT and optical HST ACS imaging is available for RDCS J1252.9-2927 . These data have been used to show that a clear CM relation in RDCS J1252.9-2927 is observed at this high redshift. The slope and scatter of the CM relation in RDCS J1252.9-2927 are consistent with those observed at lower redshift and in the local universe, indicating that the CM relation is due to metallicity and not to age. The observed CM relation can be reproduced by models where early-types are formed in a instantaneous, single-burst at solar metallicity, followed by passive evolution. These models predict that stellar populations in early-types in RDCS J1252.9-2927 were formed at $z_f \sim 3$.

- The formation redshift derived for early-types in RDCS J1252.9-2927 indicates that the age of the stars within these galaxies is about 2.7 Gyrs. The existence of such an early stellar population is supported by the detection of a significant H_δ feature in the combined spectrum of the 10 brightest cluster members. These observations are in agreement with the fact that the early-type CM relation in RDCS J1252.9-2927 is bluer than the CM relation of early-types in Coma.

- ACS imaging of RDCS J1252.9-2927 , particularly of late spectral type galaxies, supports the hypothesis that the morphological Hubble sequence was not fully in place at $z = 1.2$. We observed only a hint of grand-design spiral structure in one of the star forming members, in contrast with observations of RX J0152.7-1357 at $z = 0.83$, an epoch when the classical Hubble classification has already emerged. A similar picture has been obtained from studies of field galaxies.

- The observed CM relation in RX J0152.7-1357 and RDCS J1252.9-2927 and the spectro-photometric properties of their member galaxies suggest a more complex picture for the mass assembly history of cluster galaxies which cannot be simply described by either the classical model or the hierarchical model. These findings will surely stimulate further investigations and will challenge simple models of galaxy formation.

Future directions

The continuation of the present work can be summarized as follows:

- The same analysis carried out on the sample of nearby clusters may be carried out on more distant systems in order to test the evolution with redshift of the correlations found. Chandra and XMM data can be used in order to perform such a study. Also, a sample of clusters from hydrodynamical simulations could be used in a similar study.

- In addition, the observed correlation between the shape and scale parameters of the Sérsic profile applied to clusters could be used as a distance indicator, in an analogous way to the methods proposed for galaxies in nearby clusters. However, this correlation should be seen with caution and a more detailed study should be performed in order to establish whether this correlation is due to physical properties or is just an artifact of the mathematical nature of the Sérsic profile and fitting procedure. Note that the uncertainties in the distance derived from this correlation may be larger than those derived from standard photometric redshift methods.

- The discovery of the red emission line members in RX J0152.7-1357 raises interesting questions on the way in which these galaxies were formed. A more complete analysis of their spectro-photometrical properties, as well as possible identification of similar systems in other clusters might reveal whether the cluster mass and/or physical conditions of the local environment play a dominant role.

- A complete morphological analysis of the galaxy population in RX J0152.7-1357 and RDCS J1252.9-2927 is one of the main issues in the future of this project. This analysis is of great importance in order to understand the environmental effects on the galaxy population and evolutionary effects according to galaxy type. This information integrated to the already available spectro-photometric information will provide the most complete picture of two distant clusters of galaxies ever seen. This will have a great impact on constraining models of galaxy formation and evolution.

- Weak and strong lensing analysis of our two distant clusters will be used to obtain accurate mass distributions, specifically the slope of the inner mass profile which provides a stringent test of CDM models. The identification of the arc (at $z = 3.36$) in RDCS J1252.9-2927 has opened the way to map the mass distribution of the most distant lensing cluster known so far. The spectroscopic identification with the VLT of a large number of multiple images in our two clusters is under way.

Appendix A

List of publications

Refereed Journal Articles:

Demarco, R.; Magnard, F.; Durret, F.; Márquez, I. *A study of dark matter halos and gas properties in clusters of galaxies from ROSAT data.* A&A, 407, 437. 2003.

Lidman, C.; Rosati, P.; **Demarco, R.**; Mainieri, V.; Toft, S. *Deep near-infrared imaging of RDCS J1252.9-2927 at z=1.237. I. The colour-magnitude diagram.* A&A, 2003. In press. [astro-ph/0310516]

Rosati, P.; Tozzi, P.; Ettori, S.; Mainieri, V.; **Demarco, R.**; et al. *Chandra and XMM-Newton observations of RDCS J1252.9-2927, a massive cluster at z=1.24.* AJ, Jan. 2004. In press. [astro-ph/0309546]

Blakeslee, J.; Franx, M.; Postman, M.; Rosati, P.; Holden, B.; Illingworth, G.; Ford, H.; Cross, J.; Gronwall, C.; Benítez, N.; Bouwens, R.; Broadhurst, T.; Clampin, M.; **Demarco, R.**; Golimowski, D.; et al. *Advanced Camera for Surveys Photometry of the Cluster RDCS 1252.9-2927: The Color-Magnitude Relation at z=1.24.* ApJL, 596, 143. 2003.

Toft, S.; Mainieri, V.; Rosati, P.; Lidman, C.; **Demarco, R.**; Nonino, M.; Stanford, S. A. *K_s-band luminosity function of the z=1.237 cluster of galaxies RDCS J1252.9-2927.* Submitted to Astronomy & Astrophysics.

Conference Proceedings:

Demarco, R. et al. 2003 *The Structure and Galaxy Population of the Most Distant Massive Clusters in the Southern Sky.*

Carnegie Observatories Astrophysics Series, Vol. 3: Clusters of Galaxies: Probes of Cosmological Structure and Galaxy Evolution , ed. J. S. Mulchaey, A. Dressler, and A. Oemler (Pasadena: Carnegie Observatories,

http://www.ociw.edu/ociw/symposia/series/symposium3/proceedings.html)

Durret, F.; **Demarco, R.**; Magnard, F. & Gerbal, D. *Clusters of galaxies as self-gravitating systems.* Rencontres de Moriond, March 10-17, 2001, Les Arcs (Savoie), Ed. D. Neumann et al. [astro-ph/0105496].

Demarco, R.; Durret, F.; Magnard, F. & Gerbal, D. *Specific Entropy in X-ray Clusters of Galaxies.* Constructing the Universe with Clusters of Galaxies, IAP 2000 meeting, Paris, France, July 2000, Florence Durret & Daniel Gerbal Eds.

In preparation:

Demarco, R.; Rosati, P. et al. *RX J0152.7-1357 : A Forming Cluster of Galaxies at z=0.83.* To be submitted to Astronomy & Astrophysics.

Bibliography

[1] Abell, G. O. ApJ Supplement Series, 3, 211. 1958.

[2] Abell, G. O. In Galaxies and the Universe, Stars and Stellar Systems, Vol. IX, eds. A. Sandage, M. Sandage and J. Kristian. 1975.

[3] Abell, G. O., Corwin, H. G. & Olowin, R. P. ApJ Supplement Series, 70, 1. 1989.

[4] Allen, S., Ettori, S. & Fabian A. MNRAS 324, 877. 2001.

[5] Allen, S., Schmidt, R. & Fabian A. MNRAS 328, L37. 2001.

[6] Appenzeller, I & Rupprecht, G. The ESO Messenger, March 1992, p.18.

[7] Arimoto, N. & Yoshii, Y. A&A, 173, 23. 1987.

[8] Arnaud, M., & Evrard, A. E. MNRAS, 305, 631. 1999.

[9] Bahcall, N. A. ARA&A, 26, 631. 1988.

[10] Bahcall, N. A. & West, M. J. ApJ, 392, 419. 1992.

[11] Bahcall, N. A. & Cen, R. ApJ, 407, L49. 1993.

[12] Bahcall, N. A., Fan, X. & Cen, R. ApJ, 485, 53. 1997.

[13] Bahcall, N. A. In Formation of Structure in the Universe ed. Avishai Dekel and Jeremiaa Ostriker. Cambridge: Cambridge Univ. Press. 1999.

[14] Bahcall, N. A. et al. ApJ, 585, 182. 2003.

[15] Bahcall, N. A. et al. [astro-ph/0307102]

[16] Balogh, M. L. et al. MNRAS, 326, 1228. 2001.

[17] Bardeen, J. M. et al. ApJ, 304, 15. 1986.

[18] Barazza, F. D., Binggeli, B. & Jerjen, H. A&A, 407, 121. 2003.

[19] Bauer, F. E. et al. AJ, 124, 2351. 2002

[20] Beers, T. C. & Geller, M. J. ApJ, 274, 491. 1983.

[21] Beers, T. C. et al. AJ, 100, 32, 1990.

[22] Benítez, N. ApJ, 536, 571. 2000.

[23] Bennett C. L. et al. ApJ, 2003. In press. [astro-ph/0302207]

[24] Bertin, E. & Arnouts, S. A&AS, 117, 393. 1996.

[25] Bertschinger, E. ApJ Supplement Series, 58, 39. 1985.

[26] Bertschinger, E. ARA&A, 36, 599. 1998.

[27] Bessell, M. S. PASP, 102, 1181. 1990.

[28] Binney, J. & Tremaine, S. Galactic Dynamics. Princeton Series in Astrophysics. Princeton Univ. Press. 1987.

[29] Binney, J. & Merrifield, M. Galactic Astronomy. Princeton Series in Astrophysics. Princeton Univ. Press. 1998.

[30] Binney, J. & Evans, N. MNRAS 327, L27. 2001.

[31] Birkinshaw, M. In The cosmic microwave background: 25 years later. eds. N. Mandolesi and N. Vittorio. Dordrecht, Netherlands, Kluwer Academic Publishers. 1990.

[32] Birkinshaw, M. Carnegie Observatories Astrophysics Series, Vol. 3: Clusters of Galaxies: Probes of Cosmological Structure and Galaxy Evolution ed. J.S. Mulchaey, A. Dressler, and A. Oemler. Cambridge: Cambridge Univ. Press. 2003.

[33] Biviano, A. In Constructing the Universe with Clusters of Galaxies, eds. F. Durret and D. Gerbal. Paris. 2000.

[34] Blakeslee, J. P. et al. ApJL, 596, 143. 2003.

[35] Bolzonella, M., Miralles, J.-M. & Pelló, R. A&A, 363, 476. 2000.

[36] Bonnor, W. B. MNRAS, 116, 351. 1956.

[37] Borgani, S. et al. ApJ, 517, 40. 1999.

[38] Borgani, S. et al. ApJ, 561, 13. 2001.

[39] Bower, R. G., Lucey, J. R., & Ellis, R. S. MNRAS, 254, 601. 1992.

[40] Bower, R. G., Kodama, T. & Terlevich, A. MNRAS, 299, 1193. 1998.

[41] Bower, R. G. et al. In Star Formation in Early Type Galaxies, ASP Conference Series 163, ed. P. Carral & J. Cepa. 1999.

[42] Bower, R. G. et al. MNRAS, 325, 497. 2001.

[43] Braine, J., Henkel, C. & Wiklind, T. A&A, 321, 765. 1997.

[44] Broadhurst, T. et al. ApJ, 534, L15. 2000.

[45] Bruzual, G. ApJ, 273, 105. 1983.

[46] Bruzual, G. & Charlot, S. ApJ, 405, 538. 1993.

[47] Bunn, E. F. & White, M. ApJ, 480, 6. 1997.

[48] Burke, D. J. et al. ApJ, 488, L83. 1997.

[49] Butcher, H. & Oemler, A. ApJ, 219, 18. 1978.

[50] Butcher, H. & Oemler, A. ApJ, 285, 426. 1984.

[51] Calzetti, D., Kinney, A. L. & Storchi-Bergmann, T. ApJ, 429, 582. 1994.

[52] Caon, N., Capaccioli, M. & D'Onofrio, M. MNRAS, 265, 1013. 1993.

[53] Carroll, S.; Press, W. and Turner, E. ARA&A 30, 499. 1992

[54] Cavaliere, A. & Fusco-Femiano, R. A&A 49, 137. 1976.

[55] Chen, H.-W. et al. ApJ, 586, 745. 2003.

[56] Cimatti, A. et al. A&A, 392, 395. 2002a.

[57] Cimatti, A. et al. A&A, 391, L1. 2002b.

[58] Ciotti, L. & Bertin, G. A&A, 352, 447. 1999.

[59] Coleman, G. D., Wu, Chi-Chao & Weedman, D. W. ApJ Supplement Series, 43, 393. 1980.

[60] Colles M. M. et al. MNRAS, 328, 1039. 2001.

[61] Colles M. M. et al. 2003. [astro-ph/0306581]

[62] Couch, W. J. et al. ApJ, 430, 121. 1994.

[63] Daddi, E., Cimatti, A. & Renzini, A. A&A, 362, L45. 2000.

[64] Daddi, E. et al. ApJ, 588, 50. 2003.

[65] Davies, M. & Peebles, P. J. E. ApJ, 267, 465. 1983.

[66] Davies, R. L., Sadler, E. M. & Peletier, R. F. MNRAS, 262, 650. 1993.

[67] De Grandi, S. & Molendi, S. ApJ 567, 163. 2002.

[68] Della Ceca, R. et al. A&A, 353, 498. 2000.

[69] Demarco, R. et al. A&A, 407, 437. 2003a.

[70] Demarco, R. et al. Carnegie Observatories Astrophysics Series, Vol. 3: Clusters of Galaxies: Probes of Cosmological Structure and Galaxy Evolution, ed. J. S. Mulchaey, A. Dressler, and A. Oemler (Pasadena: Carnegie Observatories, http://www.ociw.edu/ociw/symposia/series/symposium3/proceedings.html). 2003b.

[71] De Propris, R. et al. ApJ, 503, L45. 1998.

[72] De Propris, R. et al. AJ, 118, 719. 1999.

[73] De Propris, R. et al. MNRAS, 342, 725. 2003.

[74] de Vaucouleurs G. Ann. d'Astroph. 11, 247. 1948.

[75] Dey, A. et al. ApJ, 498, L93. 1998.

[76] de Zeeuw, P. T. et al. MNRAS, 329, 513, 2002.

[77] Djorgovski, S & Davies, M. ApJ, 313, 59. 1987.

[78] Donahue, M. et al. ApJ, 502, 550. 1998.

[79] Donas, J. & Deharveng, J. M. A&A, 140, 325. 1984.

[80] Dolag, K. & Schindler, S. A&A, 364, 491. 2000.

[81] Dressler, A. ApJ, 236, 351. 1980.

[82] Dressler, A. & Gunn, J. E. ApJ, 270, 7. 1983.

[83] Dressler, A. et al. ApJ, 313, 42. 1987a.

[84] Dressler, A. & Shectman, S. AJ, 94, 899. 1987b.

[85] Dressler , A. & Shectman, S. A. AJ, 95, 985, 1988.

[86] Dressler, A. et al. ApJ, 490, 577. 1997.

[87] Dressler, A. et al. ApJ Supplement Series, 122, 51. 1999.

[88] Driver, S. P. et al. ApJ, 496, L93. 1998.

[89] Durret, F. et al. A&A 287, 733. 1994.

[90] Ebeling, H. et al. MNRAS 281, 799. 1996.

[91] Ebeling, H. et al. ApJ, 534, 133. 2000.

[92] Eggen, O. J., Lynden-Bell, D. & Sandage, A. R. ApJ, 136, 748. 1962.

[93] Eke, V. R. et al. MNRAS, 298, 1145. 1998.

[94] Ellis, R. S. et al. MNRAS, 280, 235. 1996.

[95] Ellis, R. S. ARA&A, 35, 389. 1997.

[96] Emerson, D. Interpreting astronomical spectra. John Wiley and Sons. 1996.

[97] Faber, S. M. ApJ, 179, 731. 1973.

[98] Faber, S. M. & Jackson, R. E. ApJ, 204, 668. 1976.

[99] Fabian, A. C. ANA&A, 32, 277. 1994.

[100] Fan, X., Bahcall, N. A. & Cen, R. ApJ, 490, 123. 1997.

[101] Ferguson, H. C., Dickinson, M. & Williams, R. ARA&A, 38, 667. 2000.

[102] Fernández-Soto, A. et al. ApJ, 513, 34. 1999.

[103] Fernández-Soto, A. Ap&SS, 276, 965. 2001.

[104] Fillmore, J & Goldreich, P. ApJ, 281, 1. 1984.

[105] Finoguenov, A., Reiprich, T. H. & Böhringer, H. A&A, 368, 749. 2001.

[106] Fioc, M. & Rocca-Volmerange, B. A&A, 326, 950. 1997.

[107] Flores, R. & Primack, J. R. ApJ 427, L1. 1994.

[108] Forman, W. et al. ApJ 178, 309. 1972

[109] Franx, M., Illingworth, G. & Heckman, T. AJ, 98, 538. 1989.

[110] Fritz, G. et al. ApJ 164, 81. 1971

[111] Fukugita, M., Shimasaku, K. & Ichikawa, T. PASP, 107, 945. 1995.

[112] Geller, M. J. & Beers, T. C. PASP, 94, 421. 1982.

[113] Gerbal, D. et al. A&A 253, 77. 1992.

[114] Gerbal, D. et al. MNRAS, 285, L41. 1997.

[115] Giacconi, R. et al. ApJ Supplement Series, 139, 369. 2002.

[116] Gilli, R. et al. ApJ, 592, 721. 2003.

[117] Giogia, I. et al. ApJ, 356, L35. 1990a.

[118] Gioia, I. et al. ApJ Supplement Series, 72, 567. 1990b.

[119] Giogia, I. et al. AJ, 117, 2608. 1999.

[120] Giogia, I. et al. ApJ, 553, L109. 2001.

[121] Gonzalez, A. H., Zaritsky, D. & Wechsler, R. H. ApJ, 571, 129. 2002.

[122] Graham, A. & Colless, M. MNRAS, 287, 221. 1997.

[123] Graham, A. et al. AJ, 125, 295. 2003.

[124] Grego, L. et al. ApJ, 539, 39. 2000.

[125] Gursky, H. et al. ApJ 165, 43. 1971a

[126] Gursky, H. et al. ApJ 167, 81. 1971b

[127] Guzmán, R. et al. MNRAS, 257, 187. 1992.

[128] Hamuy, M. et al. PASP, 104, 533. 1992.

[129] Hamuy, M. et al. PASP, 106, 566. 1994.

[130] Hashimoto, Y. et al. A&A, 381, 841. 2002.

[131] Hasinger, G. A&A, 365, L45. 2001.

[132] Hawkins, E. et al. MNRAS, 2003. In press. [astro-ph/0212375]

[133] Heath, D. J. MNRAS, 179, 351. 1977.

[134] Helsdon, S.F. & Ponman, T.J. MNRAS 315, 356. 2000.

[135] Henry, J. P. et al. ApJ, 386, 408. 1992.

[136] Herschel, F. W. Phil. Trans. 75, 213. 1785

[137] Hicks, A. et al. ApJ 580, 763. 2002.

[138] Hinshaw, G. et al. ApJ, 464, L17, 1996a.

[139] Holden, B. et al. AJ, 124, 33. 2002.

[140] Hu, W., & White, M. ApJ, 486, L1. 1997.

[141] Hubble, E. P. Proc. Nat. Acad. Sci. (Wash), 15, 168. 1929.

[142] Hubble, E. P. & Humason, M. L. ApJ, 74, 43. 1931.

[143] Hubble, E. The Realm of the Nebulae. Yale University Press, 1936

[144] Huchra, J. P. et al. ApJ Supplement Series, 72, 433. 1990.

[145] James, F. CERN Program Library Long Writeup D506. 1994.

[146] Jang-Condell, H. & Hernquist, L. ApJ 548, 68. 2001.

[147] Jerjen, H. & Tammann, G. A. A&A, 321, 713. 1997.

[148] Jing, Y. P. & Suto, Y. ApJ 529, L69. 2000.

[149] Joergensen, I., Franx, M., & Kjaergaard, P. MNRAS, 280, 167. 1996.

[150] Jones, C. & Forman, W. In Clusters and Superclusters of Galaxies (NATO AS1 Vol. 366), ed. A. C. Fabian, (Dordrecht/Boston/London: Kluwer). 1992.

[151] Jones, L. R. et al. ApJ, 495, 100. 1998.

[152] Kaiser, N. ApJ, 284, L9. 1984.

[153] Karzas, W. J. & Latter, R. ApJ Supplement Series, 6, 167. 1961.

[154] Kauffmann, G. MNRAS, 281, 487, 1996.

[155] Kauffmann, G. & Charlot, S. MNRAS, 297, 23, 1998a.

[156] Kauffmann, G. & Charlot, S. MNRAS, 294, 705, 1998b.

[157] Kellogg, E. M. et al. ApJ 174, 65. 1972

[158] Kellogg, E., Baldwin, J. R. & Koch, D. ApJ, 199, 299. 1975.

[159] Kennicutt, R. ApJ, 272, 54. 1983.

[160] Kennicutt, R. C. ApJ, 388, 310. 1992a.

[161] Kennicutt, R. C. ApJ Supplement Series, 79, 255. 1992b.

[162] Kennicutt, R. C. ARA&A, 36, 189. 1998.

[163] King, I. ApJ, 174, L123. 1972.

[164] Kinney, A. L. et al. ApJ, 467, 38. 1996.

[165] Kodama, T. & Arimoto N. A&A. 320, 41. 1997

[166] Kolb, E. W. & Turner, M. S. The Early Universe. Redwood City, California: Addison-Wesley Publishing Co. 1990.

[167] Krywult, J., MacGillivray, H. T. & Flin, P. A&A, 351, 883. 1999.

[168] Kurtz, M. J. et al. In Astronomical Data Analysis Software and Systems I, A.S.P. Conference Series, Vol. 25. Diana M. Worrall, Chris Biemesderfer, and Jeannette Barnes, eds. 1992.

[169] Landy, S. D. & Szalay, A. S. ApJ, 388, 310. 1993.

[170] Lanzoni, B. Ph.D. Thesis, Université Paris VII. 2000.

[171] Larson, R. B. MNRAS, 173, 671. 1975.

[172] Larson, R. B. "The origing of the Hubble sequence". Procedings of the 27th Rencontre de Moriond, Les Arcs, France. Eds.: T. Xuan Thuan, C. Balkowski & T. Thanh Van. 1992.

[173] Le Borgne, J.-F. et al. A&A, 402, 433. 2003.

[174] Lewis, A. et al. ApJ, 586, 135. 2003.

[175] Lidman, C. et al. A&A, 2003. Submitted.

[176] Lilly, S. J. et al. ApJ, 455, 108. 1995.

[177] Lima Neto, G. B., Gerbal, D. & Márquez, I. MNRAS, 309, 481. 1999.

[178] Lloyd-Davies, E.J., Ponman, T.J. & Cannon D.B. MNRAS 315, 689. 2000.

[179] Longair, M. S. Galaxy Formation. A&A library. Springer-Verlag, 1998.

[180] Madau, P. et al. MNRAS, 283, 1388. 1996.

[181] Maddox, S. J. et al. MNRAS, 243, 692. 1990

[182] Magnard, F. Ph.D. Thesis, Université Paris VI. 2002.

[183] Markevitch, M. et al. ApJ 503, 77. 1998.

[184] Markevitch, M. ApJ, 504, 27. 1998.

[185] Markevitch, M. et al. ApJ, 567, L27. 2002.

[186] Marleau, F. & Simard, L. ApJ, 507, 585. 1998.

[187] Márquez, I. et al. A&A, 353, 873. 2000.

[188] Márquez, I. et al. A&A, 379, 767. 2001.

[189] Massarotti, M. et al. A&A, 380, 425. 2001.

[190] Massarotti, M. et al. A&A, 404, 75. 2003.

[191] Massey, P., Valdes, F. & Barnes, J. A User's Guide to Reducing Slit Spectra with IRAF. April 1992.

[192] Massey, P. A User's Guide to CCD Reductions with IRAF. February 1997.

[193] Mattig, W. Astron. Nachr. 284, 109. 1958.

[194] Maughan, B. J. et al. ApJ, 587, 589. 2003.

[195] Mellier, Y. & Mathez, G. A&A 175, 1. 1987.

[196] Mellier, Y. ARA&A, 37, 127. 1999.

[197] Menanteau, F., Abraham, R. G. & Ellis, R. S. MNRAS, 322, 1. 2001.

[198] Messier, C. Connaissance des Temps. Paris, 1784

[199] Metevier, A. J., Romer, A. K., & Ulmer, M. P. AJ, 119, 1090. 2000.

[200] Moore, B. et al. MNRAS 310, 1147. 1999.

[201] Morgan, W. W. & Dreiser, R. D. ApJ, 269, 438. 1983.

[202] Navarro, J., Frenk, C. & White, S. ApJ 462, 563. 1996.

[203] Navarro, J., Frenk, C. & White, S. ApJ 490, 493. 1997.

[204] Navarro, J. Astrophysical Supercomputing Using Particles. IAU Symposium, Vol. 208. eds., J. Makino and P. Hut. 2001.

[205] Nichol, R. C. et al. ApJ, 521, L21. 1999.

[206] Oemler, A. ApJ, 194, 1. 1974.

[207] Oke, J. B. & Gunn, J. E. ApJ, 266, 713. 1983.

[208] Oke, J. B. et al. PASP, 107, 375. 1995.

[209] Padmanabhan, T. Cosmology and Astrophysics through problems. Cambridge: Cambridge Univ. Press. 1996.

[210] Peacock, J. A. & Heavens, A. F. MNRAS, 217, 805. 1985.

[211] Peebles, P. J. E. The Large Scale Structure of the Universe. Princeton: Princeton Univ. Press. 1980.

[212] Peebles, P. J. E. Principles of Physical Cosmology. Princeton Series in Physics. Princeton Univ. Press. 1993.

[213] Peletier, R. F. et al. AJ, 100, 1091. 1990.

[214] Penzias, A. A. & Wilson, R. W. ApJ, 142, 419. 1965.

[215] Perlman, E. S. et al. ApJ Supplement Series, 140, 265. 2002.

[216] Peterson, J. R. et al. A&A, 365, L104. 2001.

[217] Pierpaoli, E., Scott, D. & White, M. MNRAS, 325, 77. 2001.

[218] Pislar, V. Ph.D. Thesis, Université Paris VI. 1998.

[219] Poggianti, B. M. A&AS, 122, 399. 1997.

[220] Poggianti, B. M. & Barbaro, G. A&A, 325, 1025. 1997.

[221] Poggianti, B. M. et al. ApJ, 518, 576. 1999.

[222] Ponman, T. J., Cannon D. B. & Navarro J. F. Nature, 397, 135. 1999.

[223] Postman, M. & Geller, M. ApJ, 281, 95. 1984.

[224] Press, W. H. & Schechter, P. ApJ, 187, 425. 1974.

[225] Primack, J. R. In Critical Dialogues in Cosmology, ed. N. Turok (World Scientific). 1996. [astro-ph/9610078]

[226] Prugniel, P. & Simien, F. A&A, 321, 111. 1997.

[227] Raymond, J. C. & Smith, B. W. ApJ Supplement Series, 35, 419. 1977.

[228] Reiprich, T. H. & Böhringer, H. ApJ, 567, 716. 2002.

[229] Reisenegger, A. et al. AJ, 120, 523. 2000.

[230] Renzini, A. ApJ 488, 35. 1997.

[231] Rhoads, J. E. et al. AJ, 125, 1006. 2003.

[232] Rich, J. Fundamentals of Cosmology. Springer-Verlag. 2001.

[233] Roberts, M. S. & Haynes, M. P. ARA&A, 32, 115. 1994.

[234] Romer, A. K. et al. ApJ Supplement Series, 126, 209. 2000.

[235] Rosati, P. et al. ApJ, 445, L11. 1995.

[236] Rosati, P. et al. ApJ, 492, L21. 1998.

[237] Rosati, P. et al. AJ, 118, 76. 1999.

[238] Rosati, P. et al. In Large Scale Structure in the X-Ray Universe, ed. M. Plionis, I. Georgantopoulos, p.13. Paris: Atlantisciences. 2000.

[239] Rosati, P., Borgani, S. & Norman, C. ARA&A, 40, 539. 2002.

[240] Rosati, P. Highlights in modern observational cosmology. In Modern cosmology. eds. S. Bonometto, V. Gorini and U. Moschella. Series in high energy physics, cosmology and gravitation. Institute of Physics Publishing. 2002.

[241] Rosati, P. et al. AJ, 2004. In press. [astro-ph/0309546]

[242] Rubin, V. C., Thonnard, N. & Ford, W. K., Jr. ApJ, 238, 471. 1980.

[243] Rudnick, G. et al. AJ, 122, 2205. 2001.

[244] Salpeter, E. E. ApJ, 121, 161. 1955.

[245] Sandage, A. In Galaxies and the Universe, edited by A. Sandage, M. Sandage and J. Kristian, 1975.

[246] Sarazin, C. X-Ray Emission from Clusters of Galaxies. Cambridge: Cambridge Univ. Press. 1988.

[247] Scharf, C. A. et al. ApJ, 477, 79. 1997.

[248] Schechter, P. ApJ, 203, 297. 1976.

[249] Schmidt, M. Nature, 197, 1040. 1963.

[250] Schneider, D. P., Gunn, J. E. & Hoessel J. G. ApJ, 264, 337. 1983.

[251] Schutz, B. F. A First Course in General Relativity. Cambridge: Cambridge Univ. Press. 1990.

[252] Sérsic, J. L. Atlas de Galaxias Australes, Observatorio Astronómico de Córdoba, Argentina. 1968.

[253] Seyfert, C. K. ApJ, 97, 28. 1943.

[254] Shapley, A. E. et al. ApJ, 588, 65. 2003.

[255] Shapley, H. Harvard Coll. Obs. Bull. 874, 9. 1930

[256] Shectman, S. A. et al. ApJ, 470, 172. 1996.

[257] Sheth, R. K. & Tormen, G. MNRAS, 308, 119. 1999.

[258] Silva, D. R. & Cornell, M. E. ApJ Supplement Series, 81, 865. 1992.

[259] Smail, I. et al. ApJ, 479, 70. 1997.

[260] Smith, R. W. The Expanding Universe: Astronomy's 'Great Debate' 1900 - 1931. Cambridge: Cambridge University Press. 1982

[261] Snowden, S. L. & Freyberg, M. J. ApJ, 404, 403. 1993.

[262] Snowden, S. L. et al. ApJ, 424, 714. 1994.

[263] Stanek, K. Z. et al. ApJ, 477, 163. 1997.

[264] Stanford, S. A., Eisenhardt, P. R. & Dickinson, M. ApJ, 492, 461. 1998.

[265] Stanford, S. A. et al. ApJ, 552, 504. 2001.

[266] Stanford, S. A. et al. AJ, 123, 619. 2002.

[267] Steidel, C. C. et al. ApJ, 462, L17. 1996.

[268] Steidel, C. C. et al. ApJ, 519, 1. 1999.

[269] Stevens, R. & Lacy, M. MNRAS, 325, 897. 2001.

[270] Strauss, M. A. et al. AJ, 124, 1810. 2002.

[271] Sunyaev, R. A. & Zeldovich, Ya. B. Comments Astrophys. Space Phys., 2, 66. 1970.

[272] Tamura, T. et al. A&A, 365, L87. 2001.

[273] Terlevich, A. I., Caldwell, N. & Bower, R. G. MNRAS, 326, 1547. 2001.

[274] Teyssier, R. A&A 385, 337. 2002.

[275] Toft, S., Soucailm G. & Hjorth, J. MNRAS, 344, 337. 2003.

[276] Toft, S. et al. A&A, 2003. Submitted.

[277] Tonry, J. & Davis, M. AJ, 84, 1511. 1979.

[278] Tozzi, P. et al. ApJ, 593, 705. 2003.

[279] Tran, K. H. et al. ApJ, 522, 39, 1999.

[280] Treu, T. et al. MNRAS, 326, 237. 2001.

[281] Treu, T. et al. ApJ, 564, 13. 2002.

[282] Trümper, J. Adv. Space Res., 2, No. 4, 241. 1983.

[283] Trümper, J. Science 260, 1769. 1993.

[284] van den Bosch, F. C. & Swaters, R. A. MNRAS 325, 1017. 2001.

[285] Van Dokkum, P. G. et al. ApJ, 500, 714. 1998a.

[286] Van Dokkum, P. G. et al. ApJ, 504, L17. 1998b.

[287] Van Dokkum, P. G. et al. ApJ, 520, L95. 1999.

[288] Van Dokkum, P. G. et al. ApJ, 552, L101. 2001.

[289] Van Dokkum, P. G. & Stanford, S. A. ApJ, 585, 78. 2003.

[290] Viana, P. T. P. & Liddle, A. MNRAS, 281, 323. 1996.

[291] Vikhlinin, A. et al. ApJ, 498, 21. 1998a.

[292] Weinberg, S. Gravitation and Cosmology: principles and applications of the general theory of relativity. John Wiley & Sons, Inc. 1972.

[293] Wells, L. A. Rectifying and Registering Images Using IRAF. April 1994.

[294] Whitmore, B. C. & Gilmore, D. M. ApJ, 367, 64. 1991.

[295] Williams, R. E. et al. AJ, 112, 1335. 1996.

[296] Wu, X.-P., Xue, Y.-J. & Fang L.-Z. ApJ 524, 22. 1999.

[297] Yee, H. K. C. et al. ApJ Supplement Series, 129, 475. 2000.

[298] Zel'dovich, Ya. B. & Sunyaev, R. A. Astrophys. Space Sci., 4, 301. 1969.

[299] Zwicky, F. Helv. Phys. Acta 6, 110. 1933.

[300] Zwicky, F. PASP, 50, 210. 1938

List of Tables

List of Figures